

ELECTRICAL CHARACTERISATION, MODELLING AND  
SIMULATION OF  $\text{Cu}(\text{In,Ga})(\text{Se,S})_2$  SOLAR CELLS

**Dissertation**

zur Erlangung des Doktorgrades der Ingenieurwissenschaften  
(*Dr. Ing.*)

der

Naturwissenschaftlichen Fakultät II  
Chemie, Physik und Mathematik

der Martin-Luther-Universität  
Halle-Wittenberg

vorgelegt von

Frau TETIANA LAVRENKO  
geb. am 09.10.1986 in der Ukraine



Erstgutachter: Prof. Dr. Roland Scheer (Betreuer)

Zweitgutachter: Prof. Dr. Thomas Walter (THU)

Drittgutachter: Prof. Dr. U. Rau (FZ Jülich)

Datum der Einreichung: 19. Juni 2019

Datum der öffentlichen Verteidigung: 19. Dezember 2019

Mitglieder der Promotionskommission: Prof. Dr. G. Schmidt (Vorsitz), Prof. Dr. R. Scheer, Prof. Dr. T. Walter, Prof. Dr. U. Rau, Prof. Dr. H. Roggendorf, Prof. Dr. P. Dold, Prof. Dr. J. Schilling, Prof. Dr. G. Woltersdorf, Prof. Dr. J. Berakdar





Dedicated to my parents:  
*mum*, who told me to be brave and try,  
and  
*dad*, who taught me to be strong and patient.



## **Declaration**

I hereby declare that except where specific reference is made to the work of others, the contents of this dissertation are original and have not been submitted in whole or in part for consideration for any other degree or qualification in this, or any other university. This dissertation is my own work and contains nothing which is the outcome of work done in collaboration with others, except as specified in the text and Acknowledgements.

Tetiana Lavrenko  
June 2019



## Acknowledgements

It is said that a book is not written by a single person. Any book is a result of interaction of the author with other people who directly (via communication, discussions) or indirectly (by encouraging, motivation or just being there at the right time) trigger the author to express him- or herself. The same is true for the presented thesis. There is a number of people whom I would like to thank heartily for contributing to this work in word or deed:

- My supervisors Prof. Dr. Roland Scheer and Prof. Dr. Thomas Walter for helpful discussions, great guidance and enormous patience. Especially I would like to thank Prof. Dr. Thomas Walter for always finding a right word for me to encourage or correct my vector of movement and Prof. Dr. Roland Scheer for giving me a chance to write this thesis. Furthermore, I would like to thank Prof. Dr. Uwe Rau for kindly agreeing to be an examiner and personally coming to the defence. Prof. Dr. Hubert Mantz is greatly acknowledged for his permanent support during the final stage of my writing.
- My colleagues at University of Applied Sciences Ulm who made my work not only meaningful in scientific sense but also more enjoyable and memorable. Special credit I would like to give
  - Dennis Mücke for helping with the admittance measurements and the evaluation of the data of the samples with modified S-profiles;
  - Ricardo Vidal-Lorbada for his readiness to help and advise.
- My colleagues from other research groups with whom I was lucky to work in the course of this work, especially
  - Janet Neerken and Dr. Stephan Heise from University of Oldenburg for providing the SEM images and discussing them.
  - Dr. Matthias Maiberg from University of Halle-Wittenberg for helping me with whatever I needed during my visits to Halle.
  - Torsten Hölscher for doing the TRPL measurements and helping to process the experimental results.
- My gratitude is addressed to the former employees of *BOSCH CISTech Solar* for providing the samples and finding time in their busy schedule to discuss the results and share new ideas.

- My family and friends for their unconditional support and always being there for me, no matter how far away we were from each other.
- Finally, Antons who in his unique way motivated me to move forward. His help in editing and bug-fixing in  $\LaTeX$  is also greatly acknowledged.

## Abstract

In this thesis,  $\text{Cu}(\text{In, Ga})(\text{Se, S})_2$  (CIGSSe) solar cells from an industrial sequential growth process have been investigated. The evaluation of the cell performance has been performed based on the electrical and optoelectronic characterisation in combination with analytical modelling and simulations. The emphasis has been set on studying the impact of compositional gradients — such as  $\text{Ga}/(\text{Ga} + \text{In})$  (GGI) and  $\text{S}/(\text{S} + \text{Se})$  (SSSe) — within the absorber layer on the final device performance. The results showed that a S-incorporation into the surface region and a Ga-accumulation at the back contact lead to the formation of bandgap grading inducing quasi-electric fields, and therefore affecting charge carrier transport properties. It has been demonstrated that it is possible to separate recombination processes from absorption and photocurrent collection by a S-incorporation into the absorber surface. The sulfurisation of the surface region enhances the effective bandgap for recombination at the absorber/buffer interface, whereas the absorber bulk responsible for the photocurrent generation remains unchanged. Furthermore, it has been found that the application of the reciprocity relation (RR) between luminescent emission and external quantum efficiency as a diagnostic tool for solar cells with S- and Ga-gradients have to be handled with care, as under certain conditions deviations between the measured and calculated spectra can be observed. The violation of the RR can be induced by a back grading as a result of the Ga-segregation at the back contact as has become evident from the experimental results. The compliance between the collection probability and excess charge carrier distribution profile within the absorber layer is the main requirement for the RR to hold. However, it was revealed that the collection probability of charge carriers is enhanced due to a Ga-gradient which directs the photogenerated carriers towards the collecting junction and not equal anymore to the injected charge carrier distribution profile which is restricted by a graded region of the absorber. Besides that, locally reduced charge carrier mobility has been recognised as another limiting factor for the validation of the RR, which in fact showed the best fit to the discussed measurements. Taking into accounts all the findings of this thesis, it has been concluded that bandgap grading is an efficient way to improve the final device performance as it allows to separate the effective bandgap for recombination from absorption and photocurrent collection processes.





## Abriss

In der vorliegenden Arbeit wurden  $\text{Cu}(\text{In}, \text{Ga})(\text{Se}, \text{S})_2$  (CIGSSe)-Dünnschichtsolarzellen aus einem industriellen, sequentiellen Beschichtungsprozess charakterisiert und bewertet. Hierfür wurden elektrische und optische Charakterisierungsverfahren in Kombination mit analytischer Modellbildung sowie Simulation eingesetzt und appliziert. Der Schwerpunkt der Arbeit lag bei der Auswirkung von Materialgradienten ( $\text{Ga}/(\text{Ga} + \text{In})$  und  $\text{S}/(\text{S} + \text{Se})$ ) in der Absorberschicht auf die optoelektronischen Eigenschaften der Solarzellen. Die Ergebnisse zeigen, dass der Einbau von Schwefel an der Grenzfläche und die Akkumulation von Gallium am Rückkontakt Gradienten der Bandlückenenergie verursachen, die über quasielektrische Felder den Ladungsträgertransport beeinflussen können. Die Möglichkeit, Rekombinationsprozesse von der Photostromsammlung räumlich zu trennen konnte durch den Einbau von Schwefel an der Absorbergrenzfläche nachgewiesen werden. Diese Anreicherung von Schwefel an der Grenzfläche erhöht die effektive Bandlückenenergie für die Rekombination am Absorber/Puffer-Übergang, während die Bandlückenenergie für die Photostromerzeugung im Volumen des Halbleiters unverändert bleibt. Darüber hinaus konnte aufgezeigt werden, dass die Anwendung des Reziprozitätstheorems zwischen Lumineszenzemission und photovoltaischer Quantenausbeute als diagnostisches Werkzeug für Dünnschichtsolarzellen mit Schwefel- und Gallium-Gradienten mit Vorsicht zu behandeln ist, da unter bestimmten Bedingungen Abweichungen zwischen den gemessenen und berechneten Spektren beobachtet wurden. Abweichungen vom Reziprozitätstheorem als Folge der Gallium-Segregation am Rückkontakt wurden aus experimentellen Ergebnissen ersichtlich. Die Übereinstimmung zwischen der Ladungsträgersammlung photogenerierter Ladungsträger und dem Verteilungsprofil injizierter Minoritäten innerhalb der Absorberschicht ist die Hauptanforderung für die Gültigkeit des Reziprozitätstheorems. Es zeigte sich jedoch, dass die Ladungsträgersammlung durch einen Gallium-Gradienten im Bereich des Rückkontaktes begünstigt wird, während die Injektion von Minoritäten in diesen Bereich durch elektrische Felder limitiert ist. Darüber hinaus wurde eine lokal reduzierte Beweglichkeit der Ladungsträger als weiterer limitierender Faktor für die Validierung des Reziprozitätstheorems identifiziert. Mit dem letzteren Modell konnten die beobachteten Abweichungen vom Reziprozitätstheorem erklärt und interpretiert werden. Unter Berücksichtigung aller Ergebnisse wurde in dieser Arbeit gezeigt, dass der gezielte Einsatz von Gradienten der Bandlückenenergie zu einer signifikanten Steigerung des Wirkungs-

grades dieser Solarzellen führt, da hiermit, eine räumliche Trennung der effektiven Bandlücke für die Rekombination sowie der Bandlücke für die Photostromsammlung möglich wird.

# Publications

- [1] T. Lavrenko, F. Schönberger, Y. Wang, M. Teukam, T. Walter, T. Hahn, and P. Pistor. “Advanced Luminescence Imaging of CIGS Solar Cells”. eng. In: *27th European Photovoltaic Solar Energy Conference and Exhibition; 2174-2178* (2012). DOI: 10.4229/27theupvsec2012-3bo.4.3.
- [2] T. Lavrenko, T. Walter, A. Steigert, and R. Klenk. “Stability Issues of Sputtered Zn(O,S) Buffer Layers for CIGS Thin Film Solar Cells”. eng. In: *28th European Photovoltaic Solar Energy Conference and Exhibition; 2393-2397* (2013). DOI: 10.4229/28theupvsec2013-3bv.6.22.
- [3] T. Lavrenko, T. Ott, and T. Walter. “Benefits of Double Bandgap Grading for Highly Efficient Cu(In,Ga)(Se,S)<sub>2</sub> Thin Film Solar Cells”. eng. In: *29th European Photovoltaic Solar Energy Conference and Exhibition; 1781-1785* (2014). DOI: 10.4229/eupvsec20142014-3dv.2.4.
- [4] T. Ott, T. Lavrenko, T. Walter, R. Schäffler, and H.-J. Fecht. “On the Importance of the Back Contact for Cu (In, Ga) Se<sub>2</sub> Thin Film Solar Cells”. eng. In: *29th European Photovoltaic Solar Energy Conference and Exhibition; 1725-1729* (2014). DOI: 10.4229/eupvsec20142014-3dv.1.26.
- [5] T. Lavrenko, T. Walter, and B. Plesz. “On the Interpretation of Photoluminescence and Vibrating Kelvin Probe Method for Quality Control of Cu(In,Ga)(Se,S)<sub>2</sub> Thin Films”. eng. In: *32nd European Photovoltaic Solar Energy Conference and Exhibition; 1190-1193* (2016). DOI: 10.4229/eupvsec20162016-3cv.4.4.
- [6] T. Lavrenko, R. Vidal Lorbada, D. Muecke, T. Walter, B. Plesz, and R. Schaeffler. “Towards an Improved Understanding of CIGS Thin Film Solar Cells”. eng. In: *33rd European Photovoltaic Solar Energy Conference and Exhibition* (2017), pp. 1013–1016. DOI: 10.4229/eupvsec20172017-3ao.8.3.
- [7] Tetiana Lavrenko, Kerstin Marzinzig, Thomas Walter, Balázs Plesz, and Sándor Röss. “On the application of the vibrating Kelvin probe method for quality control of Cu(In,Ga)(Se,S)<sub>2</sub> thin-film solar modules”. In: *Progress in Photovoltaics: Research and Applications* 24.12 (Feb. 2016), pp. 1554–1565. DOI: 10.1002/pip.2746.

- 
- [8] T. Lavrenko, K. Marzinzig, and T. Walter. "Performance analysis of Cu(In,Ga)(Se,S)<sub>2</sub> thin film solar cells". In: *2015 IEEE 42nd Photovoltaic Specialist Conference (PVSC)*. IEEE, June 2015. DOI: 10.1109/pvsc.2015.7355789.
- [9] Dennis Muecke, Tetiana Lavrenko, Ricardo Vidal Lorbada, and Thomas Walter. "On the Determination of the Back Contact Barrier Height of Cu(In,Ga)(S,Se)<sub>2</sub> Thin Film Solar Cells". In: *2018 IEEE 7th World Conference on Photovoltaic Energy Conversion (WCPEC) (A Joint Conference of 45th IEEE PVSC, 28th PVSEC and 34th EU PVSEC)*. IEEE, June 2018. DOI: 10.1109/pvsc.2018.8547841.
- [10] Ricardo Vidal Lorbada, Thomas Walter, David Fuertes Marrón, Tetiana Lavrenko, and Dennis Muecke. "A Deep Insight into the Electronic Properties of CIGS Modules with Monolithic Interconnects Based on 2D Simulations with TCAD". In: *Coatings* 9.2 (Feb. 2019), p. 128. DOI: 10.3390/coatings9020128.
- [11] Saoussen Merdes, Florian Ziem, Tetiana Lavrenko, Thomas Walter, Iver Lauer mann, Max Klingsporn, Sebastian Schmidt, Frank Hergert, and Rutger Schlatmann. "Above 16% efficient sequentially grown Cu(In,Ga)(Se,S)<sub>2</sub>-based solar cells with atomic layer deposited Zn(O,S) buffers". In: *Progress in Photovoltaics: Research and Applications* 23.11 (Jan. 2015), pp. 1493–1500. DOI: 10.1002/pip.2579.
- [12] Tetiana Lavrenko, Thomas Ott, and Thomas Walter. "Impact of sulfur and gallium gradients on the performance of thin film Cu(In,Ga)(Se,S)<sub>2</sub> solar cells". In: *Thin Solid Films* 582 (May 2015), pp. 51–55. DOI: 10.1016/j.tsf.2014.11.024.
- [13] Tetiana Lavrenko, Thomas Walter, and Balazs Plesz. "A closer look into metastable effects of Cu(In,Ga)Se<sub>2</sub>". In: *physica status solidi c* 14.6 (2017), p. 1600197. DOI: 10.1002/pssc.201600197. URL: <https://onlinelibrary.wiley.com/doi/pdf/10.1002/pssc.201600197>.

# Table of contents

<b>List of figures</b>	<b>xix</b>
<b>List of tables</b>	<b>xxv</b>
<b>Introduction</b>	<b>1</b>
<b>1 Solar cells based on chalcopyrite thin films</b>	<b>5</b>
1.1 State-of-the-art . . . . .	5
1.2 Chalcopyrite crystal structure . . . . .	7
1.3 Thin film growth . . . . .	8
1.3.1 Absorber preparation techniques . . . . .	9
1.4 Defect chemistry and compositional gradients . . . . .	11
1.4.1 Intrinsic defects . . . . .	11
1.4.2 Impact of alkali ion impurities . . . . .	12
1.5 Charge carrier transport . . . . .	13
1.6 Band diagram . . . . .	15
<b>2 Performance limitation and optimisation of solar cells</b>	<b>19</b>
2.1 Shockley-Queisser limit . . . . .	19
2.2 Recombination . . . . .	21
2.2.1 Recombination processes . . . . .	21
2.2.2 Regions of recombination . . . . .	23
2.3 Bandgap engineering . . . . .	27
<b>3 Experimental</b>	<b>29</b>
3.1 Investigated sample sets . . . . .	29
3.1.1 Cell fabrication process . . . . .	29
3.1.2 Samples under investigation . . . . .	30
3.1.3 In-depth variations of gallium and sulfur distributions . . . . .	32
3.2 Characterisation techniques . . . . .	34
3.2.1 Current-voltage characteristics . . . . .	34

3.2.2	Admittance measurements . . . . .	37
3.2.3	Quantum efficiency . . . . .	40
3.2.4	Luminescence measurements . . . . .	42
<b>4</b>	<b>Modelling and simulations</b>	<b>45</b>
4.1	SCAPS modelling . . . . .	45
4.2	Analytical modelling . . . . .	46
4.2.1	Impact of a back grading on charge carrier diffusion . . . . .	47
4.2.2	Back contact passivation due to a Ga-grading . . . . .	49
4.2.3	Field-assisted photocurrent collection . . . . .	57
4.2.4	CIGS/CdS interface passivation due to a S-grading . . . . .	63
4.3	Verification of the reciprocity relation for graded gap solar cells . . . . .	72
4.4	Conclusion . . . . .	84
<b>5</b>	<b>Performance enhancement due to a Ga-gradient</b>	<b>87</b>
5.1	Enhancement of the effective bandgaps for recombination and current collection	87
5.1.1	Motivation: Ga-induced increase in a bandgap energy $E_g$ . . . . .	87
5.1.2	Experiment and Discussion . . . . .	89
5.2	Impact of a Ga-grading on non-Ohmic back contacts . . . . .	96
5.2.1	Motivation: Back contact passivation . . . . .	96
5.2.2	Literature review . . . . .	98
5.2.3	Simulations . . . . .	99
5.2.4	Experiment . . . . .	103
5.3	Conclusions on a Ga-gradient . . . . .	111
<b>6</b>	<b>Impact of a S-incorporation</b>	<b>115</b>
6.1	Motivation: a S-induced increase in $E_g$ . . . . .	115
6.2	Literature review . . . . .	117
6.3	Results and discussion . . . . .	119
6.3.1	Enhancement of the effective bandgap for recombination . . . . .	119
6.3.2	Impact on photocurrent collection and absorption . . . . .	123
6.3.3	Impact on minority carrier lifetimes . . . . .	124
6.3.4	Impact on admittance measurements (in terms of non-ohmic contacts)	132
6.4	Conclusion . . . . .	139
	<b>Summary</b>	<b>141</b>
	<b>Conclusion</b>	<b>145</b>

# List of figures

1.1	(a) Chalcopyrite crystal structure. After [34]; (b) correlation between the lattice constant and the bandgap of the chalcopyrite material. After [35] . . . . .	8
1.2	Schematic drawing of a ZnO/CdS/CIGS heterojunction solar cell. After [54] . .	16
2.1	Band diagram with possible recombination mechanisms in CIGS solar cells: (1) CIGS/CdS interface recombination; (2) QNR recombination; (3) CIGS/Mo back contact interface recombination; (4) SCR recombination. The image is adapted from [34] . . . . .	23
3.1	Schematic of a two-stage absorber formation process. Adopted from [11] . . .	30
3.2	SEM micrographs of the cross-section of the samples with a varied S-amount and chalcogenisation temperature. . . . .	31
3.3	Reference in-depth variations of the Ga- and S-distribution. . . . .	33
3.4	In-depth variations of the Ga-distribution after different diffusion times. . . . .	33
3.5	GDOES depth profiles for (a) low temperature, and (b) high temperature samples with different S-contents. . . . .	34
3.6	Calculated $E_g$ from the GDOES depth profiles for the samples with different S-contents. . . . .	35
3.7	Schematic drawing of an equivalent circuit of a solar cell based on the one-diode model. . . . .	35
3.8	Reference JV-characteristics with the performance parameters. . . . .	36
3.9	Representation of a quantum efficiency curve of one of discussed devices and associable loss mechanisms. Adopted from [81]. . . . .	41
4.1	Simulated band diagram. . . . .	46
4.2	Schematic of the absorber grading profile. . . . .	47
4.3	Impact of the absorber thickness on the effective diffusion length for high (blue line) and low (red line) back surface recombination velocities. . . . .	51

4.4	Impact of the absorber thickness on the device $V_{oc}$ for high (blue line) and low (red line) back surface recombination. The corresponding relative $V_{oc}$ changes are shown with dashed lines. The location of the back contact has to be considered at d. . . . .	52
4.5	Ratio of the D/C-terms with respect to electric field strengths. . . . .	54
4.6	Impact of a back grading on electron diffusion. Electron concentration versus absorber thickness. . . . .	56
4.7	Impact of a back grading on diffusion current as a function of the QNR thickness over diffusion length ratio. . . . .	56
4.8	Impact of effective force field on the collection probability in comparison to a diffusion-limited case of a non-graded absorber. . . . .	58
4.9	Impact of effective force field on the collection function with respect to the field strength. In the calculations, $S_b = 10^6 \frac{cm}{s}$ and $\mu_n = 100 \frac{cm^2}{Vs}$ are used. . . . .	61
4.10	Ratio of the contribution of the C4/C3 terms with respect to varied electric field strengths and back contact recombination velocities. . . . .	62
4.11	Schematic band diagram depicting the conduction band $E_C$ , valence band $E_V$ , Fermi energy level $E_F$ . The parameters to be used in analytical modelling: $E_{G0}$ is the principle bandgap energy; $E_{G1}$ is the energy between the conduction band $E_C$ and Fermi level $E_F$ at $x = 0$ ; $E_{g,rec}$ is the effective bandgap for nonradiative recombination at the position $E_{g0}/2$ . $x = 0$ indicates the onset of the space charge region, and $x = w$ - the CIGS/CdS interface with $E_C$ being an offset of the $E_C$ above the $E_F$ . . . . .	64
4.12	Contour-plot demonstrates the dependence of the relative increase in the effective bandgap for recombination $\left(\frac{\Delta E_{g,rec}}{\Delta E_g}\right)_{exp}$ as a function of parameter $m$ and an overall bandgap enhancement $\Delta E_g$ . . . . .	67
4.13	Simulated VB in the SCR for different grading profiles. . . . .	70
4.14	Simulated $V_{oc}(T)$ -characteristics for different grading profiles. . . . .	70
4.15	EQE measurements (a) and spectral PL responses (b) of the devices with different diffusion times. . . . .	74
4.16	Comparison between the calculated emission based on black body radiation and measured PL emission spectra for the samples with different diffusion times (different Ga-profiles). . . . .	75
4.17	EQE measurements (a) and spectral PL responses (b) of the devices with different S-contents and process temperatures. . . . .	76
4.18	Comparison between the calculated emission based on black body radiation and measured PL emission spectra for the samples with different S-contents for low and medium deposition temperatures. . . . .	77



4.19	Comparison between the calculated emission based on black body radiation and measured PL emission spectra for the samples with different S-contents for high deposition temperatures. . . . .	78
4.20	Comparison of the EQE measured and calculated from the spectral PL. Normalisation has been done for the maximum emission of the measured PL spectra at $E = 1.04 \text{ eV}$ . . . . .	80
4.21	Schematic comparison between the excess charge carrier and the collection function profiles with respect to the bandgap profile in the QNR. . . . .	81
4.22	(a) Simulated in SCAPS electron concentration $n_{ph}$ , and (b) electron current density $J_n$ for different $\mu_n$ values. The orange line schematically represents the bandgap profile. The position of the back contact at $x=0$ . . . . .	83
4.23	Impact of the charge carrier mobilities on the JV-characteristics. . . . .	84
5.1	SCAPS simulated $V_{oc}(T)$ -characteristics for different bandgap energies. . . . .	88
5.2	Light JV-characteristics of the samples with different diffusion . . . . .	90
5.3	Dark JV-characteristics on a semilogarithmic scale for the samples with different annealing times. . . . .	91
5.4	Capacitance-voltage characteristics (a) and doping profiles (b) of the devices with different annealing times . . . . .	92
5.5	Temperature-dependence of the open circuit voltages for the devices with different annealing times . . . . .	92
5.6	Correlation between $V_{oc}$ at room temperature vs. the effective bandgap for absorption (extracted from the spectral PL measurements) with respect to varying annealing times. . . . .	95
5.7	Correlation between the relative increase of $\Delta V_{oc}$ at room temperature versus optical and electrical bandgaps with respect to the reference device for different annealing times. . . . .	96
5.8	Band diagram for a standard CIGS solar cell (without Ga-grading) with a back contact barrier. . . . .	97
5.9	Band diagram of a standard CIGS solar cell with a Ga-step and a back barrier at the back contact. . . . .	97
5.10	Two diode model which represents the main diode and the Schottky diode at the back contact operating in the 'wrong' direction. . . . .	99
5.11	Simulated illuminated JV-characteristics with an Ohmic back contact (blue), with a Ga-step (red), with a back barrier of $300 \text{ meV}$ (green) and with the barrier and Ga-step at the back contact (brown) at $180 \text{ K}$ . . . . .	100
5.12	Simulated Suns – $V_{oc}$ -characteristics for three cases: the flat band alignment at the back contact (blue), an enlarged back contact barrier (red), and a back contact barrier with a Ga-gradient. . . . .	101

5.13	Impact of the back contact barrier and a Ga-gradient on the $V_{oc}$ saturation based on SCAPS simulation. . . . .	101
5.14	Experimental intensity-dependent JV-characteristics at 180 K of two devices: with and without Ga-gradient. . . . .	104
5.15	Temperature dependence of $V_{oc}$ for different illumination intensities for the samples with and without Ga-gradient. . . . .	105
5.16	Temperature dependence of a diode ideality factor A derived from JV-characteristics in the dark and under illumination for the device (a) with a Ga-gradient and (b) without Ga-gradient. . . . .	106
5.17	Temperature-dependent admittance measurements: (a) frequency-dependence of the capacitance; (b) temperature-dependence of $-\omega \cdot \frac{dC}{d\omega}$ for the sample with long annealing time. . . . .	108
5.18	Arrhenius plot for the samples with different annealing times. . . . .	109
5.19	Experimental JV(T)-characteristics of the samples with different annealing times. . . . .	110
5.20	Comparison of the JV(T)- and Cf(T)-characteristics of two devices. The roll-over behaviour of the forward current corresponds to the capacitance step observed at low temperatures, and <i>vice versa</i> . . . . .	112
6.1	Simulated band diagram with a front grading due to the S-incorporation. The effect of S can be seen in the down shift of the VB. . . . .	116
6.2	SCAPS simulation of (a) $V_{oc}(T)$ -characteristics and (b) EQE-spectra for two devices: without (Se) and with a S-rich layer at the absorber surface (Se+S). . . . .	117
6.3	Light JV-characteristics of the samples with different S-contents. . . . .	119
6.4	Dark JV-characteristics on a semi-logarithmic scale for the samples with different S-contents. . . . .	120
6.5	Dependence of the open circuit voltages over temperature for different sulfur contents. . . . .	121
6.6	Capacitance-voltage characteristics (a) and doping profiles (b) of the devices with different S-contents and deposition temperatures. . . . .	122
6.7	External quantum efficiency and spectral PL-measurements on the samples with different sulfur contents and deposition temperatures. . . . .	123
6.8	Correlation between $V_{oc}$ at room temperature versus optical and electrical bandgaps with respect to different S-contents, high temperature process. . . . .	124
6.9	Comparison of TRPL measurements for the samples with different S-contents. Excitation level is 100%. . . . .	125
6.10	Correlation between $V_{oc}$ at room temperature and minority carrier lifetimes $\tau_n$ with respect to varied S-contents and process temperatures for the discussed samples. . . . .	126

---

6.11	Excitation- and temperature-dependence of TRPL measurements of the samples with different S-contents. . . . .	128
6.12	Excitation- and temperature-dependence of TRPL measurements of the samples with different S-contents. . . . .	129
6.13	Calculated minority carrier lifetimes from the experimental data for the discussed samples with different sulfur contents for low deposition temperatures. . . . .	131
6.14	Calculated minority carrier lifetimes from the experimental data for the discussed samples with different sulfur contents for medium and high deposition temperatures (for the diffusion coefficient for electrons $D_n=2.56 \frac{cm^2}{s}$ ). . . . .	131
6.15	Comparison of temperature-dependent JV-measurements of the samples with a varied S-content and chalcogenised at low temperature. . . . .	133
6.16	Comparison of temperature-dependent JV-measurements of the samples with a varied S-content and chalcogenised at high temperature. . . . .	134
6.17	Frequency-dependent admittance measurements of the low temperature process samples for different S-contents. . . . .	136
6.18	Frequency-dependent admittance measurements of the high temperature process samples for different S-contents. . . . .	137
6.19	Arrhenius plots of the devices with varied S-content with extracted activation energies $E_a$ which color corresponds to the color of the corresponding curve. . . . .	138



# List of tables

1.1	Electrical activity of the native point defects. . . . .	11
3.1	Fabrication details of the investigated sample sets . . . . .	32
4.1	Input parameters . . . . .	68
4.2	Comparison of grading profiles with respect to the effective bandgap for recombination $E_{g,rec}$ and the relative increase in the effective bandgap for recombination $\frac{\Delta E_{g,rec}}{\Delta E_g}$ based on the modelling and SCAPS simulation results. . . . .	68
4.3	Impact of diffusion time on the effective bandgap for absorption and current collection for different Ga-profiles. . . . .	74
4.4	Fitting parameters for the samples with different annealing times . . . . .	76
4.5	Impact of a sulfur content and a sulfurisation temperature on the effective bandgap for absorption and current collection . . . . .	79
4.6	Fitting parameters for the samples with different S-contents (low temperature process) . . . . .	79
4.7	Fitting parameters for the samples with different S-contents (high temperature process) . . . . .	80
5.1	Performance parameters of the studied solar cells. . . . .	89
5.2	Extracted bandgap energies from EQE-measurements . . . . .	94
5.3	Extracted bandgap energies . . . . .	94
5.4	Comparison of the barrier heights extracted from the $V_{oc}(T)$ - and $C_f(T)$ -measurements of the devices with different annealing times. . . . .	110
6.1	Performance parameters of the devices with varied S-contents and process temperatures. . . . .	121
6.2	Extracted $E_g$ from $V_{oc}(T)$ - and EQE-measurements in comparison to the device $V_{oc}$ at room temperature and doping density $N_a$ . . . . .	122
6.3	Measured $V_{oc}$ at room temperature and $\tau_n$ with extracted $E_g$ from $V_{oc}(T)$ -measurements for varied S-contents and deposition temperatures. . . . .	130

6.4 Comparison of activation energies extracted from JV(T)- and Cf(T)-measurements. . . . .	135
6.5 Short summary on the investigated solar cells . . . . .	144

# Introduction

*It worked first, was explained later. [1]*

Cu(In, Ga)Se<sub>2</sub> / Cu(In, Ga)(Se, S)<sub>2</sub> (CIGS) solar cells is a thin film technology with the highest level of cell efficiencies of 23.35%. [2] The production of CIGS solar cells is well-controlled on both laboratory and industrial scales and therefore cost-effective. [3, 4, 5] The recent efficiency improvements have been very impressive and positioned these solar cells as a serious counterpart to the market-ruling Si-technology. If this tendency is to be continued, CIGS will have the best qualifications for a further strong market growth. To promote commercialisation, an optimised fabrication process which can transfer the laboratory scale efficiencies to commercial products has to be established. Such a process is a pledge of success not only for a manufacturing company but for the CIGS technology in general.

CIGS solar cells which are fabricated nowadays have basically a similar device structure. [6, 7, 8, 9] The major difference, however, is the absorber growth process. Two processes already able to demonstrate the world champions in terms of the device efficiency are coevaporation and sequential growth methods. The coevaporation technique requires the simultaneous and homogeneous thermal evaporation of the constituent elements in the certain proportions to form high quality CIGS absorbers. The sequential or sulfurisation after selenisation (SAS) processes have been developed as the alternative way of the absorber layer deposition. In this approach, the metallic precursors such as a Cu/Ga alloy and In targets are usually deposited by sputtering. Next, the metal layers are converted to CIGS in a chalcogen containing atmosphere (sequential selenisation/sulfurisation process). [10]

In this thesis, Cu(In, Ga)(Se, S)<sub>2</sub> (CIGSSe) solar cells from an industrial sequential growth process have been investigated. The evaluation of the cell performance has been performed based on the electrical and optoelectronic characterisation in combination with analytical modelling and simulations. The aim of this thesis is to correlate results from different measurement techniques with the device performance. This approach allows, first of all, to see whether a particular measurement method relates to the device performance, and, secondly, to build a comprehensive understanding of the mechanisms taking place in CIGS solar cells. The emphasis has been set on studying the impact of compositional gradients – such as Ga/(Ga + In) (GGI) and S/(S + Se) (SSSe) – within the absorber layer on the final device performance. An in-depth variation of the GGI ratio is an inherent and rather undesired feature of a sequential

growth process. Due to the slow diffusion properties, Ga-atoms accumulate in the vicinity of the CIGS/back contact interface. This leads to the phase segregation of the CuInSe<sub>2</sub> layer with a low bandgap  $E_g$  close to the pn-junction and the wide-gap CuGaSe<sub>2</sub> layer at the backside of the absorber. Such growth kinetics have a rather detrimental effect on the cell open circuit voltage  $V_{oc}$  due to a low  $E_g$  in the SCR. The incorporation of S into the absorber surface has been found an effective approach to enhance the  $E_g$  and to reduce recombination losses.[11, 12] The sulfuration step investigated in this thesis has been realised with reactive chalcogen compounds (gaseous process in H<sub>2</sub>Se and H<sub>2</sub>S). The impact of both S- and Ga-gradients on the back contact has been reported. Therefore, after analysing the discussed gradients with respect to the overall device performance and stability the effectiveness of the sequential growth process has been assessed. The advantages and weak points of the investigated solar cells have been outlined. Furthermore, possible optimisation approaches have been suggested which could be viewed in terms of the potential industrial implementation.

The thesis is structured in the following way. **Chapter 1** provides fundamental information on CIGS solar cells which has to facilitate a better understanding of the experimental results. The state of the art of the CIGS thin film technology is briefly discussed.

The maximum theoretical conversion efficiency of a solar cell can be defined using *Shockley-Queisser limit* also known as *the radiative efficiency limit*. The latter name implies radiative recombination as a main and only efficiency loss in an ideal solar cell. The principle statements of the limit are described in **Chapter 2**. Furthermore, other non-radiative recombination mechanisms are presented which limit the efficiency of real solar cells. As a potential ‘cure’ and performance optimisation approach, bandgap engineering in terms of bandgap grading due to the in-depth variations of the S/(S + Se) and Ga/(Ga + In) ratios is discussed.

**Chapter 3** opens up the experimental part of the thesis. The absorber fabrication processes of the investigated samples are described first. As the absorber profile has a double graded structure, the GDOES data is analysed with respect to the in-depth variations of the Ga- and S-distribution throughout the absorber layer. Next, the characterisation techniques used in the course of the research are given. The working principles of the measurement setups are described. Additionally, the reciprocity relation (RR) between (electro/photo)luminescence and quantum efficiency of a solar cell is presented. The RR theorem is discussed as a non-classical (alternative) quality assessment tool which can be used during the fabrication process.

**Chapter 4** is an analytical part which deals with mathematical modelling of graded bandgap solar cells. In order to verify the theoretical models (which inevitably are based on many assumptions and simplifications) SCAPS-1D simulation results are shown. Apart from the analysis of the Ga- and S-gradients, the validity of the reciprocity theorem for graded bandgap absorbers is discussed.

The impact of a Ga-gradient on the device performance is investigated in **Chapter 5**. The chapter starts with a short literature review and the motivation to study this question. Next, SCAPS-simulation results are intended to visualise certain physical processes and to predict the



measurement outcome. The experimental evidence on the Ga-impact on the optical and electrical parameters as well as on the stability of solar cells with different Ga-distribution profiles finalise the chapter. A short summary on the experimental findings comes in the end.

The outline of **Chapter 6** on the effect of a S-gradient on the overall performance of a solar cell is similar to the one of the previous chapter. After the theoretical part, the experimental results of the samples with different S-distribution profiles induced by varied chalcogenisation process temperatures and S-contents are presented. A short summary on the observations closes up the chapter.

The experimental results and simulations discussed in this thesis will be summarised in **Conclusions**. The methods which are already implemented (as deduced from the measurement data of the discussed samples) to optimise/enhance the overall device performance as well as possible suggestions for a further improvement will be discussed.



# Chapter 1

## Solar cells based on chalcopyrite thin films

### 1.1 State-of-the-art

Research and development of solar cells based on chalcopyrite absorber layers have been conducted for more than 40 years. [13] Having been born accidentally in the beginning of the 1970s during the development of broad-band photodetectors for optical communication, CIGS solar cells have covered a long way and experienced numerous modifications before being able to reach the current world record efficiency of 23.35%. [13, 14] One of the most important events which can be considered as a beginning of their evolution was the addition of Ga to the CuInSe<sub>2</sub> thin film. This technological step allowed to grow absorber layers with varying bandgaps in order to match optimally the solar spectrum for the specific applications. [15, 4] Using a Ga/(Ga + In) ratio of 23%, the conversion efficiencies of more than 10% have been reported by Mickelsen and Chen in 1987 [16].

After the successful presentation of the efficiencies at *Boeing Aerospace Company*, the co-evaporation growth process has been adopted by *ARCO Solar Inc.* which after some time gave birth to the 2-stage sequential process as a way for a lower-cost commercialisation of CIGS-based solar cells. This company was the first to introduce hybrid chalcogenisation processes consisting of solid-state Se and hydride gases: H<sub>2</sub>Se for the improvement of the optoelectronic properties and H<sub>2</sub>S for the bandgap increase at the surface region of the absorber layers. [17] These modifications led to significant efficiency improvements due to the enhancement of the device V<sub>oc</sub>. This process provided a groundwork for the *sulfurisation after selenisation* approach for the absorber growth implemented nowadays at *Solar Frontier*.

The discovery of the beneficial effect of higher temperatures on the CIGS crystal growth allowed to improve significantly the absorber quality and to design optimal temperature profiles at different growth phases.

The implementation of the CdS film grown by chemical bath deposition (CBD) as a highly-resistive buffer layer significantly improved the interface quality between the absorber and buffer layers. This resulted not only in increased short circuit current densities  $J_{sc}$ , but also in higher open circuit voltages  $V_{oc}$  of the devices. [18] Since then CBD became a standard method for the deposition of CdS buffer layers as it allowed the easily controlled and well-adapted junction formation with chalcopyrite absorbers. From this point the life and optimisation of CIGS solar cells in the configuration as they are known today has begun.

Another breakthrough in the course of the development of CIGS solar cells is related to the discovery of the effect of Na on the electronic properties and the crystal growth of CIGS thin films reported in 1993. [19] Na impurities from the substrates (soda-lime glass) [19], from the precursor layer (NaF) deposited between the back contact and the substrate [20] or after the absorber layer growth as the post-deposition treatment (PDT) [21] resulted in the superior morphology of thin films and significantly enhanced the doping level of the absorber layers.

A great boom of reported efficiencies has begun after the introduction of the heavy alkali elements as the PDT of CIGS absorbers. 20.4% has been achieved by *Swiss Federal Laboratories for Materials Science and Technology (EMPA)* after the introduction of KF-PDT in 2013. [22] The efficiency of 20.8% has been announced one year later by *ZSW*. [23] This achievement indicated the beginning of a new era for CIGS solar cells. The efficiency territory which earlier belonged solely to the Si-technology opened up for CIGS. One more year later the efficiency increased to 21.7% with the RbF-PDT. [24] Further careful optimisation of growth processes and additional modification of the layer structure resulted in the current world record efficiency. [25, 14] However, despite the continuous advances CIGS solar cells still have not reached their technically feasible limit of 30%. [26]

An intermediate goal on the way to the predicted technical limit is 25%. [6, 27] The lacking percentage points are to be achieved by addressing the key efficiency limiting factors in the state-of-the-art CIGS solar cells. The factors are non-radiative recombination and light absorption losses. The improvement of the absorber material is one way to reduce recombination events. A better match to the solar spectrum can be accomplished by employing novel doping concepts to CIGS. [28] The heavy alkali metal dopants favor the formation of the secondary phases with a large  $E_g$ , which can modify the electronic structure of the absorber material. Moreover, this can lead to the passivation of the absorber surface and the grain boundaries having a beneficial effect on minority carrier lifetimes. Intrinsic grain boundaries (GB) introduce localised deep states within the absorber  $E_g$  which act as recombination centers being detrimental to the cell performance. The concept of GB engineering is under active investigation and aimed at the elimination of the deep states and creation of the hole barriers and electron sinkers which have to promote the effective charge separation at the GBs and to improve the overall carrier collection. Furthermore, the mitigation of the detrimental effect of the potential fluctuations can be realised by the K-treatment and bandgap grading.

About 2% efficiency improvement is expected to be obtained by the introduction of novel concepts to the surfaces and interfaces based on the adaptation of the well-established technological processes for Si-based solar cells (the concept of the passivated emitter and rear cells (PERC)). The effects of the point-contact openings through a passivation layer both at the back and front contact are studied. The idea of a point pn-junction has been demonstrated in [29] by incorporating ZnS nano-dots into the  $\text{In}_2\text{S}_3$  buffer layer leading to the improved device performance. The author found that the positive surface charge induced by the passivation layer leads to the occurrence of band-bending having a beneficial impact on the device  $V_{oc}$  and efficiency. Recently, this approach has been transformed to the surface nano-patterning technique based on the self-assembling of alkali condensates at the CIGS front surface. [30] The nano-sized point contacts for the absorber/back contact interface has been actively investigated for ultra-thin absorber solar cells. However, till now this concept has not been considered for the application to conventional solar cells as back contact recombination was believed to be negligible due to a Ga-back grading.

The optimisation of light management in CIGS solar cells can have multiple realisations. Parasitic absorption in the buffer and window layers is diminished by the application of wider gap materials. [7, 6, 15]. Furthermore, alkali-PDT improves the morphology of the absorber surface enabling to use thinner buffer/window layers which also benefits  $J_{sc}$  as has been reported in [7]. Optical losses associated with insufficient absorption of light entering the absorber layer can be reduced by enhancing light path inside the absorber. However, the macroscopic approaches are limited by geometric optics. Therefore, the investigation of the nano-optical concepts is ongoing. [31] The concept of a dielectric spacer which was also borrowed from the Si-technology is aimed at the reduction of the device rear reflection losses and to the enhancement of light in the CIGS layer. The realisation of this concept can be done by using the  $\text{MgF}_2/\text{Al}_2\text{O}_3$  bi-layer between the absorber and Mo back contact according to [32].

Furthermore, an innovative method for contacting the cells on the module level has been developed by *Solibro*. This company implements a metal grid on the top of the window layer to reduce the front contact resistive losses. Moreover, a thinner TCO layer can be used which further reduces transmission losses on module level.

## 1.2 Chalcopyrite crystal structure

The  $\text{Cu}(\text{In}, \text{Ga})\text{Se}_2$  alloy is formed from the  $\text{CuInSe}_2$  and  $\text{CuGaSe}_2$  compounds which belong to the I-III-VI<sub>2</sub> material family and crystallise in the tetragonal chalcopyrite structure. These ternary materials in the chalcopyrite structure can be viewed as an analogue of a binary II-VI compound in the cubic zinc-blende structure similar to ZnSe but where the Zn-sites are alternately occupied by the Cu- and In-atoms. [33]

The sketch of the crystal structure of the chalcopyrite is shown in Figure 1.1a. The bandgap energy  $E_g$  of the alloy can be varied by changing the ratio of the group III elements, In and Ga,

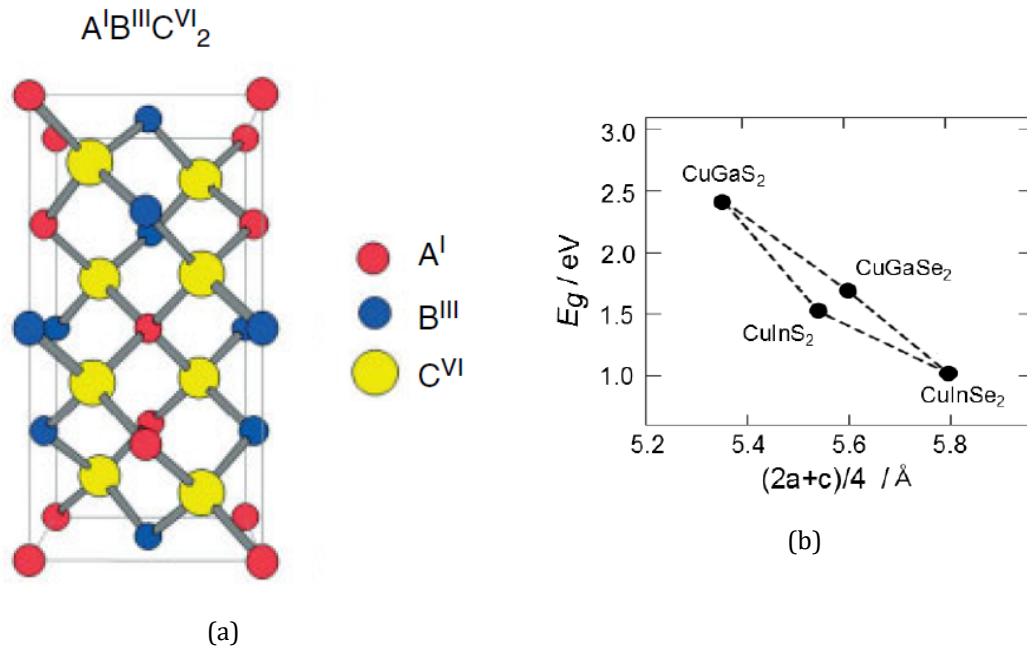


Figure 1.1: (a) Chalcopyrite crystal structure. After [34]; (b) correlation between the lattice constant and the bandgap of the chalcopyrite material. After [35]

from 1.03 eV for the pure CuInSe<sub>2</sub> up to 1.68 eV for the pure CuGaSe<sub>2</sub> material. Furthermore, changing the ratio of the group VI elements, Se and S,  $E_g$  can be adjusted from 1.03 eV for the CuInSe<sub>2</sub> up to 1.53 eV for the CuInS<sub>2</sub> material, or in case of the Ga-based compounds — from 1.68 eV for the CuGaSe<sub>2</sub> up to 2.43 eV for the CuGaS<sub>2</sub>. Figure 1.1b clearly demonstrates how the adjustment of the Ga/(Ga + In) and S/(S + Se) ratios can modify the lattice constants and thus the bandgap energies of the corresponding compounds within the Cu(In, Ga)(Se, S)<sub>2</sub> system. The mentioned parameters vary approximately linear with respect to the atomic ratios of the constituents following Vegard's law. This implies that any desired compound can be produced within this pentenary system, as there is no miscibility gap in the whole composition range. [33] This outstanding material property gives a huge potential to the bandgap engineering process by enabling to control the alloy composition or to grow layered films with alternating in-depth compositions in order to boost efficiencies of the devices based on these modified materials. The practical implementation of this material property constitutes the basis of this thesis.

### 1.3 Thin film growth

The preparation of the CIGS-based solar cells usually begins with the deposition of the absorber material on a Mo-coated glass substrate. The heterojunction is formed by growing a thin n-type (traditionally CdS) buffer layer. Transparent conducting oxides (TCO) are applied as the

front contact. The typical front contact consists of a thin layer of the intrinsic ZnO followed by the Al-doped ZnO layer. A more detailed description of the functional layers can be found elsewhere. [34, 10]

### 1.3.1 Absorber preparation techniques

Despite a wide range of the absorber growth processes, there are two methods which dominate both research and large scale production:

**Coevaporation process** — material deposition and the chalcogenide film formation take place at the same processing step;

**Selenisation process** — two stage process where the film formation requires a second step, also known as a chalcogenation stage.

#### 1.3.1.1 Coevaporation process

During the coevaporation process the Cu-In-Ga-Se elements are deposited from the different sources onto the heated substrate. Thereby, the chalcogenide film is formed already out of the gas phase. The adjustment of the individual evaporation rates enables to optimize the growth process and introduce desired compositional gradients. The composition of the deposited material with respect to the metals corresponds to their evaporation rates. The stoichiometry (concentration of the VI element relative to the metals) is maintained by the group VI element overpressure in the initial state of cooling down the substrate. The molecularity (the ratio of the group I metal over the group III metal concentration) has to be adjusted by a precise control of the metal source temperatures. [10]

The advantages of this process:

- the simultaneous material deposition and film formation. However, the film growth can be done in one step (so-called *a single layer coevaporation process*) or in two- or three stages when certain constituent fluxes are directed alternately onto the substrate.
- a precise control over the film composition and bandgap is possible. [4]
- a high rate and low cost method suitable for an industrial inline process. Significant cost reduction by using the coevaporation growth has been demonstrated by *First Solar* in the production of CdTe solar cells. [5]

The disadvantages of the coevaporation method:

- the desired Cu-evaporation can be difficult to control [36];
- scaling-up to large areas and high rates is difficult while maintaining the composition and microstructure uniformity in order to ensure highly efficient devices. [37] However, implementing this method, large area modules and high efficiencies have been achieved by Manz, Solibro. [38, 39]

### 1.3.1.2 Selenisation process

The selenisation process, also known as the sequential deposition, consists of two different processing steps. During the first stage, a metallic precursor is deposited by sputtering. Due to the low melting point of Ga, the Cu/Ga alloy and In targets are used. The semiconductor is formed in the second step after exposing the precursors to a chalcogen atmosphere at elevated temperatures (selenisation/sulfurisation).

The advantages of the method [10]:

- the Cu/III ratio can be precisely controlled at the first stage;
- sputtering is scalable easily;
- good reproducibility and large area uniformity of the thickness of the individual layers.

The disadvantages:

- additional processing steps needed;
- the film formation heavily depends on the thermodynamics and phase formation kinetics. Fortunately, the in-depth variations of the element concentrations after the selenisation step prove to be close to optimal, especially, if the sulfurisation step is involved (see Chapter 6 and 7);
- high temperature and chemically aggressive environment cause enhanced equipment degradation.

### 1.3.1.3 Alternative processes

In search of alternative methods to improve the quality of semiconductor films or to reduce production costs on large area scale, other absorber growth techniques have been developed. High-quality semiconducting films can be prepared by using molecular beam epitaxy or metal organic chemical vapour deposition methods. However, these methods are usually applied for research purposes in order to study the intrinsic semiconductor properties.

Non-vacuum absorber preparation processes are another economic solution for large mass production. CIGS absorbers have been prepared by the particle-based screen printing technique followed by rapid thermal annealing densification. This method retains the ideal stoichiometric ratio due to the CIGS particles in the coating paste and thereby eliminates the necessity of the conventional selenisation process. [40] A two-step process based on the electrodeposition of the metal precursors with a subsequent atmospheric pressure thermal treatment to produce  $\text{Cu(In, Ga)(Se, S)}_2$  absorbers by reacting with elemental Se and S resulted in 17.3% solar cell and 14% full scale module efficiencies. No hydride gases were used in this non-vacuum growth process making it more environment friendly and less expensive at the same time. [41]



## 1.4 Defect chemistry and compositional gradients

### 1.4.1 Intrinsic defects

The electronic properties of semiconductors strongly depend on their doping level. Unlike Si and GaAs semiconductors which are doped extrinsically, the electronic properties of CIGS material are determined by intrinsic defects. These defects stem from the deviation from the ideal

Table 1.1: Electrical activity of the native point defects.

Point defect	Electrical activity
$Cu_i, Se_{Cu}, In_{Se}$	single donor
$V_{Se}, In_{Cu}$	double donor
$In_i$	triple donor
$V_{Cu}, Se_{In}, Cu_{Se}$	single acceptor
$Se_i, Cu_{In}$	double acceptor
$V_{In}$	triple acceptor

stoichiometry in the chalcopyrite crystal. There exist 12 point defects which can act either as donor or acceptor levels affecting the electro-optical properties of the CIGS semiconductor:

- 3 vacancies ( $V_{Cu}$ ,  $V_{In}$ , and  $V_{Se}$ );
- 3 interstitials ( $Cu_i$ ,  $In_i$ , and  $Se_i$ );
- 6 antisites ( $Se_{Cu}$ ,  $In_{Se}$ ,  $In_{Cu}$ ,  $Se_{In}$ ,  $Cu_{Se}$ , and  $Cu_{In}$ ).

The electrical activity of the point defects is described in Table 1.1 [42]. The denotation "single", "double" and "triple" corresponds to the number of the energy levels in the forbidden gap induced by the corresponding defect. [42] The activation energies of the shallow and deep defect levels have been calculated, for example, using the effective mass theory and compared to the experimental results in [42].

The formation enthalpies of the point defects and defect complexes differ significantly. The formation energies depend on material composition and for some native defects can be very small and even negative. For example, the copper vacancy  $V_{Cu}^-$  has a negative formation energy meaning that large amount of these defects may form under equilibrium conditions. [33] The negatively charged  $V_{Cu}^-$  acts as a single acceptor and is a dominant defect center which governs the p-type doping of the CIGS semiconductor. A  $V_{Se} - V_{Cu}$  double vacancy has been reported to be the origin for different metastabilities in CIGS solar cells. [43, 44] The defect complexes  $(2V_{Cu}^- + In_{Cu}^{2+})$ ,  $(Cu_{In}^{2-} + In_{Cu}^{2+})$  have positive but very low formation energies. The dependence of the formation energy on the electron Fermi level explains the high degree of self-compensation observed in the chalcopyrite semiconductors. The growth of CIGS thin films is a complex process which is affected by many variables.

### 1.4.2 Impact of alkali ion impurities

As has been mentioned before, one of the turning points in the evolution of CIGS-based solar cells was an introduction of the alkali metals into CIGS absorber. The beneficial impact of Na on the electrical performance has been reported for the first time in [18, 19]. The Na-containing glass substrate facilitated the preferred  $\langle 112 \rangle$  crystal growth orientation and resulted in a superior morphology of CIGS thin films. Probably, even a more important effect was the enhancement of the effective p-type doping which led to increased device efficiencies due to improved  $V_{oc}$  and FF. [45] Some years later the CIGS devices were deposited on the polycrystalline alumina substrates, and the influence of different alkali-based precursors on the CIGS film growth was investigated. [20] The presence of the NaF precursor layer yielded devices with increased majority carrier concentrations and boosted efficiencies by more than  $\Delta\eta = 20\%$  compared to the control samples. A similar effect but with a smaller gain was observed after using the KF and CsF precursors. It was suggested that Na annihilates donor states stemming from the  $In_{Cu}$  point defects and therefore increases the net acceptor concentrations. However, this passivation mechanism became less effective in Cu-poor materials as the probability of forming the  $In_{Cu}$  defects was supposed to decrease. [20] An impact of the Na-diffusion after the CIGS film growth (as PDT) has been investigated in [21]. It has been found that NaF-PDT did not affect the crystal growth kinetics, but significantly increased the net carrier concentrations and conductivities compared to the sodium-free absorbers. A strong increase in the device efficiencies has been assigned to the grain boundary passivation. The chemical behaviour of Na has been investigated further in [46] and was related to the oxidation-related passivation of Se-vacancies  $V_{Se}$  present at  $Cu(In, Ga)Se_2$  surfaces and grain boundaries. However, the findings published in [47] concluded the incorporation of Na into the  $Cu(In, Ga)Se_2$  lattice replacing In or Ga. The extrinsic defects  $Na_{In}/Na_{Ga}$  were expected to act as acceptors and enhance the p-type conductivity. This conclusion was in agreement with results in [20] which indicated the increase in the unit cell volume based on x-ray diffraction measurements. Furthermore, it has been reported that the presence of sodium at different stages of the absorber deposition strongly influences the grain growth and the  $Ga/(Ga+In)$  ratio. [48] During the absorber layer formation Na impedes the interdiffusion of Ga- and In-atoms enhancing the bandgap grading. A comprehensive overview on the effects of sodium and its incorporation strategies can be found, for example, in [49].

The implementation of the K-treatment acts as a doping and a surface modification procedure. [50] Even though potassium has been often detected in CIGS films earlier, its potential impact on the device electrical properties had not got a proper attention up to 2013 when a new world record efficiency has been announced by a Swiss group [22]. The authors reported that the KF-PDT modified the CIGS surface by promoting Cd-diffusion into the Cu-depleted absorber surface and thereby improving the CIGS/CdS interface quality. After this discovery, many groups started to experiment with KF-PDT applying it during different stages of the ab-

sorber deposition process. 21.0% has been achieved from a  $1\text{ cm}^2$  laboratory cell grown by a coevaporation process at *Solibro*. A Japanese group announced 22.3% for a sequentially grown  $\text{Cu}(\text{In}, \text{Ga})(\text{Se}, \text{S})_2$  laboratory cell with a standard  $\text{CdS}/\text{ZnO}$  window material and 22.8% with a  $(\text{Zn}, \text{Mg})\text{O}/\text{Zn}(\text{O}, \text{S}, \text{OH})$  modified window. In [6], the researchers from *Solar Frontier* reported that the enhancement of  $V_{\text{oc}}$  originated from the increase of carrier concentration in the SCR and the reduction of interface recombination. Compositional and electronic changes of the CIGS surface have been also reported in [50]. A strong Cu-depletion at the near surface region has been detected in the K-treated samples. The removal of Cu-atoms from the CIGS material results in a higher bandgap and a higher amount of Cu-vacancies in this region. [51] As a result, the bandgap widening due to the lowering of the VB maximum efficiently reduced interface recombination losses and boosted the device  $V_{\text{oc}}$  by 60–70 mV. [50] Moreover, it is interesting to mention that a method of incorporating K into the absorber film can bring different by-side effects. The KF-precursor has a strongly hygroscopic nature. Therefore, an *in-situ* incorporation of K has to be preferable as an *ex-situ* incorporation may lead to enhanced surface oxidation causing decreased FF. [50] Furthermore, the K incorporation by using sputtered CuGa : KF precursors can considerably affect the Ga-distribution profile during the selenisation step. [52] In contrast to the KF-PDT which constricts the Ga-in-diffusion towards the front interface due to the formation of  $K_{\text{Cu}}$  defects, the presence of the CuGa : KF surface layer increases the Ga-content close to the interface layer resulting in a notch-type overall profile. The bandgap widening due to the K-treatment of the absorber surface has to be considered as an alternative or supplementary approach to the S-incorporation step.

The success with the Na- and K-incorporation provoked a variety of experiments with heavier alkali metals. It has been found that similar to Na and K, the incorporation of Cs and Rb as PDT improves the absorber surface morphology. Therefore, thinner CdS buffer layers could be grown resulting in improved photon absorption in the high energy wing, and thereby an increased  $J_{\text{ph}}$ . Furthermore, it has been found, both experimentally and by DFT-modelling, that light alkali are replaced by heavy alkalis on the Cu- and interstitial sites leading to an increased Cu-depleted region. Moreover, the incorporation of K, Cs and Rb leads to the formation of the secondary phases such that  $E_{\text{g}}(\text{AlkGaSe}_2) > E_{\text{g}}(\text{AlkInSe}_2)$ . Thus, the  $\text{Alk}(\text{In}, \text{Ga})\text{Se}_2$  layer may act as the passivation layer on the CIGS surface. The electronic effect of alkalis has to be still investigated.

## 1.5 Charge carrier transport

Technically, a CIGS solar cell is a complex device which comprises of several heterointerfaces. The principle heterointerface which defines the device performance is a pn-(hetero)junction formed between the p-type absorber and n-type buffer/window layers. The absorber layer with the bandgap energy  $E_{\text{g}}$  is a photosensitive semiconductor which is responsible for the absorption of incident photons with energies  $E_{h\nu} \geq E_{\text{g}}$  and where the photogeneration of electron-

hole pairs takes place. The main function of the pn-junction then is the collection and separation of photogenerated charge carriers in such a way that electrons are driven to the n-type material and holes are transported to the back contact. The collection probability can be greatly affected by geometry and bandgap gradients of the absorber layer.

Thus, the operating principle of CIGS solar cells is similar to the one of a pn-junction if the buffer layer is assumed negligibly thin. A comprehensive reading on the operation and properties of a pn-junction can be found in [53].

The transport of charge carriers within a pn-(hetero)structure is commonly formulated in terms of two physical mechanisms, drift and diffusion. A starting point for the analysis of the transport of electrons and holes is the *transport equations* given by [34]

$$J_n(x) = \mu_n n(x) \cdot \frac{dE_{Fn}(x)}{dx} \quad (1.1)$$

$$J_p(x) = \mu_p p(x) \cdot \frac{dE_{Fp}(x)}{dx}, \quad (1.2)$$

where  $J_n(x)$  and  $J_p(x)$  are the current densities of electrons and holes, respectively;  $n$  and  $p$  are the carrier densities, and  $\mu_n$  and  $\mu_p$  are their mobilities. The *physical meaning* of these equations is that the electric current in a semiconductor device is driven by a gradient of the electrostatic potential, gradients of the electron affinity and the bandgap energy as well as by gradients of the quasi-Fermi levels of electrons and holes  $E_{Fn}$  and  $E_{Fp}$ . [34]

The continuity equations are traditionally used for the analysis and the determination of the electrical parameters and characteristics of a semiconductor device. The equations introduce the particle flux densities of electrons and holes,  $J_n/q$  and  $J_p/q$ , additionally accounting for their generation and recombination (see Equ. 1.3 and 1.4 [34]).

$$\frac{\delta n(x)}{dt} = G_n(x) - U_n(x) + \frac{1}{q} \cdot \frac{dJ_n(x)}{dx} \quad (1.3)$$

$$\frac{\delta p(x)}{dt} = G_p(x) - U_p(x) - \frac{1}{q} \cdot \frac{dJ_p(x)}{dx}, \quad (1.4)$$

where  $G_n/U_n$  and  $G_p/U_p$  are the generation/recombination rates of electrons and holes, respectively. Under equilibrium conditions,  $G_n = U_n$  and  $G_p = U_p$ . In case of generation and recombination via trap states  $G_n \neq G_p$  and  $U_n \neq U_p$ .

The Poisson equation relates the charge densities and the electric potential. Under assumption of  $\epsilon = const$ , the equation reads

$$\frac{d^2\phi(x)}{dx^2} = -\frac{\rho(x)}{\epsilon}, \quad (1.5)$$

where  $\rho$  is the space charge.

The space charge can be defined as

$$\rho(x) = \frac{q}{\epsilon(x)} \cdot [p(x) - n(x) + N_D^+(x) - N_A^-(x)] \quad (1.6)$$

with  $n(x)$  and  $p(x)$  being mobile charge carriers and  $N_D^+$  and  $N_A^-$  fixed charges in the form of charged donors and acceptors, respectively.

The ideal current-voltage characteristic of a pn-device is given by Shockley [53]

$$J(V) = J_p + J_n = J_0 \cdot \left[ \exp\left(\frac{qV}{kT}\right) - 1 \right] \quad (1.7)$$

having a strong voltage-dependence with  $J_0 = \frac{qD_p n_i^2}{L_p N_D} + \frac{qD_n n_i^2}{L_n N_A}$  comprising the electron and hole current components. The Shockley equation is based on the abrupt depletion layer approximation and assumes no generation-recombination current in the depletion region. In order to account for the recombination current in the SCR, the expression 1.7 has to be rewritten as [53]

$$J(V) = q \sqrt{\frac{D_n n_i^2}{\tau_n N_A}} \exp\left(\frac{qV}{kT}\right) + \sqrt{\frac{\pi kT n_i}{2 \tau_n E_0}} \exp\left(\frac{qV}{2kT}\right) \quad (1.8)$$

where  $E_0 = \sqrt{\frac{qN_A(2V_{bi}-V)}{\epsilon_s}}$  is the electric field at the location of maximum recombination for an abrupt  $n^+p$ -junction [34].

The disadvantages of the heterojunction are the following: significant lattice mismatch can create numerous interface defects leading to the photovoltage losses; the difference in the bandgap energies can lead to unfavourable band alignments. It is where bandgap engineering comes in handy.

## 1.6 Band diagram

The performance of CIGS solar cells significantly depends on the band alignment at the interfaces and absorber bandgap profile. Thus, the electronic properties of CIGS solar cells can be investigated using the energy band model or band diagram. The band diagram describes a device behavior in terms of the energy levels between valence  $E_V$  and conduction  $E_C$  bands. The key characteristic of the semiconductor material is the energy bandgap  $E_g$ . The value of  $E_g$  is of fundamental importance to the operation of solar cells as it corresponds to the minimum energy needed to release an electron from a covalent bond to the conduction band to enable the electron to contribute to the current flow.

The equilibrium band diagram of the  $Mo/Cu(In, Ga)Se_2/CdS/ZnO$  heterostructure is sketched in Figure 1.2. The band diagram is deliberately simplified in order to explain the basic electronic transport properties of CIGS solar cells. The band diagram consists of the conduc-

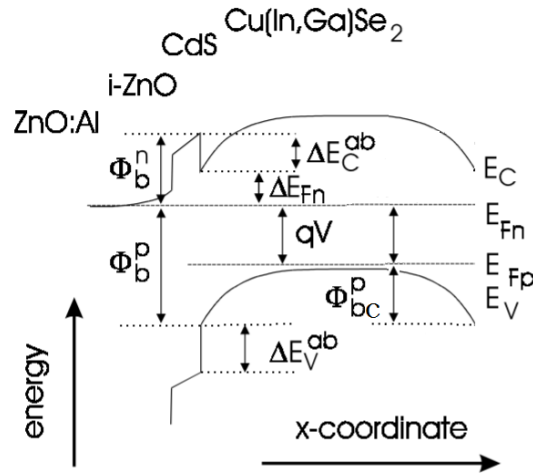


Figure 1.2: Schematic drawing of a ZnO/CdS/CIGS heterojunction solar cell. After [54]

tion  $E_C$  and valence  $E_V$  band energies of the  $\text{Cu(In, Ga)Se}_2$  absorber, CdS buffer and ZnO window layers. Apart of the  $E_g$  of the functional layers, the bandgap discontinuities or bandgap offsets play a crucial role. Here, only the interfaces between the absorber/ buffer and absorber/back contact layers will be discussed. The conduction band  $\Delta E_C^{ab}$  offset between the absorber and buffer layer defines the potential barriers  $\Phi_b^p$  and  $\Phi_b^n$  for holes and electrons, respectively.  $\Phi_b^p$  describes the barrier height which has to be overcome by holes in order to reach the absorber/buffer interface. This parameter is important in terms of interface recombination losses. The barrier height for electrons  $\Phi_b^n$  affects the fill factor of a solar cell and is determined as  $\Phi_b^n = \Delta E_{Fn} + \Delta E_C^{ab}$ , where  $\Delta E_{Fn}$  is the energy difference between the Fermi level  $E_F$  and the  $E_C$  at the absorber/buffer interface. [1] The valence band offset  $\Delta E_V^{ab}$  between the absorber and buffer layers is traditionally determined by photoelectron spectroscopy. [1] By knowing the valence band maximum (VBM) and the semiconductor bandgap energy  $E_g$ , the position of the conduction band minimum (CBM) can be calculated.

The position of the Fermi level  $E_F$  at the absorber/buffer interface is another critical aspect regarding carrier recombination losses and the device performance in general. Depending on the  $E_g$  and the composition of the absorber layer, the  $E_F$  can lie above or below the midgap. In state-of-the-art CIGS solar cells, the  $E_F$  is located close to the CB implying the inverted surface. The type inversion (from p- to n-CIGS due to the diffusion of Cd-ions during the buffer layer deposition leading to the Cd-doped CIGS surface [55]) reduces the concentration of mobile holes at the interface significantly suppressing interface recombination. The presence of the inversion layer can be also explained in terms of the electronic states at the CIGS surface. Positively charged Se-vacancies ( $V_{Se}$ ) induce band-bending at the absorber surface giving rise to the n-type inversion and pinning the position of the  $E_F$  level.

---

At the absorber/back contact interface, the potential barrier  $\Phi_{bc}^p$  describes the barrier of the transport of holes to the back contact. This barrier is equal to the Schottky barrier height between the p-CIGS and Mo-metal contact. The Schottky contact hinders the transport of majority charge carriers resulting in different JV-characteristic anomalies. [56, 57, 58]





## Chapter 2

# Performance limitation and optimisation of solar cells

*The main aim of the optimisation of a solar cell is to increase its power conversion efficiency. To attain this aim three steps have to be followed: (a) determination of the upper efficiency limit; (b) identification of efficiency loss mechanisms; (c) implementation of preventive measures with respect to the loss mechanisms. In this chapter, a general introduction to the concept of the Shockley-Queisser (SQ) limit also known as the radiative efficiency limit of a solar cells will be given. Since the efficiency limitation of real devices is not restricted only by radiative processes, other non-radiative recombination mechanisms are described additionally. As one of the approaches to optimise the performance of existing solar cells, bandgap engineering in terms of bandgap grading is discussed in the end.*

### 2.1 Shockley-Queisser limit

The detailed balance limit of the efficiency derived by Shockley and Queisser in 1961 [59] estimates the maximum conversion limit and the theoretical potential for the improvement of a photovoltaic cell. The derivation assumes a single absorber bandgap and a single pn-junction.

The SQ-model assumes the following: (1) absorption of light is solely determined by the absorber bandgap  $E_g$ : all photons with energy  $E \geq E_g$  are absorbed; (2) exactly one electron-hole pair is generated by each absorbed photon; (3) the only loss mechanism is radiative recombination of electron-hole pairs with successive emission of photons; (4) the collection probability of all photogenerated charge carriers is unity.

According to the assumption (1) and (2), the photogenerated current density can be estimated as a product of the solar spectrum  $\phi_{sun}$  and the absorber absorptance  $\alpha(E)$  which is

interpolated as a step-function [60]:

$$J_{sc} = q \int_0^{\infty} \phi_{sun}(E) \alpha(E) dE = q \int_{E_g}^{\infty} \phi_{sun}(E) dE \quad (2.1)$$

The principle of detailed balance postulates that every microscopic process in a physical system must be compensated by its respective inverse process, when the physical system is at thermodynamic equilibrium with its ambient. In agreement with the assumption (3), in the dark and without applied bias to a solar cell the absorbed and emitted photon fluxes have to be equal and counterbalance each other. Under these conditions, a solar cell behaves as an ideal black body radiator. Thermal radiation emitted by a solar cell as a black body at temperature  $T$  is given by Planck's law. The emission properties of a solar cell under non-equilibrium conditions, that is under illumination or voltage bias, are described by Würfel's generalisation of Planck's law. Non-equilibrium emission is determined by the splitting of the quasi-Fermi levels of electrons and holes  $\mu = E_{Fn} - E_{Fp}$ . The quasi-Fermi levels are flat according to the assumption (4) which implies the perfect connection of the junction to the entire volume in a solar cell. The emitted photon flux under the applied voltage  $V$  is thus given by

$$\phi(V, E) = \frac{2\pi E^2}{h^3 c^2} \cdot \frac{\alpha(E)}{\exp\left(\frac{E-qV}{kT}\right) - 1}, \quad (2.2)$$

where  $h$  is the Planck constant,  $c$  is the velocity of light in vacuum, and  $kT$  is the thermal energy. For small voltages ( $(E - qV) \geq kT$ ), Equ. 2.2 can be simplified to the product of the black body emission and voltage-dependent part

$$\phi(V, E) = \alpha(E) \frac{2\pi E^2}{h^3 c^2} \exp\left(\frac{-E}{kT}\right) \exp\left(\frac{qV}{kT}\right) = \alpha(E) \phi_{bb} \exp\left(\frac{qV}{kT}\right) \quad (2.3)$$

The emission flux described by Equ. 2.3 has to originate from the radiative recombination of the charge carriers injected by the junction and result in the recombination current  $J_{rad,rec}$  in order to fulfil the requirement (3). Therefore, the dark current density of a solar cell (with radiative recombination only) can be written as

$$J_d = J_{rad,rec} = q \int_0^{\infty} \alpha(E) \phi(V, E) dE = q \int_{E_g}^{\infty} \phi_{bb} dE \left[ \exp\left(\frac{qV}{kT}\right) - 1 \right] = J_{0,rad} \left[ \exp\left(\frac{qV}{kT}\right) - 1 \right], \quad (2.4)$$

where  $J_{0,rad}$  is the radiative saturation current density.

Under illumination and applied bias the current-voltage characteristic of a solar cell in the SQ-limit is defined as the superposition of the dark  $J_d$  and photogenerated  $J_{sc}$  current densities which are derived in Equ. 2.4 and 2.1, respectively. Therefore, the total current through a solar

cell is equal to

$$J = J_d - J_{sc} = J_{0,rad} \left[ \exp\left(\frac{qV}{kT}\right) - 1 \right] - J_{sc} \quad (2.5)$$

In order to extract the  $V_{oc}$  in the SQ-limit, the total current  $J$  has to be equated to 0 and the obtained expression solved for  $V$ . This gives

$$V_{oc} = \frac{kT}{q} \ln\left(\frac{J_{sc}}{J_{0,rad}} + 1\right) \quad (2.6)$$

The maximum achievable efficiency of a solar cell under the AM1.5 spectrum is therefore 33% according to the SQ-model. This efficiency corresponds to an absorber material with  $E_g = 1.35$  eV.

### Résumé

*The SQ-limit can be considered as one of the key contributions in the photovoltaic field. Nowadays, the conversion efficiencies calculated from this model serve as a starting point for the estimation of technically feasible efficiencies which can be achieved with CIGS absorbers but are much lower than the predicted ones. Obviously, one of the reasons is the neglect of non-radiative recombination which significantly dominates radiative events in the performance of real solar cells. This is the largest inconformity of this model. Therefore, different types of recombination mechanisms which degrade the efficiency and the regions where recombination is likely to occur in real solar cells are discussed below.*

## 2.2 Recombination

A semiconductor is said to be in thermal equilibrium if every process in the semiconductor is exactly balanced by its inverse process. In this state, in any region of the semiconductor the product of the concentrations of free electrons and holes is equal to the intrinsic carrier concentration squared

$$n \cdot p = n_i^2 \quad (2.7)$$

When thermal equilibrium is disturbed, in response to light or voltage bias, recombination ( $n \cdot p > n_i^2$ ) and generation processes ( $n \cdot p < n_i^2$ ) take place alternately in order to restore the energy balance. Any defects or impurities within or at the surface of a semiconductor promote recombination events.

### 2.2.1 Recombination processes

Absorption of a photon with sufficient energy excites an electron from the valence band to a higher energetic level in the conduction band. This process is known as generation. However,

in order to restore the energy balance in a material, the electron will tend to occupy a vacant place in a lower energetic level in the valence band again. This process is called recombination. Dominant recombination processes which take place in CIGS solar cells can be divided into following categories:

### Band-to-band recombination

The band-to-band recombination is a radiative process resulting in the emission of a photon with the energy  $E_{ph} = E_C - E_V$ . The net recombination rate under non-equilibrium conditions is proportional to the product of the electron and hole concentrations by

$$R = U_0 - G_0 = B \cdot (n \cdot p - n_i^2), \quad (2.8)$$

where  $U_0$  is the recombination rate,  $G_0$  is the thermal generation rate, and  $B$  is the recombination coefficient. The net recombination rate  $R$  is used to define the Shockley-Queisser limit for an ideal pn-junction solar cell as discussed in Section 2.1.

### Auger recombination

The Auger recombination is another intrinsic recombination process when electrons and holes recombine in a band-to-band transition but the resulting energy is transferred to a third particle (hole or electron). Since electrons are minority carriers in the p-type CIGS semiconductor, the probability of this recombination process is very low. The Auger recombination is the limiting process in case of highly doped semiconductors (e.g. Si solar cells) or under high injection conditions (e.g. solar cells under concentration) [61].

### Recombination via a defect state

The recombination via defect states complements the band-to-band recombination. As its name implies, this transition involves defect states which may arise from incorporated impurities, lattice or surface defects. Since the energy released in this sub-transition is smaller than in a band-to-band one, phonon processes (non-radiative events) dominate the energy transfer. [34] This recombination process has been studied by Shockley and Read and Hall independently, therefore it is referred as Shockley-Read-Hall (SRH) recombination. Four sub-processes are possible in this transition:

1. *capture of electrons:*

$$R_{n,c} = n \cdot \beta_n \cdot N_t \cdot (1 - n_t) \quad (2.9)$$

2. *reemission of electrons:*

$$R_{n,e} = \beta_n \cdot N_C \cdot N_t \cdot n_t \cdot \exp\left(-\frac{E_C - E_t}{kT}\right) \quad (2.10)$$

3. *capture of holes:*

$$R_{p,c} = p \cdot \beta_p \cdot N_t \cdot n_t \quad (2.11)$$

4. *reemission of holes:*

$$R_{p,e} = \beta_p \cdot N_V \cdot N_t \cdot (1 - n_t) \cdot \exp\left(-\frac{E_t - E_V}{kT}\right) \quad (2.12)$$

with  $\beta_{n,p}$  corresponding to the capture coefficients for electrons and holes, respectively;  $N_t$  - the density of defect states;  $n_t$  - the probability that a defect is occupied by an electron. According to SRH statics, the net recombination rate is given by:

$$R_{SRH} = \frac{n \cdot p - n_i^2}{\tau_n \cdot (p + p^*) + \tau_p \cdot (n + n^*)}, \quad (2.13)$$

where  $\tau_{n,p}$  is the lifetimes of electrons and holes, respectively;  $p^* = N_V \cdot \exp\left(-\frac{E_t - E_V}{kT}\right)$ ;  $n^* = N_C \cdot \exp\left(-\frac{E_C - E_t}{kT}\right)$ .  $n^*$  and  $p^*$  are the carrier densities which would emerge if the Fermi energy level  $E_F$  would coincide with the defect energy level  $E_t$ .

The defect states located in the middle of the forbidden gap will act as recombination centres, whereas the shallow levels will act as trapping states.

### 2.2.2 Regions of recombination

The limitations imposed by non-radiative recombination is one of the major reasons why the efficiency of CIGS solar is below the theoretical limit defined by radiative recombination only. The (dark) recombination current of a typical CIGS solar cell can be described by the general

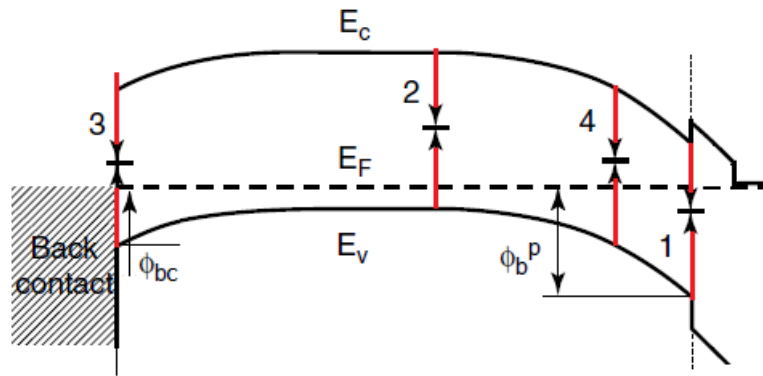


Figure 2.1: Band diagram with possible recombination mechanisms in CIGS solar cells: (1) CIGS/CdS interface recombination; (2) QNR recombination; (3) CIGS/Mo back contact interface recombination; (4) SCR recombination. The image is adapted from [34]

diode equation:

$$J_{rec} = J_0 \cdot \left[ \exp\left(\frac{qV}{AkT}\right) - 1 \right] \quad (2.14)$$

with the saturation current  $J_0 = J_{00} \cdot \exp\left(\frac{-E_a}{AkT}\right)$ , where  $E_a$  is the activation energy of the saturation current  $J_0$  and the weakly temperature dependent prefactor  $J_{00}$ . The ideality factor  $A$  and the activation energy  $E_a$  depend on the recombination mechanism which dominates  $J_0$ . Thus, defining the  $E_a$  and  $A$  the dominant recombination mechanism can be identified. The different recombination paths in a typical CIGS solar cell are indicated in Figure 2.1.

The temperature-dependent study of the recombination current density  $J_{rec}$  is one of the approaches to determine the activation energy  $E_a$  and discriminate between the limitation of bulk and interface recombination. [17] A direct correlation between the recombination current and the device  $V_{oc}$  exists. The temperature dependence of  $V_{oc}$  can be deduced from the expression for the device  $J_{sc}$  under given illumination intensity (see Equ. 2.15)

$$J_{sc} = J_0 \left[ \exp\left(\frac{qV_{oc}}{AkT}\right) - 1 \right] = J_{00} \exp\left(\frac{-E_a}{AkT}\right) \left[ \exp\left(\frac{qV_{oc}}{AkT}\right) - 1 \right] \quad (2.15)$$

From Equ. 2.15 the correlation between the device  $V_{oc}$  and the activation energy  $E_a$  for non-radiative recombination can be derived

$$V_{oc} = \frac{E_a}{q} - \frac{AkT}{q} \ln\left(\frac{J_{00}}{J_{sc}}\right) \quad (2.16)$$

Hence, the extrapolation of  $V_{oc}$  to 0K yields the activation energy for non-radiative recombination  $E_a$  as long as  $J_{sc}$  and  $J_{00}$  are temperature-independent. In the following, the limitations imposed on  $V_{oc}$  by recombination in the bulk of the absorber (QNR and SCR) and at the interfaces (CIGS/CdS and CIGS/Mo) as shown in Figure 2.1 are discussed.

### Path 1 - recombination at the CIGS/CdS interface

Electronic loss mechanism by recombination at the absorber/buffer interface may be caused by lattice mismatch or segregation of impurities. This recombination path has been a limiting factor and still is for wide-gap CGS/CdS-based solar cells. In case of interface recombination the activation energy for recombination current can be smaller than the  $E_g$  ( $E_a < E_g$ ) and be equal to the potential barrier for holes at the interface  $\Phi_b^p$ . Holes are minority at the interface, therefore the recombination rate at the interface is determined by the hole concentration. [62] The recombination current is given by [63]

$$J_{rec} = J_{00} \exp\left(\frac{-\Phi_b^p}{AkT}\right) \left[ \exp\left(\frac{qV}{AkT}\right) - 1 \right] \quad (2.17)$$

In case of  $E_a < E_g$ ,  $V_{oc}$  can be limited by a small value of  $\Phi_b^p$  as a result of enhanced interface recombination. There is a linear correlation between  $V_{oc}$  and  $\Phi_b^p$  [1]

$$V_{oc} = \frac{\Phi_b^p}{q} - \frac{kT}{q} \ln \left( \frac{qS_p N_V}{J_{sc}} \right), \quad (2.18)$$

where  $S_p$  is the interface recombination velocity for holes.

### Path 2 - recombination in the QNR

Under assumption of long lifetime, most of injected charge carriers pass the SCR without recombination and diffuse to the QNR. Being minority carriers they are subjected to recombination via defect states. [34] Under conditions that the absorber thickness is much larger than the diffusion length of minority carriers, that is  $d \gg L_n$ , back surface recombination can be neglected. Therefore, the recombination current in the limit of QNR recombination can be calculated from the continuity equation for electrons using the SRH statistics. [34] The expression for the recombination current reads

$$J_{rec} = J_{00} \exp \left( \frac{-E_g}{kT} \right) \left[ \exp \left( \frac{qV}{kT} \right) - 1 \right] \quad (2.19)$$

with  $A=1$ . The device  $V_{oc}$  in the limit of QNR recombination can be defined as [1]

$$V_{oc} = \frac{E_g}{q} - \frac{kT}{q} \ln \left( \frac{qD_n N_C N_V}{J_{sc} N_a L_n} \right) \quad (2.20)$$

resulting in the activation energy equal to the absorber bandgap  $E_a = E_g$ .

### Path 3 - recombination at the CIGS/Mo back contact interface

Back contact recombination can be considered as a dominating loss mechanism under conditions when  $d \ll L_n$ . In this case, injected electrons diffuse to the back contact and recombine there with abundant holes. [34] In the limit of back surface recombination different operating regimes of a solar cell can be distinguished. [64] "Solar cell regime" is a normal diode-like behaviour observed at high temperatures. The activation energy for SRH nonradiative recombination is determined by the bandgap of the absorber, that is  $E_a = E_g$ . The recombination current is defined similar to Equ. 2.19. The expression for  $V_{oc}$  is similar to Equ. 2.20 but the diffusion length of minority carriers  $L_n$  has to be replaced by the effective diffusion length  $L_{eff}$  [1]

$$L_{eff} = L_n \cdot \frac{\cosh(l^{-1}) + s_b \sinh(l^{-1})}{s_b \cosh(l^{-1}) + \sinh(l^{-1})}, \quad (2.21)$$

where  $s_b = S_b L_n / D_n$  and  $l = L_n / d$ .

The "double-diode" behaviour can be usually detected at low temperatures when the CIGS/Mo contact forms a Schottky contact. Such a contact induces significant resistive losses due to the Schottky barrier. The Schottky contact is a rectifying junction with the polarity opposite to the polarity of the main junction. Under conditions when the Schottky diode is activated, the measured  $A$  can be significantly larger than two. Performance losses with respect to the device  $V_{oc}$  have been detected even though the presence of the back contact barrier has not been reflected in JV-characteristics. [65]

The Schottky back contact model can be extended to the phototransistor model. [58] This model is applicable to the cases when the diffusion length of charge carriers is in the range or larger than the absorber thickness leading to the significant carrier injection to the back contact. In this case, the Schottky contact demonstrates pronounced minority carrier collection properties acting reciprocally to the "electronic mirror" induced by the (quasi)-back surface field. The expression for  $V_{oc}$  in the limit of the phototransistor behaviour reads

$$V_{oc} = \frac{E_g - \Phi_{bc}}{q} - \frac{kT}{q} \ln \left( \frac{\alpha J_{E00}}{J_{C00}} \right), \quad (2.22)$$

where  $\Phi_{bc}$  is the Schottky barrier height at the back contact,  $\alpha$  is the amplification factor,  $J_{E00}$  and  $J_{C00}$  are the temperature-independent prefactors of the main and Schottky diode, respectively. From Equ. 2.22 one can see that the device  $V_{oc}$  becomes independent of the  $J_{ph}$  and therefore illumination intensity what is one of the characteristic features of the phototransistor model.

#### Path 4 - recombination in the SCR

Recombination rates in the SCR are governed by the SRH statistics. Maximum SCR recombination occurs at the position with  $\tau_p n = \tau_n p$ . The recombination current density in the SCR is given by [1]

$$J_{rec} = J_{00} \exp \left( \frac{-E_g}{AkT} \right) \left[ \exp \left( \frac{qV}{AkT} \right) - 1 \right] \quad (2.23)$$

with  $A=2$  and  $E_a = E_g$ . The device  $V_{oc}$  in the limit of SCR recombination can be written in the form

$$V_{oc} = \frac{E_g}{q} - \frac{AkT}{q} \ln \left( \frac{AkTD_n \pi \sqrt{N_C N_V}}{J_{sc} F_m L_n^2} \right), \quad (2.24)$$

where  $F_m = \sqrt{\frac{2qN_a V_{bm}}{\epsilon_s}}$  is the electric field at the position of maximum recombination. The parameter  $F_m$  is a function of the doping density  $N_a$ , band-bending  $V_{bm}$  and the dielectric constant of the absorber  $\epsilon_s$ . The term  $\pi kT/qF_m$  can be interpreted as an effective width of the recombination zone. [34]



## 2.3 Bandgap engineering

CIGS material used to fabricate highly efficient solar cells usually has the bandgap in the range of 1.0 - 1.2 eV depending on the deposition process. [3, 7] These values are somewhat lower than predicted to achieve the maximum conversion efficiency. [59] Bandgap engineering has been recognised as an efficient way to increase the efficiency of CIGS-based solar cells by tuning the absorber electronic properties (by varying the absorber  $E_g$ ) in order to enhance absorption and photocurrent collection and to mitigate recombination processes. This approach is based on alloying the absorber with Ga and/or S depending on the absorber deposition method. [7, 6] The incorporation of the heavy alkali atoms have been also found effective in the modification of the electronic properties of CIGS absorbers. [25, 28]

Recent world record efficiencies have been achieved by using absorber films with a double graded structure. [7, 6] A wide gap material was ensured towards the front (CIGS/CdS) and back (CIGS/Mo) interfaces with a characteristic notch of a low gap material in-between by means of the depth-dependent  $[Ga]/[In]+[Ga]$  and/or  $[S]/[Se]+[S]$  ratios. In literature and hereafter, the notation "front" and "back" grading with respect to the corresponding interface is used. Such composition gradients directly affect the  $E_g$ -profile and thereby the device electronic properties. The beneficial effects of an optimised  $E_g$ -grading can be seen in the reduction of the recombination probability, and therefore charge carrier losses. However, the modification of the light absorption properties in solar cells by introducing a wide gap material has to be kept in mind. In this context, a wide bandgap alloy would be preferred at the front and back interfaces to reduce recombination losses whereas the absorber bulk should have a low  $E_g$  to enhance absorption. Such a double graded approach effectively separates two mutually exclusive processes, recombination and collection of charge carriers. Suppressed recombination at the interface(s) by a wide  $E_g$  material increases the device  $V_{oc}$  whereas a preserved low  $E_g$  material in the bulk does not deteriorate the device  $J_{ph}$ . This approach is often referred as the **separation of recombination processes from absorption and photocurrent collection**. [66]

Due to the technological aspects, a S-incorporation into the absorber surface close to the front interface is traditionally used for the sequentially grown absorbers. [67, 6, 12] S shifts the valence band edge downwards leading to the hole depleted surface and decreased interface recombination with electrons from the CdS layer. [66] Furthermore, increasing the  $E_g$  at the absorber surface by varying  $S/(S+Se)$ -gradients has a minor impact on  $E_C$ , and therefore a favourable band alignment between the absorber and buffer layers is not affected.

In coevaporated CIGS, a Ga-gradient for the front grading is used. In contrast to S, Ga predominantly changes the conduction band minimum  $E_C$  lifting it upwards which indeed results in an increased bandgap close to the interface, but additionally changes the band alignment between the absorber and buffer layers. Therefore, the role of an increased bandgap towards CdS due to a Ga-grading is not always conclusive with respect to the overall efficiency improvement of coevaporated devices. [7] An optimal Ga-concentration and a gradient slope is very impor-

tant for the device performance. [7, 68, 69] Moreover, the position of a Ga-notch relative to the front interface has to be also considered. [7]

Furthermore, an increased  $E_g$  towards the Mo back contact as a result of a Ga-accumulation proved to be beneficial for both coevaporation and sequential technologies. Acting as a quasi-back surface field (also known as "electron mirror"), a  $E_c$ -grading accelerates close to the back contact generated electrons towards the pn-junction. This improves the carrier collection as well as reduces back contact recombination and suppresses the phototransistor effects.

A recent trend in the absorber optimisation approach is the development of the postdeposition treatment based on the incorporation of heavier (than widely used Na) alkali atoms such as K, Cs and Rb. [23, 25] The implementation of the KF post-treatment modifies the absorber surface leading to the formation of the surface layer with a larger  $E_g$  [50], presumably the  $KInSe_2$  secondary phase [28]. The impact of Cs and Rb is still under investigation, but the similar action to K has been predicted theoretically [28] and observed experimentally [25]. These findings emphasise the potential of the alkali-based post-deposition treatment in terms of the absorber surface modification and further optimisation of the overall performance of CIGS-based devices.

# Chapter 3

## Experimental

*In this chapter, the process of  $\text{Cu}(\text{In}, \text{Ga})(\text{Se}, \text{S})_2$  absorber formation will be described. Fabrication details of the investigated solar cells will be given. Data on compositional gradients, such as in-depth profiles of gallium and sulfur, necessary to understand the diode characteristics and optoelectronic properties of the studied devices will be also outlined. Moreover, a general introduction to the measurement techniques used in this work will be provided. A brief theoretical background is followed by the description of the corresponding measurement setup.*

### 3.1 Investigated sample sets

#### 3.1.1 Cell fabrication process

The standard process sequence to fabricate  $\text{Cu}(\text{In}, \text{Ga})(\text{Se}, \text{S})_2$ -based solar cells is described in [70, 3]. It starts with dc magnetron sputtering of the  $0.4 \mu\text{m}$  thick molybdenum back electrode on the preconditioned soda lime glass ( $3 \text{ mm}$ ). Then, laser patterning of the molybdenum contact (P1-scribe) is performed to define the cell width for the monolithic cell interconnection. The two-stage absorber growth process comes next. In the first step, the metallic CuGaIn precursor stack is sequentially deposited by dc magnetron sputtering from separate CuGa alloy and In targets. Alternating layers of CuGa and elemental In are sputtered at elemental ratios of  $[\text{Cu}]/([\text{In}] + [\text{Ga}]) = 0.92$  and  $[\text{Ga}]/([\text{In}] + [\text{Ga}]) = 0.26$ . The chalcopyrite is formed in the second step. During the chemical reaction process, the metallic precursors were first exposed to a  $\text{H}_2\text{Se} : \text{Ar}$  gaseous mixture at around  $400^\circ\text{C}$  for about  $60 \text{ min}$  to form composite alloys consisting of binary selenides and I-III-VI ternary alloy. Next, the samples are heated to reaction temperatures of about  $550^\circ\text{C}$  in the presence of  $\text{H}_2\text{S}$  diluted in Ar to produce single-phase  $\text{Cu}(\text{In}, \text{Ga})(\text{Se}, \text{S})_2$  absorbers. The duration of chalcogenisation is  $2 \text{ h}$ . The reaction of the metallic precursor and the chalcogens is controlled via the concentration of the reactive species and the temperature profile of the process. The schematic of this absorber formation technology is demonstrated in Figure 3.1.

As a next step, the films are processed to complete solar cells by growing a 50 nm thick CdS buffer layer in a wet chemical bath. Afterwards, reactive RF magnetron sputtering of the 50 nm intermediate layer of intrinsic ZnO (i-ZnO) comes followed by the second patterning step (P2) which integrates cell series connection. In the end, the 1.2  $\mu\text{m}$  thick transparent front electrode is deposited from a ceramic ZnO : Al<sub>2</sub>O<sub>3</sub> by dc magnetron sputtering. The third patterning scribe (P3) is performed to insulate the front electrode and the neighbouring cells.

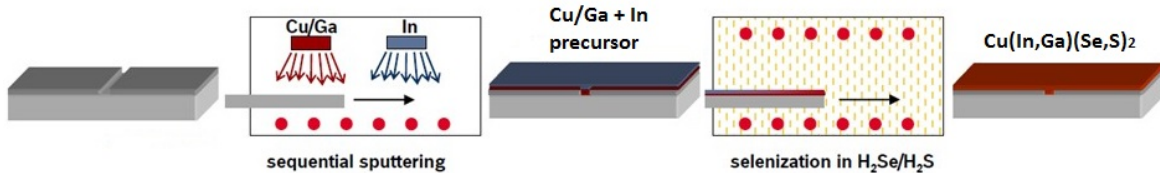


Figure 3.1: Schematic of a two-stage absorber formation process. Adopted from [11]

As the absorber film is formed from stacked elemental layers and its growth process is driven by the interdiffusion of elements, the exact control over composition is very difficult for this deposition method. Therefore, unintentional elemental gradients in the absorber film can adversely affect the efficiency of potential solar cells. The formation of the CuInSe<sub>2</sub> phase is faster than that of the CuInGa<sub>2</sub> phase as the film growth starts from the top. As a result, most of the Ga-atoms are concentrated at the back surface of the absorber. To the contrary, S from the sulfurisation step is found at the surface region of the absorber film. Therefore, a non-uniform bandgap through the absorber thickness is formed. The in-depth variation of Ga- and S-distributions will be discussed in the following section.

The discussed absorber growth process has been first demonstrated at the University of Johannesburg and then applied on a commercial level by *Johanna Solar Technology GmbH*. [71] Later, this company has been transformed in *BOSCH Solar CISTech GmbH* which provided the discussed samples for investigation.

### 3.1.2 Samples under investigation

Due to complex reaction chemistry between intermetallic phases the chalcogenisation of the precursor films result in phase-segregated multinary alloys. The spatial variations in Ga/III and S/VI ratios therefore result in compositionally graded absorber films. In order to study the impact of the in-depth variations of Ga and S on the performance of solar cells, the absorber formation process has been modified in the following ways:

#### (a) Ga-gradient

To produce samples with different Ga-gradients, the temperature profile and duration of the selenisation step has been altered. A better homogenisation of Ga-distribution has been ensured by increased temperatures from 400°C to 580°C during selenisation of the sputtered metallic precursors CuInGa. The time window of this high temperature step varied from 45 min

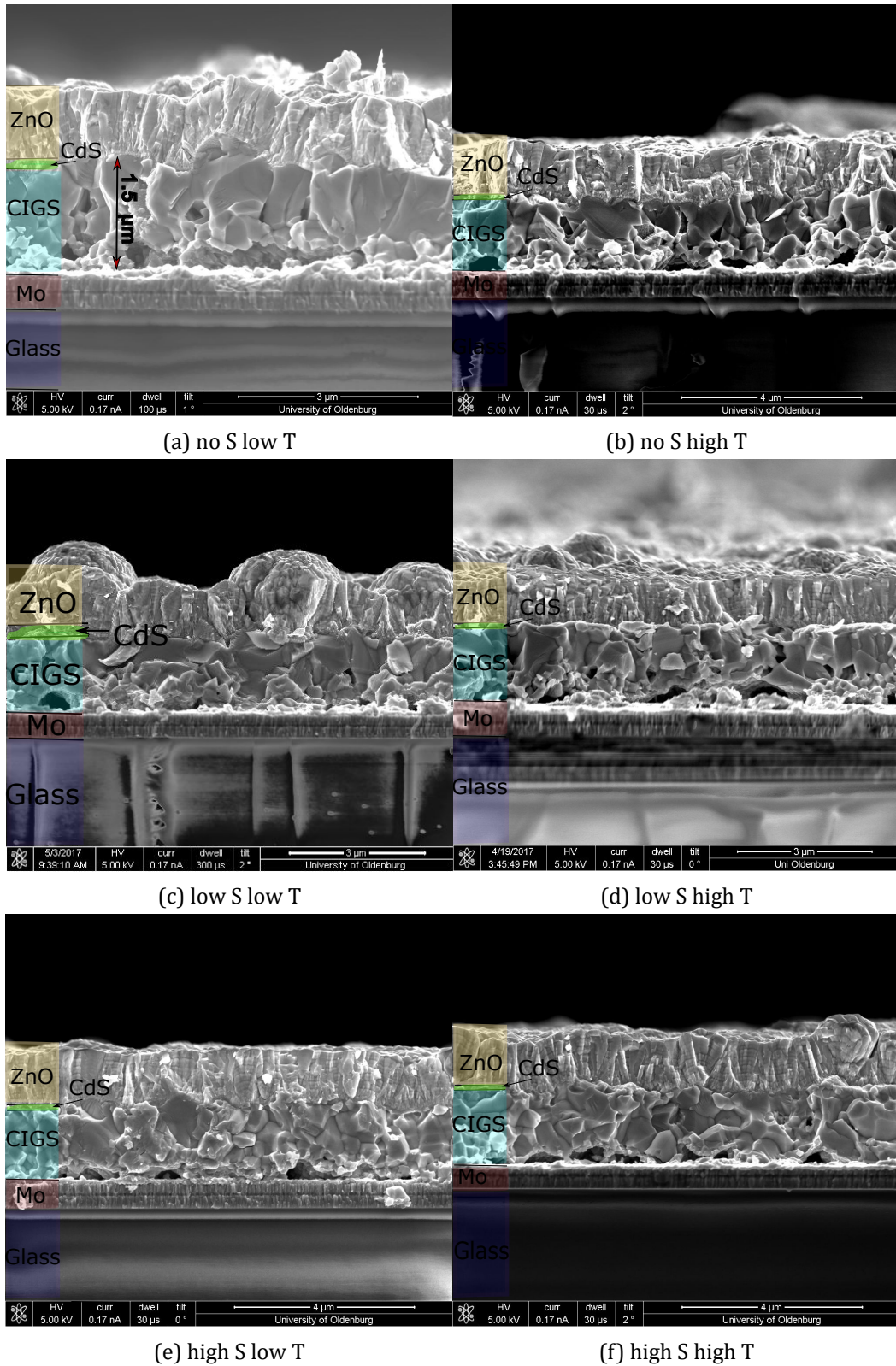


Figure 3.2: SEM micrographs of the cross-section of the samples with a varied S-amount and chalcogenisation temperature.

up to 60 *min* which correspond to the samples with medium and high diffusion times (see Table 3.1), respectively. A soda lime glass which serves as a substrate for the reference process has been changed to a special high temperature glass. It has to be noted that a high temperature glass usually contains less alkali ions in order to increase the melting point and transition temperature of the glass. This, in turn, should also affect the sodium diffusion from the substrate into the absorber layer compared to the reference case where the SiO<sub>2</sub> diffusion barrier on soda-lime glass is sputtered.

*(b) S-gradient*

A control over S-profiles was enabled via different S-supplies and process temperatures. The S-incorporation was done by evaporating S in combination with a H<sub>2</sub>S : Ar transport gas at 475°C, 500°C, and 525°C which are assigned to ‘low’, ‘medium’, and ‘high’ temperature process. Moreover, the S-supply was varied by using different amounts of evaporated S: 0 *g* corresponds to ‘no S’; 18 *g* → ‘low S’, and 70 *g* → ‘high S’ cases. These S-amounts are relevant for the ‘low’ and ‘high’ temperature modifications of the sulfurisation step whereas only 30 *g* was used for the ‘medium’ temperature variation.

The fabrication details of the investigated sample sets are summarised in Table 3.1.

Table 3.1: Fabrication details of the investigated sample sets

Investigated set	Sample	Diffusion time, <i>min</i>	Diffusion temperature, °C	Chalcogenisation temperature, °C	S content, <i>g</i>	
reference	reference	60	400	550	70	
S-incorporation	high T	no S	60	400	525	0
		low S	60	400	525	18
		high S	60	400	525	70
	low T	no S	60	400	475	0
		low S	60	400	475	18
		high S	60	400	475	70
med T	med S	60	400	500	35	
Ga annealing	medium	45	580	550	70	
	long	60	580	550	70	

The microstructure of the modified absorbers (see the S-incorporation samples in Table 3.1) can be analysed from the SEM micrographs shown in Figure 3.2. Large grains at the CIGS/CdS interface change to smaller ones close to the CIGS/Mo interface. The region of smaller CIGS grains is associated with an increasing Ga-content as has been reported in [72].

### 3.1.3 In-depth variations of gallium and sulfur distributions

The concentrations of elements in the absorber layer have been obtained from glow discharge optical emission spectroscopy (GDOES). Unfortunately, details on the setup of this characteri-

sation technique are not available as the measurements have been performed externally by a private company. The principle of operation of this optical spectroscopy technique is described in [17].

GDOES-profiling gives an insight into the elemental distribution versus a film depth. Unfortunately, the data discussed in this work correspond to the samples with modified deposition parameters, and there is no data on a reference sample. However, the results demonstrate a corresponding proportionality with respect to a varying parameter. The absorber thickness has been determined from the Mo signal at the point where it reaches half its intensity. [67].

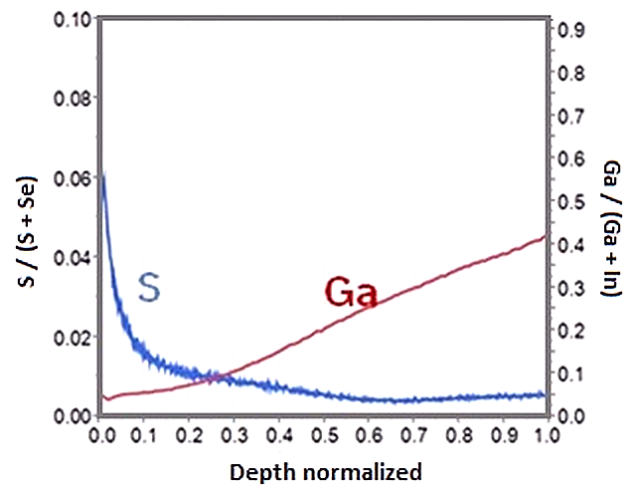


Figure 3.3: Reference in-depth variations of the Ga- and S-distribution.

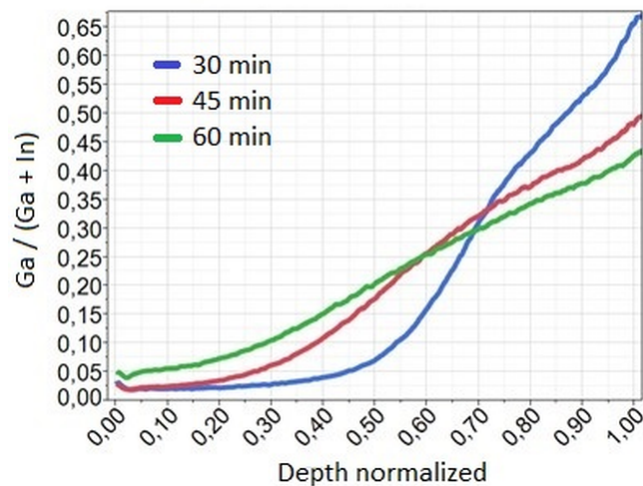


Figure 3.4: In-depth variations of the Ga-distribution after different diffusion times.

The ratio of the emission intensity of S over the intensity of (Se+S) is reproduced in Figure 3.5a and 3.5b. The ratio of the emission intensity of Ga over the intensity of (Ga+In) is not

shown here as it is similar to the reference sample (see Figure 3.3). Varying process parameters with respect to the S-incorporation do not affect the Ga-distribution profiles in the studied samples. Using the GDOES data, the variations in  $E_g$  profiles with a Ga-content  $x$  and a S-content

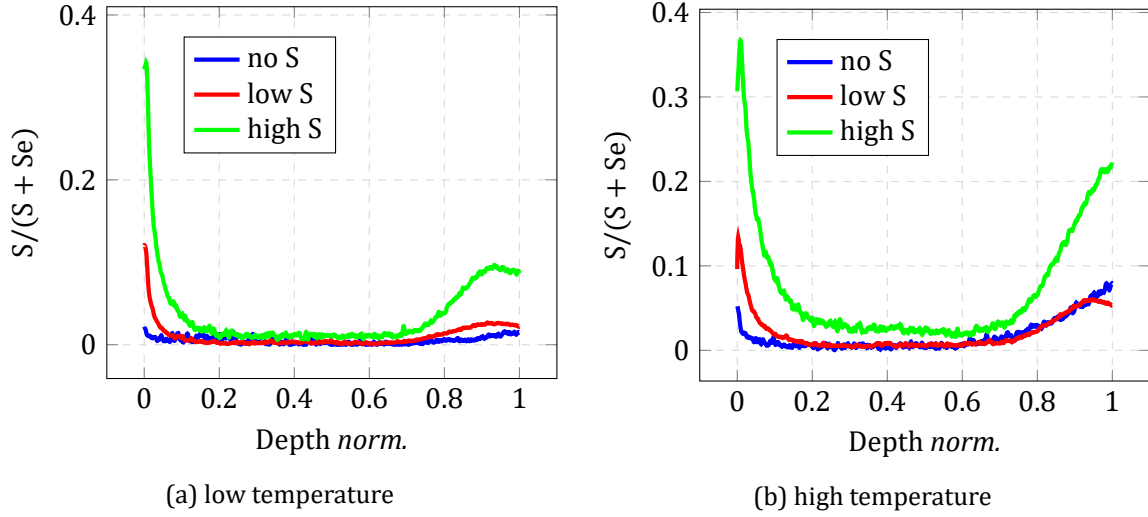


Figure 3.5: GDOES depth profiles for (a) low temperature, and (b) high temperature samples with different S-contents.

$y$  can be estimated by the relation given in [73]:

$$E_g = 1 + 0.13 \cdot x^2 + 0.08 \cdot x^2 y + 0.13 \cdot xy + 0.55 \cdot x + 0.54 \cdot y \quad (3.1)$$

The calculated  $E_g$ -grading profiles for the low and high temperature processes are shown in Figure 3.6. As one can see the grading profile of the studied samples is U-shape (plateau-type) with the basically unaffected  $E_g$  in the bulk. Except for the device with the high S-content from the high temperature process which exhibits some modifications of the bulk  $E_g$ . The slightly increased  $E_g$  at the back contact interface can be related to the increased S-concentration.

## 3.2 Characterisation techniques

### 3.2.1 Current-voltage characteristics

#### Theory

A typical solar cell can be represented by the electrical circuit based on the one-diode model shown in Figure 3.7. The one-diode equivalent circuit of a solar cell is a current source in parallel with a single diode. Additionally, series resistance  $R_s$  represents series resistance losses originated from contact and sheet resistances which limit the current flow through the cell.  $R_s$



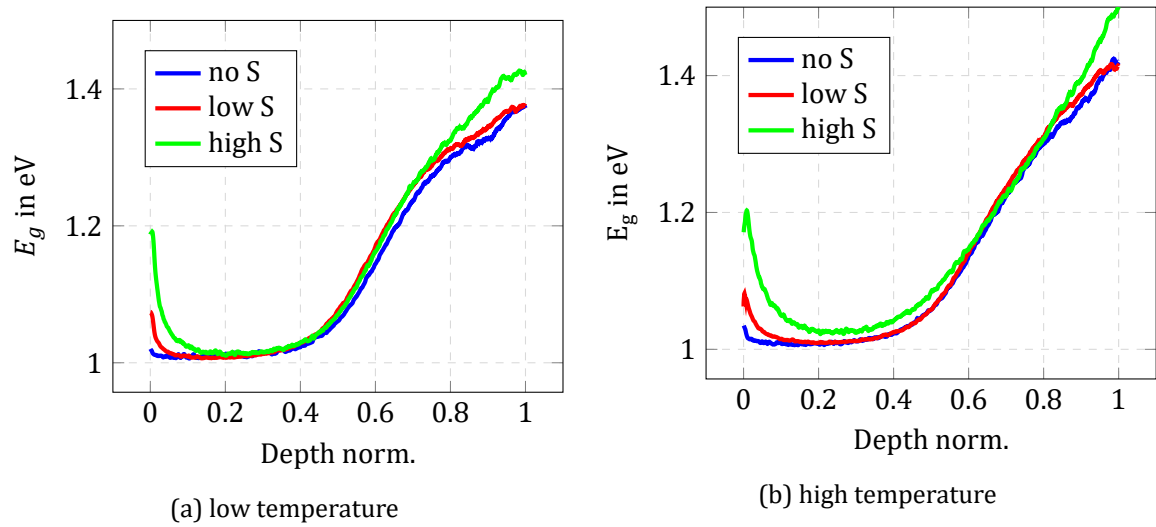


Figure 3.6: Calculated  $E_g$  from the GDOES depth profiles for the samples with different S-contents.

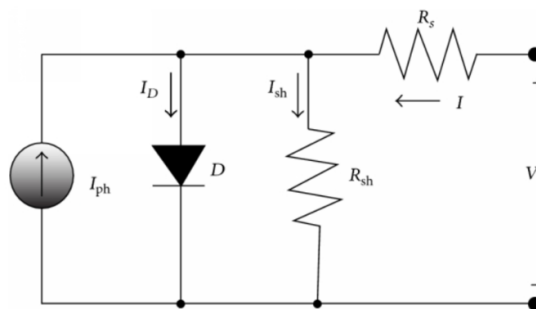


Figure 3.7: Schematic drawing of an equivalent circuit of a solar cell based on the one-diode model.

reduces the solar cell efficiency by dissipating the power in thermal form. The leakage current from the manufactured defects in the solar cell are described by parallel or shunt resistance  $R_{sh}$ . Under illumination, the current delivered by the solar cell can be expressed via the photocurrent density  $J_{ph}$ , the current density through the diode  $J_d$  and the leakage current via shunts  $J_{sh}$  using Kirchoff's law

$$J = J_d - J_{ph} + J_{sh} \quad (3.2)$$

The expression 3.2 modifies the Shockley equation to the following form

$$J = J_0 \cdot \left[ \exp\left(\frac{q(V - JR_s)}{AkT}\right) - 1 \right] + \frac{V - JR_s}{R_p} - J_{ph}, \quad (3.3)$$

where  $A$  is the diode ideality factor. Electrical characterisation of a solar cell involves measuring the current density-voltage (JV)- characteristics and determination of the equivalent circuit parameters in order to calculate the power conversion efficiency,  $\eta$ . The efficiency of the solar cell is defined as a ratio of the electrical power output from the solar cell to the incoming power of the solar irradiance,  $\eta = \frac{P_{out}}{P_{in}}$ .

The typical current-voltage response of the studied solar cells are demonstrated in Figure 3.8. The maximum power output of an ideal cell is equal to the product of the open circuit

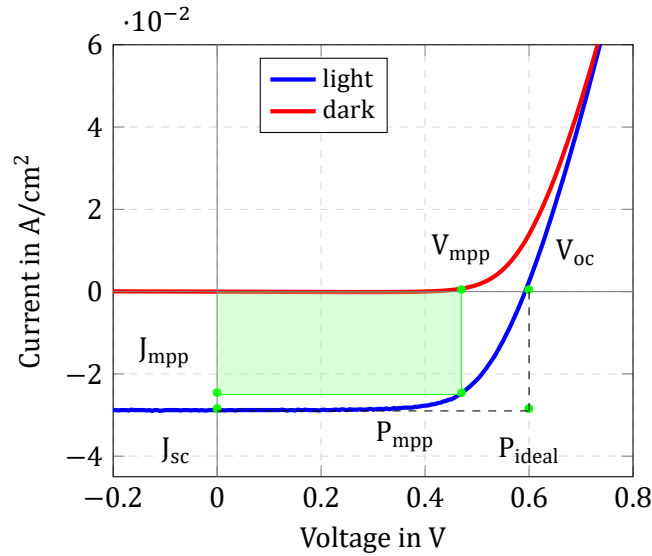


Figure 3.8: Reference JV-characteristics with the performance parameters.

voltage,  $V_{oc}$ , and the short circuit current,  $J_{sc}$ , where  $V_{oc}$  is the cell voltage when the current in the circuit is equal 0, i.e. open circuit conditions; and  $J_{sc}$  is the current available from a cell when the voltage is 0, i.e. short circuit conditions,  $P_{ideal} = V_{oc} \cdot J_{sc}$ . Since  $P_{ideal}$  represents a theoretical limit, the performance of a real cell can be characterized by the fill factor, FF, which measures

the 'squareness' of the current-voltage curve in the power quadrant in comparison to the ideal solar cell. FF is calculated as a ratio of the products of  $V_{mpp}$  and  $J_{mpp}$ , which are the voltage and the current at the maximum power point,  $P_{mpp}$  over the product of  $V_{oc}$ , and  $J_{sc}$ , that is, gives a fraction of  $P_{mpp}$  and  $P_{ideal}$ :

$$FF = \frac{P_{mpp}}{P_{ideal}} = \frac{V_{mpp} \cdot J_{mpp}}{V_{oc} \cdot J_{sc}} \quad (3.4)$$

Further electrical parameters which are critical to the solar cell performance and important to determine performance losses are series resistance,  $R_s$ , parallel or shunt resistance,  $R_{sh}$ , and the diode ideality factor,  $A$ . These parameters will be also included into the analysis process of JV-characteristics.

As the electrical behaviour of a solar cell depends considerably on the external factors, such as device temperature, irradiation spectrum, and illumination intensity, its electrical performance is measured under standard test conditions (STC) which specify a cell temperature,  $T_{cell} = 25^\circ\text{C}$  and integrated illumination intensity of  $1000 \text{ W/m}^2$  with air mass (AM1.5G) to ensure comparable evaluation conditions.

### Measurement setup

*In this work, current-voltage measurements have been performed using Keithley 4200-SCS semiconductor characterization system. This system includes software with a graphical interface and a mathematical formulator which allows direct derivation of the measurement parameters. The Keithley 707A switching matrix provides the possibility of automatic switching between different measurements. All measurements are done in a black box with blackened interior to avoid the impact of ambient light and reduce interference with reflected light inside the box. The temperature of a sample is maintained constant with help of a heating plate. To test the behaviour of a solar cell under illumination, the sun simulator from LOT based on the 300 W Xe short arc lamp with the integrated collimating and collecting optics is used. This optical system meets class A solar spectrum match specifications. The constant current to the lamp is provided by the power supply LSN252 to ensure constant light flux. The intensity of the light beam is adjusted using a reference Si-photodiode calibrated at the Centre for solar energy and hydrogen research Baden-Württemberg (ZSW) in Stuttgart.*

### 3.2.2 Admittance measurements

#### Theory

An admittance measurement is widely used to investigate bulk and interface properties of CIGS solar cells. An alternating voltage with a frequency  $\omega = 2\pi f$  is applied to a solar cell. The

response to the applied AC signal is the complex admittance of a pn-junction which writes as follows:

$$A(\omega) = G(\omega) + j\omega C(\omega), \quad (3.5)$$

where  $\omega = 2\pi f$  is the angular frequency,  $G(\omega)$  is the conductance and  $C(\omega)$  is the capacitance of the pn-junction, respectively. The conductance  $G$  is described by shunt and series resistances, material bulk resistance, contact resistances, etc. Meanwhile, the capacitance is deduced from the imaginary part of the measured admittance and assigned to the SCR capacitance. Therefore, the evaluation of the capacitance value is based on the analysis of the equivalent circuit consisting of a capacitance and a conductance in parallel.

The measurement of the pn-junction capacitance is traditionally carried out as a function of a voltage bias, a frequency of an alternating voltage or temperature.

Free carrier densities, depletion widths, deep trap densities and potential barriers can be obtained from the AC response of the pn-junction. [74]

### 3.2.2.1 Capacitance-voltage profiling

The pn-junction capacitance originates from the SCR in a solar cell which is fully depleted of free charge carriers and considered as the insulating layer. Therefore, it is calculated based on the parallel plate capacitor approximation of the depletion region.

The space charges which are located in the depletion region on both sides of the metallurgical boundary of the pn-junction are of equal magnitude but of opposite sign. After applying a small voltage bias to the pn-junction, the charges are added and removed only at the edges of the depletion region, so that the capacitance depends only on the dielectric constant  $\epsilon_{\text{CIGS}}$  of the absorber layer, the width of the SCR  $w$ , and the device area  $A$ :

$$C_{\text{SCR}} = \frac{\epsilon_0 \epsilon_{\text{CIGS}} A}{w}, \quad (3.6)$$

where  $\epsilon_0$  is the vacuum permittivity. This capacitance imitates the capacitance of a parallel plate capacitor with the distance between the plates equal to the depletion layer width.

Assuming one-sided abrupt pn-junction, Equ. 3.6 can be represented as

$$C_{\text{SCR}} = \sqrt{\frac{q\epsilon_0\epsilon_{\text{CIGS}}N_a A}{2(V_{bi} - V)}}, \quad (3.7)$$

where  $V$  is an applied voltage bias. Measuring the capacitance versus voltage, the built-in  $V_{bi}$  and the doping density  $N_a$  can be obtained. According to the Mott-Schottky analysis, the reciprocal of the square of the capacitance  $1/C^2$  has a linear dependence on the applied voltage  $V$

(see Equ. 3.8)

$$\frac{1}{C^2} = \frac{2}{qN_a\epsilon_0\epsilon_{\text{CIGS}}A} \cdot (V_{bi} - V) \quad (3.8)$$

which allows to extract the doping density  $N_a$  from the slope of the  $1/C^2(V)$  curve as following

$$N_a = \frac{2}{q\epsilon_0\epsilon_{\text{CIGS}}A} \cdot \left[ -\frac{d\left(\frac{1}{C^2}\right)}{dV} \right]^{-1} \quad (3.9)$$

From the extrapolation of  $1/C^2$  to 0 in Equ. 3.8, the built-in voltage  $V_{bi}$  can be determined.

### 3.2.2.2 Capacitance-frequency spectroscopy

The carrier concentration in the CIGS absorber is not controlled by the introduction of doping elements, but determined by the intrinsic defects and defect complexes. The shallow defects govern the doping level of CIGS absorbers and therefore the pn-junction formation whereas deep defects are responsible for recombination of photogenerated carriers and metastable behavior of CIGS solar cells. [13] Furthermore, in addition to intrinsic defects, doping in CIGS absorbers can be influenced by defects introduced by impurity atoms which can be incorporated intentionally or diffuse from the substrates (Na, K, O from the soda-lime glass; Fe from the steel foils). [75, 76, 49] The occupation of defect states by charge carriers (carrier trapping) contributes to the space charge, and therefore to the measured capacitance. Thus, charging and discharging the trapping states will directly affect the measurement outcome. In order to contribute to the junction capacitance, trapping and re-emission events have to be fast enough to follow the applied AC frequency. Therefore, the defect contribution to the device capacitance will be detected in a low frequency measurement, but not in a high frequency one where the capacitance will decrease and approach its geometrical value  $C_{\text{geo}}$ . Such a frequency-dependence gives rise to the capacitance step which occurs at the characteristic frequency  $\omega_0$  given by [77]

$$\omega_0 = 2\beta_p N_v \exp\left(-\frac{E_\omega}{kT}\right), \quad (3.10)$$

where  $\beta_p$  is the capture coefficient for holes, and  $E_\omega$  is the defect energy level which is given by

$$E_\omega = kT \cdot \ln\left(\frac{2\beta_p N_v}{\omega}\right), \quad (3.11)$$

The capture and re-emission of trapped carriers are thermally-activated processes. By measuring the small signal admittance as a function of frequency and temperature, the discrete trap levels in the bulk of the material (predominantly, majority carrier traps [78]) as well as the interface states (minority carrier traps [79]) can be analysed.

The position of the capacitance step can be visualised by plotting the derivative of the capacitance as a function of the angular frequency  $\omega \frac{dC}{d\omega}$ . Such representation of the admittance data is very comfortable as the characteristic frequency can be easily determined from the extremes. Plotting extracted  $\omega_0$  for different temperatures as a function of  $1000/T$ , the energy level of a defect can be determined from the slope of the Arrhenius plot. The intercept of the plot with the y-axis will give the capture-cross-section  $\sigma$  and the attempt-to-escape frequency  $\nu_0$  in agreement with Equ. 3.10.

If the defects are energetically continuous and spatially homogeneous, the evaluation of the defect distribution can be performed based on the dependence of the capacitance on the angular frequency as proposed in [77]. The density of states  $N_t$  as a function of the energy  $E_\omega$  can be evaluated using Equ. 3.12

$$N_t(E_\omega) = -\frac{V_{bi}}{qw} \cdot \frac{dC}{d\omega} \cdot \frac{\omega}{kT}, \quad (3.12)$$

where  $V_{bi}$  is the built-in potential,  $w$  is the SCR width.

However, the interpretation of admittance measurements is not limited to the defect analysis. Comprehensive information on other possible interpretations can be found in [80] and will be discussed in the experimental parts of Chapter 6 and 7.

### Measurement setup

*In this work, CV-measurements were performed using Keithley 4200-SCS semiconductor characterisation system which is coupled to the Keithley 707A switching matrix. All measurements were carried out at room temperature in the dark. The measurement frequency is 100 kHz and applied voltage is 50 mV RMS.*

*Cf-measurements were performed using Hewlett Packard 4192 LF impedance analyser in the frequency range of 0.1–1 000 kHz. The measurements were recorded from 80K to 360K in 20K steps inside an evacuated Optistat DN2-V cryostat cooled with liquid Nitrogen. The same cooling system has been used to measure JV(T)-characteristics. All measurements were carried out in the dark.*

### 3.2.3 Quantum efficiency

#### Theory

Apart from the power conversion efficiency, the operation of a solar cell can be characterized in terms of the quantum efficiency (QE) which is literally the spectrally resolved measurement of  $J_{sc}$ . By definition, the external quantum efficiency, (EQE), is a ratio of the total number of the collected electrons over the total number of the incident photons per unit area of a solar cell:

$$EQE(E_{ph}) = \frac{1}{q} \cdot \frac{dJ_{sc}(E_{ph})}{d\Phi(E_{ph})}, \quad (3.13)$$

where  $d\Phi(E_{ph})$  is the incident photon flux in  $cm^{-1}s^{-1}$  in the photon energy range  $E_{ph}$  per time unit resulting in  $dJ_{sc}$ .

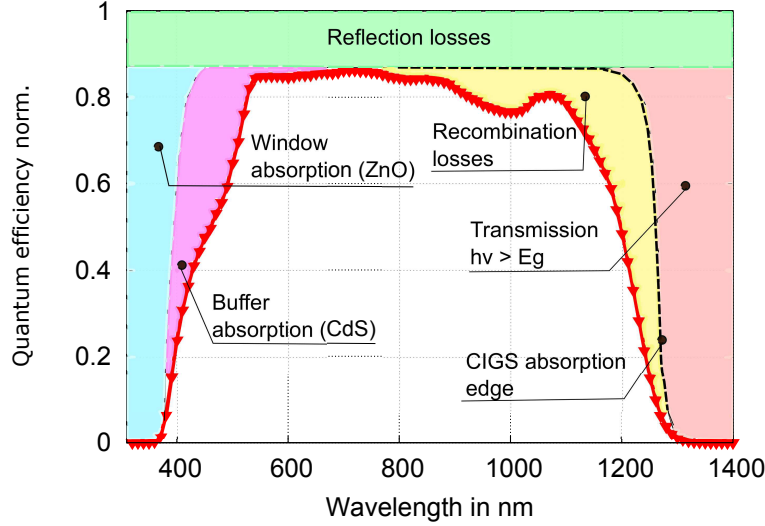


Figure 3.9: Representation of a quantum efficiency curve of one of discussed devices and associated loss mechanisms. Adopted from [81].

Unlike to JV-measurements which provide only the absolute value of  $J_{sc}$  produced by a solar cell, QE identifies the loss mechanisms which are responsible that not all generated electrons are collected. According to the *detailed balance limit* discussed in Chapter 2.1, each photon with energy greater than  $E_g$  must produce one electron-hole pair which to be collected at the terminals of a solar device. However, in reality parasitic absorption, recombination and reflection losses lead to the significant deviation of  $J_{ph}$  from the theoretically justified value.

From the absolute value of EQE it is possible to calculate  $J_{sc}$  by integrating over the complete wavelength range for a given illumination spectrum:

$$J_{sc} = q \cdot \int_0^{\infty} EQE(\lambda) \Phi(\lambda) d\lambda \quad (3.14)$$

Due to the mismatch of the most solar simulators, an EQE-measurement gives a more precise value of  $J_{sc}$  than a regular JV-measurement.

Figure 3.9 reproduces the EQE-spectrum of a reference solar cell investigated in this work. While in the ideal case EQE has the square shape with  $EQE(E_{ph}) = 1$  for  $E_{ph} \geq E_g$  and  $EQE(E_{ph}) = 0$  for  $E_{ph} < E_g$ , in the reality the following loss mechanisms will lower it to a certain extent:

- **reflection losses** occur at the material interfaces and can be minimized by using anti-reflective coatings. The discussed solar cells have no such coating;

- **transmission losses** are inherent to any semiconductor as no light is absorbed below its bandgap energy;
- **buffer absorption** causes a charge collection loss in the blue region of the solar spectrum and scales with the buffer thickness. Similarly, **absorption in the window layer** reduces EQE in the short wavelength region, but these losses are usually neglected;
- **recombination losses** are related to the reduced charge collection probability due to the deep generation or low diffusion length.

### Measurement setup

*EQE-measurement setup used in this work is based on imaging spectrometer Horiba i320. The monochromator is equipped with a filter wheel in order to provide light in a continuous spectrum for a measurement. Photocurrents are measured from both a solar cell and the reference detector. Then the measurement data is transferred to the computer and the calculation of EQE is done by the LabVIEW program. The measurements are recorded in the range of 320–1400 nm. As a light source a combination of the Xe and Ha lamp spectra is employed.*

### 3.2.4 Luminescence measurements

#### Theory

By definition, luminescence is the non-thermal optical emission in response to external excitation. The thermal equilibrium can be disturbed by different excitation sources. In case of optical excitation, the absorption of light with sufficient energy by a solid matter results in the transition of an electron from a higher occupied electronic state in the  $E_v$  to a lower unoccupied state in the  $E_c$ . Afterwards in order to restore the equilibrium the electron relaxes back to the initial state with a consequent photon emission inducing *photoluminescence* (PL). The photon energy then is approximately equal to the semiconductor  $E_g$ . However, radiative transitions may also involve localised defects or impurity levels. In this case, the analysis of the PL-spectrum can help to identify the localised states. The basic recombination transitions in a semiconductor can be divided into three main groups: (a) interband transitions; (b) transitions involving chemical impurities or physical defects; (c) intraband transitions. [53] The detection of PL at a certain energy indicates that an electron populated the state associated with this transition energy. The probing of discrete electronic states underlies the principle of PL spectroscopy. At low temperatures, the PL-spectrum is dominated by the exciton transitions and the transitions via impurity levels, whereas at high temperatures (room temperature) impurities and excitons become ionised, and therefore the band-to-band and free-to-bound transitions become most probable. [17] Therefore, deviations in stoichiometry have to be reflected in the PL-spectrum. This makes a spectrally-resolved PL-measurement a powerful tool in the investigation of CIGS absorbers with different Ga/(Ga + In) and S/(S + Se) in-depth concentrations.



However, not all transitions are radiative. Nonradiative recombination occurs via deep defects in the  $E_g$ . This limits significantly the measured recombination lifetime to much smaller values than the radiative lifetime and is related to defect densities. [17] Therefore, a PL intensity decay as a function of time is extensively used in time-resolved PL (TRPL) measurements in order to extract minority carrier lifetimes and evaluate the quality of the absorber layer.

### 3.2.4.1 Reciprocity relation between luminescence and quantum efficiency of a solar cell

The analysis of a luminescent spectra of a solar cell can be extended using the reciprocity relation (RR) between electroluminescent emission and photovoltaic quantum efficiency discussed in [82]. This theorem is a direct consequence of the principle of detailed balance but with the extrapolation to a non-equilibrium situation. RR connects two reciprocal phenomena: light absorption and light emission which represented by injection and radiative recombination with absorption and charge carrier collection processes, respectively.

According to RR the emission spectrum can be calculated from EQE-measurements and black body radiation:

$$\phi_{em}(E_\gamma) = EQE_{PV}(E_\gamma)\phi_{bb}(E_\gamma) \quad (3.15)$$

Next, the reciprocity theorem has been extended to the case of photoluminescence emission [83]. A linear superposition between EL and PL emission spectra is given by

$$\phi_{em}(E) = \phi_{sc}(E, \phi_{exc}) + \phi_{EL}(E, V) = \phi_{sc}(E, \phi_{exc}) + Q_E \cdot \phi_{bb}(E) \cdot \left[ \exp\left(\frac{qV}{kT}\right) - 1 \right] \quad (3.16)$$

implying that the combined EL and PL emission is a sum of the EL part governed by the junction voltage  $V$  and the PL part driven by optical excitation  $\phi_{exc}$  of a solar cell under short-circuit conditions.

The application of the RR allows a detailed characterisation of photovoltaic properties of a solar cell only by measuring its luminescent (either EL or PL) spectra or vice versa.

### Measurement setup

*In this work, spectral PL emission is detected using a near infrared camera/photodiode based on the InGaAs detector. The excitation source is a laser with an excitation wavelength of  $\lambda=830$  nm working at room temperature. PL-decays have been measured on CIGS absorbers after removing the CdS buffer layer with diluted hydrochloric acid (5%-HCl). The etching duration is 5 min. To induce luminescence, a pulsed diode laser with an excitation wavelength of  $\lambda=638$  nm and the pulse duration of 88ps was used. The maximum incident photon density per pulse is about  $9 \cdot 10^{11} \text{ cm}^{-2}$  (hereafter as 100% excitation). For temperature-dependent PL-measurements, investigated samples were heated up by injecting current into the Mo layer. The sample temperature was controlled*

*by fixing a thermocouple in a distance of 1..3 mm from the laser spot on the sample surface. To vary the excitation level, a filter wheel with different neutral density filters was employed.*

## Chapter 4

# Modelling and simulations

*In this section, a short introduction to the baseline parameters of CIGS solar cells and the corresponding SCAPS model are presented. This SCAPS model will be used to verify and support the results of analytical modelling demonstrated and discussed thereafter. It will be shown in agreement with the experimental results that a Ga-gradient acts as a passivation layer at the back contact reducing back contact recombination and thereby improving  $V_{oc}$ . Additionally, the dependence of the effective back surface recombination on the electron mobility and the strength of quasi-electric field induced by a Ga-grading will be highlighted. Moreover, an enhancement of the charge carrier collection and therefore photocurrent will be verified due to a Ga-rich layer at the back contact. On the other hand, different grading profiles due to a S-incorporation into the absorber surface will be investigated. The maximum achievable increase in the bandgap which defines the activation energy for recombination in the SCR relative to the overall bandgap increase in the SCR will be estimated. The application of the reciprocity relation theorem solar cells with graded gap absorber will be discussed.*

### 4.1 SCAPS modelling

SCAPS is a simulation tool based on numerical modelling of physical processes in thin film solar cells using the finite element method. It allows to test the viability of proposed models developed to explain the underlying physics and to predict the changes in the device performance after varying certain parameters. Since the aim of this thesis does not include exact modelling and fitting of CIGS solar cell parameters, but rather focuses on the interpretation of the experimentally observed behaviour, only relevant parameters will be discussed neglecting those which do not play a primary role in the discussed situation. Therefore, the baseline parameters which are constantly used throughout the work are given hereafter, if not stated otherwise in the text. The effective masses for electrons and holes are set to  $0.09 \cdot m_0$  and  $0.71 \cdot m_0$ , respectively, in accordance to [34] with the mass of free electron  $m_0$ . The effective density of states  $N_C$  and  $N_V$  are then calculated to be equal to  $1.5 \cdot 10^{19} \frac{1}{cm^3}$  and  $7 \cdot 10^{17} \frac{1}{cm^3}$  in the CB

and the VB accordingly. The mobilities of electrons and holes  $\mu_n$  and  $\mu_h$  are inversely proportional to their effective masses and equal to 100 and  $25 \frac{cm^2}{V \cdot s}$ . The dielectric permittivity of CIGS material is set to  $13.6 \cdot \epsilon_0$ . The minority charge carrier lifetime and diffusion length are set to  $\tau_n = 10 ns$  and  $L_n = 1.6 \mu m$ , respectively. The carrier concentration in the absorber layer  $N_a$  has been experimentally determined from CV-measurements and assigned to  $2 \cdot 10^{16} \frac{1}{cm^3}$ . However, some authors report that capacitance measurements overestimate the real doping level in CIGS absorbers [84] whereas others claim that the doping density is underestimated [85]. The effective bandgap for absorption which is equal to the minimum  $E_g$  within the absorber layer has been extracted from EQE-measurements and equals  $\approx 1 eV$ . This value has been assigned to the non-graded region of the absorber. The bandgaps for the front and back grading due to S- and Ga-gradients will be discussed in the appropriate sections. The thickness of the absorber layer is  $1.5 \mu m$  with the SCR width of about  $0.3 \mu m$ .

## 4.2 Analytical modelling

A band diagram of a representative solar cell with a graded absorber structure which is simulated in SCAPS-1D and will be used for modelling is reproduced in Figure 4.1. The absorber layer can be divided in three parts: (1) SCR with a front grading due to the in-depth S-variation; (2) QNR with the uniform  $E_{G,min} = 1 eV$  (this value has been justified by EQE- and spectral PL-measurements); (3) graded due to a Ga-gradient.

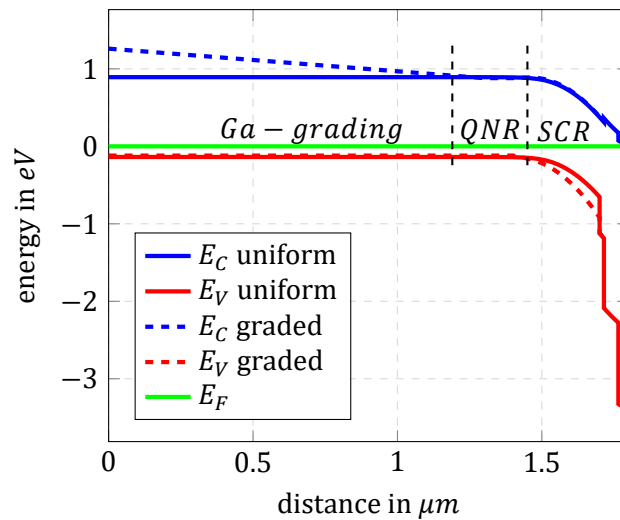


Figure 4.1: Simulated band diagram.

The schematic of the absorber layer is shown in Figure 4.2. The characteristic points are:  $x = -d$  corresponds to the SCR edge with  $d$  being the thickness of QNR;  $x = 0$  is the boundary between the homogeneous and graded regions, the diffusion lengths of electrons in these re-

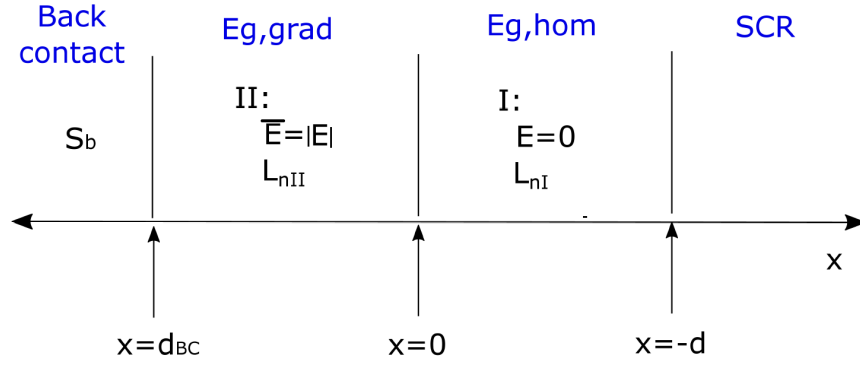


Figure 4.2: Schematic of the absorber grading profile.

gions are  $L_{nI}$  and  $L_{nII}$ , respectively, as will be explained in the next subsection;  $x = d_{BC}$  is the position of the back contact which is characterised by the back contact recombination velocity  $S_b$ . The graded region presupposes quasi-electric field of strength  $E$  due to a gradient in the CB. The aim of this section is to establish the correlation between the absorber geometry and device parameters. The approach is to solve the continuity equations in the region of interest setting appropriate boundary conditions.

#### 4.2.1 Impact of a back grading on charge carrier diffusion

The relevant parameter for the evaluation of the band gradients will be the minority carrier density. When electrons are injected into the p-type CIGS absorber with a density  $n(x)$  they can travel by diffusion before they recombine. The diffusion length is the mean distance electrons can move between generation and recombination. Recombination in the QNR and at the back contact require transport of electrons by diffusion to the recombination sites inducing diffusion limited current. In terms of the device performance the reduction of this current is desirable. The effect of a back surface gradient is to suppress minority carrier recombination at the back contact. This would enhance the photocurrent and decrease the diode current. The continuity equation for electrons which describes the particle flux density and generation / recombination rates throughout the absorber layer is given by [34]

$$\frac{\delta n(x)}{\delta t} = G_n(x) - U_n(x) + \frac{1}{q} \cdot \frac{dJ_n(x)}{dx} \quad (4.1)$$

The diffusion process of electrons in the field-free region of the absorber is characterised by the diffusion length  $L_n$ . This parameter can be described by means of the continuity equation for electrons (see Equ. 4.1) by considering steady-state conditions, when the net rate of increase must be zero  $\frac{\delta n(x)}{\delta t} = 0$ , implying the generation rate  $G(x) = 0$ , and recombination rate  $U_n(x) = \frac{n(x)}{\tau_n}$ . The electron current density  $J_n$  is composed of the diffusion term  $J_{n,diff}(x) = qD_n \cdot \frac{dn(x)}{dx}$

and the effective force field term  $J_{n,\text{drift}} = q\mu E \cdot n(x)$ . In the discussed case, the latter originates from a quasi-electric field due to the CB edge gradient as a result of the Ga-grading. Thus, under the assumption of a constant electric field  $E = \text{const}$  the equation reads:

$$0 = -\frac{n(x)}{\tau_n} + \mu_n \cdot \frac{d}{dx} \left( n(x)E + \frac{kT}{q} \cdot \frac{dn(x)}{dx} \right) = -\frac{n(x)}{\tau_n} + \mu_n E \cdot \frac{dn(x)}{dx} + \mu_n \cdot \frac{kT}{q} \cdot \frac{d^2n(x)}{dx^2} \quad (4.2)$$

With ansatz  $n(x) \sim \exp\left(\frac{-x}{L_n}\right)$  and after some mathematical manipulations Equ. 4.2 can be rewritten as

$$L_n^2 + \tau_n \mu_n E \cdot L_n - \mu_n \tau_n \cdot \frac{kT}{q} = 0 \quad (4.3)$$

By solving this quadratic equation with respect to  $L_n$  one gets the following expression:

$$L_{n1,2} = \frac{-\tau_n \mu_n E \pm \tau_n \cdot \sqrt{(\mu_n E)^2 + 4 \cdot \frac{\mu_n \cdot kT}{\tau_n \cdot q}}}{2} \quad (4.4)$$

Next, two situations can be considered:

- **$E = 0$ , field free region**

Assuming no electric field, the expression for the effective diffusion length corresponds to the one of the conventional diffusion length in the uniform absorber region which depends on the diffusion constant  $D_n$  and lifetime  $\tau_n$  of charge carriers, i.e.  $L_{n1,2} = \pm \sqrt{D_n \cdot \tau_n}$ . Two identical solutions with the opposite signs mean that excess electrons can move either direction, towards the main junction and/or the back contact in the QNR. According to Figure 4.2, it corresponds to  $L_{nI}$ .

- **$E \neq 0$ , back surface field region**

In the presence of the quasi-electric field  $E$ , the effective diffusion length also has two solutions. Both solutions have to be considered as described below. This diffusion length is denoted as  $L_{nII}$  in Figure 4.2 characterising diffusion processes in the graded region. Simplifying Equ. 4.4 with  $D_n = \mu_n \cdot \frac{kT}{q}$ , one gets

$$L_{nII} = \frac{\tau_n \mu_n E}{2} \cdot \left( -1 \pm \sqrt{1 + 4 \cdot \frac{D_n}{\mu_n^2 E^2 \tau_n}} \right) \quad (4.5)$$

After applying a Taylor expansion, the expression for a diffusion length in the presence of electric field  $E$  becomes:

- **positive solution**

$$L_{nII+} = \frac{\tau_n \mu_n E}{2} \cdot \left( -1 + 1 + \frac{1}{2} \frac{4D_n}{E^2 \mu_n^2 \tau_n} - \frac{1}{8} \frac{16D_n^2}{E^4 \mu_n^4 \tau_n^2} \right) \approx \frac{V_T}{E}, \quad (4.6)$$

where  $V_T = \frac{kT}{q}$  is the thermal voltage. The expression 4.6 defines the effective diffusion length of electrons moving towards the back contact against the quasi-electric field and determines the penetration depth of electrons into the graded region. Self-evident, this expression has to be as small as possible in order to prevent the injection of electrons to the back contact, and thereby to suppress back contact recombination.

- **negative solution**

$$L_{nII-} = -L_n^2 \cdot \frac{E}{V_T} \quad (4.7)$$

The expression 4.7 describes the case of drift-assisted diffusion process when both processes are in the same direction. This expression has to be large in order to enhance the current collection and improve the photocurrent.

In order to get some rough estimates for a quasi-electric back surface field and to evaluate its efficiency with respect to the obtained diffusion lengths in the graded region, one can assume  $\Delta E_C = 0.4 \text{ eV}$  (following the GDOES data for the studied samples) and the width of the graded region of  $d = 1.0 \mu\text{m}$ . A constant electric field of  $E \sim 4 \cdot 10^3 \text{ Vcm}^{-1}$  can be obtained. The estimated diffusion length of electrons towards the back contact will be then  $L_{nII+} = \frac{V_T}{E} \sim 6.5 \cdot 10^{-2} \mu\text{m}$ . This expression implies that due to effective force fields induced by a proper Ga-gradient the diffusion length of electrons becomes  $L_{nII+} \ll L_n$ . Self-evident, a reduced back contact recombination will lead to an improved device efficiency, especially facilitating a higher device  $V_{oc}$ . On the other hand, speaking about the drift-assisted diffusion length under assumption of no back surface recombination the effective diffusion length theoretically can reach as high as  $L_{nII-} = L_n \cdot \left( L_n \cdot \frac{E}{V_T} \right) \sim 25 \cdot L_n$  which describes clearly the available potential of a strong back surface field.

### Résumé

*An optimised charge carrier transport throughout the absorber layer is one of the benefits of graded gap absorbers. A quasi-electric field due to a Ga-gradient suppresses the back contact recombination by preventing the injection of electrons to the back contact. This will result in a lower diode current and a higher device  $V_{oc}$ . On the other hand, drift-assisted diffusion of electrons towards the collecting junction is possible leading to a better collection efficiency, and therefore increased photocurrent.*

#### 4.2.2 Back contact passivation due to a Ga-grading

Recombination at the back contact is one of the efficiency limiting processes which directly affects the device  $V_{oc}$ . The passivation of the back contact has to be considered (beneficial) when (a) the back surface recombination velocity,  $S_b$  is too high (the enhancement of  $V_{oc}$  both

experimentally and in simulations has been observed after the improvement of the back contact in works of Vermang [86, 87]), and (b) the diffusion length of electrons,  $L_n$ , is comparable to the width of the quasi-neutral region (QNR) of the absorber layer. Both conditions are relevant for CIGS solar cells. Referring to thin absorbers, a conventional definition of the diffusion length  $L_n = \sqrt{D_n \cdot \tau_n}$  has to be replaced by the effective diffusion length,  $L_n^*$ , as follows [33]:

$$L_n^* = L_n \cdot \frac{\cosh(l^{-1}) + s_b \cdot \sinh(l^{-1})}{s_b \cdot \cosh(l^{-1}) + \sinh(l^{-1})}, \quad (4.8)$$

where  $s_b = S_b \cdot L_n / D_n$ , and  $l = L_n / d$  with  $d$  is the width of the QNR.

The samples under investigation have an absorber thickness in the range of the diffusion length as has been discussed earlier. Therefore, it could be of interest to estimate the impact of the absorber thickness  $d$  on the effective diffusion length  $L_n^*$ , and therewith  $V_{oc}$ ; moreover, to assess the relevance of the back contact recombination  $S_b$  with respect to these two parameters. To analyse the impact of the effective diffusion length  $L_n^*$  and back surface recombination  $S_b$ , the definition of  $V_{oc}$  can be used. Under the assumption that recombination takes place only in the neutral region of the absorber (no recombination in the SCR), the correlation between  $V_{oc}$  and  $L_n^*$  is given by [33]

$$V_{oc} = \frac{E_g}{q} - \frac{kT}{q} \cdot \ln \left( \frac{q D_n N_c N_v}{J_{sc} N_A L_n^*} \right) \quad (4.9)$$

To demonstrate the correlation graphically, the values of  $V_{oc}$ ,  $E_g$ ,  $J_{sc}$  and  $N_a$  are readily available from the experimental data, whereas the other parameters are as described in Section 4.1. The impact of  $S_b$  on  $L_n^*$  can be deduced from Equ. 4.8. Two situations can be distinguished:

- **$S_b$  high**, therewith Equ. 4.8 simplifies to

$$L_n^* = L_n \cdot \tanh(l^{-1}), \quad (4.10)$$

- **$S_b$  negligible**, therewith

$$L_n^* = L_n \cdot \operatorname{ctanh}(l^{-1}) \quad (4.11)$$

The situation for  $S_b$  **high** has been derived by neglecting the summands not multiplied by  $s_b$ , and vice versa for the situation with  $S_b$  **low**. High back surface recombination implies  $S_b \approx S_{b,max} = v_{th}$ , where  $v_{th}$  is the thermal velocity. Meanwhile, reading  $S_b$  **low** means  $S_b \approx 0$  what is an idealised case of the perfect back surface passivation. However, in real solar cells, low back surface recombination has to be given by  $S_{b,min} = v_{th} \sigma N_{d,bulk}^{\frac{2}{3}}$  with  $\sigma$  being the charge carrier capture cross section and  $N_{d,bulk}$  being the defect density in the absorber bulk. [34] In the course of this work,  $S_{b,high} \approx 10^6 \frac{cm}{s}$  and  $S_{b,low} \approx 10^2 \frac{cm}{s}$  are used.

The correction for  $L_n^*$  with respect to a back grading will be discussed hereafter in this subsection. The correlation between the diffusion length normalised to the width of the QNR  $L_n/d$



and: (a) the effective diffusion length  $L_n^*$  normalised to the conventional diffusion length  $L_n$ ; (b) the change in the device  $V_{oc}$  for high and low back surface recombination  $S_b$  is graphically visualised in Figure 4.3 and 4.4, respectively.  $V_{oc}$  in the discussed graph means the value obtained with the conventional  $L_n$ , whereas  $V_{oc}^*$  denotes the value with the effective  $L_n^*$  either for low or high recombination velocity  $S_b$ . For a given set of parameters and under the assumption of high  $S_b$ ,  $L_n^*$  gradually decreases with an increasing  $L_n/d$  ratio, and equals half of  $L_n$  when  $L_n/d \approx 2$ . Reducing the absorber further results in  $L_n^*$  below 10% of the  $L_n$  value when  $L_n/d$  approaches 10. Meanwhile,  $V_{oc}$  (see Figure 4.4) reduces by  $\approx 60$  mV due to high recombination at the back contact solely. To the contrary, for a low back surface recombination velocity  $S_b$  the effective diffusion length increases linearly with decreasing the absorber thickness. Under these conditions, the injected electrons get reflected from the back contact and continue travelling towards the window material. This in turn results in an increased  $V_{oc}$  by  $\approx 60$  mV as can be seen from Figure 4.4. Negligible losses in  $V_{oc}$  ( $< 1$  mV) are expected when the absorber layer is two times thicker than the diffusion length of photogenerated electrons. The maximum achievable change in  $V_{oc}$  would approach 10% according to Figure 4.4.

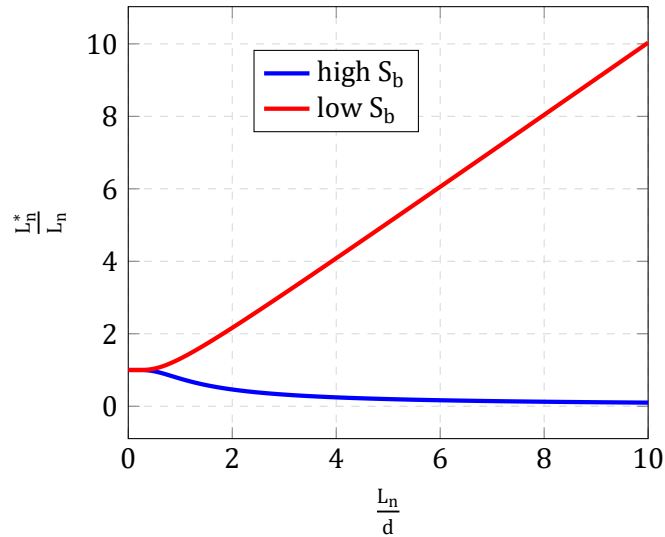


Figure 4.3: Impact of the absorber thickness on the effective diffusion length for high (blue line) and low (red line) back surface recombination velocities.

As a next step, a bandgap grading can be considered and the impact of the back gradient on the diffusion current and therefore on  $V_{oc}$  can be estimated. The illustrative schematic of the absorber layer is shown in Figure 4.2. The absorber layer can be divided into three parts which correspond to: SCR (not of interest at the moment), a region without an  $E_C$  gradient (this region is referred as a grading notch in literature and has a uniform  $E_g = E_{g,min}$ , and a region with a graded  $E_g$ . These two regions are denoted hereafter as region I and II, respectively. The corre-

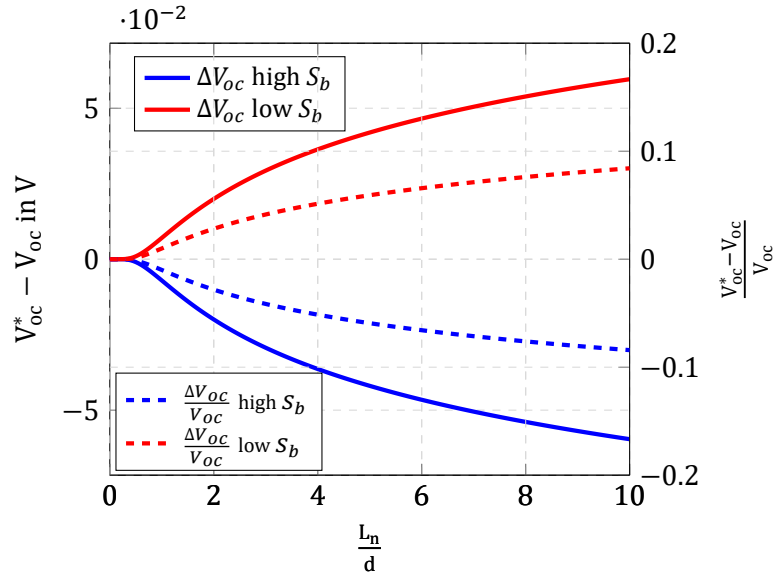


Figure 4.4: Impact of the absorber thickness on the device  $V_{oc}$  for high (blue line) and low (red line) back surface recombination. The corresponding relative  $V_{oc}$  changes are shown with dashed lines. The location of the back contact has to be considered at  $d$ .

sponding band diagram is demonstrated in Figure 4.1 which covers two situations: a uniform bandgap absorber (solid lines) and an absorber with a back grading (dashed lines). The region I is equivalent to a QNR part of the diagram whereas the region II corresponds to a Ga-grading part. A SCR which contains a front grading is not discussed in this subsection. According to Equ. 4.2 gradients in the band edges act as effective force fields and give rise to the additional currents. Herefrom one can assume that the field in the region II is equal to the gradient of  $E_C$  whereas there is no electric field in the region I. Hence, the current density  $J_{nI}$  in the region I will be determined by the diffusion component and can be written as:

$$J_{nI} = qD_n \cdot \frac{dn_I}{dx} \quad (4.12)$$

with the position-dependent electron concentration  $dn_I/dx$ . Accordingly, the current density  $J_{nII}$  in the region II will consist of the diffusion and drift components and can be defined as:

$$J_{nII} = qD_n \cdot \frac{dn_{II}}{dx} + q\mu_n E \cdot n_{II} \quad (4.13)$$

with the position-dependent electron concentration  $\frac{dn_{II}}{dx}$ .

The diffusion of electrons takes place from the edge of the SCR towards the back contact along the  $x$ -axis until being counteracted by the back surface field  $E$ . The electron diffusion

from the edges of the SCR follows an exponential voltage-dependence which can be written as

$$n_p(V) = \frac{n_i^2}{N_a} \cdot \exp\left(\frac{qV}{kT}\right) \quad (4.14)$$

$x = 0$  is chosen at the border between the uniform and graded regions. The width of the uniform layer is  $d$ . The diffusion lengths in the region I and II are  $L_{nI}$  and  $L_{nII}$ , respectively. An ansatz to solve the equations for the regions I and II can be defined as follows:

$$(I) \quad n_I = A \cdot \exp\left(\frac{x}{L_{nI}}\right) + B \cdot \exp\left(\frac{-x}{L_{nI}}\right), \text{ and}$$

$$(II) \quad n_{II} = C \cdot \exp\left(\frac{-x}{L_{nII+}}\right) + D \cdot \exp\left(\frac{-x}{L_{nII-}}\right).$$

For the boundary conditions, the following assumptions can be applied:

1. the electron concentration at the SCR edge,  $x=-d$ , is equal to the excess minority carrier concentration of a voltage-biased device in the dark as given by Equ. 4.14 [34]

$$n_I(x = -d) = \frac{n_i^2}{N_a} \cdot \exp\left(\frac{qV}{kT}\right) = A \exp\left(\frac{-d}{L_{nI}}\right) + B \exp\left(\frac{d}{L_{nI}}\right) \quad (4.15)$$

2. the electron concentration at  $x=0$  from both sides is equal according to the current continuity requirement

$$n_I(x = 0) = n_{II}(x = 0) \rightarrow A + B = C + D \quad (4.16)$$

3. analogically, the current density at  $x=0$  is also equal from both sides

$$J_I(x = 0) = J_{II}(x = 0) \rightarrow \frac{qD_n}{L_{nI}} \cdot (A - B) = q\mu_n E \cdot (C + D) + qD_n \cdot \left(-\frac{D}{L_{nII-}} - \frac{C}{L_{nII+}}\right) \quad (4.17)$$

4. the current density at the back contact is equal to [88]:

$$J_{II}(x = d_{BC}) = q \cdot \left( D_n \cdot \frac{dn_{II}(d_{BC})}{dx} + \mu_n E \cdot n_{II}(d_{BC}) \right) = -qS_b \cdot n_{II}(d_{BC}) \quad (4.18)$$

Thus, a system of four equations has been obtained. The system equations can be solved to calculate the minority carrier distribution throughout the QNR of the absorber for all  $E \neq 0$  and the back contact recombination velocity  $S_b \neq 0$ . However, in case of a strong electric field ( $E > 10^3 \frac{V}{cm}$ ) the  $D$  – term in the solution for the graded region can be omitted as all minority charge carriers will be drifted away from the back contact resulting in a semiinfinite case. Inserting the ansatz into Equ. 4.18, one can see that the ratio  $\frac{D}{C}$  at  $x = d_{BC}$  is  $\approx 10^{-3}$  for  $E > 1 \cdot 10^3 \frac{V}{cm}$ , indicating that the  $D$ -term can be neglected (see Figure 4.5).

As the discussed solar cells have a Ga-gradient which induces a quasi-electric field higher than  $10^3 \frac{V}{cm}$ , in the following discussion the  $D$ -term is set to 0 and the boundary condition (4) is neglected resulting in the semiinfinite case. This will simplify the system to 3 equations. The procedure to calculate  $A$ ,  $B$ , and  $C$  coefficients is following. After inserting the equation 2 into 3

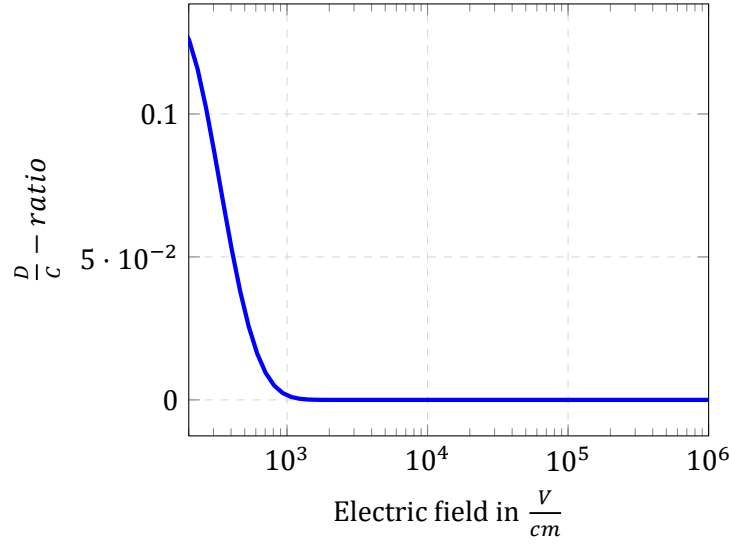


Figure 4.5: Ratio of the D/C-terms with respect to electric field strengths.

and separating A, B can be readily calculated:

$$B = \frac{n_p(V) \cdot \left(\frac{D_n}{L_{nl}} - y\right)}{\left(\frac{D_n}{L_{nl}} + y\right) \cdot \exp\left(\frac{-d}{L_{nl}}\right) + \left(\frac{D_n}{L_{nl}} - y\right) \cdot \exp\left(\frac{d}{L_{nl}}\right)}, \quad (4.19)$$

where  $y = \mu_n \cdot E - \frac{D_n}{L_{nl}}$ . Afterwards with knowledge of B, A and C can be defined. Those are

$$A = \frac{n_p(V) \cdot \left(\frac{D_n}{L_{nl}} + y\right)}{\left(\frac{D_n}{L_{nl}} + y\right) \cdot \exp\left(\frac{-d}{L_{nl}}\right) + \left(\frac{D_n}{L_{nl}} - y\right) \cdot \exp\left(\frac{d}{L_{nl}}\right)}, \quad (4.20)$$

$$C = \frac{2 \cdot n_p(V) \cdot \frac{D_n}{L_{nl}}}{\left(\frac{D_n}{L_{nl}} + y\right) \cdot \exp\left(\frac{-d}{L_{nl}}\right) + \left(\frac{D_n}{L_{nl}} - y\right) \cdot \exp\left(\frac{d}{L_{nl}}\right)}. \quad (4.21)$$

The diffusion current with a back surface grading becomes:

$$J_{\text{diff}}(x = -d) = qD_n \cdot \left(\frac{dn(x = -d)}{dx}\right) = \frac{qD_n}{L_{nl}} \cdot \left(A \cdot \exp\left(\frac{-d}{L_{nl}}\right) - B \cdot \exp\left(\frac{d}{L_{nl}}\right)\right) \quad (4.22)$$

Substituting coefficients A and B in Equ. 4.22 with the expressions from Equ. 4.20 and 4.19, respectively, one gets:

$$J_{\text{diff}} = -q \cdot \frac{D_n}{L_{nI}} \cdot \frac{n_i^2}{N_A} \cdot \left( \frac{\left( \frac{D_n}{L_{nI}} + y \right) \cdot \exp\left(\frac{d}{L_{nI}}\right) - \left( \frac{D_n}{L_{nI}} - y \right) \cdot \exp\left(\frac{-d}{L_{nI}}\right)}{\left( \frac{D_n}{L_{nI}} + y \right) \cdot \exp\left(\frac{d}{L_{nI}}\right) + \left( \frac{D_n}{L_{nI}} - y \right) \cdot \exp\left(\frac{-d}{L_{nI}}\right)} \right) \cdot \exp\left(\frac{qV}{kT}\right) \quad (4.23)$$

with  $y = \mu_n E - \frac{D_n}{L_{nII}}$ . The benefit of a back grading can be realised when the electron injection to the back contact is prevented by a back surface field, and hence no current is injected to the back surface region. In such a situation, the effective diffusion length of electrons towards the back contact in the region II has to be much smaller compared to the one in the region I,  $L_{nII+} \ll L_{nI}$ . Under this assumption,  $L_{nII} = \frac{V_T}{E}$  (see Equ. 4.6), and therefore  $y \rightarrow 0$ . This situation is illustrated in Figure 4.6 where electron diffusion within an absorber layer with and without a back grading is shown schematically. The blue curve represents a conventional exponential decrease of the electron concentration towards the back contact without a back grading, whereas the red curve depicts the situation with a back grading. The dashed green curve represents the portion of electrons which were reflected by the onset of the electric field towards the collecting junction. From  $x = -d$  to  $x = 0$  the concentration of electrons is much higher compared to the case without a grading and decreases significantly slower in the direction of the grading onset. Due to the reflection, the concentration of the charge carrier in the QNR doubles if compared to the no-grading case. Furthermore, the electron concentration in the vicinity of  $x=0$  on the right hand side is not equal to 0 as might have been expected, but a large value which decreases rapidly contributing solely to the recombination current.

Under these conditions,  $y \rightarrow 0$  and Equ. 4.23 reads:

$$J_{\text{diff}} = -q \cdot \frac{D_n}{L_{nI}} \cdot \frac{n_i^2}{N_A} \cdot \exp\left(\frac{qV}{kT}\right) \cdot \left( \frac{\exp\left(\frac{d}{L_{nI}}\right) - \exp\left(\frac{-d}{L_{nI}}\right)}{\exp\left(\frac{d}{L_{nI}}\right) + \exp\left(\frac{-d}{L_{nI}}\right)} \right) = -q \cdot \frac{D_n}{L_{nI}} \cdot \frac{n_i^2}{N_A} \cdot \exp\left(\frac{qV}{kT}\right) \cdot \tanh\left(\frac{d}{L_{nI}}\right). \quad (4.24)$$

From Equ. 4.24 one can see that the diffusion current with a Ga-gradient  $J_{\text{diff-grad}}$  is equal to the diffusion current without grading, i.e. with a uniform bandgap material,  $J_{\text{diff}}$  multiplied by a certain factor which can be expressed in the following way:

$$\frac{J_{\text{diff-grad}}}{J_{\text{diff}}} = \tanh\left(\frac{d}{L_{nI}}\right). \quad (4.25)$$

Hereafter Equ. 4.25 will be considered for further analysis. A practical application of Equ. 4.25 can be demonstrated with the help of Figure 4.7. According to Equ. 4.25, the relation between  $J_{\text{diff-grad}}$  and  $J_{\text{diff}}$  is described via the hyperbolic tangent  $\tanh$  being a function of the  $\frac{d}{L_n}$  ratio. From Figure 4.7 it is clear that a back grading becomes irrelevant when the  $\frac{d}{L_n}$  ratio exceeds

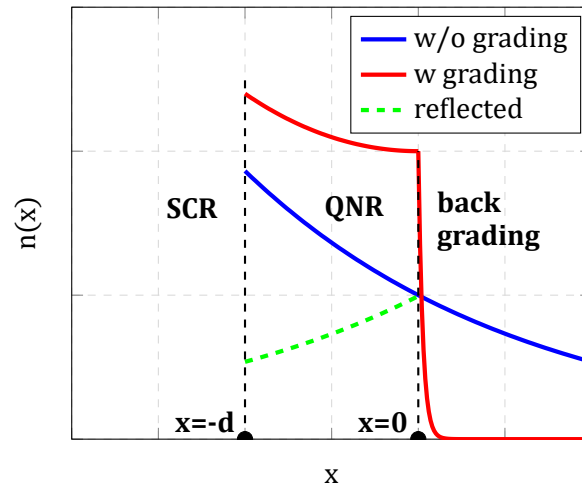


Figure 4.6: Impact of a back grading on electron diffusion. Electron concentration versus absorber thickness.

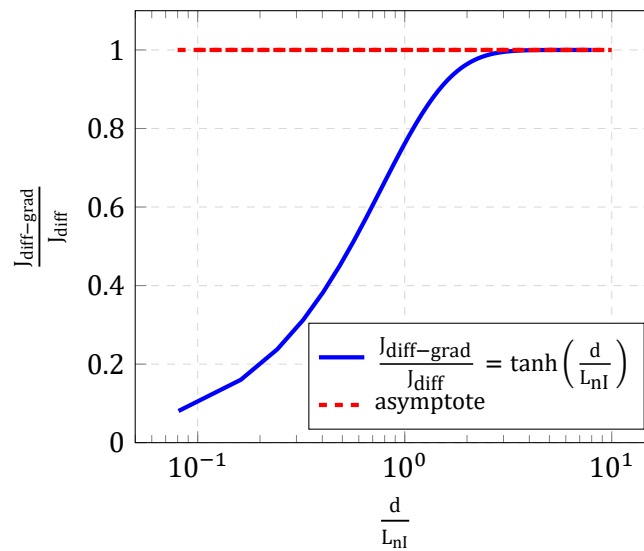


Figure 4.7: Impact of a back grading on diffusion current as a function of the QNR thickness over diffusion length ratio.

2, and the diffusion currents with and without a back gradient become equal as their ratio approaches the asymptote shown with a red line. This observation is in agreement with the conclusion from Figure 4.4 showing negligible  $V_{oc}$  losses when the effective diffusion length is at least two times shorter than the absorber thickness. With respect to the bandgap engineering and performance optimization this ratio could be considered as optimal as back surface recombination does not play an important role. Therefore, no additional measures are required for the improvement of the back contact. However, with thinner absorber layers, back contact recombination comes into play and the passivation of the back contact either by means of a Ga-gradient or advanced rear surface passivation technologies [86, 87] is critical.

### Résumé

*According to the findings discussed above one can resume that a Ga-gradient is an effective passivation approach of the back contact interface for CIGS solar cells with thin absorbers. A benefit of a back grading on the reduced diffusion current can be already seen when the absorber thickness  $d$  is less than twice larger than the diffusion length  $L_n$ . For ultra thin absorbers  $\frac{d}{L_n} < 0.5$  a reduction in the diffusion current of more than 50% with respect to the uniform absorber can be achieved.*

### 4.2.3 Field-assisted photocurrent collection

For CIGS solar cells which belong to the pn-junction type of devices the junction collection of the photogenerated charge carriers is essential. The photocurrent extracted from the CIGS absorber is determined by two key processes: generation  $G(x)$  and collection of charge carriers. Both processes can be affected by the Ga concentration and its in-depth distribution. The generation function is determined by the local bandgap energy which depends on the local Ga content. On the other hand, a Ga-back grading can enhance the collection of charge carriers generated in QNR or close to the back contact where the probability of their loss due to the recombination at the interface is very high.

The collection probability in SCR is unity, whereas outside SCR it is determined by diffusion processes which in turn are characterized by the diffusion length  $L_n$  and the distance to the collecting junction  $x$  in the case of a uniform absorber. Thus, the presence of a quasi-back surface field due to a Ga-gradient can affect the collection function by reflecting the photogenerated electrons in the direction of the collecting junction, reducing back surface recombination and modifying the diffusion length  $L_n$  of minority charge carriers. [34, 89]

Mathematically, the collection probability outside of the SCR for a semi-infinite absorber as a function of  $x$  is given by

$$f_c(x) = \exp\left(\frac{-x}{L_n}\right). \quad (4.26)$$

In case of absorbers with a back grading, it is more appropriate to define a drift-diffusion length  $L_{n,E}$ . [90] If the drift and diffusion components of the electron current are assumed to be in the same direction, the drift-diffusion length is expected to be enhanced. [90]

The mentioned above cases are instantiated in Figure 4.8. The diffusion-limited collection is plotted from Equ. 4.26 and drift-diffusion enhanced-collection is to be derived in this section (see **positive solution** for  $L_{nII}$ ). The parameter values are adjusted to fit the parameters of the investigated solar cells. The discussed figure demonstrates the benefit of the presence of

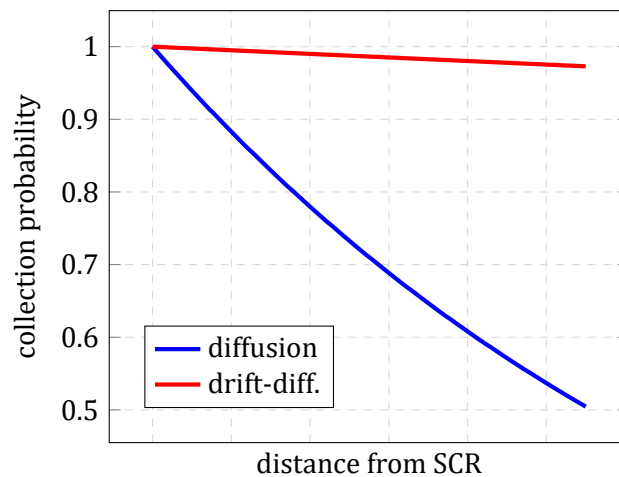


Figure 4.8: Impact of effective force field on the collection probability in comparison to a diffusion-limited case of a non-graded absorber.

an appropriate electric field with respect to the collection function. The probability, that photo-generated electrons will be collected at any point in QNR with a back grading, is only a few %-points less than 100% whereas in the uniform layer the probability falls down to 50% at the same position.

The situation mentioned above describes the collection function under assumption that back surface recombination velocity  $S_b$  is negligibly small, and diffusion and drift occurs only in the direction of the collecting junction. However, in real solar cells the diffusion of charge carriers can occur in both directions, towards the junction and towards the back contact with a considerably high recombination probability at the back contact. Moreover, in the case of a graded absorber the diffusion length in the uniform and graded regions may differ significantly and have to be defined individually. The aim of this section is to extend the model for the collection function in a graded absorber layer with a non-negligible surface recombination at the back contact, and to show an impact of the quasi-electric field on the back surface recombination velocity  $S_b$ .

The collection function can be defined using the reciprocity theorem for charge collection. [88] According to the theorem, the continuity equation for the collection function  $f_C(x)$



reads:

$$D_n \frac{d^2 f_C(x)}{dx^2} - \mu_n E \frac{df_C(x)}{dx} - \frac{f_C(x)}{\tau_n} = 0 \quad (4.27)$$

At this stage, it is necessary to point out at a negative sign in front of the electric field term (compare Equ. 4.2 and Equ. 4.27). [88] The negative sign will enforce the re-definition of the diffusion lengths in context of the collection function as compared to the minority charge carrier case discussed in Section 4.2.1. The derivation of the diffusion length for the collection function (hereafter  $L_n^{fc}$  for the sake of differentiation) is similar to the one in Section 4.2.1. With ansatz  $f_C(x) \sim \exp\left(\frac{-x}{L_n^{fc}}\right)$  the solutions are

$$L_{n1,2}^{fc} = \frac{\tau_n \mu_n E \pm \sqrt{(\tau_n \mu_n E)^2 + 4\tau_n D_n}}{2}. \quad (4.28)$$

Again, two situations have to be considered:

- $E = 0$ , **field-free region**

$$L_{n1,2}^{fc} = \pm \sqrt{D_n \tau_n} \quad (4.29)$$

The solutions for the uniform region are identical to the ones in Section 4.2.1.

- $E \neq 0$ , **back surface field region**

After applying Taylor expansion the expressions read as:

- **positive solution:**

$$\begin{aligned} L_{nII+}^{fc} &= \frac{\mu_n E \tau_n}{2} \cdot \left( 1 + \sqrt{1 + 4 \cdot \frac{D_n}{\tau_n E^2 \mu_n^2}} \right) \approx \frac{\mu_n E \tau_n}{2} \cdot \left( 1 + 1 + \frac{1}{2} \cdot \frac{4D_n}{\tau_n \mu_n^2 E^2} \right) \\ &\approx \mu_n E \tau_n + \frac{V_T}{E} \approx L_n^2 \cdot \frac{E}{V_T} + \frac{V_T}{E} \approx L_n^2 \cdot \frac{E}{V_T} \end{aligned} \quad (4.30)$$

- **negative solution:**

$$L_{nII-}^{fc} = \frac{\mu_n E \tau_n}{2} \cdot \left( 1 - \sqrt{1 + 4 \cdot \frac{D_n}{\tau_n E^2 \mu_n^2}} \right) \approx \frac{\mu_n E \tau_n}{2} \cdot \left( 1 - 1 - \frac{1}{2} \cdot \frac{4D_n}{\tau_n \mu_n^2 E^2} \right) \approx -\frac{V_T}{E} \quad (4.31)$$

In accordance with the obtained solutions the ansatz in the corresponding parts is

- uniform:

$$f_{CI} = C1 \cdot \exp\left(\frac{-x}{L_{nI}^{fc}}\right) + C2 \cdot \exp\left(\frac{x}{L_{nI}^{fc}}\right) \quad (4.32)$$

- graded:

$$f_{CII} = C3 \cdot \exp\left(\frac{-x}{L_{nII+}^{fc}}\right) + C4 \cdot \exp\left(\frac{-x}{L_{nII-}^{fc}}\right), \quad (4.33)$$

where  $L_{nl}^{fc}$  is the diffusion length in the uniform region,  $L_{nII-}^{fc}$  and  $L_{nII+}^{fc}$  are the effective diffusion lengths in the graded region.

The boundary conditions will be defined in agreement with Figure 4.2.

1. The collection function at the SCR edge -d equals 1,  $f_{CI}(-d) = 1$ :

$$C1 \cdot \exp\left(\frac{d}{L_{nl}^{fc}}\right) + C2 \cdot \exp\left(\frac{-d}{L_{nl}^{fc}}\right) = 1 \quad (4.34)$$

2. According to Equ. 4.27, the collection functions at  $x=0$  are equal,  $f_{CI}(0)=f_{CII}(0)$ :

$$C1 + C2 = C3 + C4 \quad (4.35)$$

3. According to Equ. 4.27, the derivatives of the collection functions at  $x=0$  are equal

$$\frac{df_{CI}(0)}{dx} = \frac{df_{CII}(0)}{dx}. \quad (4.36)$$

Therefore,

$$-C1 + C2 = -C3 \cdot \frac{L_{nl}^{fc}}{L_{nII+}^{fc}} - C4 \cdot \frac{L_{nl}^{fc}}{L_{nII-}^{fc}} \quad (4.37)$$

4. According to the reciprocity theorem [88]

$$\frac{df_{CII}(d_{BC})}{dx} = -\frac{S_b}{D_n} \cdot f_{CII}(d_{BC}). \quad (4.38)$$

Thus,

$$-C3 \cdot \exp\left(-\frac{d_{BC}}{L_{nII+}^{fc}}\right) \cdot \left(\frac{1}{L_{nII+}^{fc}} - \frac{S_b}{D_n}\right) - C4 \cdot \exp\left(\frac{-d_{BC}}{L_{nII-}^{fc}}\right) \cdot \left(\frac{1}{L_{nII-}^{fc}} - \frac{S_b}{D_n}\right) = 0 \quad (4.39)$$

The system of four equations with four unknowns can be solved using Cramer's rule. The coefficients are

$$C1 = \frac{\exp\left(-\frac{d_{BC}}{L_{nII+}^{fc}}\right) \cdot \left(\frac{D_n - S_b \cdot L_{nII+}^{fc}}{L_{nII+}^{fc} \cdot D_n}\right) \cdot \left(\frac{L_{nl}^{fc}}{L_{nII-}^{fc}} + 1\right) - \exp\left(\frac{-d_{BC}}{L_{nII-}^{fc}}\right) \cdot \left(\frac{D_n - S_b \cdot L_{nII-}^{fc}}{L_{nII-}^{fc} \cdot D_n}\right) \cdot \left(\frac{L_{nl}^{fc}}{L_{nII+}^{fc}} + 1\right)}{\text{denom}} \quad (4.40)$$

$$C2 = -\frac{\exp\left(-\frac{d_{BC}}{L_{nII+}^{fc}}\right) \cdot \left(\frac{D_n - S_b \cdot L_{nII+}^{fc}}{L_{nII+}^{fc} \cdot D_n}\right) \cdot \left(\frac{L_{nl}^{fc}}{L_{nII-}^{fc}} - 1\right) + \exp\left(\frac{-d_{BC}}{L_{nII-}^{fc}}\right) \cdot \left(\frac{D_n - S_b \cdot L_{nII-}^{fc}}{L_{nII-}^{fc} \cdot D_n}\right) \cdot \left(\frac{L_{nl}^{fc}}{L_{nII+}^{fc}} - 1\right)}{\text{denom}} \quad (4.41)$$

$$C3 = -2 \cdot \frac{\exp\left(\frac{-d_{BC}}{L_{nII-}^{fc}}\right) \cdot \left(\frac{D_n - S_b \cdot L_{nII-}^{fc}}{L_{nII-}^{fc} \cdot D_n}\right)}{\text{denom}} \quad (4.42)$$

$$C4 = 2 \cdot \frac{\exp\left(\frac{-d_{BC}}{L_{nII+}^{fc}}\right) \cdot \left(\frac{D_n - S_b \cdot L_{nII+}^{fc}}{L_{nII+}^{fc} \cdot D_n}\right)}{\text{denom}} \quad (4.43)$$

where

$$\begin{aligned} \text{denom} = 2 \cdot & \left( \exp\left(-\frac{d_{BC}}{L_{nII-}^{fc}}\right) \cdot \left(\frac{D_n + S_b \cdot L_{nII-}^{fc}}{L_{nII-}^{fc} \cdot D_n}\right) \cdot \left( \cosh\left(\frac{d}{L_{nI}^{fc}}\right) + \frac{L_{nI}^{fc}}{L_{nII+}^{fc}} \cdot \sinh\left(\frac{d}{L_{nI}^{fc}}\right) \right) \right. \\ & \left. - \exp\left(\frac{d_{BC}}{L_{nII+}^{fc}}\right) \cdot \left(\frac{D_n - S_b \cdot L_{nII+}^{fc}}{L_{nII+}^{fc} \cdot D_n}\right) \cdot \left( \cosh\left(\frac{d}{L_{nI}^{fc}}\right) - \frac{L_{nI}^{fc}}{L_{nII+}^{fc}} \cdot \sinh\left(\frac{d}{L_{nI}^{fc}}\right) \right) \right) \end{aligned} \quad (4.44)$$

Using the coefficients from Equ. 4.40-4.43 and inserting them into Eq. 4.32 and 4.33, the collection function throughout the absorber can be plotted. Figure 4.9 shows the collection probability for three different field strengths and the back contact recombination velocity of  $S_b = 1 \cdot 10^6 \frac{cm}{s}$ . For  $E = 1 \cdot 10^3 \frac{V}{cm}$  the  $f_c$  starts decreasing already in the uniform region

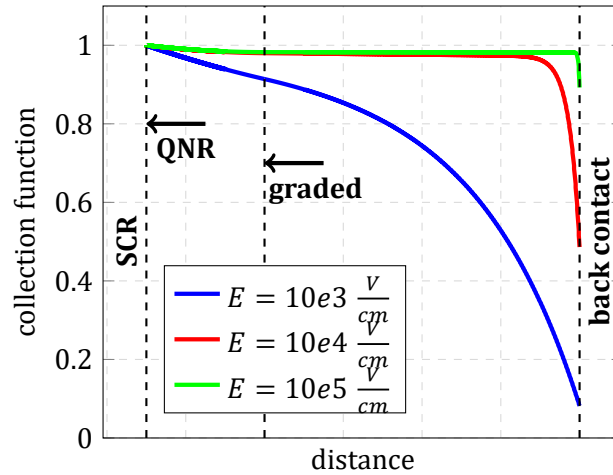


Figure 4.9: Impact of effective force field on the collection function with respect to the field strength. In the calculations,  $S_b = 10^6 \frac{cm}{s}$  and  $\mu_n = 100 \frac{cm^2}{Vs}$  are used.

and falls down to about 10 %. For higher electric fields,  $E = 1 \cdot 10^4$  and  $1 \cdot 10^5 \frac{V}{cm}$ , the loss of photogenerated electrons occurs only close to the back contact. Only electrons generated in the vicinity of the rear interface recombine at the back contact.

To get a better understanding of an impact of the electric field strength on the loss of photogenerated electrons at the back contact a ratio of the the contribution of the C4/C3-terms (see Equ. 4.43 and 4.42, respectively) at the position of the back contact  $d_{BC}$  has been extracted from Equ. 4.33. This ratio compares the number of electrons diffused and collected at the back contact (C4-term) to the number of electrons swept away (C3-term) towards the main junction.

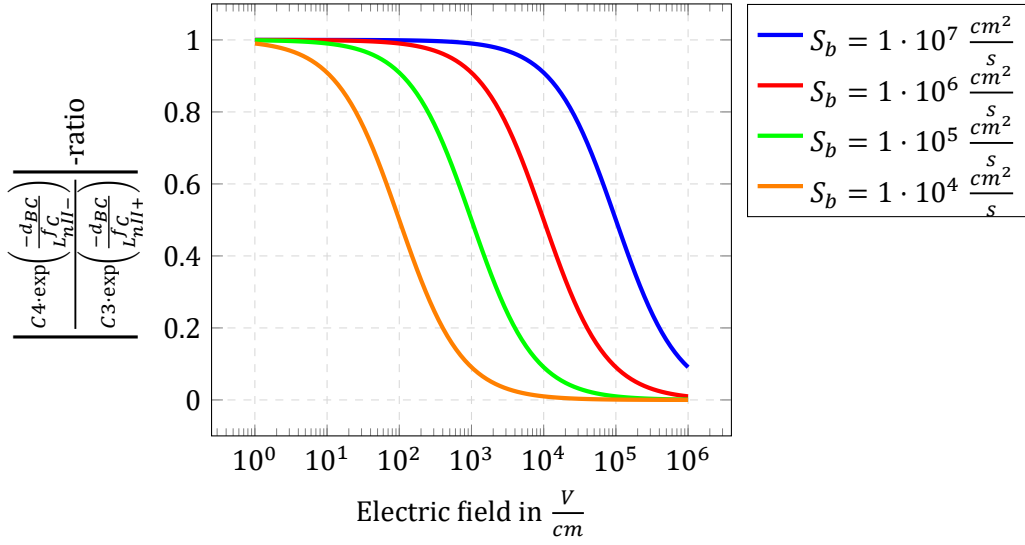


Figure 4.10: Ratio of the contribution of the C4/C3 terms with respect to varied electric field strengths and back contact recombination velocities.

The expression is

$$\left| \frac{C4}{C3} \right| = \frac{1 - \frac{D_n^2}{L_n^2 \cdot \mu_n \cdot S_b \cdot E}}{1 + \frac{\mu_n \cdot E}{S_b}}. \quad (4.45)$$

However, for the electric field strengths considered in this work the term  $\frac{D_n^2}{L_n^2 \cdot \mu_n \cdot S_b \cdot E}$  can be neglected, and Equ. 4.45 can be simplified to

$$\left| \frac{C4}{C3} \right| = \frac{1}{1 + \frac{\mu_n \cdot E}{S_b}} \quad (4.46)$$

The calculated ratios for different electric field strengths and back contact recombination velocities are plotted in Figure 4.10. If the ratio approaches 1, this indicates that  $S_b$  dominates leading to a significant loss of photogenerated electrons. With an increasing  $S_b$  a higher electric field is required to reflect electrons generated in the graded region from the back interface. With an increasing electric field  $E$  the contribution of the C4-term decreases indicating that fewer electrons can reach the collecting back contact. From Figure 4.10 one can see that an electric field of  $1 \cdot 10^4 \frac{V}{cm}$  can already provide an effective passivation of the back contact what is a relevant value for the discussed samples.

## Résumé

*A benefit of quasi-electric field due to a Ga-gradient at the back contact with respect to the photocurrent collection can be expressed in terms of the enhanced or drift-diffusion length. Diffusion*

*of charge carriers towards the collecting junction assisted by a drift component significantly improves the collection probability throughout the absorber layer. Moreover, loss of photogenerated charge carriers due to high back surface recombination can be effectively suppressed by ensuring an appropriate back surface electric field and unhindered charge carrier mobility. Quantitatively, the loss of photogenerated charge carriers can be determined by the reciprocal of the  $\mu_n \cdot E$  over  $S_b$  ratio which will define the fraction of charge carriers collected by the back contact over those drift-diffused towards the main junction.*

#### 4.2.4 CIGS/CdS interface passivation due to a S-grading

The recombination probability is inversely proportional to the bandgap energy. [53] With an increased  $E_g$  the recombination barrier increases, diminishing the recombination events. A sulfur incorporation into the surface region of the CIGS absorber enhances  $E_g$  at the absorber/buffer interface by shifting the  $E_V$  maximum downwards. This results in a decreased hole recombination at the interface as the surface becomes depleted from holes. Such bandgap enhancement is beneficial in solar cells as it acts as an interface passivation and shifts recombination further into SCR towards the material bulk. In this subsection, the impact of the sulfur incorporation on the device  $V_{oc}$  by means of the enhancement of the effective bandgap for recombination and thereby the suppression of SRH recombination in the SCR will be evaluated.

The impact of the S-incorporation can be quantified by defining the bandgap increase  $\Delta E_g$  and finding the position of the maximum recombination, and therefore the effective bandgap for recombination. According to SRH statistics, the net recombination rate is at maximum when the concentration of holes equals to that of electrons  $n = p$  (for  $\sigma_n = \sigma_p$ ) or, in other words, when the Fermi level  $E_F$  is located in the middle of the forbidden gap. In order to describe analytically the position of maximum recombination in SCR the following assumptions will be made:

1. energy bands can be approximated by a parabola;
2. at the point  $x=w$  which defines the metallurgical border between p- and n-type semiconductors, the offset of the  $E_C$  above the Fermi level is  $\Delta E_C$ ;
3. the position of the maximum recombination rate is at  $n = p$ . This assumption can be disputed as the values for  $\sigma_n$  and  $\sigma_p$  are agreed to vary a few orders of magnitude [34, 81, 8]. As a result, the position of the maximum recombination could be shifted away from the middle of the forbidden gap. However, for the sake of simplicity in modelling, we assume a moderate density of defect states which should not distort significantly the stated equality.

The schematic of the energy band alignment with the parameters of interest is shown in Figure 4.11. Implementing the parabolic approximation, the conduction band  $E_C$  can be described as:

$$E_C(x) = E_{g1} - a \cdot x^2, \quad (4.47)$$

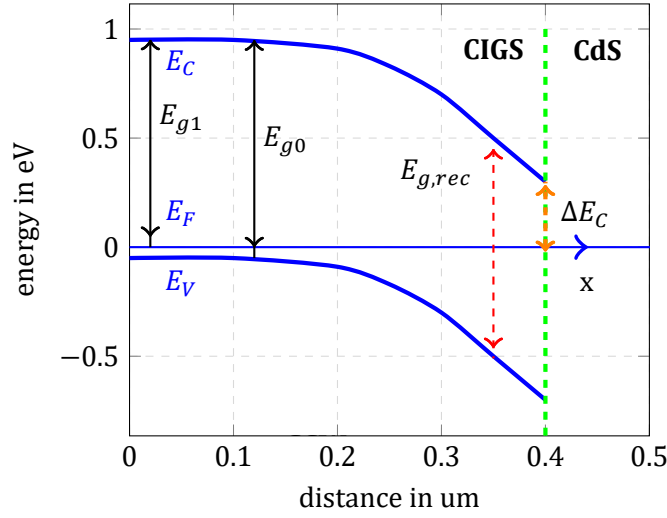


Figure 4.11: Schematic band diagram depicting the conduction band  $E_C$ , valence band  $E_V$ , Fermi energy level  $E_F$ . The parameters to be used in analytical modelling:  $E_{G0}$  is the principle bandgap energy;  $E_{G1}$  is the energy between the conduction band  $E_C$  and Fermi level  $E_F$  at  $x = 0$ ;  $E_{g,rec}$  is the effective bandgap for nonradiative recombination at the position  $E_{g0}/2$ .  $x = 0$  indicates the onset of the space charge region, and  $x = w$  - the CIGS/CdS interface with  $E_C$  being an offset of the  $E_C$  above the  $E_F$ .

where  $E_{g1} = E_C - E_F$  is the energy difference between the conduction band minimum and the Fermi level in the p-type semiconductor bulk,  $x$  is the distance from the absorber/window interface. By using a polynomial from Equ. 3.1.3 one would expect a better accuracy, but for the sake of simplicity in modelling the expression for the  $E_C$  is given by a parabola. The  $x$ -axis is aligned with the Fermi level  $E_F$  and set as a reference zero-energy level.  $a$  is the bowing coefficient. From the assumption that  $E_C(x = w) = E_{g1} - a \cdot w^2 = \Delta E_C$ , the coefficient  $a$  can be defined as  $a = \frac{E_{g1} - \Delta E_C}{w^2}$ . In order to satisfy the requirement for the maximum recombination probability, the position of the Fermi level at location  $x_0$  has to be in the middle of the bandgap  $E_F(x_0) = E_g/2$ . Thus, knowing the expression for  $E_C(x)$  and equating it with  $E_g(x_0)/2$ , the effective bandgap for non-radiative recombination can be found by defining  $x_0$ . The expression for the position-dependent conduction band  $E_C(x)$  is given below

$$E_C(x) = E_{g1} - a \cdot x^2 = E_{g1} - \frac{E_{g1} - \Delta E_C}{w^2} \cdot x^2. \quad (4.48)$$

From Equ. 4.48, the position of the effective bandgap for non-radiative recombination  $x_0$  for non-graded parabolic bands can be estimated as given below

$$x_0 = w \cdot \sqrt{\frac{2E_{g1} - E_g}{2 \cdot (E_{g1} - \Delta E_C)}}. \quad (4.49)$$

In order to evaluate different grading profiles, the corresponding expressions for  $E_g(x)$  have to be written down. Firstly, a graded **parabolic** bandgap structure can be considered. In this case, the bandgap increase as a function of  $x$  can be written as

$$E_g(x) = E_{g0} + b \cdot x^2, \quad (4.50)$$

where  $E_{g0}$  is the principle bandgap in the non-graded region,  $b$  is the bowing coefficient. The increase in the bandgap energy at the position  $x = w$  is equal to  $\Delta E_g = E_g(w) - E_{g0} = b \cdot w^2$ . The coefficient  $b$  is equal to  $b = \Delta E_g / w^2$ . Therefore, using Equ. 4.48 for the description of  $E_C(x)$  and equating it with the half of the expression in Equ. 4.50 the following equation can be obtained:

$$E_{gI} - \frac{E_{gI} - \Delta E_C}{w^2} \cdot x^2 = \frac{1}{2} \cdot \left( E_{g0} + \frac{\Delta E_g}{w^2} \cdot x^2 \right) \quad (4.51)$$

This equation can be rearranged in order to deduce  $x_0$

$$x_{0,par} = w \cdot \sqrt{\frac{2 \cdot E_{gI} - E_{g0}}{2 \cdot (E_{gI} - \Delta E_C) + \Delta E_g}} \quad (4.52)$$

After inserting  $x_{0,par}$  into the expression of  $E_g(x)$  with a graded parabolic bandgap structure (see Equ. 4.50) the effective bandgap for non-radiative recombination  $E_g(x_0)$  can be determined as given below:

$$E_{g,par}(x_{0,par}) = E_{g0} + \Delta E_g \cdot \frac{2E_{gI} - E_{g0}}{2(E_{gI} - \Delta E_C) + \Delta E_g}. \quad (4.53)$$

The **relative increase in the effective bandgap for recombination** indicates which part of the overall bandgap increase  $\Delta E_g$  ( $\Delta E_g$  is defined as the difference in  $E_g$  at the absorber surface and in the uniform absorber bulk) is engaged in the enhancement of the effective bandgap for recombination. In other words, how far the effective bandgap for recombination can be pushed by implementing a S-gradient in the SCR. The higher this part is, the more efficient a grading profile. Hereafter, this parameter will be used to assess the efficiency of different grading profiles.

The relative increase in the effective bandgap for recombination for the parabolic band structure equals to

$$\left( \frac{\Delta E_{g,rec}}{\Delta E_g} \right)_{par} = \frac{2E_{gI} - E_{g0}}{2(E_{gI} - \Delta E_C) + \Delta E_g}. \quad (4.54)$$

It is interesting to mention that assuming  $E_{g0} \approx E_{gI}$  and  $\Delta E_g \ll E_g$ , the relative increase value increases by 0.5 if  $\Delta E_C \rightarrow 0$  which is defined as the maximum threshold for this grading profile.

If a **linear** increase in  $E_g$  is assumed, an in-depth variation of  $E_{g,lin}(x)$  is given by

$$E_{g,lin}(x) = E_{g0} + c \cdot x, \quad (4.55)$$

where  $c$  is the grading coefficient and equal to  $c = \Delta E_g/w$ . Analogously to the parabolic case, from the equation

$$E_{gI} - \frac{E_{gI} - \Delta E_C}{w^2} \cdot x^2 = \frac{1}{2} \cdot \left( E_{g0} + \frac{\Delta E_g}{w} \cdot x \right) \quad (4.56)$$

$x_{0,lin}$  can be found after solving the obtained quadratic equation with the positive solution:

$$x_{0,lin} = w \cdot \frac{-\Delta E_g + \sqrt{\Delta E_g^2 - 4(E_{gI} - \Delta E_C) \cdot E_g^*}}{2 \cdot (E_{gI} - \Delta E_C)}, \quad (4.57)$$

where  $E_g^* = \frac{1}{2} \cdot E_{g0} - E_{gI}$ . Then, for the linearly graded bandgap structure

$$E_{g,lin}(x_{0,lin}) = E_{g0} + \Delta E_g \cdot \frac{x_0}{w} = E_{g0} + \Delta E_g \cdot \frac{-\Delta E_g + \sqrt{\Delta E_g^2 - 4(E_{gI} - \Delta E_C) \cdot E_g^*}}{2 \cdot (E_{gI} - \Delta E_C)} \quad (4.58)$$

with the relative increase in the effective bandgap for recombination equal to

$$\left( \frac{\Delta E_{g,rec}}{\Delta E_g} \right)_{lin} = \frac{-\Delta E_g + \sqrt{\Delta E_g^2 - 4(E_{gI} - \Delta E_C) \cdot E_g^*}}{2 \cdot (E_{gI} - \Delta E_C)} \quad (4.59)$$

Assuming  $E_{g0} \approx E_{gI}$  and  $\Delta E_g \ll E_g$ , the relative increase value increases by  $\frac{1}{\sqrt{2}}$  if  $\Delta E_C \rightarrow 0$  which makes a linear grading profile the most efficient one.

According to the GDOES measurements in Figure 3.3 the S-distribution in the absorber implies an exponential grading of the bandgap  $E_g(x)$  within 300–400 nm from the absorber/buffer interface. The exponential grading can be represented as follows

$$E_{g,exp}(x) = E_{g0} + s \cdot \left( \exp\left(\frac{x}{m}\right) - 1 \right) \quad (4.60)$$

with  $s$  and  $m$  being the grading coefficients.  $s$  can be expressed via  $m$  using the expression for the overall bandgap increase  $\Delta E_g$

$$s = \frac{\Delta E_g}{\exp\left(\frac{w}{m}\right) - 1}. \quad (4.61)$$

The expression shown in Equ. 4.62 is approximated using Taylor expansion for an exponential function with linear and quadratic terms of the series.

$$E_{g,exp}(x) = E_{g0} + s \cdot \left( \frac{x}{m} + \frac{x^2}{2m^2} \right) \quad (4.62)$$



Equating Equ. 4.62 with Equ. 4.48 and solving the obtained expression with respect to  $x$ , one finds the expression for  $x_{0,exp}$

$$x_{0,exp} = w \cdot \frac{-1 + \sqrt{1 - 4 \cdot \frac{E_{g^*}}{s} \cdot \left(1 + 4 \cdot \frac{E_{gI^*} \cdot m^2}{w^2 \cdot s}\right)}}{\frac{w}{m} + 4 \cdot \frac{E_{gI^*} \cdot m}{w \cdot s}} \quad (4.63)$$

with  $E_{g^*} = \frac{1}{2}E_{g0} - E_{gI}$  and  $E_{gI^*} = E_{gI} - \Delta E_C$ .

The relative increase in the effective bandgap for recombination due to exponential grading can be assessed as written below:

$$\left(\frac{\Delta E_{g,rec}}{\Delta E_g}\right)_{exp} = \frac{2m}{w \cdot (2m + w)} \cdot \left(x_{0,exp} + \frac{x_{0,exp}^2}{2m^2}\right) \quad (4.64)$$

The expression in Equ. 4.64 depends on the parameter  $m$ ,  $\Delta E_g$  and  $\Delta E_C$ . For further analysis it is

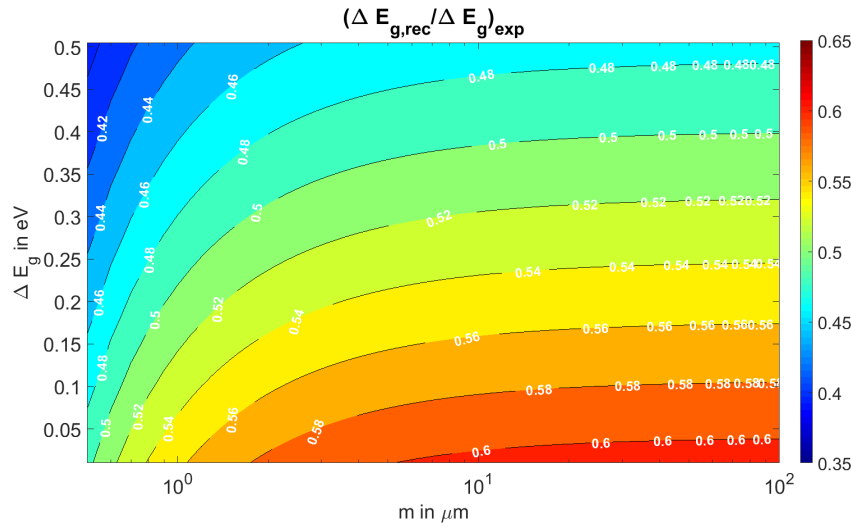


Figure 4.12: Contour-plot demonstrates the dependence of the relative increase in the effective bandgap for recombination  $\left(\frac{\Delta E_{g,rec}}{\Delta E_g}\right)_{exp}$  as a function of parameter  $m$  and an overall bandgap enhancement  $\Delta E_g$ .

assumed that  $\Delta E_C \rightarrow 0$  to reduce the number of parameters. Moreover, as has been mentioned earlier such an assumption is one of the requirements to maximise an increase in  $E_{g,rec}$ .

The dependence between  $m$  and  $\Delta E_g$  is illustrated in Figure 4.12. Taylor approximation used in 4.62 imposes restrictions on the  $\frac{x}{m}$  ratio, and thereby on the value range of  $m$ . To satisfy the requirement of  $\frac{x}{m} \ll 1$ , the values of  $m \geq 0.5 \mu\text{m}$  are only considered. Increasing the  $\Delta E_g$  by 0.5 eV can account for the increase of the effective bandgap for recombination of 0.48 for  $m \rightarrow \infty$  as can be seen from Figure 4.12.

In order to compare the effectiveness of the studied grading profiles, the effective bandgaps for recombination and their relative increase with respect to the uniform bandgap case are calculated and shown in Table 4.2. As the input for the calculations, the parameter values shown in Table 4.1 are used. The motivations for the selected values are described in the "Remarks" column.

Table 4.1: Input parameters

Parameter	Value	Remarks
$E_{g0}$	1.0 eV	justified by EQE-measurements
$\Delta E_g$	0.5 eV	max difference in $E_g$ (between CuInSe <sub>2</sub> and CuInS <sub>2</sub> )
$E_{g1}$	0.8 eV	justified by SCAPS and calculations
w	0.4 $\mu m$	justified by CV-measurements

The efficiency of exponential grading for the given parameter values can approach the linear one for a large  $m$  as it leads to linearisation of the function  $E_{G,exp}(x)$ . This leaves a linear grading as the most effective grading profile with the maximum increase in the effective bandgap for recombination approaching half of the overall bandgap increase. The least efficient grading profile for the studied parameter set is parabolic. Only 28% of the overall bandgap increase can be used to enhance the effective bandgap for recombination.

Table 4.2: Comparison of grading profiles with respect to the effective bandgap for recombination  $E_{g,rec}$  and the relative increase in the effective bandgap for recombination  $\frac{\Delta E_{g,rec}}{\Delta E_g}$  based on the modelling and SCAPS simulation results.

Grading	$E_{g,rec}$		$\frac{\Delta E_{g,rec}}{\Delta E_g}$	Remarks
	Model	SCAPS(corr.)		
parabolic	1.14	1.14	0.28	
linear	1.24	1.24	$\frac{1}{\sqrt{2}}$	
exponential	1.24*	1.24	0.48*	at $m \rightarrow \infty$

The main advantage of the presented model is its simplicity and the involvement of few parameters which can be easily estimated. On the other hand, some important parameters are neglected. Implementing a graded composition of the absorber layer, basically all material properties become position-dependent. This applies to electron affinity  $\chi(x)$ , effective density of states  $N_C(x)$  and  $N_V(x)$ , doping density  $N_a(x)$ , transport properties  $\mu_e(x)$  and  $\mu_h(x)$  and recombination kinetics  $N_t(x)$ ,  $\sigma_e(x)$  and  $\sigma_h(x)$ . Thus, with respect to the presented model, the following disadvantages can be addressed. This model does not account for the doping density  $N_a$  in the absorber layer which can affect the effective bandgap for recombination  $E_{g,rec}$ , and

thereby  $V_{oc}$ . Moreover, different grading profiles imply varied in-depth  $N_a$  concentrations, and therefore  $E_{g1} = E_C - E_F$  is not constant and depends on the doping density.

Taking into consideration the shortages of the proposed model, additional cross-check of the results has to be done. Therefore, to verify the results from the proposed model SCAPS-1D simulations have been performed. The description of the available grading profiles and interpolation laws implemented in SCAPS can be found in [91]. The insights into analysis of graded bandgap solar cells with SCAPS are given in [92]. In this work, front grading due to a S-incorporation has been implemented by splitting the absorber layer in two parts. Graded SCR has been modelled by a 300 nm thick layer with corresponding grading profiles by keeping the electron affinity  $\chi_e$  constant. The fixed  $\chi_e$  in combination with a varied  $E_g$  ensures the VB grading in accordance to the experimental S-incorporation results. (see Figure 3.5) However, it has to be mentioned that a doping density in a graded layer has to be adjusted separately in order to avoid a CB hump close to the CIGS/CdS interface. On the device level, such a CB hump may result in deteriorated performance due to the voltage-dependent photocurrent collection and reduced FF. The situation can be improved by lowering doping density in the absorber layer or shrinking a graded region. Hence, the doping density in the graded layer is set fixed to  $9 \cdot 10^{15} \frac{1}{cm^3}$  and in the bulk -  $2 \cdot 10^{16} \frac{1}{cm^3}$ , the latter is in accordance to the CV-measurements. However, these values could be debated. A decreased doping level close to the absorber/buffer interface is in agreement with [93] which reports a minimum doping concentration close to the CIGS/window junction increasing linearly to its maximum at the CIGS/back contact interface. On the other hand, the defect layer model in [94] postulates a  $p^+$ -defect layer with a high density of acceptor states at the absorber surface.

The other parameters are set to change linearly with a gradient of the bandgap energy. The other part of the absorber layer has a uniform minimum  $E_g$  of 1 eV in accordance to the EQE-measurements and calculated  $E_g$ -profiles. The back grading at the back contact is neglected to emphasise a pure front grading effect. The maximum  $E_g$  at the absorber surface corresponds to a pure  $CuInS_2$  material as has been mentioned in Table 4.1.

The corresponding VB in the SCR simulated in SCAPS for the discussed grading profiles are shown in Figure 4.13. The effective bandgaps for recombination have been determined from the temperature-dependent  $V_{oc}$ -characteristics extracted from the simulated JV-measurements for different temperatures. The corresponding curves are shown in Figure 4.14. However, one should keep in mind that the extracted activation energies from the simulated  $V_{oc}(T)$  characteristics are not straightforward.  $V_{oc}(T = 0K)$  will extrapolate to a higher value due to the temperature dependence of certain parameters.<sup>1</sup>

To assess the correction needed for extrapolated values, a  $V_{oc}(T)$ -characteristic of a device with a uniform absorber with the bandgap energy of 1 eV is considered. As one can see from

<sup>1</sup>According to fundamental semiconductor physics, the effective density of states in  $E_C$  and  $E_V$  bands,  $N_C$  and  $N_V$ , respectively, demonstrate strong temperature dependence. The impact of temperature on the diode saturation current follows a power law of third order:

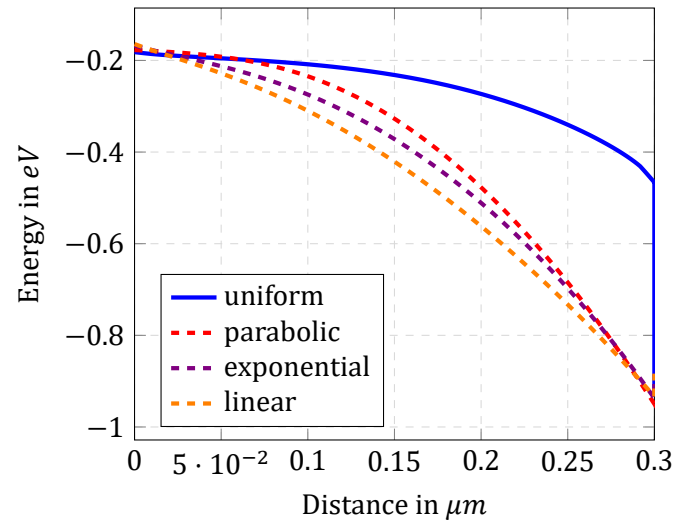


Figure 4.13: Simulated VB in the SCR for different grading profiles.

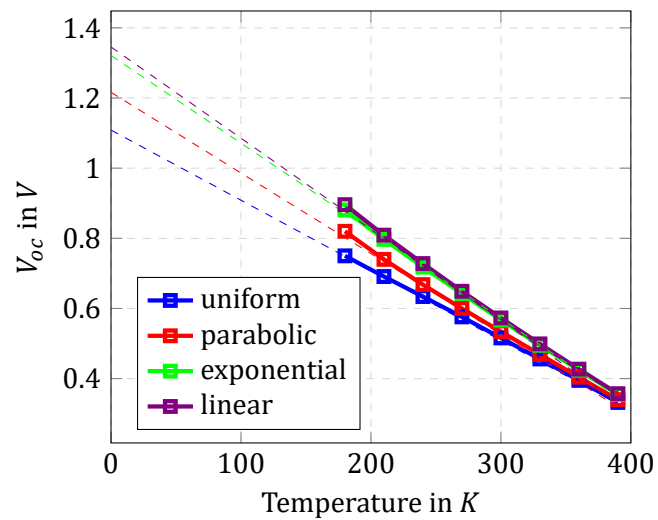


Figure 4.14: Simulated  $V_{oc}(T)$ -characteristics for different grading profiles.

Figure 4.14, the extrapolated to 0 K  $V_{oc}$  value equals to 1.1 eV. The extrapolation of the effective bandgap for recombination is by  $\approx 3 \cdot kT$  higher than the input absorber bandgap, therefore the correction by  $3 \cdot kT$  of the extracted values from SCAPS simulations is required.

The deduced and corrected effective bandgaps for recombination  $E_{g,rec}$  and the effective increase in the effective bandgaps for recombination  $\frac{\Delta E_{g,rec}}{\Delta E_g}$  for corresponding grading profiles are shown in Table 4.2. The correlation between the simulated results and modelling agrees well proving the relevance of the proposed model. However, it has to be noted that the proposed model cannot be accurately applied to assess exponential grading with  $m < 0.5 \mu m$  as has been mentioned above.

Another question which can arise after looking at the simulated  $V_{oc}(T)$ -characteristics is why the characteristics do not run in parallel as has been observed from the measurements. One has to remember that in the measurements only exponential grading profiles are considered, whereas in the simulations the grading profiles are different which can imply a different contribution from the recombination current in the SCR and the injection current. In order to obtain parallel  $V_{oc}(T)$ -characteristics in the simulations, following requirements have to be fulfilled. The doping density in the graded region has to be below  $5 \cdot 10^{15} \frac{1}{cm^3}$  and the back grading has to be present.

### Résumé

*The most important finding in this section is that the maximum increase in the effective bandgap for recombination due to front grading does not exceed  $\frac{1}{\sqrt{2}}$  of the overall bandgap increase. Moreover, the most efficient grading profile from the discussed ones is linear. The lowest efficiency has been shown by a parabolic grading with 28% for the given parameters. An exponential grading*

$$J_s = A \cdot \frac{T^3}{T_0} \cdot \exp\left(\frac{-E_G}{kT}\right), \quad (4.65)$$

where  $A$  is a temperature-independent constant,  $T$  is temperature of interest;  $T_0$  is reference temperature (usually room temperature). Following that for the injection mode, the expression for  $V_{oc}$  reads

$$V_{oc} = \frac{kT}{q} \cdot \ln\left(\frac{J_{ph}}{J_s}\right), \quad (4.66)$$

and its temperature dependence is given by Taylor expansion as

$$V_{oc}(T) = V_{oc}(T_0) + (T - T_0) \cdot \frac{dV_{oc}}{dT} \quad (4.67)$$

The two expressions combined result in the temperature dependence of the effective density of states which increases the slope of the  $V_{oc}(T)$  curve by  $3 \cdot kT_0$ . The same value has been obtained considering SRH recombination in the SCR (not shown here). Hence, the extrapolated  $E_G = q \cdot V_{oc}(T = 0)$  has to be corrected for  $3 \cdot kT_0$  (the same is valid for the activation energy of the saturation current density  $J_0$  extracted from the  $V_{oc}(T)$ -measurement).

can be considered as a compromise between the two. Varying the exponential bowing parameter  $m$  the relative increase in  $E_{g,rec}$  can be tuned accordingly. This observation gives a useful hint when the optimization of a front grading is considered as a  $S$ -distribution in the SCR plays a decisive role in the device efficiency by directly affecting  $V_{oc}$ .

### 4.3 Verification of the reciprocity relation for graded gap solar cells

The fabrication of CIGS solar cells with a depth-dependent  $E_g$  based on sequential processes can benefit from a process monitoring technique which can be applied already at the absorber level and predict the performance of finished devices. The embedment of such a monitoring technique into the production line could accelerate process optimisation and allow effective monitoring of compositional gradients formation. PL imaging due to its contactless nature and short measurement time is ideal for quality control of bare absorber layers. In combination with the reciprocity relation (RR) theorem from [82] a PL-measurement could be able to predict not only the device  $V_{oc}$ , but also its  $J_{sc}$  which can be correlated, for example, to diffusion of Ga within the absorber layer. Therefore, the aim of this section is to investigate how accurate the correlation between the RR and PL measurement for graded bandgap absorbers is.

Depending on the fabrication process, CIGS absorbers tend to segregate in a layer with a high Ga-content at the back contact and a layer with a high In-content, therefore a low Ga-part, close to the absorber/buffer interface. This intermixing leads to a graded bandgap structure and can be detected by luminescence imaging techniques as the emission wavelength is determined by the lowest bandgap energy in the absorber material. [95] As will be shown later, the Ga/(Ga+In) ratio significantly affects the optical bandgap. The changes in the effective bandgap for absorption can be seen in EQE-measurements (see Figure 4.15a for Ga-samples). With increasing the bandgap, the EQE cutoff shifts to the higher energies or to the shorter wavelength region. According to the RR, the changes in the absorption spectrum have to be reflected in the emission spectrum as well. However, it has to be emphasised that the RR in [82] has been developed for uniform bandgap absorbers without taking into consideration effective electric fields induced by bandgap gradients. Therefore, in the following, the application of the RR to different graded bandgap absorbers will be investigated. The studied samples are described in detail in Table 3.1, their respective compositional gradients (see Figure 3.5) and the in-depth  $E_g$  variations (see Figure 3.6). Firstly, the devices from the high temperature growth process with different annealing times will be analysed. These samples have different Ga-distribution profiles within the absorber layer as a result of a high processing temperature. Secondly, the devices with a modified absorber surface due to the S-incorporation of varied amounts and at different chalcogenisation temperatures will be studied. In contrast to the high temperature

samples, the S-samples have an unaffected absorber bulk but modified surface properties due to a varied in-depth S-concentration.

The RR states that the emission spectrum can be derived from EQE-measurements and the back body radiation calculated for room temperature (300 K) as given below [82]:

$$\phi_{em}(E_\gamma) = EQE(E_\gamma) \cdot \phi_{bb}(E_\gamma), \quad (4.68)$$

where the spectral photon flux density of a black body is given by

$$\phi_{bb}(E_\gamma) = \frac{2\pi E_\gamma^2}{h^3 c^2 \cdot \left[ \exp\left(\frac{E_\gamma}{kT}\right) - 1 \right]} \quad (4.69)$$

with  $\phi_{em}(E_\gamma)$  being the energy-resolved emission spectrum, and  $EQE(E_\gamma)$  representing the measured EQE.

The RR theorem relates the electroluminescent (EL) emission and external photovoltaic quantum efficiency (EQE) from the solar cells. Its experimental validation has been reported in [95], where the theorem for the first time has been applied to the graded bandgap absorbers. The authors proved that the emission spectrum could be a valuable tool for a quality control of the graded gap absorbers with respect to the detection of lateral inhomogeneities. Next, the study in [83] extended the RR to the more general case of combined EL and PL emission. Therefore, the discussed investigation is of scientific interest for the following reasons:

1. to verify whether the reciprocity relation holds between spectral PL and EQE measurements;
2. to investigate whether the RR theorem holds for solar cells with different grading profiles. The samples with varied sulfur contents imply a graded SCR, that is, a modified surface only with unaffected bulk properties. To the contrary, the high temperature process leads to different Ga-diffusion profiles throughout the absorber layers which imply the modified bulk properties to a different extent.
3. The validation of the concept would allow to consider the RR for the industrial applications as a quality assessment tool for graded bandgap absorbers where effective electric fields induced by different in-depth compositional variations are integral features of the performance optimisation approach.

Figure 4.16 reproduces the emission spectra for the investigated samples with different Ga-profiles. The emission spectra have been derived based on the calculated black body radiation spectra at room temperature and measured external quantum efficiency in accordance with the RR developed in [82]. The emission spectra derived from the black body radiation are denoted as "calculated emission" in the graphs. Afterwards, the calculated spectra have been compared to the spectral PL measurements of the same devices. As can be seen from the graphs (a-c) in Figure 4.16 the emission peaks of both spectra for the studied samples fit well. The shift of the

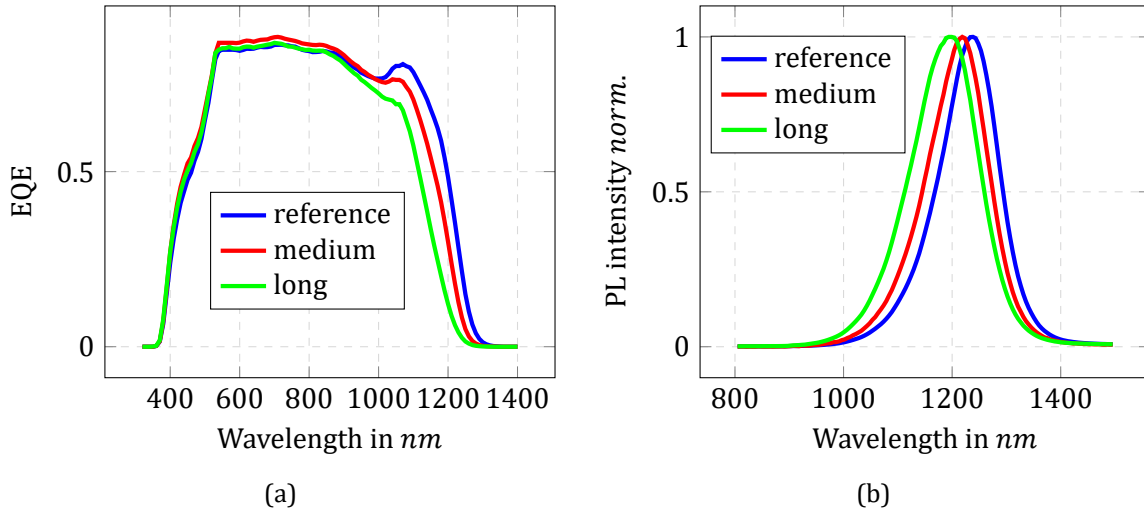


Figure 4.15: EQE measurements (a) and spectral PL responses (b) of the devices with different diffusion times.

Table 4.3: Impact of diffusion time on the effective bandgap for absorption and current collection for different Ga-profiles.

Diffusion time	$E_g^{BBR}$ , [eV]	$E_g^{PL}$ , [eV]	$E_g^{EQE}$ , [eV]
reference	1.0	1.0	1.0
medium	1.02	1.02	1.01
long	1.03	1.04	1.06

emission peaks also correlate to the shift in the EQE cutoffs and the emission wavelengths in spectral PL-measurements reproduced in Figure 4.15a and 4.15b, respectively. The GDOES data of these samples can be found in Figure 3.3 (reference) and Figure 3.4 (45 *min* and 60 *min* as medium and long diffusion, respectively). Therefore, the emission wavelength can be accurately estimated based only on the EQE measurements which allows accurately monitoring the optical bandgap. However, there is some deviation in the spectrum shape in the high energy region which becomes more pronounced with increasing diffusion times. The PL spectra become more asymmetric and wider compared to the calculated case.

A better fit between the emission wavelengths deduced from the calculated and experimental data is observed for the samples with different S-contents for varied process temperatures. The results are shown in Figure 4.18 for the varied S-amounts and low and medium chalcogenisation temperatures. The results for the high temperature process are shown in Figure 4.19c. The position of the emission peaks also correlate with the EQE-measurements and spectral PL data shown in Figure 4.17a and 4.17b, respectively. The measured spectra are superimposed irrespective of the S-content and the process temperature. Furthermore, the shapes of the emis-



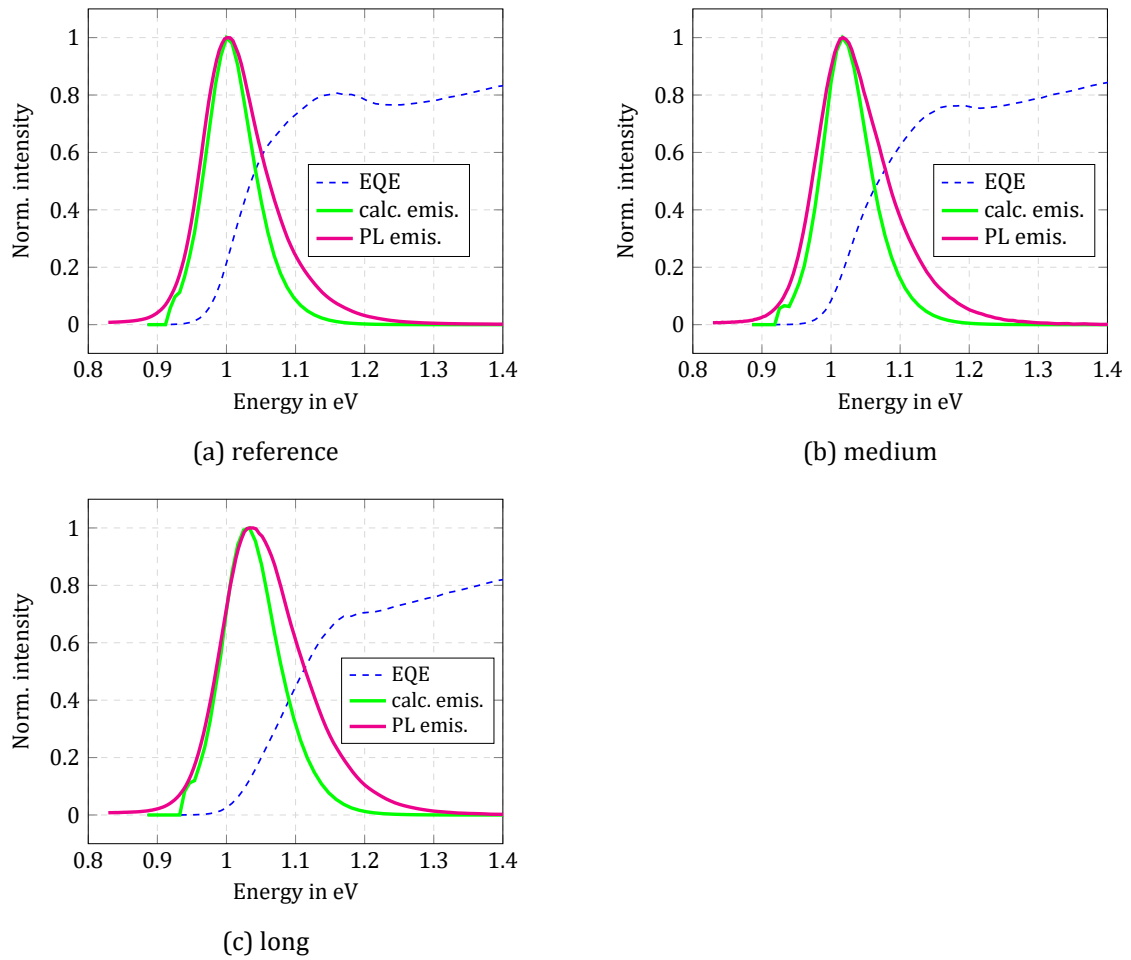


Figure 4.16: Comparison between the calculated emission based on black body radiation and measured PL emission spectra for the samples with different diffusion times (different Ga-profiles).

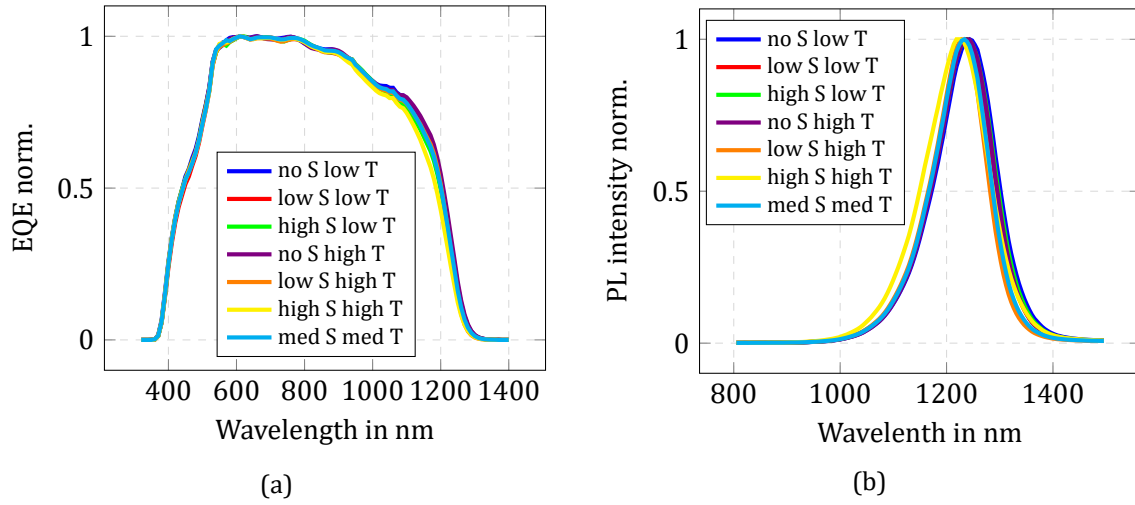


Figure 4.17: EQE measurements (a) and spectral PL responses (b) of the devices with different S-contents and process temperatures.

sion spectra – calculated and measured – of the discussed samples fit better compared to the results of the samples with different Ga-profiles. The S-incorporation affects mainly the surface region of the absorber leaving the bulk eventually unchanged and leading to the better fit between the theoretical and experimental results.

Table 4.3 shows extracted bandgaps  $E_g$  based on the EQE-measurements, spectral PL data and the emission spectra calculated from the black body radiation. The extracted values are in good agreement. To cross-check the correlation between the calculated and measured spec-

Table 4.4: Fitting parameters for the samples with different annealing times

Parameter	ref		med		long	
	BB	PL	BB	PL	BB	PL
$\mu$	1.005	1.01	1.022	1.021	1.035	1.049
$\sigma$	0.051	0.066	0.058	0.080	0.052	0.067
FWHM	0.120	0.154	0.120	0.167	0.137	0.188
R-square	0.99	0.98	0.99	0.99	0.99	0.98

tra, a peak fitting has been applied. Peak fitting is a process to extract peak parameters from an envelope function. A PL peak in  $eV$  should reflect the density of states  $N(E)$  which are normally distributed around a mean value. Under this condition, a Gaussian fit to the calculated spectra can be used. Gaussian function is defined by three parameters: (1) the height of the peak (not of importance at the moment, since the emission spectra are normalised); (2) the position of the center of the peak,  $\mu$ , which would correspond to the emission wavelength, and therefore define the optical bandgap; (3) the standard deviation,  $\sigma$ , which describes a broaden-

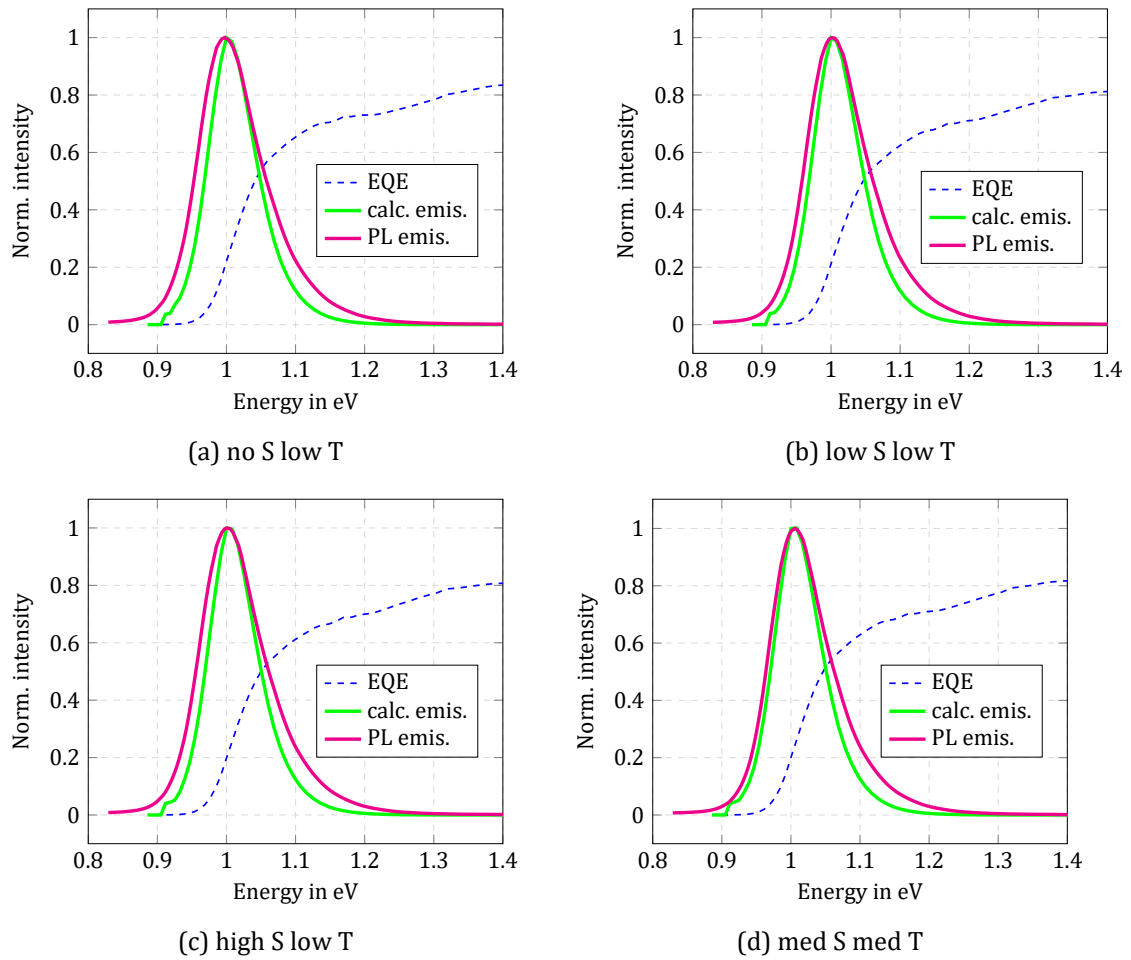


Figure 4.18: Comparison between the calculated emission based on black body radiation and measured PL emission spectra for the samples with different S-contents for low and medium deposition temperatures.

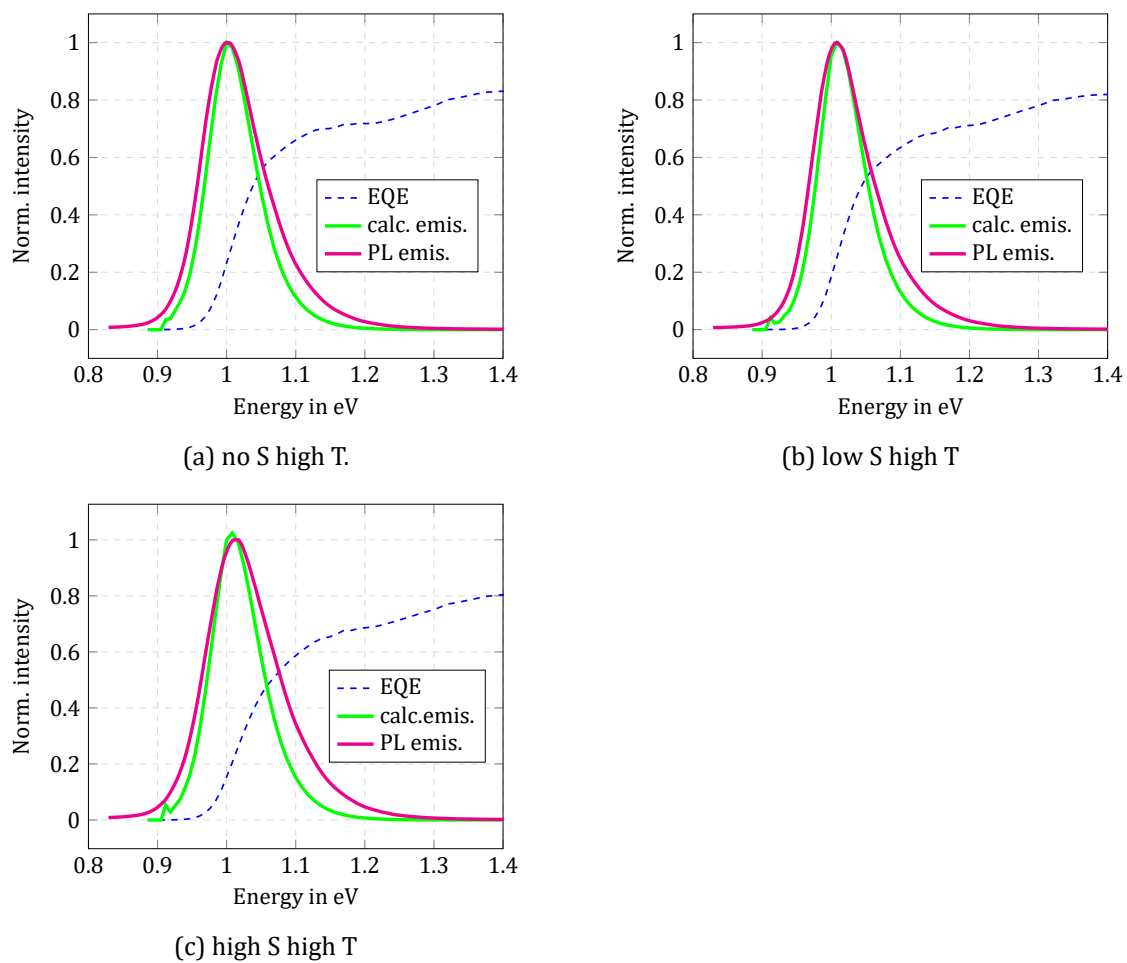


Figure 4.19: Comparison between the calculated emission based on black body radiation and measured PL emission spectra for the samples with different S-contents for high deposition temperatures.

ing of the electronic energetic levels which result in electron intraband transitions and photon emission. Full-width half maximum (FWHM) is another parameter which can be used to compare a broadening of different spectra. R-square determines the goodness of the fitting function to the measurement data. The fitting parameters for the high temperature samples are summarised in Table 4.4. The parameter  $\mu$  indicates the peak emission of the spectra which are in good agreement with the values in Table 4.3. The standard deviation  $\sigma$  of the calculated and measured spectra is within 0.05-0.08. The fitting parameters for the S-samples are given in Table 4.6 and 4.7.

Table 4.5: Impact of a sulfur content and a sulfurisation temperature on the effective bandgap for absorption and current collection

Sulfur / Temperature	$E_g^{BBR}$ , [eV]	$E_g^{PL}$ , [eV]	$E_g^{EQE}$ , [eV]
no / low	1.0	1.0	1.0
low / low	1.0	1.0	1.0
high / low	1.0	1.0	1.0
no / high	1.0	1.0	1.0
low / high	1.01	1.01	1.0
high / high	1.0	1.01	1.0
med / med	1.0	1.01	1.0

A better fit for the extracted bandgap values has been observed for S-samples. The bandgap energies determined based on the discussed methods are reproduced in Table 4.5.

Table 4.6: Fitting parameters for the samples with different S-contents (low temperature process)

Parameter	no S low T		low S low T		high S low T		med S med T	
	BB	PL	BB	PL	BB	PL	BB	PL
$\mu$	1.009	1.006	1.009	1.01	1.01	1.009	1.011	0.014
$\sigma$	0.052	0.067	0.052	0.065	0.052	0.067	0.051	0.063
FWHM	0.122	0.157	0.122	0.153	0.122	0.157	0.121	0.148
R-square	0.99	0.98	0.99	0.98	0.99	0.98	0.99	0.98

To sum up, the estimation of the emission wavelength using RR is in a good agreement with the spectral PL measurements. However, the deviations in the shape between the calculated and measured emission spectra have to be investigated further.

For further analysis, a sample with the largest discrepancy between the calculated  $\Phi_{PLcalc}$  and measured  $\Phi_{PLmeas}$  emission spectra has been chosen (see Figure 4.16c for the Ga-sample with long annealing time.) From the discrepancy in the spectra shape in the high energy wing one can deduce that a narrower spectrum of the  $\Phi_{PLcalc}$  can originate from a lower measured EQE compared to the expected one from the  $\Phi_{PLmeas}$ . Theoretically, an  $EQE_{calc}$  can be estimated

Table 4.7: Fitting parameters for the samples with different S-contents (high temperature process)

Parameter	no S high T		low S high T		high S high T	
	BB	PL	BB	PL	BB	PL
$\mu$	1.008	1.009	1.016	1.016	1.014	1.021
$\sigma$	0.051	0.065	0.049	0.062	0.053	0.073
FWHM	0.121	0.153	0.115	0.146	0.124	0.172
R-square	0.99	0.98	0.99	0.98	0.99	0.98

from the  $\Phi_{PLmeas}$  using the RR (see Equ. 4.68). The measured PL spectrum has to be divided by the calculated BB radiation for the corresponding temperature and energy range. In order to extract absolute values, the  $EQE_{calc}$  has to be normalised with respect to the measurement. As a normalisation factor the ratio of the emission intensities at the energy of maximum emission of the  $\Phi_{PLmeas}$  has been chosen:

$$EQE_{calc} = \frac{\Phi_{PLmeas}}{\Phi_{bb}} \cdot s = \frac{\Phi_{PLmeas}}{\Phi_{PLcalc}} \cdot EQE_{meas} \cdot s, \quad (4.70)$$

where  $s$  is the normalisation factor. The corresponding  $EQE_{calc}$  is plotted versus the  $EQE_{meas}$

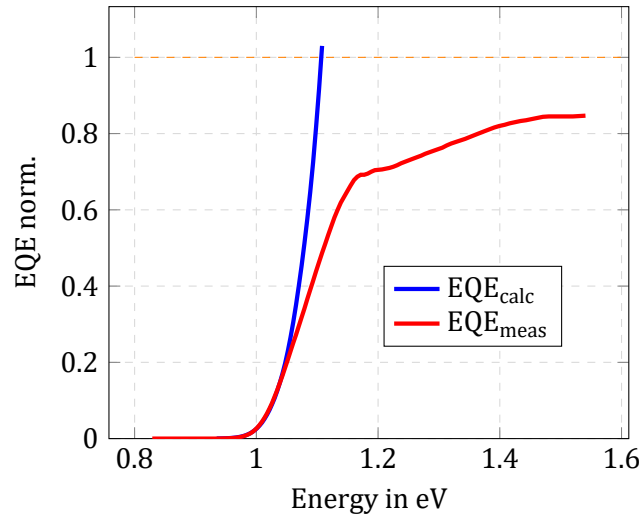


Figure 4.20: Comparison of the EQE measured and calculated from the spectral PL. Normalisation has been done for the maximum emission of the measured PL spectra at  $E = 1.04 \text{ eV}$ .

(which was used to calculate the  $\Phi_{PLcalc}$  for the discussed sample) is shown in Figure 4.20. The  $EQE_{calc}$  is indeed higher than the  $EQE_{meas}$ . However, the  $EQE_{calc}$  is  $> 1$  what contradicts the definition of EQE. This discrepancy will be discussed in the following.

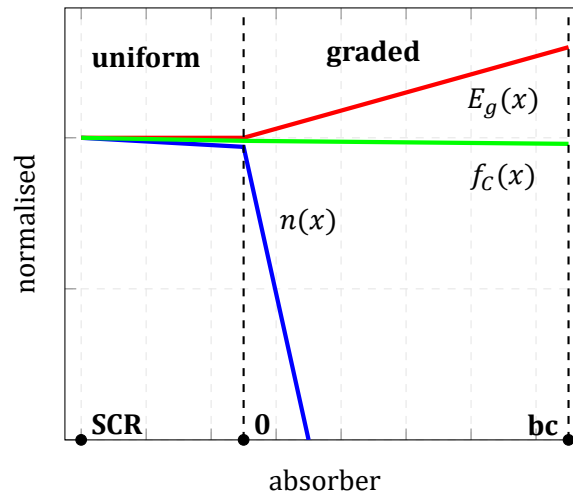
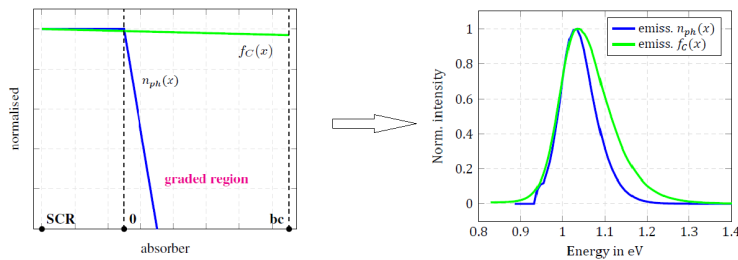


Figure 4.21: Schematic comparison between the excess charge carrier and the collection function profiles with respect to the bandgap profile in the QNR.

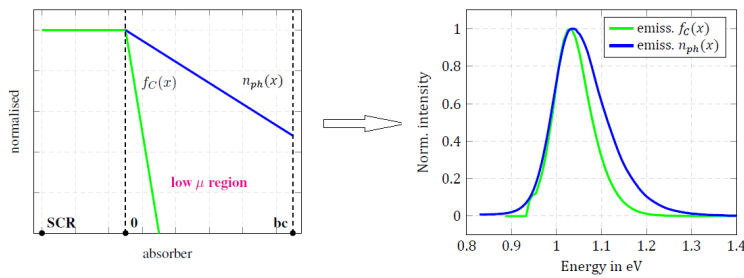
In order to continue a discussion on the deviations in the measured and calculated emission spectra possible reasons for a low EQE which may lead to the deviations in the spectrum shape will be outlined. A low EQE can be explained as follows: 1. It can result from a calibration error of the EQE measurement setup. However, the measurement setup used in this work has been calibrated using the reference cell from ZSW, therefore a calibration factor should be discarded.

2. RR is based on the thermodynamic principles requiring that absorption and emission processes in a solar cell have to be balanced. Therefore, if the balance is distorted, the RR may not hold. For



reciprocity to hold, the excess charge carrier distribution which governs the PL emission has to be similar to the collection function profile which defines the quantum efficiency. Both characteristics in their turn strongly depend on a bandgap grading profile. Figure 4.21 reproduces schematically a bandgap profile of the QNR of the studied devices (in accordance to the GDOES data in Figure 3.3) in comparison to the excess charge carrier distribution and the collection probability shown in Figure 4.6 and Figure 4.9, respectively. It is easy to see that in the uniform region of the absorber the profile of the excess minority carriers is identical to the one of the collection function. However, a back grading has an opposite impact on each of the discussed parameters. As has been discussed previously, a Ga-gradient stops minority charge car-

riers from diffusing to the back contact leading to an abrupt decrease of their concentration in the graded region. Meanwhile, photogenerated carriers from the graded region are drifted away towards the main collecting junction resulting in almost constant collection probability throughout the absorber layer. The discrepancy in the profiles in the graded region could explain significant deviations between the measured and calculated emission spectra in the high energy wing as the reciprocity between two processes is violated. However, in the discussed case, where the profile of the injected electron distribution is limited to the uniform region, one would rather expect a narrower measured PL emission spectrum as there must be no injection into the graded region (with a higher  $E_g$ ) what is **opposite to the observed case**.



3. The violation of the correlation between PL and EL emission due to a transport barrier may also lead to the distortion of the RR theorem. Assuming a potential barrier somewhere in the absorber layer, its impact on

the detected EL and PL emission can be opposite. Such a barrier will enhance recombination processes as charge carriers can be photogenerated but not transported over the potential barrier leading to a high PL yield. Meanwhile, EL emission will be reduced to a significant extent as the potential barrier will hinder the transport of injected electrons. An experimental evidence of this phenomena has been described in [96]. In the discussed devices, the location of a barrier is expected to be in the graded region close to the back contact. Moreover, this barrier must not be necessarily of a thermal nature. An area with a reduced carrier mobility can also have a similar impact on the transport properties. This phenomenon is well-known for organic solar cells. [97] Assuming a low mobility of charge carriers in the graded region, one could anticipate unhindered absorption processes. However, the collection of photogenerated electron-hole pairs will not take place for the low mobility case. Therefore, the photogenerated charge carriers will accumulate and be forced to recombine resulting in a high PL but degraded EL intensity and reduced EQE. This can be clearly seen in Figure 4.22a and Figure 4.22b where electron concentration  $n_{ph}$  and electron current  $J_n$ , respectively, are plotted for the normal ( $\mu_n = 10^2 \frac{cm^2}{Vs}$ , blue line) and reduced ( $\mu_n = 10^{-3} \frac{cm^2}{Vs}$ , red line) electron mobilities. A pronounced increase in the photogenerated electron concentration in Figure 4.22a corresponds to a reduced electron current in Figure 4.22b leading to the inconsistency between the PL ( $\uparrow$ ) and EL ( $\downarrow$ ) emission intensities. An increased  $n_{ph}$  concentration as a result of a low electron mobility will give rise a higher PL emission in a graded  $E_g$  region whereas an EQE yield will be degraded as a consequence of a hindered collection due to a low electron mobility. A considerably reduced



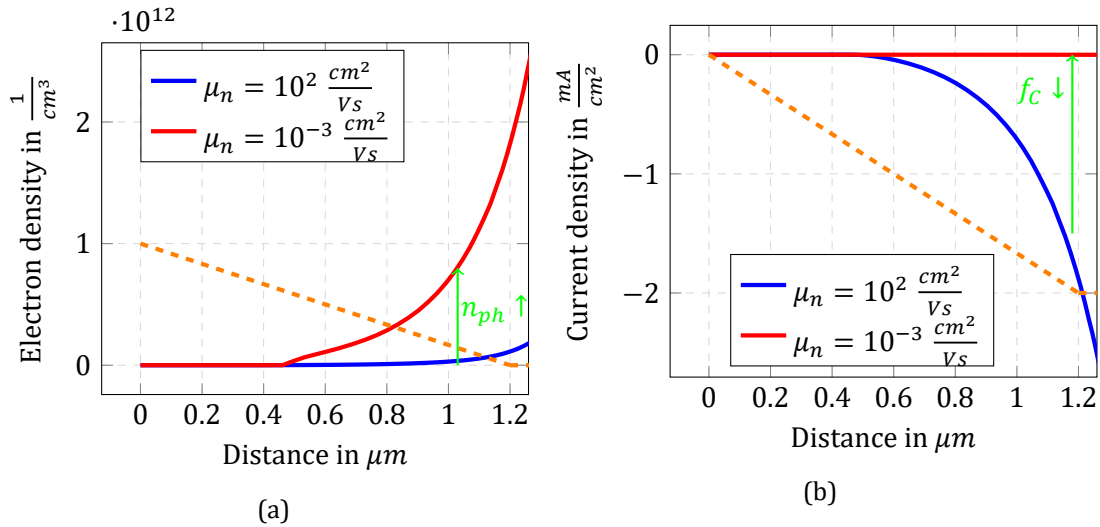


Figure 4.22: (a) Simulated in SCAPS electron concentration  $n_{ph}$ , and (b) electron current density  $J_n$  for different  $\mu_n$  values. The orange line schematically represents the bandgap profile. The position of the back contact at  $x=0$ .

electron current density with a decreasing  $\mu_n$  in Figure 4.22b which corresponds to the  $J_{ph}$  also implies a degraded EQE spectra. **The low mobility case fits best to the discussed results.**

The deduction of the trapping states which may be responsible for the degradation of the carrier mobilities is in agreement with the SEM images in Figure 3.2 where much smaller grains in the vicinity of the back contact can be clearly seen.

Furthermore, it is interesting to mention the impact of reduced charge carrier mobilities on the JV-measurements. As can be seen from Figure 4.23, a reduced  $\mu_p$  at high voltages has a similar impact on the JV-characteristics as a  $R_s$ , however, acting as a non-linear resistance (SCAPS simulations of the band diagram under forward bias are not shown) what also has a good fit to the observed characteristics.

## Résumé

*The RR theorem correlates the luminescent emission with the EQE-measurements for CIGS solar cells. In this section, the theorem has been applied to the devices with different graded bandgap structures. The changes in the effective bandgap for absorption can be successfully monitored for all investigated devices by analysing the emission spectrum either measured by the PL technique or calculated from the black body radiation. However, the inconsistency in the spectrum shape between the measured and calculated spectra leave open questions regarding its origin. An assumption of a reduced charge carrier mobility in the graded region, however, provides the best fit to the observed characteristics and can explain the discrepancy in the spectrum shapes. The results of this section suggest that the RR theorem should be handled with care when applied to solar*

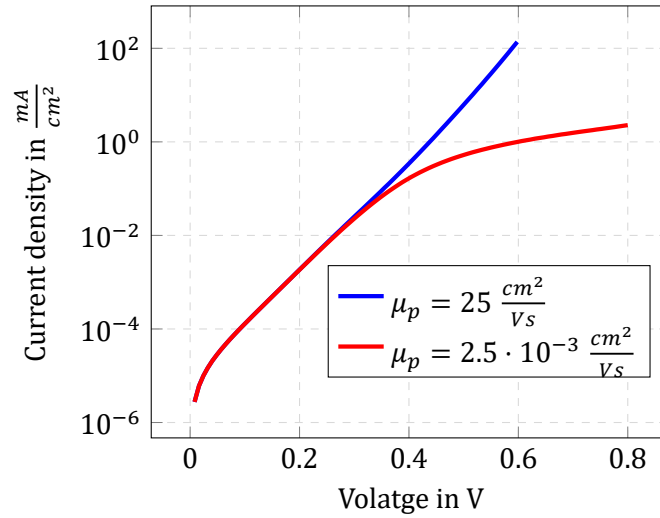


Figure 4.23: Impact of the charge carrier mobilities on the JV-characteristics.

cells with a graded bandgap absorber as for the investigated samples the RR can be approximated with some deviations only.

## 4.4 Conclusion

This chapter has been intended to support and complement the experimental results in order to get a better understanding of advantages of bandgap grading and its impact on electronic properties of CIGS solar cells.

The main conclusion which can be deduced from the experiment and verified in this chapter is the possibility to reduce recombination processes and to preserve absorption and photocurrent collection at the same time by implementing an appropriate bandgap grading profile in the SCR. It has been demonstrated analytically that a bandgap widening in the SCR leads to the enhancement of the effective bandgap for recombination which in certain cases can reach as high as  $\approx \frac{1}{\sqrt{2}}$  of the overall bandgap increase based on the evaluation of different grading profiles. The QNR is left unaffected, therefore no degradation of absorption and photocurrent collection is expected. This finding is applicable to solar cells with a S-incorporation into the surface region of the absorber as well as to those with a Ga- induced front grading. However, in the latter case the  $E_C$  offset between the absorber and buffer layers has to be investigated thoroughly.

Next, the mathematical definition for the effective diffusion lengths for injected as well as photogenerated minority charge carriers have been presented with respect to the presence of a back gradient. It has been found that with a back gradient the excess minority carrier profile differs from the one of the collection probability. This finding pointed out at the inconsistencies in the reciprocity relation between luminescence and EQE-measurements applied to solar cells with a graded bandgap structure. However, a discrepancy in the spectrum shape between

the calculated and measured PL emission could not be explained unambiguously. A theory of a reduced electron mobility in a graded region provides a good fit to the experimental observations though. This theory could be also supported by the SEM images of the investigated samples which reveal a finer granularity close to the back contact region.

With respect to a back grading, it has been mathematically shown that an appropriate back gradient can significantly reduce the back contact recombination by limiting the diffusion current density towards the absorber/back contact interface, and thereby enhance the device  $V_{oc}$ . This is of high importance for solar cells with a thin absorber layer. The limit for an absorber thickness has been also indicated when a back gradient has no pronounced impact on the reduction of the diffusion current density in the vicinity of the back contact for thick absorbers.

Moreover, as has been shown in the calculations a slope of the gradient (or the strength of an induced electric field) plays an important role in as how far back contact recombination can be suppressed with respect to the injected current density. Furthermore, the same back gradient is able to improve the current collection profile by reflecting photogenerated charge carriers towards the main junction. An improved carrier collection probability has been analytically described for the absorber with the uniform and back contact graded regions. It has been shown that in the presence of a back grading which leads to drift-assisted diffusion of minority carriers towards the main junction the collection probability can approach 100% with an appropriate back grading. The expression which relates an electric field strength and back contact recombination velocity with the collection of photogenerated electrons by the leaky back contact has been presented.



## Chapter 5

# Performance enhancement due to a Ga-gradient

*Nowadays, sequentially grown as well as coevaporated absorbers exhibit a back surface grading with a gradual decrease in  $E_g$  towards the bulk and a low bandgap region close to SCR which is referred to as a grading notch in the literature. Such a grading shape was widely accepted to fabricate the devices with the world record efficiencies. A grading notch aims at improved absorption of low energy photons to recover  $J_{sc}$  and to boost the cell efficiency. An increased annealing time during the sequential absorber deposition process at high temperatures reduces a Ga-accumulation at the back contact, and therefore the back surface grading, by enhancing a Ga-out-diffusion towards the main junction, and hence increasing the bandgap in the absorber bulk. Therefore, issues to be addressed in this chapter are (1) to find out what impact a Ga-redistribution has on the device performance with a double graded absorber, and (2) to investigate how far a Ga-accumulation affects the non-Ohmic back contacts. The samples used for the investigation are described in Table 3.1 as the reference Ga and-annealing set. The GDOES data is reproduced in Figure 3.3 for the reference sample and in Figure 3.4 for the samples with different annealing times.*

### 5.1 Enhancement of the effective bandgaps for recombination and current collection

#### 5.1.1 Motivation: Ga-induced increase in a bandgap energy $E_g$

Since for photovoltaic applications devices with higher voltages are preferred over those with higher currents, the factors which directly impact the device voltage are of high importance. The correlation between  $E_g$  and  $V_{oc}$  is given by Equ. 2.16. The effect of an increasing bandgap on  $V_{oc}$  can be seen in Figure 5.1. With an increasing  $E_g$  from 1.0 eV up to 1.4 eV, the  $V_{oc}$  improvement can reach as far as 0.4 V if all other parameters are kept unchanged. It has to be mentioned that the  $3 \cdot kT$  increase in the extrapolated activation energies is also visible, as

the temperature-dependence of relevant parameters is taken into account by the SCAPS algorithm. In this context, the  $\text{Cu(In, Ga)Se}_2$  quaternary material possesses outstanding features. Reasonably high efficiencies can be still obtained for large deviations from the stoichiometry to the Ga-, In-rich side of the phase diagram in comparison to the pure ternary  $\text{CuInSe}_2$  one. A vast amount of experimental works has been dedicated to study the influence of a varied Ga-content in graded and uniform  $\text{Cu(In, Ga)Se}_2$  absorbers on the performance of solar cells. [98, 68, 99] The results confirmed a  $V_{oc}$  increase according to the bandgap for a wide range of CIGS compositions. [100, 101, 89, 99]

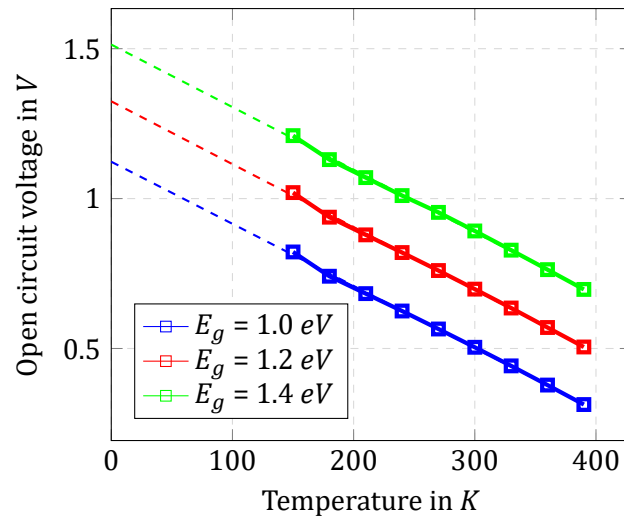


Figure 5.1: SCAPS simulated  $V_{oc}(T)$ -characteristics for different bandgap energies.

However, considering solar cells with an unintentionally localised wide-gap material due to a Ga-segregation, the impact of a Ga-distribution on the optoelectronic properties of solar cells can be ambiguous. A first published attempt (to the author's knowledge) to flatten an unintentional Ga-gradient has been made by a Taiwanese group in [99]. The authors claimed that flatter Ga-profiles give rise to the higher  $V_{oc} \times J_{sc}$  by improved bandgap matching to the solar spectrum that is hard to achieve with a Ga-gradient. Furthermore, other groups reported that the amount of Ga added to the CIGS alloy can change not only the bandgap energy but have a major impact on the transport mechanisms and the defect environment in the absorber. [78, 102] This follows from the fact that a chemical gradient due to a varying Ga-content may lead to a gradient in the lattice constants, therefore inducing the defect formation. [34]

A proficient manipulation of the absorber bandgap profile is an important prerequisite for the further advancement in achieving high efficiencies. A strong influence on the formation of a Ga-gradient has been observed from varying the substrate temperature or high temperature annealing times [66], the Na or other alkali metal supply, Se- and S-rates [103], Cu-poor or Cu-rich conditions [104]. However, dealing with the differences in the GGI ratios induced by high

temperature annealing processes, special care has to be taken with respect to certain features of a Ga-gradient: a front or back gradient, a slope, single or double grading, a position of the GGI minimum; as all these parameters affect the final device performance. [105] In this context, a Ga-redistribution both in the uniform and graded absorber profiles presents a great interest with respect to its effect on the performance of CIGS solar cells.

### 5.1.2 Experiment and Discussion

The solar cells with different Ga-distribution profiles investigated in this chapter are described in Section 3.1 (see Table 3.1). To evaluate the electrical performance of the cells, JV-characteristics in the dark and under white light illumination were measured. Figure 5.3 repro-

Table 5.1: Performance parameters of the studied solar cells.

Annealing time	$V_{oc}$ , [mV]	$J_{ph}(EQE)$ , [ $mA/cm^2$ ]	FF, [%]	A, (dark/ $J_{sc}-V_{oc}$ )	$J_0$ , [ $mA/cm^2$ ]	$R_{sh}$ , [ $k\Omega \cdot cm^2$ ]	$R_s$ , [ $\Omega/cm^2$ ]
ref	596	34.6	66	2.52/1.64	4.0e-7	0.26/0.192	6.75/7.75
med	608	34.6	66	2.53/1.70	2.8e-7	0.56/0.296	7.0/11.0
long	628	33.1	67	2.54/1.71	3.8e-7	0.48/0.296	6.25/7.5

duces the corresponding JV-curves. The extracted performance parameters are summarized in Table 5.1. For A,  $R_{sh}$  and  $R_s$ , the values were extracted from both dark and light measurements and are given slash-separated as "dark / light measurement".  $R_s$  parameters have been determined following an approach proposed in [106]. A conductance over current,  $G/J_d$ , was plotted versus conductance G in order to get a better approximation to the steep slope as compared to a conventional  $R_s = dV/dJ_d$  at high forward bias voltage method. The diode ideality factor values have been also determined following the procedure in [106].

In comparison to the reference sample there is a systematic increase in the  $V_{oc}$  value of about  $\Delta V_{oc} = 30$  mV with increasing annealing times. The ideality factors A have been extracted from  $J_{sc} - V_{oc}$ -measurements in order to eliminate the impact of the series resistances and then compared to those determined from the dark JV-characteristics. This comparison can provide a deeper insight whether illumination influences recombination processes in the absorber layer. However, the impact of  $R_s$  of the back contact on A has to be kept in mind. The ideality factor  $A \rightarrow 2$  indicates that the device performance is limited by the carrier recombination via mid-gap states in the SCR, or Shockley-Read-Hall recombination. A Ga-outdiffusion towards the front interface slightly increases the value of A compared to the reference sample from 1.64 to about 1.7 as has been deduced from  $V_{oc} - J_{sc}$ -measurements. This increase can imply that a higher Ga-concentration towards the absorber/buffer interface slightly enhances the SRH recombination rates in SCR by decreasing the QNR recombination. This behaviour has been studied in [107]. However, the increase in A did not reflect in a FF decrease as FF of the devices is similar being slightly below 70% for all three devices. Furthermore, the A values extracted

from dark JV-characteristics are significantly higher,  $A \sim 2.5$ , compared to those from  $V_{oc} - J_{sc}$ -measurements which indicates that in the dark a different mechanism controls the voltage dependence of the diode current. This observation will be discussed later in this section. The reference sample has considerably lower shunt resistance  $R_{sh} = 0.26 \text{ k}\Omega \cdot \text{cm}^2$  compared to the high temperature samples with  $R_{sh} = 0.56 \text{ k}\Omega \cdot \text{cm}^2$ . It is a common observation that in the initial state samples from the reference process require additional heat treatment in order to improve their performance by reducing leakage currents. Apparently, this step is not necessary for the samples grown at high temperatures. Under illumination,  $R_{sh}$  significantly decreases for all three samples. To the contrary, series resistance is comparable within the tested devices and remains invariant under illumination. The light-induced current,  $J_{ph}$ , deduced from EQE-measurements is rather similar for the reference and sample with medium annealing time, whereas long annealing time deteriorates the photocurrent by  $1.5 \text{ mA/cm}^2$ . Correlating improved  $V_{oc}$  and decreased  $J_{ph}$ , the following interpretation of the experimental results can be proposed. Prolonged deposition at high temperatures promotes a Ga-outdiffusion from the back contact towards the front interface resulting in a widening of the absorber bandgap. However, the impact of Ga on other parameters have to be inspected for consistency.

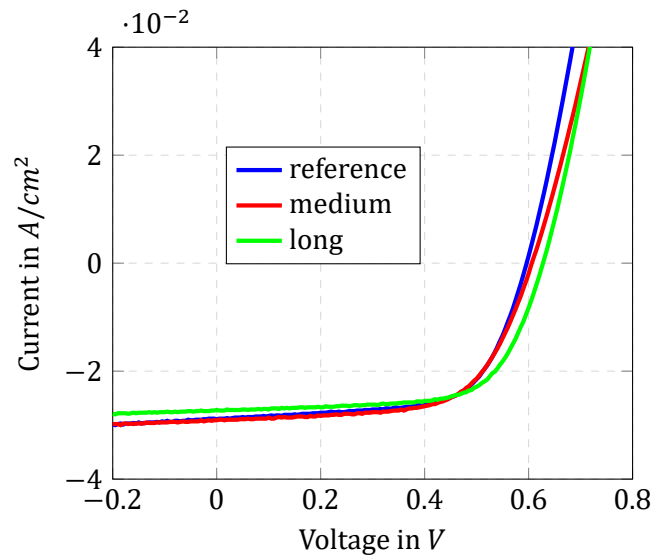


Figure 5.2: Light JV-characteristics of the samples with different diffusion

Another possibility to explain the  $V_{oc}$  improvement is the increase of the net acceptor density. Capacitance-voltage (CV) measurements can provide information on the depth profile of the doping distribution and the space charge width as has been described in Chapter 3.2.1. The CV-measurements and calculated doping profiles of the discussed samples are reproduced in Figure 5.4. The value of net acceptor density  $N_a$  is estimated from the minimum of the U-shape doping profile plotted in Figure 5.4b. The doping concentration  $N_a$  for these samples changes



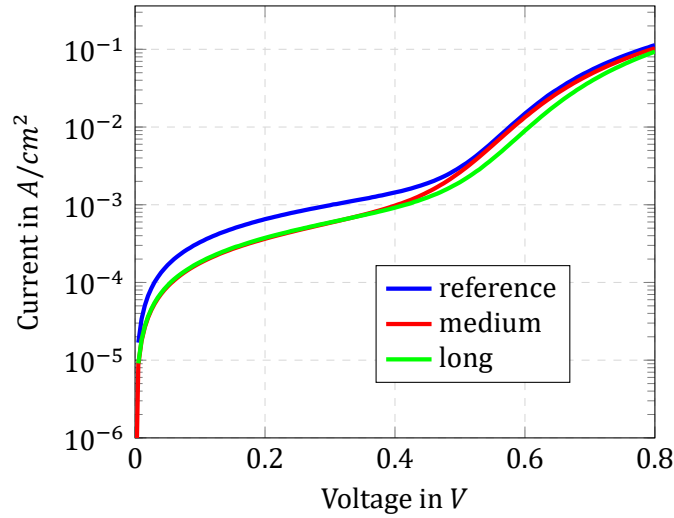


Figure 5.3: Dark JV-characteristics on a semilogarithmic scale for the samples with different annealing times.

negligibly and equals to about  $1 \cdot 10^{16} \frac{1}{\text{cm}^3}$ . Such minor deviation in the doping concentration is not able to explain the  $V_{oc}$  improvement of around  $30 \text{ mV}$  since the change in the doping density by one order of magnitude is expected to change  $V_{oc}$  at about  $\Delta V_{oc} = (kT \cdot \log 10)/q = 60 \text{ mV}$ .

From another side, changes in recombination rates or dominant recombination mechanisms can be also responsible for the changes in  $V_{oc}$ . In order to investigate the impact of Ga on the  $V_{oc}$ -limiting recombination processes, temperature-dependent JV-measurements have been performed. This measurement approach allows to identify the dominant recombination mechanism, i.e. interface- or bulk-limited by defining the activation energy of the recombination current. Since these recombination mechanisms are active in parallel, the strongest one will dominate the recombination loss. [34] A direct relation between  $V_{oc}$  and the activation energy  $E_a$  can be deduced from the fact that at open circuit conditions the total recombination current completely compensates  $J_{sc}$ , and  $V_{oc}$  at a given illumination intensity can be written as

$$V_{oc} = \frac{E_a}{q} - \frac{AkT}{q} \cdot \log\left(\frac{J_{00}}{J_{sc}}\right) \quad (5.1)$$

In this case, the activation energy of a dominating recombination process can be determined from the temperature dependence of  $V_{oc}$  by extrapolating its value to  $0 \text{ K}$ . Figure 5.5 shows  $V_{oc}(T)$ -curves of the investigated devices with dashed lines extrapolating them to  $T = 0 \text{ K}$ . However, the extracted values have to be corrected by  $3 \cdot kT$  as has been explained in footnote 1, Page 71. The extracted activation energies demonstrate an upward shift of the effective bandgaps for recombination with increasing annealing times. This finding is consistent with the aforementioned surmise of the bandgap widening and the measured  $V_{oc}$  values at room

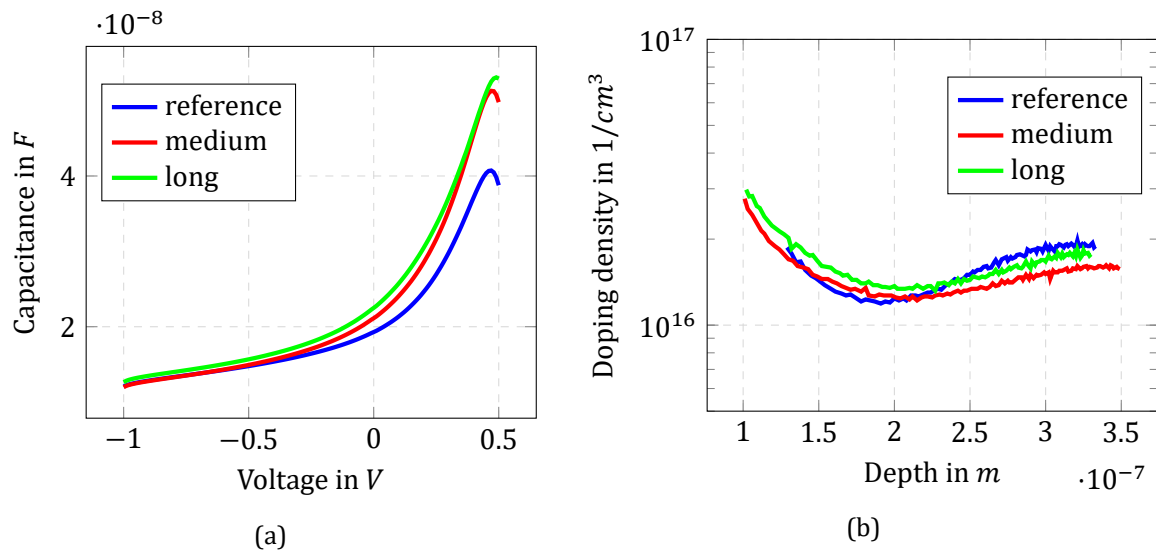


Figure 5.4: Capacitance-voltage characteristics (a) and doping profiles (b) of the devices with different annealing times

temperature. As can be seen from Table 5.3 an increase in the bandgap by  $30 \text{ meV}$  corresponds to the  $V_{oc}$  improvement by  $\approx 30 \text{ mV}$ .

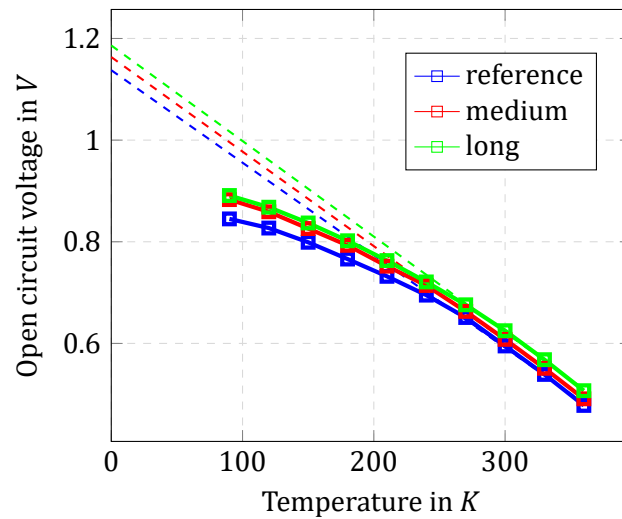


Figure 5.5: Temperature-dependence of the open circuit voltages for the devices with different annealing times

The impact of a promoted Ga-redistribution on the optical processes in the CIGS absorber has been studied by measuring EQE and photoluminescence spectra (PL). EQE quantifies a spectrally resolved contribution of the incident photons of a particular wavelength to the to-

tal photocurrent of a solar cell. As an in-depth variation of a relative Ga-concentration changes the bandgap energy, the onset of the EQE response in the long wavelength or in the short photon energy regions will determine the minimum  $E_g$  ( $E_{g,\min}$ ) present within the absorber layer.  $E_{g,\min}$  or hereafter the effective bandgap for absorption is traditionally estimated from the intersection of the linear interpolation of the squared EQE and the photon energy axis. This method is based on the semi-empirical expression of the proportionality between the absorption coefficient and the square root of the photon energy for direct semiconductors. [34] However, one can anticipate that localized states in the bandgap due to bandgap gradients complicate the determination of  $E_g$  from EQE response. To extract the bandgap from the EQE spectra three different methods will be compared. The above mentioned approach to extract the effective bandgap for absorption and photocurrent collection uses the relationship between the absorption constant  $\alpha$  and the bandgap  $E_g$  for direct transition:

$$(E_{ph} \cdot EQE)^2 \propto E_{ph} - E_g \quad (5.2)$$

Equ. 5.2 that is denoted as Method I assumes a constant reflection and parasitic absorption at energies close to  $E_g$ . Its generalized form (after Taylor expansion) reads [108]:

$$[E_{ph} \cdot \ln(1 - EQE)]^2 \propto E_{ph} - E_g \quad (5.3)$$

Method II is based on Equ. 5.3. However, both Equ. 5.2 and 5.3 assume constant absorption throughout the absorber depth what is not the case for graded bandgap absorbers. An analytical model for quantum efficiency in double graded bandgap solar cells has been developed in [109], considering the effects of sub-bandgap absorption and grading-dependent carrier collection properties. This model assumes linearly graded absorber and takes into account Urbach band-tail absorption, hereafter it will be denoted as Method III:

$$\left[ -\ln(1 - EQE) - \frac{2B}{3\beta} \frac{E_u^{3/2}}{\sqrt{2}} \right]^{2/3} \propto E_{ph} - E_g, \quad (5.4)$$

where  $B$  is the constant for fundamental absorption and equals to  $5 \cdot 10^4 \text{ cm}^{-1} \text{ eV}^{-1/2}$ ,  $\beta$  is the grading parameter which is determined as  $\beta = (E_{g,\text{back}} - E_{g,\text{front}})/d$  with the absorber thickness  $d$ , and  $E_u$  is the Urbach band-tail energy. To implement Equ. 5.4 for the bandgap extraction, the following assumptions have been made.  $E_{g,\text{back}}$  was calculated using the expression for a bandgap energy [110] based on the GGI ratio obtained from the GDOES-measurement shown in Figure 3.3 and 3.4.  $E_{g,\text{front}}$  was calculated analogically to the  $E_g$  at the back contact. The extracted  $E_g$  based on Equ. 5.2-5.4 are summarised in Table 5.2. Among the discussed models the best correlation to the spectral PL and  $V_{oc}$ -measurements is given by Method III. Its values for the effective bandgap for absorption will be used for further analysis.

Table 5.2: Extracted bandgap energies from EQE-measurements

Sample	Method I	Method II	Method III
reference	1.0	1.03	0.98
medium	1.01	1.06	0.99
long	1.06	1.09	1.03

The EQE-curves for the studied samples have been reproduced in Figure 4.15a. The difference in absorption cutoffs is consistent with the  $V_{oc}(T)$ -measurements from Figure 5.5. With an increasing bandgap energy due to an increased Ga-concentration in the absorber bulk, the absorption edge shifts to the lower wavelength range as can be seen from Figure 4.15a. The tailing in the long wavelength region is most pronounced after the longest annealing time. This can result from enhanced sub-bandgap absorption due to a stronger disorder in the material with a higher Ga-content. However, the Urbach energies for  $\text{CuInSe}_2$  as well as for  $\text{CuGaSe}_2$  materials have been found in the range of  $kT$  at room temperature which suggests that the disorder is due to thermal vibration of lattice atoms. [34] The change in the effective bandgap for absorption can be also confirmed from the PL-spectra reproduced in Figure 4.15b. The PL peak position with increasing annealing time shifts towards lower wavelengths from around  $1240 \text{ nm}$  to  $1190 \text{ nm}$  meaning that the effective bandgap for absorption increases. The shape of the PL-spectra for all three samples is rather similar with full width half maximum (FWHM) of about  $10 \text{ meV}$ .

Table 5.3: Extracted bandgap energies

Annealing time	$V_{oc}$ , [mV]	$E_g(T = 0)$ , [eV]	$E_g(EQE)$ , [eV]	$E_g(PL)$ , [eV]
reference	596	1.08	0.98	1.0
medium	608	1.09	0.99	1.02
long	628	1.11	1.03	1.04

The experimental results including  $V_{oc}$  and the extracted bandgap energies from  $JV(T)$ <sup>2</sup>-, EQE- and spectral PL-measurements are summarized in Table 5.3. As one can see, the improvement in the  $V_{oc}$  values by  $32 \text{ mV}$  with increasing annealing times correlates with the increase in the energy bandgap by  $30 \text{ meV}$  as deduced from  $JV(T)$ -measurements. The similar tendency is observed for the optical bandgaps extracted from EQE- and spectral PL-measurements. An increase in  $E_g$  by  $\sim 40 \text{ meV}$  can be deduced from the PL-spectra. The discrepancy between the values extracted from EQE- and spectral PL-measurements can be related to the enhanced tailing of the EQE-curve for long annealing, and therefore to the inaccuracy of the extraction method. As can be seen from Figure 5.6, an increase in  $V_{oc}$  due to the outdiffusion of Ga from

<sup>2</sup>corrected for  $3 \cdot kT$ .

the back contact towards the front interface correlates almost linearly ( $\Delta V_{oc}/\Delta E_g \rightarrow 1$ ) with the increase in the effective bandgap for absorption extracted from the spectral PL-measurements. Small deviations from the linearity within the set of the studied solar cells might imply that a

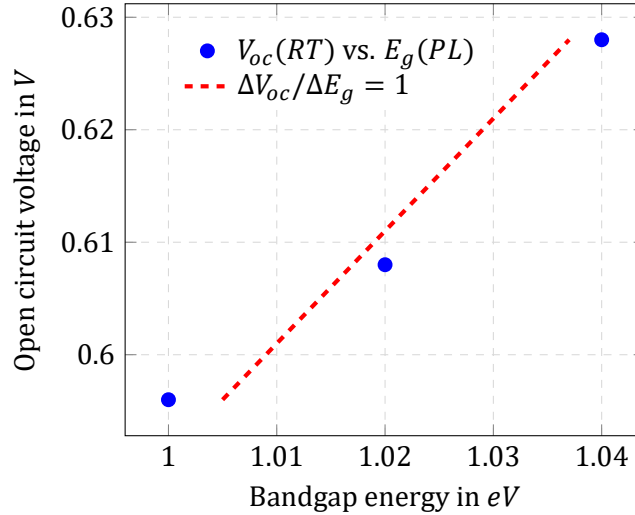


Figure 5.6: Correlation between  $V_{oc}$  at room temperature vs. the effective bandgap for absorption (extracted from the spectral PL measurements) with respect to varying annealing times.

Ga-diffusion enforced by high temperature annealing does not lead to the absorber layer with an uniform  $E_g$ .

The correlation between the relative increase in  $V_{oc}$  at room temperature versus the optical (extracted from the PL-spectra) and electrical bandgaps for different annealing times with respect to the reference sample is visualised in Figure 5.7.

The results indicate that high temperatures during absorber deposition processes enhance a Ga-diffusion towards the heterojunction reducing a Ga-gradient at the back contact and leading to a more homogeneous distribution within the absorber layer which in turn affects both the optical and electrical bandgaps. As a consequence, the separation of recombination and absorption processes is not possible to achieve using this approach as the enhancement of the effective bandgap for recombination is accompanied by the enlargement of the effective bandgap for absorption and photocurrent collection.

### 5.1.2.1 Résumé

*The out-diffusion of Ga from the back contact towards the front interface as a result of prolonged high temperature annealing increases the device  $V_{oc}$  by widening the  $E_g$  as has been observed from the temperature-dependent  $V_{oc}$  measurements. However, the effective bandgap for absorption extracted from the spectral PL measurements has been found also affected by an increased Ga-concentration in the absorber bulk. This implies that the separation of recombination and ab-*

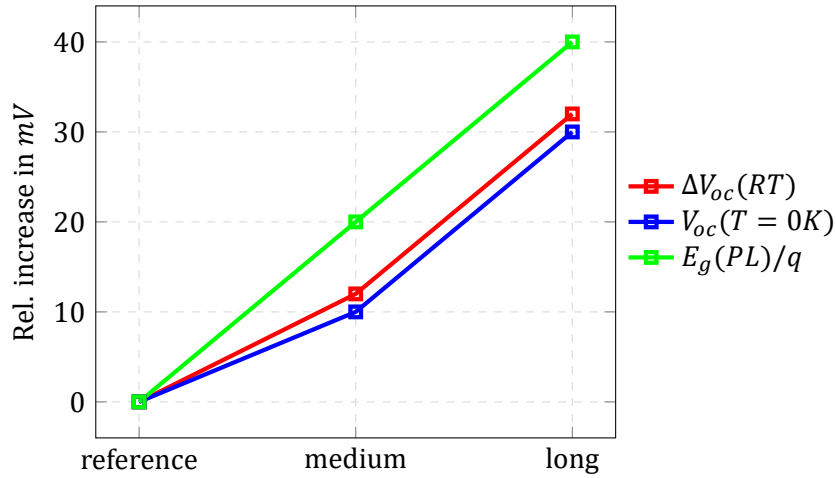


Figure 5.7: Correlation between the relative increase of  $\Delta V_{oc}$  at room temperature versus optical and electrical bandgaps with respect to the reference device for different annealing times.

*sorption processes in order to achieve a trade-off between the device  $V_{oc}$  and  $J_{sc}$  cannot be realised solely by the thermally-induced flattening of the Ga-distribution profile.*

## 5.2 Impact of a Ga-grading on non-Ohmic back contacts

### 5.2.1 Motivation: Back contact passivation

To be considered as a good back contact to a p-type CIGS absorber, a material has to provide a low resistance ohmic contact for majority charge carriers (holes) and to repel minority carriers (electrons) preventing their recombination at the back contact interface.

However in practice, the Schottky contact at the CIGS/Mo interface is often observed instead. The presence of a Schottky contact leads to the enhanced minority charge carrier transport to the back contact region. As a result, recombination rates at the absorber/Mo interface increase which may cause pronounced  $V_{oc}$  losses and performance degradation depending on the barrier height. This situation is highlighted in the simulated band diagram in Figure 5.8.

The situation changes when a wide bandgap material is inserted between the back contact and absorber layer. Figure 5.9 depicts the band diagram with such a passivation layer. The layer thickness used in the simulations is equal to 100 nm with  $E_g$  of 1.68 eV which corresponds to the pure CuGaSe<sub>2</sub> material. An insertion of a wide bandgap layer with a uniform  $E_g$  is a very rough representation of a Ga-segregation at the back contact, but it is very demonstrative when an impact of a high energetic barrier on carrier transport has to be studied.

Therefore, a wide-gap material introduced at the back interface can be a passivation approach for a collecting contact. The energetic barrier introduced by the upward shift of the CB

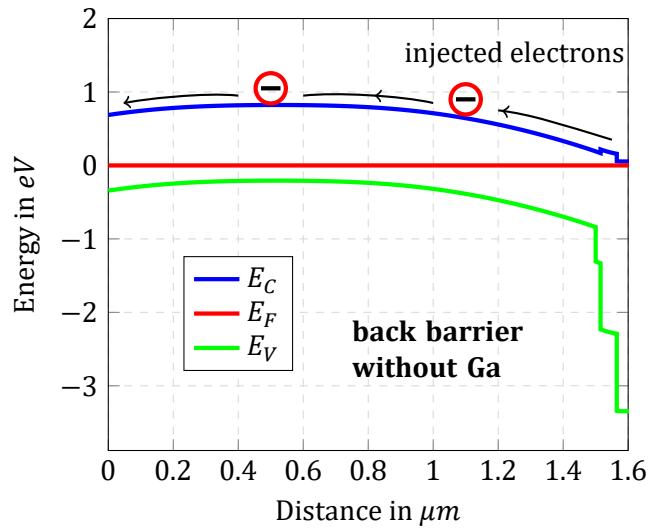


Figure 5.8: Band diagram for a standard CIGS solar cell (without Ga-grading) with a back contact barrier.

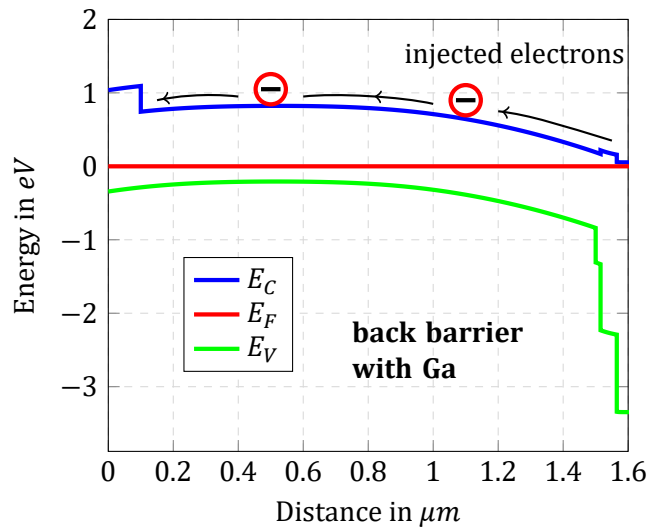


Figure 5.9: Band diagram of a standard CIGS solar cell with a Ga-step and a back barrier at the back contact.

minima can hinder the injection of electrons to the back contact and their consequent recombination without affecting the majority carrier transport.

### 5.2.2 Literature review

In the majority of fabricated CIGS solar cells nowadays, the back contact is represented by a sputtered Mo layer. This material is traditionally chosen by many solar cells manufacturers due to its high electrical conductivity, low thermal expansion coefficient, good adhesion to the glass substrate and good resilience to the Se-atmosphere that is vital for further CIGS absorber growth. [111, 112].

Attempts to replace Mo by other elements (such as W, Ta, and Nb) to use as alternative back contact materials have been made by K. Orgassa. [113] Good results were obtained with Ta and Nb films as their reflective properties turned out to be superior to those of Mo and W films leading to decreased optical losses. On the other hand, K. Orgassa has shown that the CIGS/Ta and CIGS/Nb interfaces had to be passivated (in his case, by the back surface grading) in order to improve  $V_{oc}$ , whereas the back contacts with Mo and W seemed to provide a sufficient self-passivation. As a possible explanation for this behaviour different material properties of the interfacial selenide layer were suggested.

During the absorber formation process, a Mo back contact forms an ohmic contact to the CIGS absorber via an interfacial  $MoSe_2$  layer which provides a low resistance path to majority carriers [114, 115] and improves the adhesion between the Mo layer and the CIGS absorber. [116] However, some authors found that a Schottky contact is formed instead. [117] Moreover, the formation and properties of the  $MoSe_2$  layer strongly depend on the CIGS deposition method and the growth recipes. [116]

When a Schottky contact is formed, substantial problems with resistive losses due to a Schottky barrier at the back contact arise. In the equivalent circuit, a back contact barrier can be represented with a diode whose polarity is opposite to the polarity of the main diode. The schematic of a solar cell with a back contact barrier is illustrated in Figure 5.10. The fingerprints of the Schottky barrier at the back contact which can be observed from JV-measurements especially at low temperatures are following:

- S-shape of JV-characteristics. In particular, a blocking behaviour of the forward current;
- a  $V_{oc}$ -saturation with temperature and intensity. Most often observed on solar cells based on coevaporated absorbers;
- a cross-over of the dark and illuminated JV-characteristics.

In case of a moderate Schottky barrier, the contact introduces a low potential barrier which has an influence on the device performance only at low temperatures. However, long term endurance tests and accelerated ageing enhance the barrier height at the absorber/back contact interface leading to the deterioration of the device performance already at room temperatures. [118, 57]



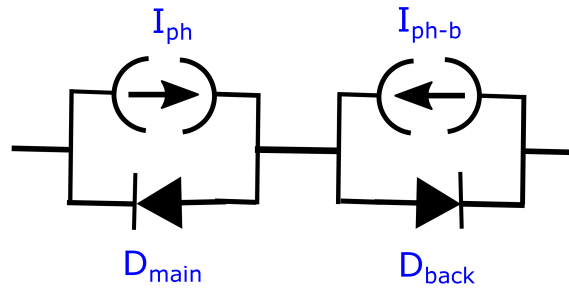


Figure 5.10: Two diode model which represents the main diode and the Schottky diode at the back contact operating in the 'wrong' direction.

The influence of the back contact barrier on the overall device performance and stability has been extensively investigated experimentally [118, 57, 119] and by means of simulations [34]. The results demonstrate that the back barrier height has a pronounced impact, first of all, on FF and  $V_{oc}$ . The strongest impact of the back contact barrier can be expected on the devices with thin absorbers or devices whose charge carrier diffusion length is in the range of the absorber thickness. CIGS solar cells deposited by coevaporation processes proved to be most vulnerable to the back contact issues. [111, 118] Moreover, it has been shown that under certain conditions the behaviour of CIGS solar cells can be interpreted in terms of a phototransistor behaviour which is most often observed at low temperatures or after accelerated ageing tests already at room temperatures. The underlying physics behind this phenomena is discussed in [58, 120]. A similar behaviour has been reported for CdTe solar cells in [121, 122] and was discussed in terms of reach-through diodes.

### 5.2.3 Simulations

On a device simulation level, an enhanced energetic barrier for majority carriers which is equivalent to a Schottky contact can be introduced by varying the metal work function of the back contact. [58] An impact of a back barrier on the carrier transport can be seen in Figure 5.11 where light JV-characteristics simulated in SCAPS-1D at 180 K are reproduced. The simulations instantiate four cases: flat bands, flat bands with a Ga-step, a back contact barrier, and a back barrier with a Ga-step.<sup>3</sup>

Under flat band conditions, i.e., with an Ohmic contact between the back contact and absorber layer, the JV-curves demonstrate a diode-like behaviour with a  $V_{oc}$  of about 700 mV. An insertion of a Ga-step improves the  $V_{oc}$  by 40 mV. However, an introduction of the back barrier height of 300 meV leads to a significant degradation of  $V_{oc}$  ( $\approx 40$  mV) and a blocking of the forward current. The back contact barrier blocks the hole transport, and the device supplies

<sup>3</sup>The simulation parameters in this section are as described in Section 4.1 if not stated otherwise.

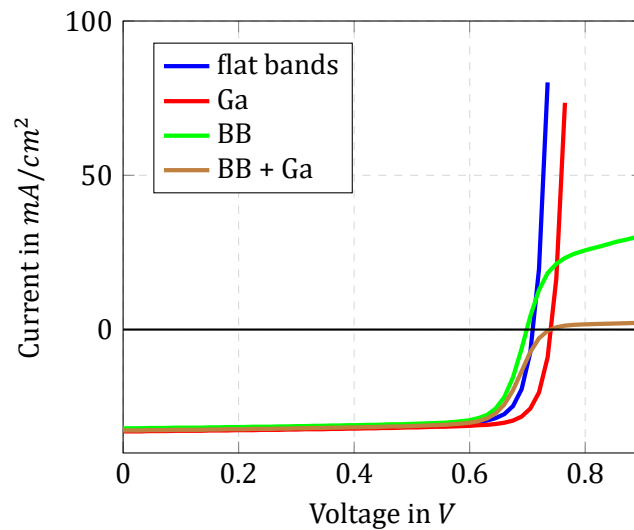


Figure 5.11: Simulated illuminated JV-characteristics with an Ohmic back contact (blue), with a Ga-step (red), with a back barrier of  $300\text{ meV}$  (green) and with the barrier and Ga-step at the back contact (brown) at  $180\text{ K}$ .

no current anymore, forcing photogenerated electron-hole pairs to recombine. The situation improves when a Ga-rich layer at the back contact is inserted. Nevertheless, it is not easy to see from the figure, but  $V_{oc}$  increases compared to the flat band case as might be expected from the back contact passivation. Yet, the blocking of the forward current becomes even more pronounced as a result of the enhanced barrier due to a Ga-step for the injected electrons at the back contact and still a still present barrier for holes.

The impact of the barrier height on  $V_{oc}$  is demonstrated in Figure 5.12. As has been discussed above, a Ga-accumulation at the back contact can modify the band alignment at the back contact/absorber interface. Therefore, the  $Suns - V_{oc}$ -characteristics have been simulated for three cases: flat bands, a back contact barrier, and a back contact barrier with a Ga-step. Introducing a barrier height of  $300\text{ meV}$ , while keeping other parameters same, degrades  $V_{oc}$  by approximately  $40\text{ mV}$  at 1 sun. It is interesting to note that at low intensities, the slope of the  $Suns - V_{oc}$ -curve with the back barrier differs significantly from the slope under higher illumination levels. The behaviour of the  $Suns - V_{oc}$ -curve can be correlated with the device ideality factor  $A$ . In the dark or under low illumination, a larger slope induced by a non-Ohmic back contact indicates the increased  $A$ , whereas under illumination the  $A$  is expected to be significantly smaller than the normally observed values what can be deduced from the slope approaching  $\infty$  when with a back barrier  $V_{oc}$  becomes rather independent of the illumination level.

In agreement with the simulated JV-curves in Figure 5.11, inserting a Ga-step at the back contact not only recovers the initial values of  $V_{oc}$  but slightly improves them.

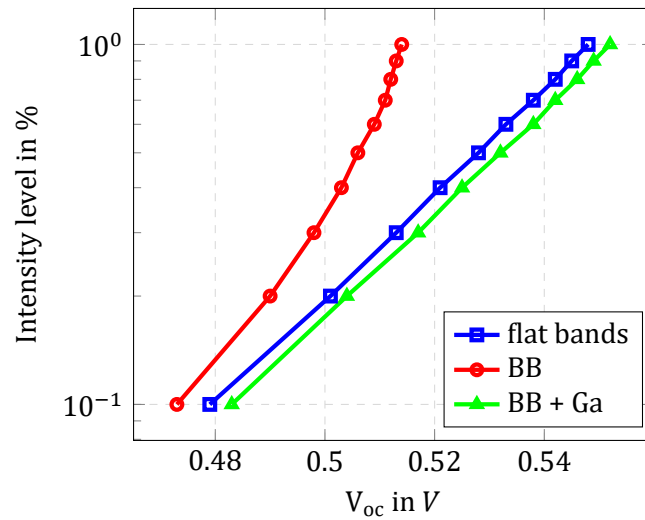


Figure 5.12: Simulated Suns –  $V_{oc}$ -characteristics for three cases: the flat band alignment at the back contact (blue), an enlarged back contact barrier (red), and a back contact barrier with a Ga-gradient.

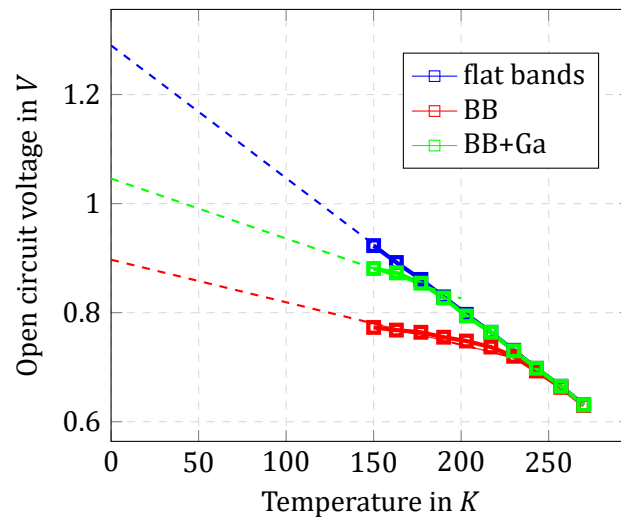


Figure 5.13: Impact of the back contact barrier and a Ga-gradient on the  $V_{oc}$  saturation based on SCAPS simulation.

The Suns –  $V_{oc}$ -measurements emphasise a role of a Ga-gradient in the  $V_{oc}$  improvement if a back contact barrier is enlarged. Furthermore, there is a pronounced impact of the back contact barrier and a Ga-gradient on the low temperature behaviour of a solar device as has been already seen in Figure 5.11. Figure 5.13 reproduces the temperature dependence of the device  $V_{oc}$  at temperatures below 240 K where the  $V_{oc}$  saturation is usually observed. [118] In this simulation, the barrier height is intentionally enlarged up to 400 meV in order to intensify its impact on the device  $V_{oc}$ . According to [123], the height of the back barrier can be easily estimated from the temperature-dependent characteristics of the device  $V_{oc}$ . The extrapolation of  $V_{oc}$  to 0 K gives an activation energy for the device with the flat band alignment at the back contact. However, for the device with a Schottky contact the saturation of its  $V_{oc}(T)$ -characteristics at low temperatures is expected. Thus, the extrapolation of the saturating section of a  $V_{oc}(T)$ -curve to 0 K for the device with a Schottky-diode at the back contact will be reduced by the value equal to the height of the back barrier. [123] Therefore, the difference between the extrapolated values for the activation energies of the device with the flat band alignment and the device with a Schottky-diode at the back contact gives the Schottky barrier height in agreement with [123].

However, as can be seen from Figure 5.13 the situation becomes more complicated when a Ga-step is introduced. The deduced barrier height from the simulated curve is not equal anymore to the set value ( $\Phi_{bc} = 400$  mV) as the  $V_{oc}$  saturation is shifted to lower temperatures. As a result, the extrapolated value increases lowering the back barrier height. This has to be kept in mind when the contact barrier height has to be estimated based on the measurements of sequentially grown solar cells where a Ga-step at the back contact is an inherent feature of the absorber deposition process.

Based on the presented simulations, following conclusions can be drawn:

- (1) an enhanced blocking behaviour of the forward current with an introduction of the Ga-rich layer proves the validity of the electron injection to the back contact;
- (2) a back contact passivation by a Ga-gradient recovers  $V_{oc}$  in the presence of a significant back contact barrier ( $\geq 300$  meV), but does not tend to improve FF which is still affected by the hole barrier. (The study of an impact of a back contact on the device FF is out of scope of this thesis, but it has to be mentioned in order to discuss approaches to improve the quality of the back contact.)

In order to find an optimal solution to the problem of the Schottky contact, the requirements to the ideal back contact listed above have to be fulfilled. That is, a back contact has to be able to reflect minority charge carriers and at the same time to ensure an ohmic contact for majority carriers. In this context, a Ga-gradient can meet the first requirement and its beneficial impact can be understood as a decrease of minority carrier recombination at the back contact. However, the hole transport is still impeded as the  $E_V$  maximum is down-shifted and not affected by a Ga-grading. A novel rear contacting structure for CIGS solar cells has been reported in [124, 86, 87]. The scientists from Taiwan have shown that  $Al_2O_3$  grown by atomic

layer deposition (ALD) can be an efficient edge passivator due to its induced field effect. The fixed negative charges in the  $\text{Al}_2\text{O}_3$  bulk would repel electrons from the rear interface or CIGS edges if P3-scribing passivation, for example, is considered. Moreover, their first principle calculations indicated that the deposition of  $\text{Al}_2\text{O}_3$  of about 5 nm already can reduce of  $\approx 35\%$  of the interface defect density. [124] Vermang et al. have developed this approach further. They combined the  $\text{Al}_2\text{O}_3$  rear surface passivation with nano-sized local point contacts and achieved an average  $V_{oc}$  improvement of 14 mV. The  $V_{oc}$  increase has been attributed to a decrease of rear surface recombination of a few orders. [86] However, a drawback of this method is a need for extra Na supply as a  $\text{Al}_2\text{O}_3$  film acts at the same time as a barrier for Na-diffusion from soda lime glass. A pronounced roll-over effect in JV-characteristics is usually observed in Na-free devices. [125, 126, 127] Interestingly, the way to achieve a 'loss free' electronic back contact can be inherent to the absorber deposition technique itself. A study on the electronic level alignment at the deeply buried absorber/Mo interface for S-free and S-containing samples with direct and inverse photoemission demonstrated that the absorber/Mo interface is strongly influenced by the presence or absence of S. [128] This finding in [128] may explain why solar cells based on sequentially grown absorbers have superior back contact properties compared to those based on coevaporated absorbers without S.

### Résumé

*Back surface potential barrier at the Mo/CIGS interface as a result of a Ga-accumulation is beneficial as it acts as an additional measure to prevent photogenerated electrons from recombination at the back contact. Since Ga affects only the CB minimum, it presents no substantial resistance to the majority charge carriers while repelling the electrons as the minority carriers. However, this approach does not solve the problem with the hindered hole transport which arises when a significant Schottky barrier is formed at the rear interface. The alternatives to improve the properties of the back interface have been discussed.*

## 5.2.4 Experiment

### Suppression of the phototransistor effects

The phototransistor behaviour is directly related to a Schottky barrier at the back contact. [58] The phototransistor model was developed to explain the experimental features which could not be interpreted in terms of the 'classical' back diode model. [56, 58] These features are the temperature- and illumination independence of  $V_{oc}$  at temperatures below 200 K and the saturation of the forward current at values much higher than a possible photocurrent from the back diode.

A solar cell starts operating in the phototransistor mode when a significant Schottky back barrier (hundreds of meV) is built-up and the photogenerated hole current exceeds the satu-

ration current at the Schottky back diode. [58] This behaviour is usually observed at low temperatures as has been mentioned above. Figure 5.14 reproduces illumination-dependent JV-characteristics at 180 K of the devices with and without a Ga-gradient at the back contact. It has to be mentioned here that the device without a Ga-gradient does not belong to the investigated set. Its introduction is meant to support the chosen interpretation of the results observed from the investigated devices. The device with a Ga-grading can be referred as a reference device in Table 3.1.

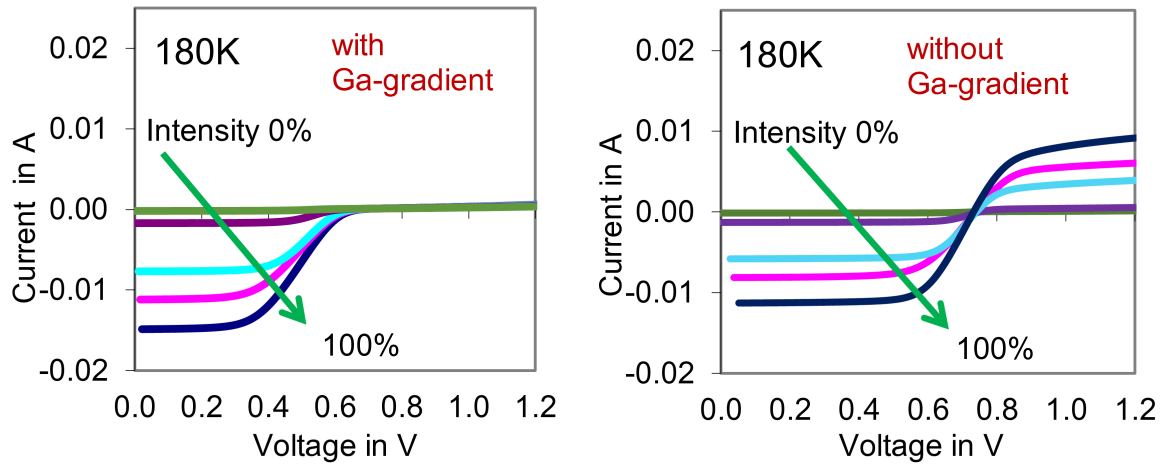


Figure 5.14: Experimental intensity-dependent JV-characteristics at 180 K of two devices: with and without Ga-gradient.

The JV-characteristics of the device without a Ga-gradient in the first quadrant resemble the output characteristics of a transistor. With increasing intensity the output current increases reaching the photocurrent values. The measurement fits well with the simulations shown in Figure 5.11. Furthermore,  $V_{oc}$  of this device becomes intensity-independent and saturates at low temperatures as can be seen in Figure 5.15b. Remarkably, the phototransistor behaviour is not observed on the device with a back surface gradient as can be seen in Figure 5.14. Due to a wider bandgap material at the back contact, a barrier for the electron injection into the back diode region exists leading to the blocking behaviour of the forward current and suppressing the phototransistor effect.

The height of the back contact barrier is a key parameter which determines at what temperature the phototransistor behaviour is detected. According to [64], the extrapolation of  $V_{oc}$  to 0 K returns the activation energy (solar cell mode at high temperatures) reduced by the Schottky barrier height (phototransistor mode at low temperatures). Comparing the temperature dependence of  $V_{oc}$  without and with a Ga-gradient from Figure 5.15, one can see that the saturation of  $V_{oc}$  occurs at much lower temperatures when a Ga-grading is present. However, to

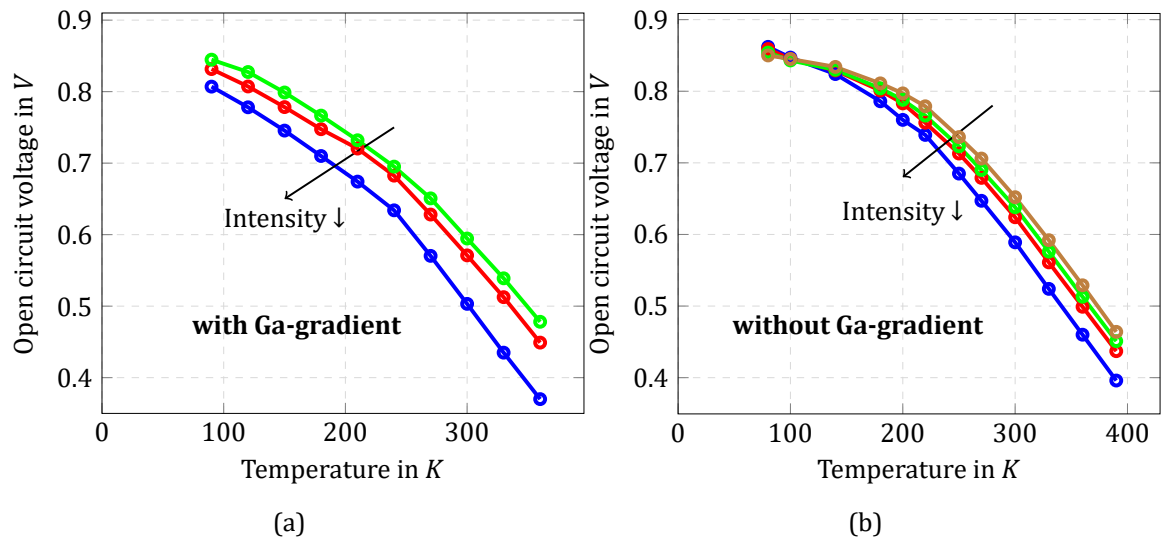


Figure 5.15: Temperature dependence of  $V_{oc}$  for different illumination intensities for the samples with and without Ga-gradient.

extract a particular value of the back barrier from the device with a Ga-gradient is somewhat difficult as its  $V_{oc}(T)$ -characteristics do not show a pronounced saturation at low temperatures but rather the tendency to bend what is in good agreement with the simulations in Figure 5.13. It has to be mentioned that the bending of  $V_{oc}(T)$ -characteristics at lower temperatures can be also affected by the presence of shunting paths which under conditions of the complete current blocking (due to the presence of the back barrier and the Ga-step) can be expected to have a significant influence on the  $V_{oc}$ -extraction. This can be easily seen in Figure 5.11 for the case of "BB + Ga". Moreover, the intensity-dependence of  $V_{oc}$  still exists for the sample with a back grading in contrast to the sample without a Ga-gradient as can be seen from Figure 5.15.

Figure 5.16 reproduces the temperature dependencies of  $A$  in the dark and under illumination of the devices with and without a Ga-gradient. For the sample with a Ga-grading, the values of  $A$  in the dark are greater than two and increase with decreasing temperatures. A similar temperature-dependence of  $A$  is observed for the sample without a back contact gradient. Several theories have been proposed to explain  $A > 2$ , including tunnelling enhanced recombination within SCR [129], recombination via coupled defects [130], and effects of bandgap energy fluctuations [54]. However, since the ideality factor describes to a certain extent the voltage-dependence of the current flow, the impact of the back contact barrier on the ideality factor can be another explanation for the observed behaviour of  $A$ . If the Schottky-diode is formed,  $A$  extracted from the JV-characteristics cannot be used anymore to describe the current conduction mechanism through the device. Under the assumption of the reverse-polarity two-diode model which represents the case with a Schottky diode at the back contact, the joint effect of two rectifying junction on the device ideality factor  $A$  has to be taken into consideration. [131] In the

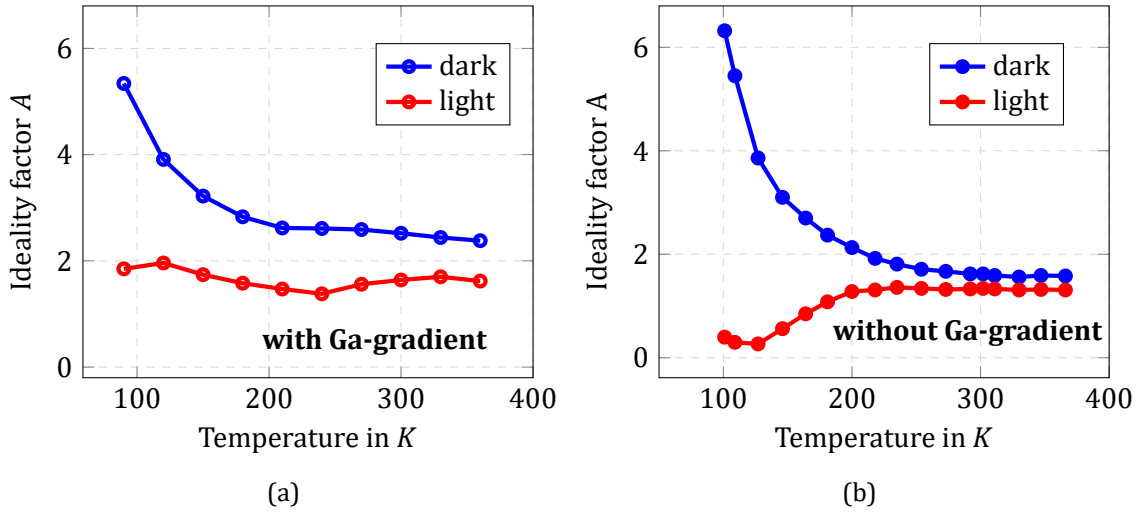


Figure 5.16: Temperature dependence of a diode ideality factor  $A$  derived from JV-characteristics in the dark and under illumination for the device (a) with a Ga-gradient and (b) without Ga-gradient.

limit of high contact resistance, the back contact can be considered as a reverse-biased Schottky diode, whose reverse saturation current  $J_{s,bc}$  will define the current flow through the device. When  $J_{s,bc}$  is larger than the diode dark current  $J_d$ , the back contact demonstrates an Ohmic behaviour and no distortion in JV-characteristics can be seen. This means that the contribution of the back contact to the measured ideality factor is rather minor. This situation is valid for high temperature measurements. However, at low temperatures, when  $J_{s,bc}$  is much smaller than  $J_d$ , the Schottky diode blocks the current flow resulting in the flattening of JV-characteristics and increasing the measured  $A$ . This model can justify anomalously high ideality factors measured experimentally on the discussed samples. The transition between these two regimes (where the impact of the Schottky contact is / is not detectable) can be clearly seen in the  $V_{oc}(T)$ -characteristics for the device without a Ga-grading shown in Figure 5.15b. Considering this device, it is easy to see that the flattening of the  $V_{oc}(T)$ -characteristics mentioned earlier correspond to the temperature region with anomalously high  $A$ . This means that the stronger the impact of the Schottky contact (i.e. the more rectifying, the contact), the higher the ideality factors are measured, and vice versa.

A pronounced impact of a Ga-gradient on the back contact can be seen from the  $A(T)$ -curves under illumination. The values of  $A$  for the device with a Ga-gradient are below two and essentially temperature independent. Such behaviour indicates a thermally activated recombination mechanism. However, the device without a Ga-rich layer demonstrate the anomalously low  $A$  ( $\approx 0$ ) extracted from the temperature region where the back diode is activated (in contrast to the dark measurement). Such low values can be correlated with a temperature and inten-



sity independence of the device  $V_{oc}$  which are the typical fingerprints of the phototransistor mode. In the dark, the blocking of the forward current is caused by the potential barrier for the majority charge carriers induced by the Schottky back diode. This effect is most pronounced at low temperatures as can be seen from significantly increased  $A$  in Figure 5.16. Under illumination, a positive bias dropping across the principal and back contact junctions lowers the respective barriers for electrons and holes. The saturation of  $V_{oc}$  occurs when the photogenerated hole current exceeds the saturation current of the Schottky diode as has been mentioned before. [58]

The problem with the back Schottky diode can be solved by introducing a wide gap material at the back contact. This deduction can be drawn from Figure 5.14 where no phototransistor effect is observed in the JV-characteristic of the sequentially grown device. Furthermore, the issue with the back contact diode can be solved, for example, by incorporating elemental S under optimised conditions to the back contact to ensure the formation of the interfacial layer with improved metallic properties.

### Résumé

*Another beneficial aspect of a Ga-gradient can be observed with respect to the back contact issues detected at low temperatures. It has been shown that a Ga-gradient suppresses the phototransistor behaviour and shifts the  $V_{oc}$  saturation to lower temperatures compared to the devices without a Ga-grading. Since a Ga-grading is an inherent feature of sequential growth processes, no transistor effect has been observed for the investigated devices. From this follows that an introduction of a Ga-rich layer can be a solution to prevent the phototransistor effects for coevaporated absorbers.*

### Impact of non-ohmic contacts on admittance measurements

As has been already discussed, the formation of the Schottky contact at the Mo/CIGS interface changes the equivalent circuit of a solar cell introducing a second junction. A relation between the presence of the back contact diode and the capacitance step in the admittance measurements has been reported already in [56]. The results of a systematic investigation of different CIGS devices presented in that study contradicted the previously accepted interpretation of the admittance step (also known as the N1-response in the literature) as a defect at the interface. The proposed model of a non-Ohmic back contact could explain the admittance step together with the cross-over and roll-over effects in the JV-characteristics which were difficult to interpret by the defect states only. Hereafter, an impact of the back contact on the admittance measurements will be investigated based on the JV(T)- and Cf(T)-measurements of the discussed devices.

The frequency dependence of the capacitance for the reference, with medium and long annealing times devices followed a similar pattern. Therefore, only the results of the device with

a long annealing time are to be presented here. The admittance measurements of the device for different frequencies and temperatures are reproduced in Figure 5.17. The capacitance decreases with increasing frequency and increases towards elevated temperatures. These features of the  $C_f(T)$ -measurements have to be discussed in more details. At higher temperatures, there is a pronounced gradient with respect to frequencies and upward shift of the  $C_f$ -characteristics. Since the measured capacitance consists of the charge contributions from the space charge region and defect states, charging and discharging the defect states may be responsible for the measurement outcome. The capture and re-emission of trapped carriers strongly depend on temperature, therefore the device capacitance increases at elevated measurement temperatures as can be seen in Figure 5.17(a).

At low temperatures (90 K–130 K) and high frequencies ( $> 10^5$  Hz) - under these conditions a measured  $C$  should correspond to the geometric  $C$  of the device - an increase in the capacitance values with respect to temperature is observed. The reason for this phenomenon is not clearly known but can be interpreted as follows. Assuming  $N_a = \text{const}$ , a shift of the  $E_F$  with increasing temperatures away from the  $E_V$  can take place. Furthermore, metastable effects due to carrier freeze-out can also impact the  $C$  values.

The capacitance step (observed at low temperatures only) which originates from both frequency and temperature dependencies is another characteristic feature of these devices. The comprehensive overview of the possible interpretations of the capacitance steps can be found in [80]. However, in this work the admittance step will be correlated to the non-Ohmic contact at the absorber/back contact interface.

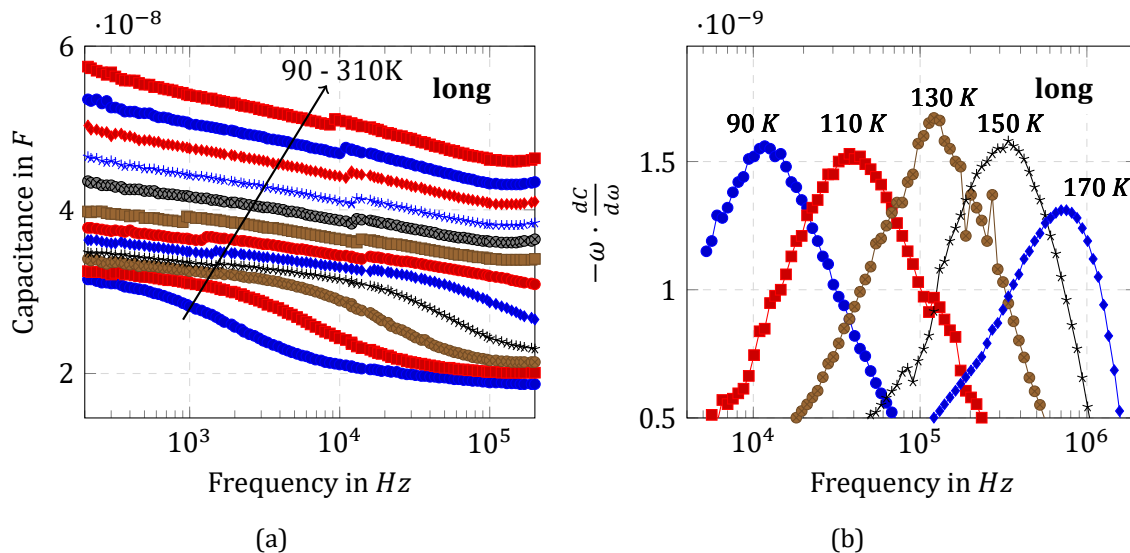


Figure 5.17: Temperature-dependent admittance measurements: (a) frequency-dependence of the capacitance; (b) temperature-dependence of  $-\omega \cdot \frac{dC}{d\omega}$  for the sample with long annealing time.

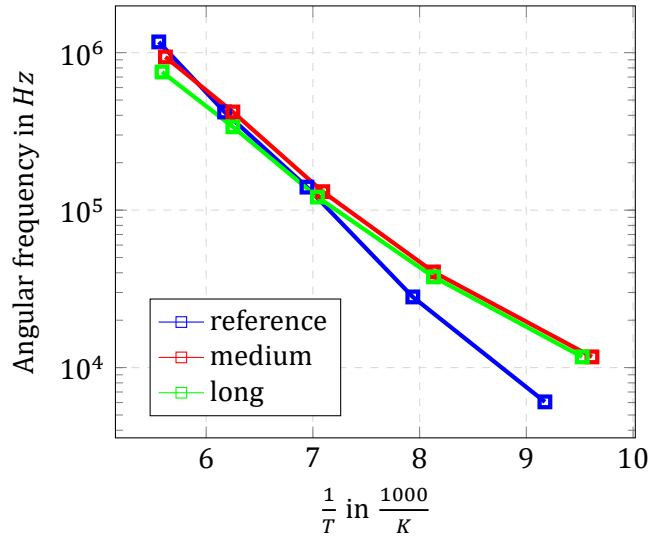


Figure 5.18: Arrhenius plot for the samples with different annealing times.

The position of the capacitance step with respect to the characteristic frequency is visualized by plotting the derivative of the capacitance as a function of angular frequency following [77]. The characteristic frequency for different temperatures corresponds to the peaks in the  $\omega \frac{dC}{d\omega}$  graphs reproduced in Figure 5.17(b). Such representation of the admittance is very demonstrative as the characteristic frequencies whereat the capacitance drops can be easily determined for the further evaluation. Plotting the extracted  $\omega_0$  for different temperatures as a function of  $1000/T$ , the activation energy for the observed capacitance step can be determined from the slope of the Arrhenius plot. [77]. The Arrhenius plots for the discussed devices are shown in Figure 5.18. The extracted activation energies for the studied samples which correspond to the observed capacitance steps are shown in Table 5.4. The activation energies are rather small which implies a modest barrier at the back contact. However, the contact barrier heights extracted from the  $V_{oc}(T)$ -characteristics deviate significantly from the latter ones showing much larger values. The reason for the deviation between the results of these extraction methods is unclear. However, it can be speculated that an equivalent electrical circuit chosen to interpret Cf-measurements does not describe correctly the complexity of the real devices. Similar problem has been reported in [119]. The correlation between the extracted values for the back contact barriers depended significantly on the absorber growth process and the back contact treatment.

In order to investigate how far the back barrier affects the current transport properties of the discussed samples,  $JV(T)$ -characteristics have been measured (see Figure 5.19). At low temperatures, up to  $170\text{ K}$ – $190\text{ K}$ , the blocking of the forward current is observed. For the devices with prolonged annealing times the current flow at  $90\text{ K}$  is almost completely blocked. The

Table 5.4: Comparison of the barrier heights extracted from the  $V_{oc}(T)$ - and  $C_f(T)$ -measurements of the devices with different annealing times.

Annealing time	$\Phi_{bc}(C_f(T))$ , [meV]	$\Phi_{bc}(V_{oc}(T))$ , [meV]
reference	125	240
medium	95	200
long	92	220

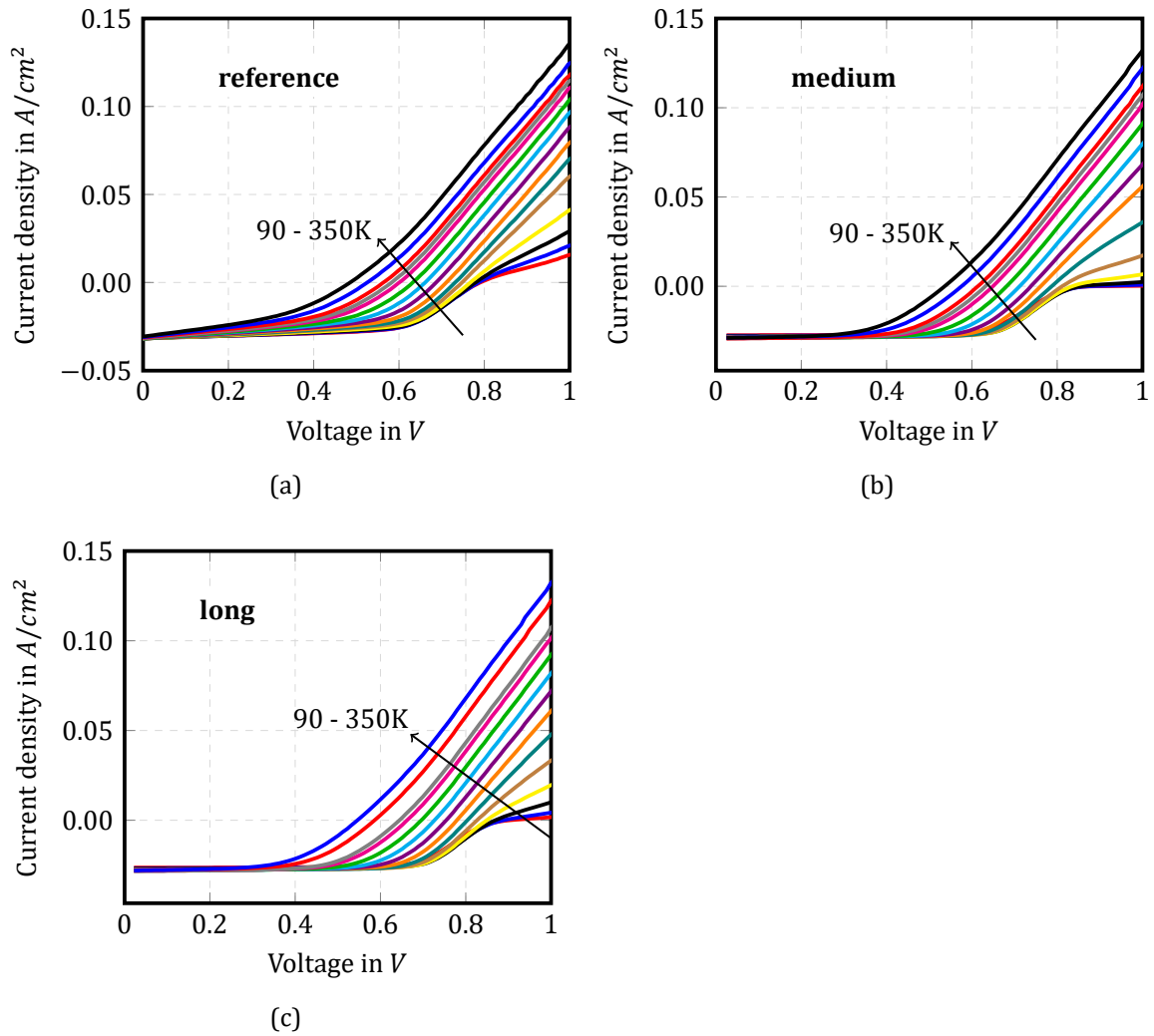


Figure 5.19: Experimental JV(T)-characteristics of the samples with different annealing times.

$C_f(T)$ -characteristics shown in Figure 5.17 demonstrate the capacitance steps at corresponding low temperatures which once again suggests the correlation between the saturation of the forward current due to a back contact and the admittance step.

In order to investigate further the common mechanism behind the admittance step and the anomalies in the  $JV(T)$ -characteristics discussed above two other devices will be introduced. These new devices do not belong to the investigated sample sets and are only meant to strengthen the arguments in favour of the back contact influence. In order to show that the roll-over behaviour of the forward current at low temperatures directly correlates with the presence of the admittance step the temperature-dependent  $JV$ -characteristics of two samples with and without the roll-over behaviour are reproduced in Figure 5.20 and compared to the corresponding admittance responses for different temperatures of the same devices. It is easy to see that the sample which does not demonstrate the roll-over behaviour of the forward current has no capacitance step as well. To the contrary, the sample which demonstrates a pronounced roll-over effect also has capacitance steps at the corresponding temperatures. The sample with no roll-over is based on the sequentially grown absorber. This implies - as has been discussed earlier - a Ga-gradient close to the back contact. This observation provokes a question whether the ideal back contact can be ensured by a co-optimisation, in other words, by the synergistic effect of the Ga- and S-gradients as the only S-incorporation method was different for this sample in comparison to the studied samples.

The presented  $JV(T)$ - and  $Cf(T)$ -measurements are in agreement with the previous results and the literature. [56, 119, 57] The results support the theory of the back contact barrier rather than any bulk or interface defects which cause capacitance steps at low temperatures.

### Résumé

*A temperature dependence of the Cf-spectra for the investigated samples demonstrated a capacitance steps which are rather assigned to the back contact barrier than to a bulk or interface defect level. The barrier height is reduced for the high temperature devices compared to the reference one. It might be an indication that prolonged thermal treatment can improve the back contact properties by enhancing the  $Mo(Se, S)_2$  interfacial layer formation.*

## 5.3 Conclusions on a Ga-gradient

A Ga-gradient at the back contact is an inherent feature of sequentially grown CIGS absorbers. Therefore, an objective evaluation of the benefits and disadvantages of the presence of a Ga-accumulation at the back contact with respect to its impact on the overall device efficiency is not possible as CIGS solar cells based on a sequentially grown absorber with a uniform in-depth Ga-distribution are not available for fair comparison. The conclusions presented hereafter are rather plausible deductions from the experimentally observed tendencies which could be supported by simulations or analytical modelling.

In terms of the device performance and bandgap engineering the following conclusions can be drawn:

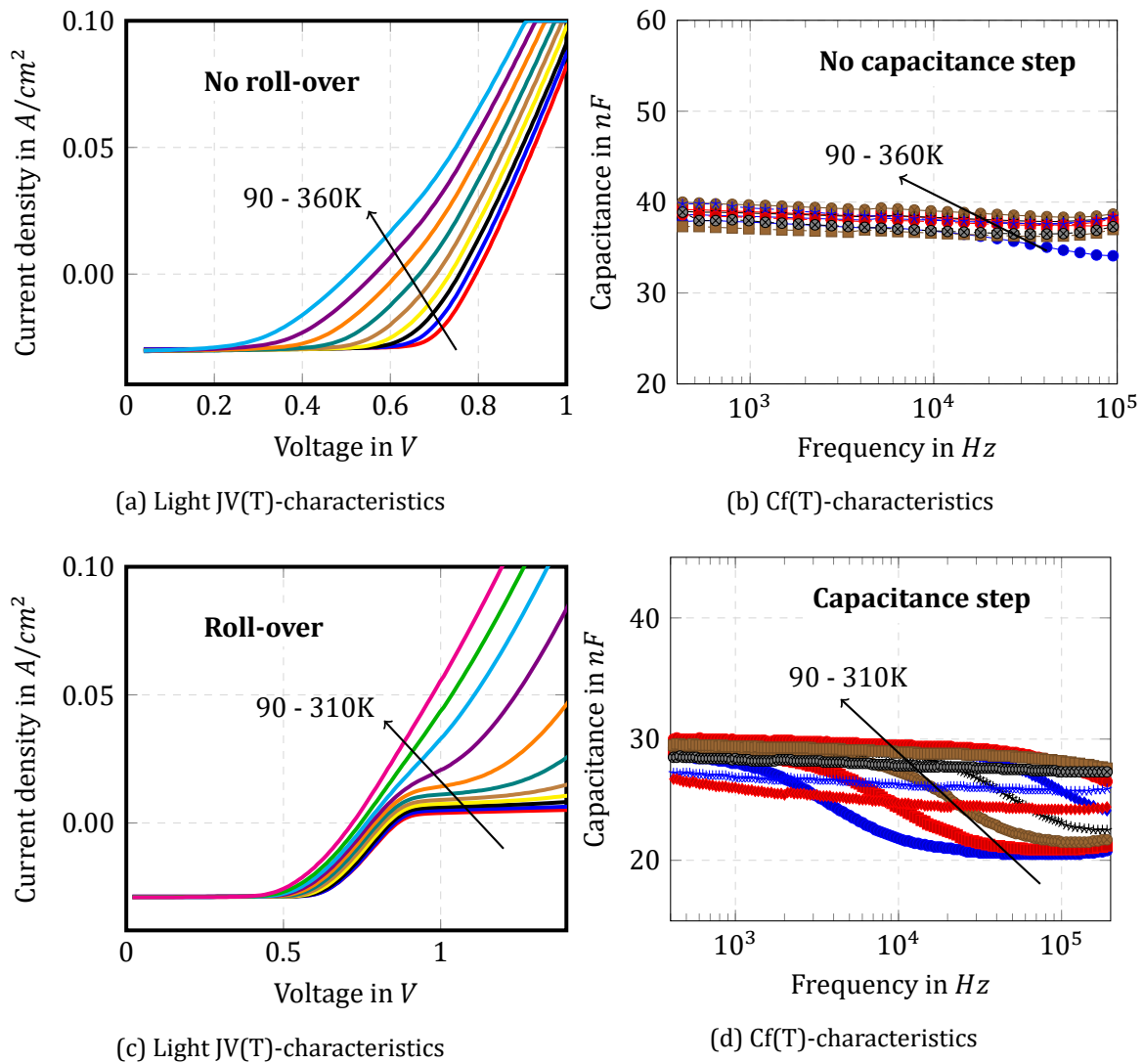


Figure 5.20: Comparison of the JV(T)- and Cf(T)-characteristics of two devices. The roll-over behaviour of the forward current corresponds to the capacitance step observed at low temperatures, and *vice versa*.

- a Ga-outdiffusion from the back contact towards the front interface as a result of prolonged treatment at high temperatures enhances the effective bandgap for recombination increasing the device  $V_{oc}$ . This is accompanied by the simultaneous enlargement of the effective bandgap for absorption and photocurrent collection. However, the consequent  $J_{ph}$  degradation for the studied devices has not been so pronounced.
- the correlation between  $V_{oc}$  at room temperature versus the effective bandgap for absorption with respect to varying annealing times is linear for the investigated sample set.
- an increased Ga-content in the absorber bulk after its outdiffusion from the back contact does not affect significantly the admittance measurement. The capacitance step is still observed at low temperatures. However, the activation energy for the high temperature processes samples is lower compared to the one of the reference device. One may speculate that prolonged thermal treatment improves the back contact properties by enhancing the  $\text{Mo}(\text{Se}, \text{S})_2$  layer formation.
- the correlation between the blocking behaviour of the forward current at low temperatures and the observed capacitance step leads to the conclusion that the contact barrier formed at the CIGS/back contact interface is the origin of the observed step. The introduction of the sample with a similar Ga-gradient but a modified S-incorporation process compared to the investigated devices has shown that the back contact issues related to the anomalies of the  $JV(T)$ -characteristics can be eliminated. This is important finding and has to be considered for further optimisation of the discussed solar cells.
- nevertheless some authors claim a Ga-confinement at the back contact to be a limiting factor in the sequential CIGS technology, the most pronounced effect of a Ga-accumulation is the passivation of the back contact and the consequent  $V_{oc}$  improvement as has been shown by the simulations. A significant  $V_{oc}$  improvement can be expected if the Schottky is formed at the back interface.
- the presence of a Ga-gradient suppresses the phototransistor effect usually observed for the devices based on coevaporated absorbers at low temperatures or as reported in literature after long term endurance testing. This conclusion has been drawn from both experimental and simulation results presented in this chapter.





## Chapter 6

# Separating recombination from generation / collection effects by surface sulfurisation

*A sulfur incorporation into the surface region of sequentially grown CIGS absorbers is the next step to optimize the device efficiency by means of bandgap engineering. A sulfurisation step is attempted to enhance the device  $V_{oc}$  by increasing the bandgap of the absorber near the interface. In this case, the effect of a S-incorporation is twofold. Firstly, it increases the effective bandgap for recombination, and, secondly, acts as a passivation agent of the absorber/buffer interface. In contrast to the Ga action, a S-incorporation reduces the  $E_V$  maxima shifting the VB edge downwards. Thus, a S-rich absorber surface will lead to an increased  $E_g$  in the SCR and result in an enhanced recombination barrier for holes at the pn-junction reducing interface recombination. In this context, an impact of a S-content as well as the width of the S-rich layer has to be carefully analysed. The S-amount can be controlled, for instance, by varying the duration of the selenisation and sulfurisation steps, whereas the penetration depth can be controlled by the process temperature and element supply rates. In this chapter, the influence of different S-gradients as a result of varied S-contents in combination with varied chalcogenisation process temperatures will be investigated. All samples discussed in this chapter are described in Section 3.2. The GDOES data are represented in Figure 3.5 as well as the SEM micrographs in Figure 3.2.*

### 6.1 Motivation: a S-induced increase in $E_g$

As has been shown in Figure 3.5 the sulfurisation step in the  $H_2S$  atmosphere leads to a S-gradient in the surface region of the absorber layer. The thickness of the S-rich layer is appr. 250-400 nm as has been reported by different authors [66, 132, 12]. This implies that the main impact of a S-incorporation is expected on  $E_g$  in the SCR, nevertheless some S-

accumulation has been also detected at the back contact which modified the back contact properties. [128, 133] The simulated (in SCAPS) band diagram with a front grading due to the S-incorporation is shown in Figure 6.1. In order to visualise the impact of the wide bandgap material in SCR on the device performance, simulations have been performed. For the sake of a fair comparison to real sequentially grown absorbers, a back contact gradient due to a Ga-accumulation is also inserted in agreement with Chapter 5 (however, it is not shown in the figure). Figure 6.2 reproduces simulated  $V_{oc}(T)$ -characteristics and EQE spectra which correspond to the devices with a uniform  $E_g$  without a S-gradient (denoted as 'Se') and with a front grading due to a S-gradient in SCR (denoted as 'Se+S'). The S-gradient has been modelled by inserting a thin layer of 300 nm whose bandgap changes exponentially from 1.38 eV to 1.0 eV from the CIGS/CdS interface towards the absorber bulk. These values were extracted from the experimental  $V_{oc}(T)$  and EQE data. The increase in the device  $V_{oc}$  at room temperature by 65 mV corresponds to the shift in the activation energies from 1.04 eV to 1.11 eV as can be seen from Figure 6.2a. Remarkably, the EQE-cutoffs do not change after the addition of a wide-gap material at the surface as can be seen from Figure 6.2b. The absorption edge of the corresponding samples still coincide. It has to be mentioned that a parallel shift in the

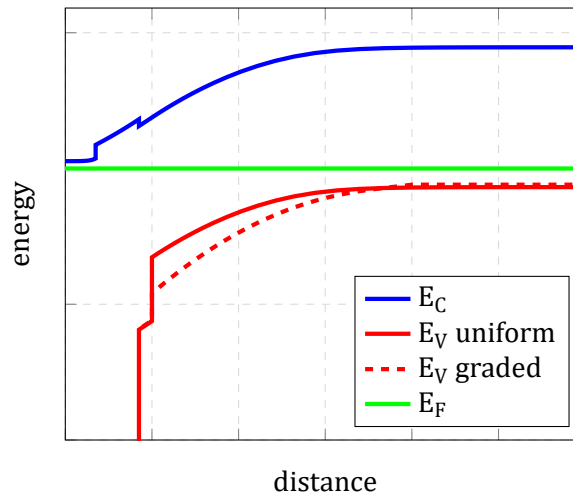


Figure 6.1: Simulated band diagram with a front grading due to the S-incorporation. The effect of S can be seen in the down shift of the VB.

$V_{oc}(T)$ -characteristics is achieved only if a back surface grading is introduced. With the flat band alignment and the back surface recombination of  $1 \cdot 10^7$  cm/s the  $V_{oc}(T)$ -curves demonstrate different slopes without a back grading. A back gradient prevents electron injection to the back contact significantly reducing back surface recombination, and consequently  $V_{oc}$  losses. This observation proves once again the importance of the back contact in terms of the overall de-

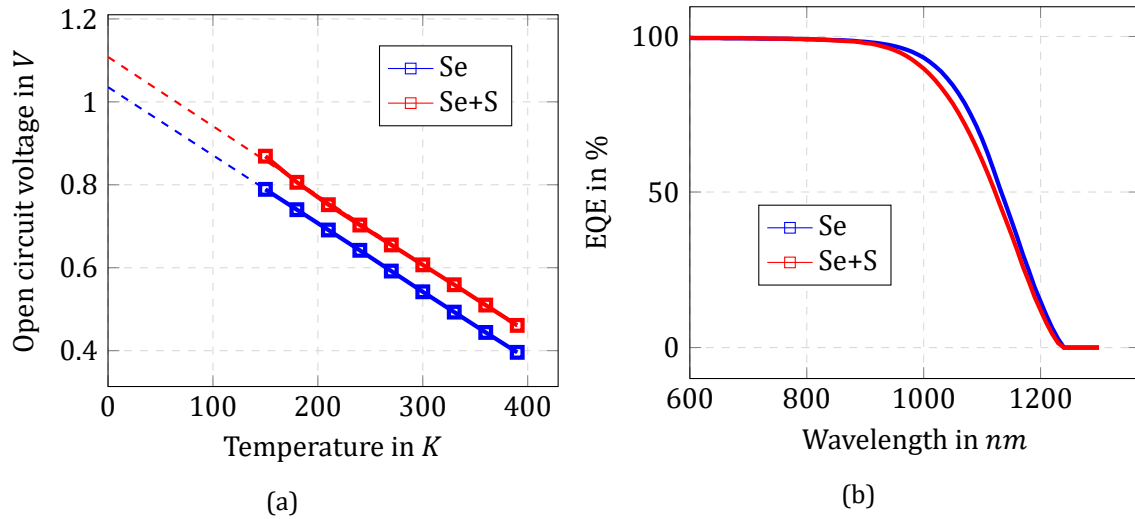


Figure 6.2: SCAPS simulation of (a)  $V_{oc}(T)$ -characteristics and (b) EQE-spectra for two devices: without (Se) and with a S-rich layer at the absorber surface (Se+S).

vice efficiency and the necessity of the co-optimisation of back and front gradings in order to improve the device performance.

## 6.2 Literature review

In sequential deposition processes, the bandgap widening at the absorber surface, also referred to as a front grading, is difficult to achieve due to different reaction kinetics of the binary phases of  $\text{CuInSe}_2$  and  $\text{CuGaSe}_2$ . [12] A sulfurisation step after the selenisation of the metallic precursor films is then introduced. The effect of a S-incorporation on the device performance is diversified. The sulfurisation treatment leads to the formation of the  $\text{Cu}(\text{In, Ga})(\text{S, Se})_2$  or  $\text{Cu}(\text{In, Ga})\text{S}_2$  layers at the absorber surface. A wider  $E_g$  in SCR as well as at the back contact will lead to higher  $V_{oc}$  values and improved FF as a result of reduced interface recombination. Meanwhile, the bandgap in the bulk has to be kept low in order to prevent the degradation of absorption processes and, thereby  $J_{ph}$ . [66] However, implementing a front grading by a Ga-gradient may lead to an excessive CB upward lifting inducing an electronic potential barrier which will deteriorate the device FF. [134] In this context, a S-incorporation is preferable. S-atoms substitute Se-atoms, and therefore change the interaction between the cation Cu  $d$  and anion Se  $p$  orbital repulsion. This results in the down-shift of the VB maximum. [135] The VB lowering does not hinder the electron transport but repels holes from the interface. On the other hand, in terms of material properties, S-atoms occupy Se or Cu vacancies or replace Se due to its higher reactivity compared to Se. As a result, the density of compensating donors is reduced leading to the passivation of the absorber surface [136, 132], and a net doping density increase [137]. Moreover,

a S-rich surface is electrically different compared to a S-free one. [132] The authors claim that the passivation of deep defects at the surface and at grain boundaries by a S-addition results in a higher work function of the  $\text{Cu}(\text{In, Ga})(\text{Se, S})_2$  films, and therefore, a stronger band-bending compared to the  $\text{Cu}(\text{In, Ga})\text{Se}_2$  films. As a result of the S-induced passivation effect and bandgap enhancement at the surface, the corresponding films resulted in the devices with higher device voltages, and therefore efficiencies. In addition, it has been found that a S-incorporation improves minority carrier lifetimes. The passivation of recombination centres in the absorber layer has been concluded. [12]

Two approaches are most often used for S-incorporation:  $\text{H}_2\text{S}$  gaseous atmosphere and elemental S supply. From alternative methods, the sequential evaporation of the  $\text{In}_2\text{S}_3$  powder on top of a  $\text{Cu}(\text{In, Ga})\text{Se}_2$  film proved to be an efficient approach for the absorber sulfurisation. The remarkable improvement in  $V_{\text{oc}}$  and FF has been reported as a result of an effective front grading. [138] The advantage of the elemental incorporation is a precise control of the concentration of the supplied element and more uniform distribution in the film [67]. This incorporation method is preferred when a compositional homogeneity of a film is required. Yet, the S/S + Se ratio is very critical with respect to the device performance. Firstly, with the ratios above 0.6 a drastic deterioration of the device efficiency is reported due to a reduced FF in response to an increased series resistance with an increased S-content. [67] This effect is known in literature as 'oversulfurisation'. [99] An increased  $R_s$  can be attributed to the modified back contact behaviour when the  $\text{Mo}(\text{S, Se})_2$  interfacial layer is formed, and the band alignment at the absorber/back contact is changed. [139] From this follows that the S-addition into the absorber film has to be optimised as it may affect both the absorber material properties and the charge carrier transport.

Moreover, a sulfurisation step can also affect the compositional gradients throughout the CIGS film. [103] It has been found that an enhanced sulfurisation degree promotes a Ga-diffusion towards the absorber/buffer interface in sequential processes. However, excessive sulfurisation causes parasitic resistance losses which deteriorate the device efficiency by reducing FF. [5] Therefore, a new absorber formation method has been presented which allows to modulate a Ga-profile under low S-incorporation. [103] The thermodynamic interaction between the Ga- and S-distribution due to the preferable reaction of Ga-S rather than In-S enabled to obtain flatter Ga-profiles with steeper S-gradients at the surface resulting in the world record efficiency on module level. [103]

Another perspective implementation of a S-front gradient can be in wide-gap CIGS absorbers. The wide-gap solar cells suffer from the  $V_{\text{oc}}$  saturation due to a cliff-like band alignment at the absorber/buffer interface which provokes drastic interface recombination losses. This problem can be overcome by introducing a S-rich layer at the CIGS surface which will ensure a required bandgap widening by shifting the VB maximum downwards without affecting the CB, and thus a beneficial spike-like CB offset between the absorber and buffer layers.

## 6.3 Results and discussion

### 6.3.1 Enhancement of the effective bandgap for recombination

The effect of a front grading can be interpreted in different ways, in particular, in terms of a peculiar surface modification. The surface of CIGS absorbers suffer from a large density of surface defects including Cu- and Se-vacancies [140] which can play a critical role in the overall cell performance. Several studies have reported that a sulfurisation of the CIGS films improves the device  $V_{oc}$  and FF compared to the S-free samples. Furthermore, the bandgap increase at the absorber surface due to a S-incorporation results in reduced recombination events at the absorber/buffer interface. [136, 141] The latter has a straightforward beneficial effect on the performance parameters of S-incorporated CIGS devices. Figure 6.4 reproduces the results of the

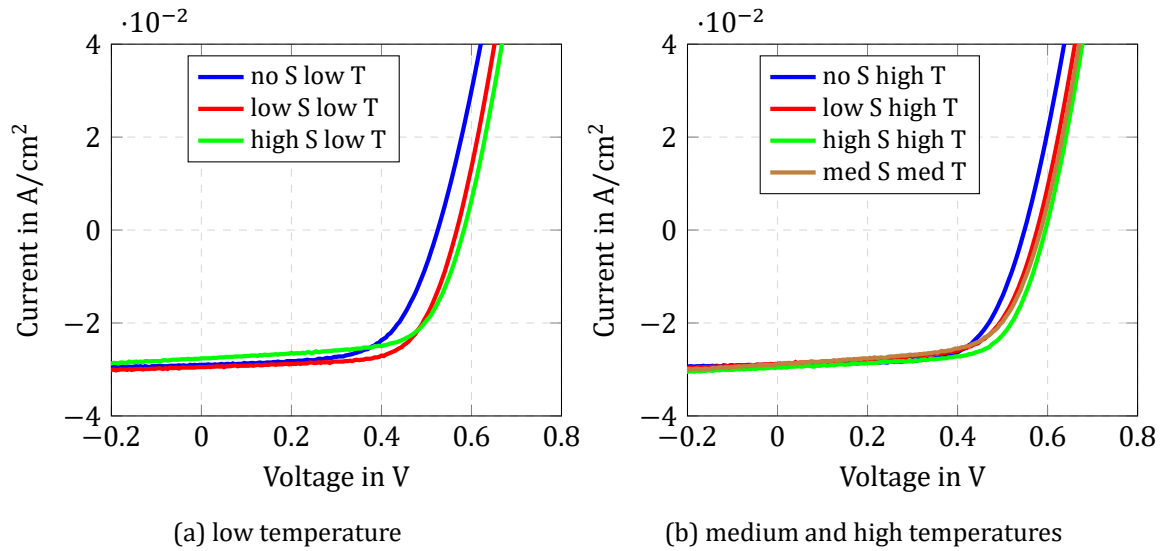


Figure 6.3: Light JV-characteristics of the samples with different S-contents.

JV-measurements in the dark and under illumination of the cells with different modifications of the absorber surface. The diode ideality factor,  $A$ , series resistance,  $R_s$ , and shunt resistance,  $R_{sh}$  are extracted from the measured JV-characteristics in accordance with [106], whereas the diode saturation current density,  $J_0$ , was estimated from the linear part of the natural logarithm from the dark current. The performance parameters of these devices are summarized in Table 6.1.

After studying the parameter table one can see that the most pronounced impact of a sulfur incorporation is observed with respect to the  $V_{oc}$  values. An increase of  $\approx 60$  mV and 45 mV can be seen between *no sulfur* and *high sulfur* samples deposited at low and high temperatures, respectively. The diode ideality factors at room temperature vary within 1.52–1.84 which implies that recombination in the SCR is the predominant recombination mechanism for the studied samples. Decreasing  $A$  with an increasing S-content indicates the shift in the balance

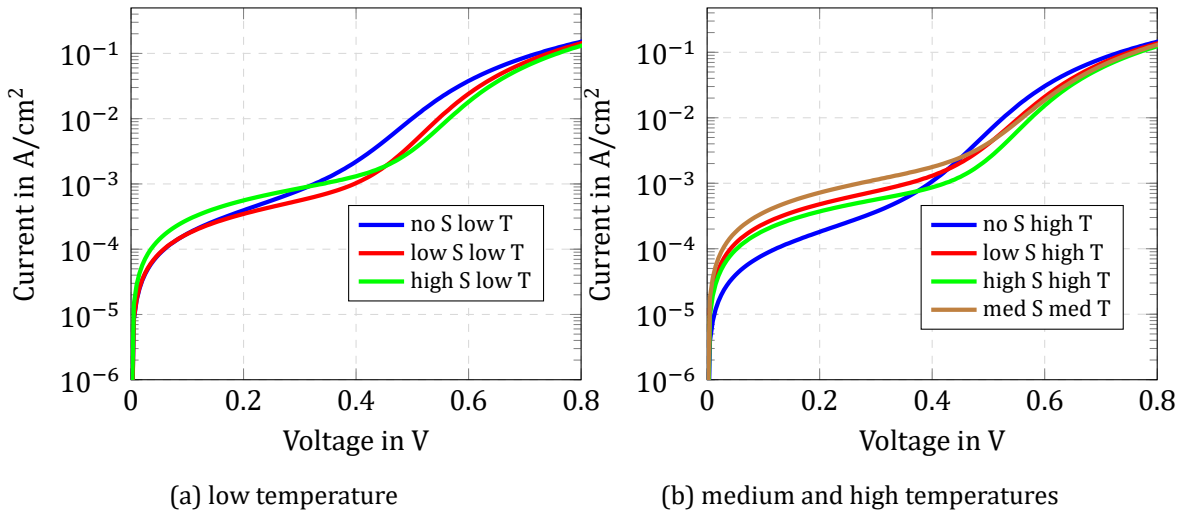


Figure 6.4: Dark JV-characteristics on a semi-logarithmic scale for the samples with different S-contents.

between the SRH and QNR recombination rates towards decreasing SRH recombination rates and increasing QNR recombination in the absorber farther away from the interface. Moreover, the higher  $V_{oc}$  values also correlate with the lower diode ideality factors and lower dark saturation current densities compared to the less efficient devices. With an increasing S-content the recombination rates in the SCR decreases leading to the larger quasi-Fermi level splitting, and thereby higher  $V_{oc}$ . Remarkably, there is no significant impact of the sulfur content on the photogenerated current density as deduced from the comparison of the  $J_{ph}$  extracted from EQE measurements. Slight deviations in  $J_{ph}$  among the samples can be explained rather due to variations in the absolute EQE values (different optical losses in the window layers) than due to changes in the bulk  $E_g$ , and thereby the absorption cutoff. The comparable FF and  $R_s$  in these devices indicate that there is no 'oversulfurisation effect' which can result in significant parasitic losses. It is somewhat puzzling that  $R_{sh}$  for the studied devices seems to decrease with an increasing sulfur content. The performance of the device with the medium S-content from the medium process temperature is somewhere between the low and high S devices from the high temperature process. This confirms once again the superior effect of a S-content on the device performance.

Temperature-dependent current density-voltage measurements are another method to obtain information on dominating recombination mechanisms. The measurements have been performed on the same devices with varied sulfur contents and deposition temperatures. The temperature dependence of  $V_{oc}$  of the studied samples deposited at low and high temperatures are reproduced in Figure 6.5a and 6.5b, respectively. The extracted activation energies from the extrapolation of  $V_{oc}$  to 0 K which gives the effective bandgap for recombination are displayed in

Table 6.1: Performance parameters of the devices with varied S-contents and process temperatures.

Sulfur content	Deposit. temp.	$V_{oc}$ , [V]	$J_{sc}$ , [mA/cm <sup>2</sup> ]	FF, [%]	$R_s$ , [ $\frac{\Omega}{cm^2}$ ]	$R_{sh}$ , [ $k\Omega \cdot cm^2$ ]	A	$J_0$ [mA/cm <sup>2</sup> ]
no	low	0.525	29	63	7.75	0.584	1.84	2.0e-6
low	low	0.567	29	67	7.0	0.544	1.61	2.4e-7
high	low	0.583	28	65	6.5	0.324	1.61	2.1e-7
no	high	0.549	29	66	7.5	1.192	1.65	3.2e-7
low	high	0.577	29	66	6.5	0.38	1.68	4.0e-7
high	high	0.595	30	67	7.0	0.472	1.52	8.8e-8
medium	medium	0.585	29	64	6.0	0.26	1.84	7.7e-7

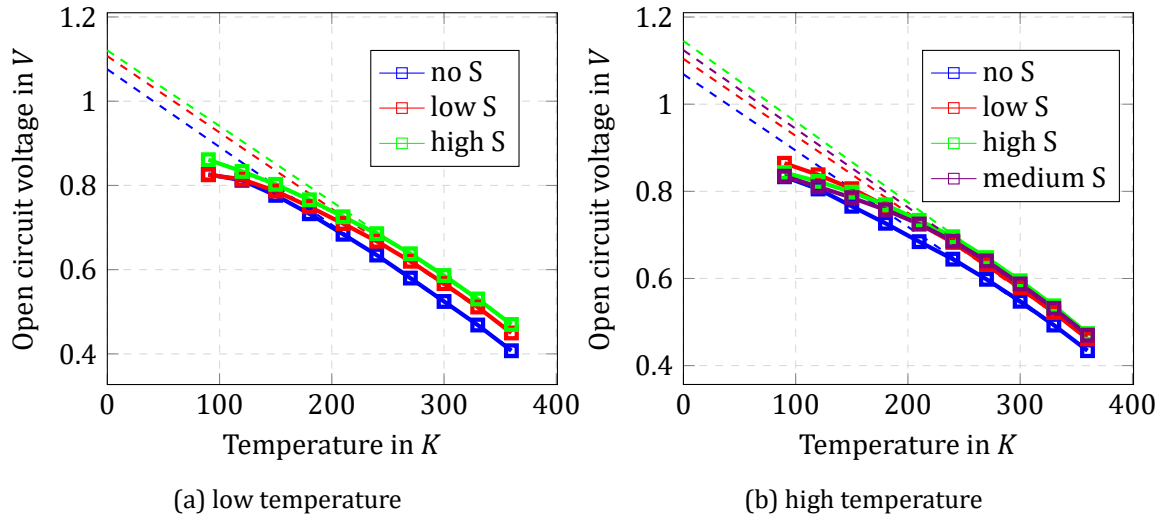


Figure 6.5: Dependence of the open circuit voltages over temperature for different sulfur contents.

Table 6.2. A shift in the activation energies with an increasing S-content for both temperatures indicates the enhancement of the effective bandgap for recombination, and therefore can explain the increase in the device  $V_{oc}$ . The shift in the activation energies by 60 meV corresponds to the  $V_{oc}$  increase by 58 mV for the low chalcogenisation temperature, whereas for the high temperature 80 meV and 46 mV, respectively. The slopes of the  $V_{oc}(T)$ -curves for both temperatures are rather similar, which implies that an impact of sulfur on minority charge carrier lifetimes, mobilities and doping density should not be pronounced. However, the variations in  $V_{oc}$  for the S-free samples for both low and high process temperatures have to be investigated

further as the difference in the extracted activation energies does not correspond to the device  $V_{oc}$ . A difference in  $V_{oc}$  values can be also explained by different doping concentrations in the

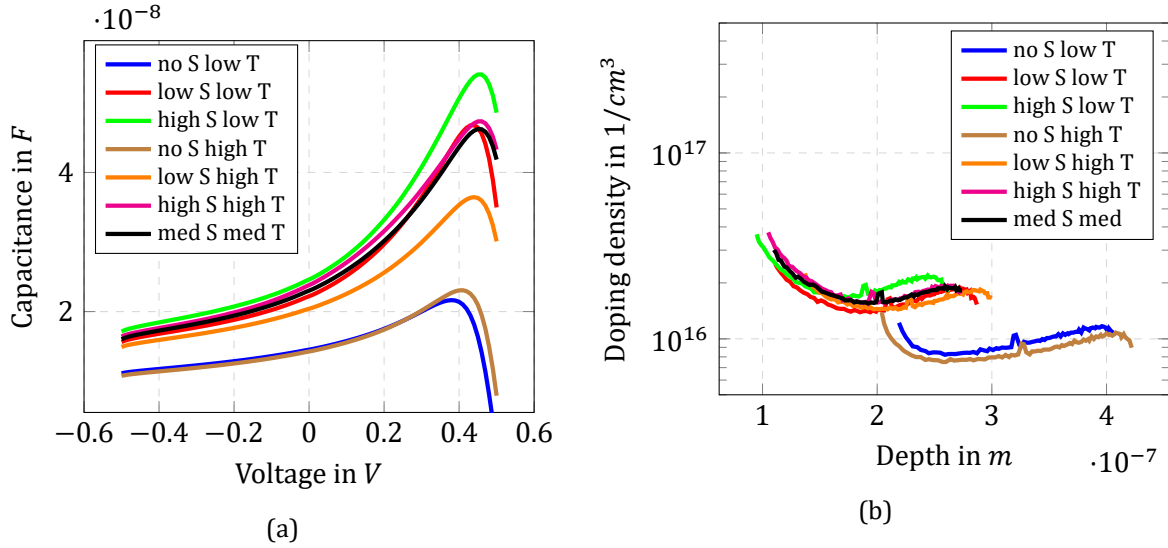


Figure 6.6: Capacitance-voltage characteristics (a) and doping profiles (b) of the devices with different S-contents and deposition temperatures.

Table 6.2: Extracted  $E_g$  from  $V_{oc}(T)$ - and EQE-measurements in comparison to the device  $V_{oc}$  at room temperature and doping density  $N_a$ .

Sulfur content	Temperature	$V_{oc}$ [V]	$N_a$ [ $1/cm^3$ ]	$E_g(V_{oc}(0K))$ , [eV]	$E_g(EQE)$ , [eV]
no	low	0.525	$8.3e+15$	1.0	1.0
low	low	0.567	$1.4e+16$	1.03	1.0
high	low	0.583	$1.7e+16$	1.06	1.0
med	med	0.585	$1.6e+16$	1.07	1.0
no	high	0.549	$7.7e+15$	1.01	1.0
low	high	0.577	$1.5e+16$	1.05	1.0
high	high	0.595	$1.6e+16$	1.09	1.01

absorber layers. Capacitance-voltage measurements are used to estimate the spatial variations of the doping density in the absorber film by modulating the SCR width by applying a voltage bias. The CV-measurements and derived doping profiles of the studied devices are shown in Figure 6.6. The capacitance value at 0 V bias and the doping density in the discussed devices do not differ significantly among the S-containing samples. However, the doping density in the S-free samples is twice lower compared to the sulfurised ones as can be seen from Table 6.2. The doping variations between the S-free and S-containing samples from low and high process



temperatures can account for  $\approx 18.5$  and  $19$  mV of the  $V_{oc}$  difference. In contrast to [12], the SCR width at  $0$  V bias of the S-containing samples is about  $200$  nm smaller than the one of the S-free samples which is consistent with the higher doping densities.

### 6.3.2 Impact on photocurrent collection and absorption

EQE-measurements of solar cells derived from the process variations with respect to different S-amounts and chalcogenisation temperatures are reproduced in Figure 6.7a. A varied sulfur content does not have a pronounced impact on the absorption properties of the studied devices as can be deduced from Figure 6.7a. The absorption edge irrespective of a sulfur content corresponds approximately to the bandgap of pure  $\text{CuInSe}_2$  material and equals  $\approx 1$  eV. The EQE results are in a good agreement with the spectral PL-measurements on the same devices shown in Figure 6.7b. The respective emission spectra have an identical shape and emission peaks at  $\approx 1$  eV. A slight deviation from the observed behaviour is demonstrated by the device with *high S and high T*. A slight shift of the EQE absorption edge and the corresponding PL emission peak towards lower wavelengths indicates some widening of the optical bandgap. The bandgap widening can be explained by the increased S-content in the QNR as can be deduced from Figure 3.5b. A high processing temperature with an increased S-supply may facilitate a better S-indiffusion into the absorber bulk enhancing the optical bandgap, and thereby degrading long wavelength absorption. In order to conclude on the impact of a S-incorporation into

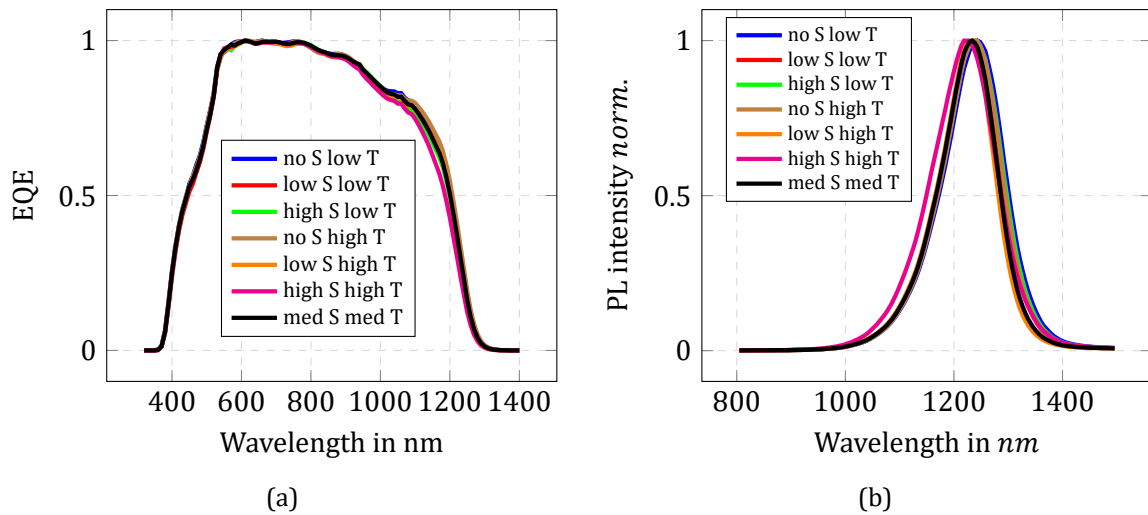


Figure 6.7: External quantum efficiency and spectral PL-measurements on the samples with different sulfur contents and deposition temperatures.

the absorber surface in terms of the device performance, Figure 6.8 is inserted. Figure 6.8 describes the correlation between the development of the effective bandgap for recombination  $E_{g,eff} = q \cdot V_{oc}(T = 0K)$  and the device  $V_{oc}$  with respect to an increasing S-content and com-

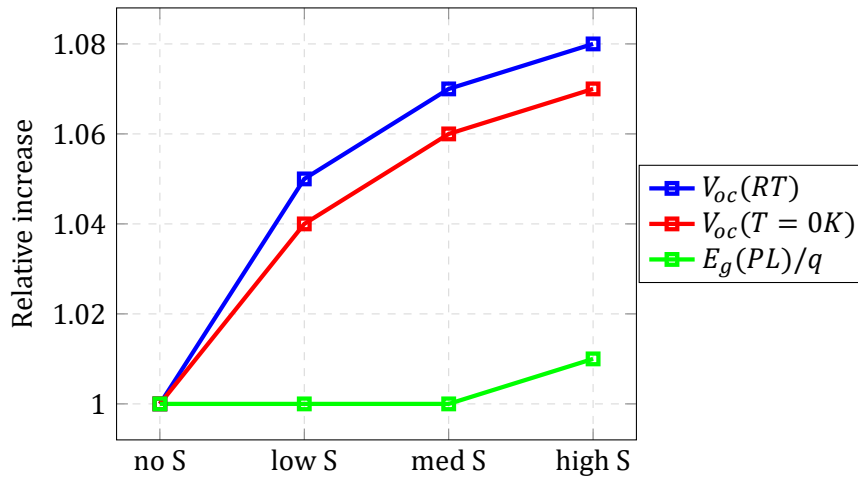


Figure 6.8: Correlation between  $V_{oc}$  at room temperature versus optical and electrical bandgaps with respect to different S-contents, high temperature process.

compares it to the effective bandgap for absorption and photocurrent collection extracted from the spectral PL-measurements. An increase in the device  $V_{oc}$  follows an upward shift in the effective bandgap for recombination with an increasing S-content. To the contrary, the effective bandgap for absorption remains basically unchanged which shows an advantage of a S-incorporation with respect to the  $V_{oc} - J_{sc}$ -tradeoff.

### 6.3.2.1 Résumé

*A sulfurisation of the absorber surface leads to the bandgap widening in the SCR without affecting the absorber bulk. A wider  $E_g$  in the SCR leads to the enhancement of the effective bandgap for recombination which in turn decreases the recombination probability, and therefore improves  $V_{oc}$ . Meanwhile, a sulfurisation of the absorber surface does not affect the absorber bulk which implies that the effective bandgap for absorption and photocurrent collection is not affected by the sulfurisation step. This suggests that the S-incorporation into the absorber surface leads to the separation of the recombination processes from the absorption and photocurrent collection in the sequentially grown CIGS-based solar cells.*

### 6.3.3 Impact on minority carrier lifetimes

The impact of the sulfur incorporation on minority carrier lifetimes has been studied by means of time-resolved photoluminescence measurements. In this measurement technique, excess carriers are injected into the absorber layer by a short laser pulse. Such optical excitation creates non-equilibrium carrier concentrations provoking different recombination mechanisms in order to restore an equilibrium state. A luminescence decay as a result of radiative recombination processes is detected and recorded as a function of time. The experimental details of the

measurement as well as the absorber etching procedure prior to the TRPL measurement are highlighted in Section 3.2.5.

CIGS absorbers have a high absorption coefficient of  $\approx 10^5 \text{ cm}^{-1}$ , therefore incident photons are expected to be absorbed within the first 400 nm of the absorber layer. It implies that measured PL-transients, and therefore extracted minority carrier lifetimes can be affected by the material properties which can be altered by a compositional grading such as the bandgap  $E_g$ , the carrier density, the defect density and their energetic distribution. As has been discussed an increased S-concentration at the absorber surface leads to the  $E_g$  enhancement in the SCR. A higher  $E_g$  has to correlate with lower SRH recombination, and thus with changes in minority carrier lifetimes  $\tau_n$ . Moreover, a front grading as a result of a S-incorporation can lead to the separation of the photogenerated charge carriers what in turn can also affect the measured  $\tau_n$ .

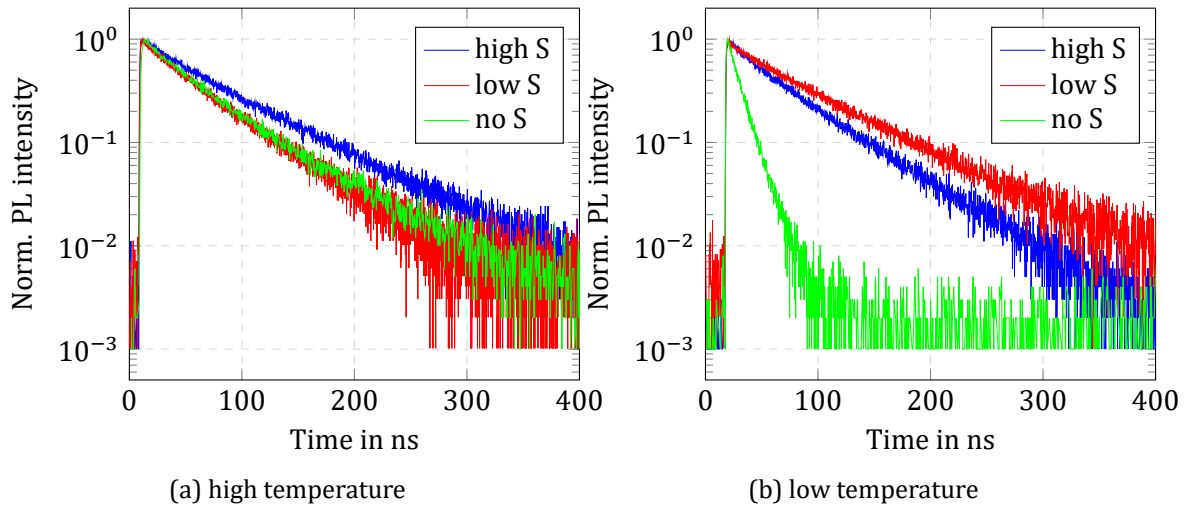


Figure 6.9: Comparison of TRPL measurements for the samples with different S-contents. Excitation level is 100%.

Figure 6.9a reproduces TRPL-decays on the CIGS absorbers deposited at high temperature. The TRPL decays are rather monoexponential and do not differ significantly. The extracted minority carrier lifetimes are in the range of 50–70 ns with a higher value for the high S and high T sample (see Table 6.3). TRPL-decays on the CIGS absorbers deposited at low temperature are shown in Figure 6.9b). An interesting trend is observed for the low temperature processed samples. The S-incorporated absorbers demonstrate PL-transients with decay times of  $\approx 40$ –45 ns whereas the S-free sample has a very short decay of about 5 ns (see Table 6.3). This observation correlates well with the temperature-dependent  $V_{oc}$ -measurements discussed in Section 6.2.1. The S-free samples from the low and high temperature processes demonstrated the  $V_{oc}$  difference of 24 mV for the difference in the activation energies of about 10 meV when compared to each other.

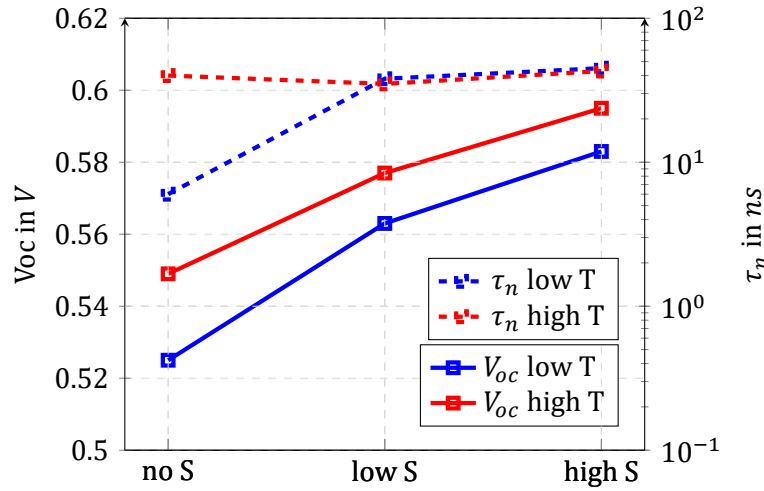


Figure 6.10: Correlation between  $V_{oc}$  at room temperature and minority carrier lifetimes  $\tau_n$  with respect to varied S-contents and process temperatures for the discussed samples.

The correlation between the device  $V_{oc}$  and minority carrier lifetimes for the low and high temperature processes is shown in Figure 6.10. The  $\tau_n$  values have been estimated by fitting corresponding TRPL decays and calculating the average value for  $\tau_n$  using the equation:

$$\tau_{avg} = \frac{\sum_{i=1}^n A_i \cdot \tau_i}{\sum_{i=1}^n A_i} \quad (6.1)$$

with  $n$  being the number of decays, and  $A$  is the amplitude of a decay section.

For the high temperature samples, a  $V_{oc}$  increase with an increasing S-content can be attributed to the enhancement of the effective bandgap for recombination as the minority carrier lifetimes remain basically unaffected with respect to the S-presence. To the contrary, in case of the low temperature samples a S-incorporation has a double effect. Firstly, it improves semiconductor quality, most probably by passivating the midgap defects and/or grain boundaries [12], as a result, minority carrier lifetimes improve. Interestingly, such an effect is not observed for the devices from the high temperature process. Secondly, similarly to the other set of samples, a S-incorporation widens the bandgap energy in the SCR enhancing the effective bandgap for recombination and pressing down the non-radiative recombination rates. To sum up, the low lifetime value and consequently the low  $V_{oc}$  indicate that the thermal budget of the low temperature samples is not sufficient. Optimal heat treatment is an important factor which affects the device performance (mainly  $V_{oc}$  and  $\tau_n$ ) and has to be considered additionally to a S-amount.

Several studies have reported that a S-treatment, either as an incorporation into the absorber surface or annealing in S-containing atmosphere (absorber post-treatment) has a pronounced impact on the defect environment. [12, 136, 138] This implies that minority carrier

lifetimes and consequently PL-transients can be also influenced by a S-inclusion. Indeed, the correlation between the S-presence in the absorber and minority charge carriers can be already seen in Figure 6.9 from the TRPL-measurements on the low temperature process samples where a pronounced improvement in  $\tau_n$  is detected in the sulfurised absorbers compared to the S-free one. The study of a S effect on minority carrier lifetimes will be conducted following the approach in [142, 143], where the author investigated recombination dynamics analysing TRPL-decays at different illumination intensities and temperatures.

The impact of a sulfur incorporation on TRPL-decays measured on absorbers grown at low temperatures can be seen in Figures 6.11, where excitation and temperature dependences of the S-free and S-containing samples have been reproduced. Under low excitation the sample without S shows a biexponential behaviour with a short first decay and a very long second one. Upon increasing intensity level, the second decay shortens, and the PL-transients approach a monoexponential shape. No temperature dependence is observed for this sample under 50% illumination. Meanwhile, the sample with a high sulfur content demonstrates shorter PL decay times under low intensity level which transform to longer monoexponential transients under high illumination level. Unlike the S-free sample, this sample has a strong temperature dependence, where a temperature increase leads to shorter PL decays.

A similar tendency for the PL-response towards varying excitation intensities and temperatures is observed for the samples with absorbers grown at high temperatures (see Figure 6.12). A strong excitation dependence of the second decay is recorded from the S-free sample, whereas the temperature dependence of this sample is very weak. The sample with a high S-content demonstrates both strong excitation and temperature dependences of the PL-decays. With an increasing intensity, the PL-transients become longer whereas an increasing temperature leads to the shorter PL-transients.

As has been already reported by different groups, the S-free surface of CIGS films has a large density of defects. [132] Localized charges in the defect states in semiconductors induce downward band-bending in p-type material. [144] Strong band-bending would lead to a fast separation of photogenerated charge carriers [145], and therefore, to shorter PL-transients, and thereby shorter  $\tau_n$ . Moreover, the transients can demonstrate a biexponential behaviour with a short and long decay. The short decay is governed by the electric field induced by band-bending whereas the long one has to correlate with carrier re-emission from the traps (or the buffer layer). With an increasing excitation intensity, band-bending is expected to flatten, and thus longer PL-transients have to be detected. Band-bending is a temperature independent phenomena, therefore no pronounced temperature dependence of TRPL-decays is expected. This situation clearly describes the behaviour of the TRPL-decays measured on the S-free absorbers.

The situation changes when the TRPL-decays are measured on the S-containing films. The PL-transients demonstrate both excitation and temperature dependence. Such behaviour can be interpreted in terms of carrier trapping [143]. By enhancing electron emission, either by

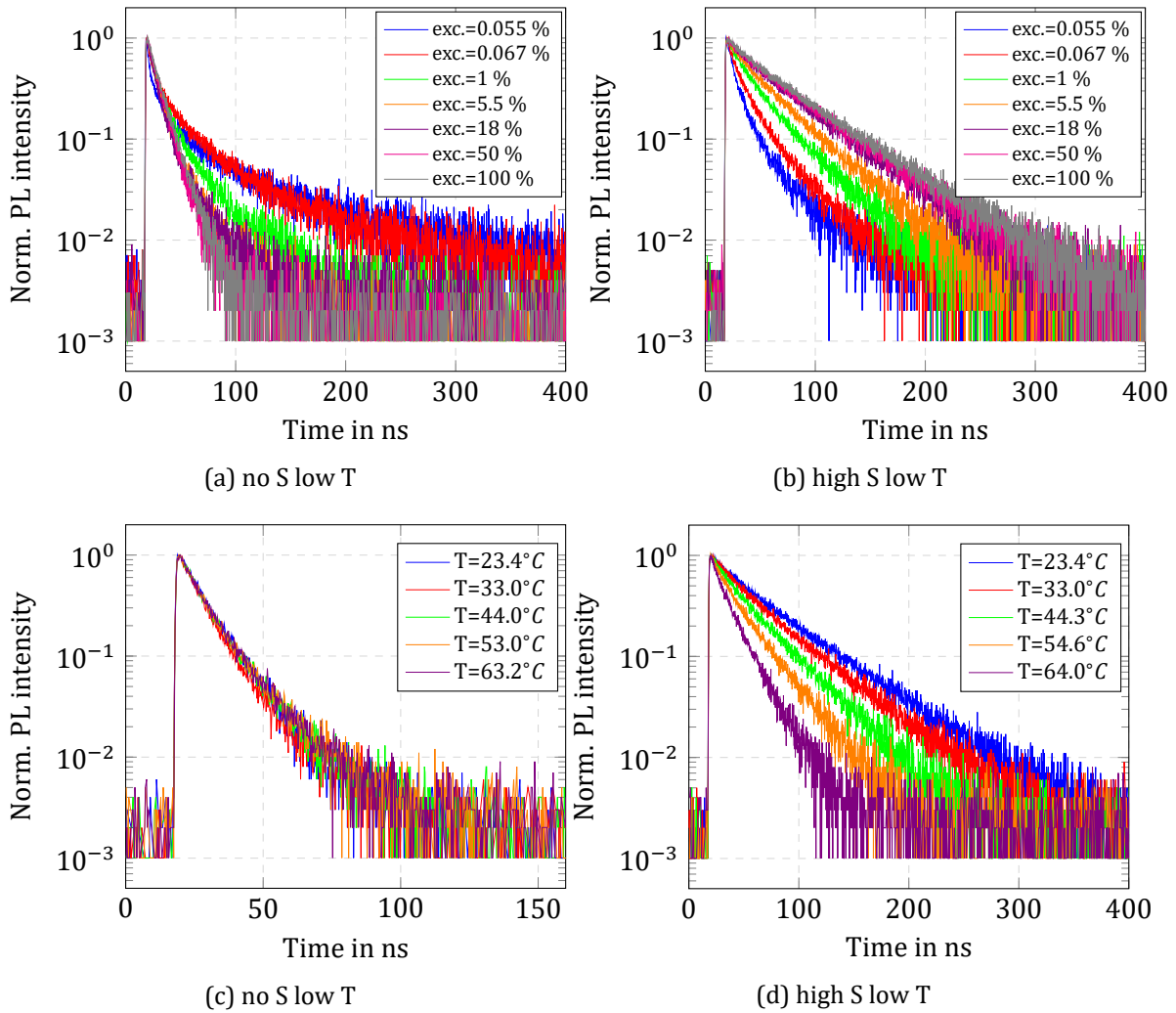


Figure 6.11: Excitation- and temperature-dependence of TRPL measurements of the samples with different S-contents.

increasing the temperature of a sample or by increasing carrier injection level, the trapping effects can be unfolded.

Thus, collating the observed behaviour from TRPL-measurements to the results discussed above the following conclusions can be drawn. In agreement with the findings of other groups [132, 136], S-atoms act as a passivation agent at the surface or at the grain boundaries in CIGS films leading to better bulk quality and significantly improved efficiencies on device level. However, as a by-effect of the passivation action, some trapping states may be induced which can be charged and contribute to the device capacitance. The latter deduction agrees well with CV-measurements showing a slightly higher capacitance and  $N_a$  for the S-containing devices.

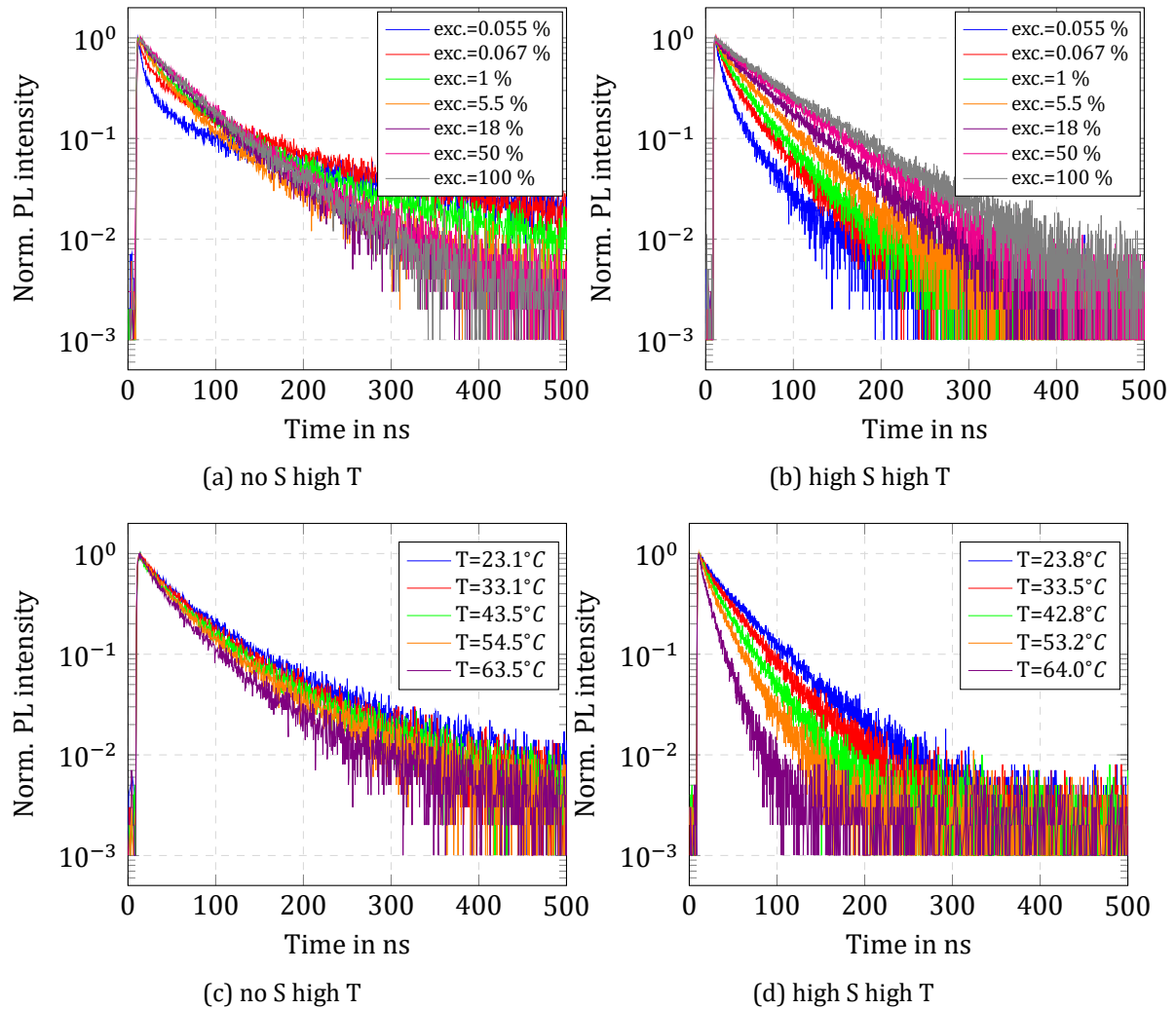


Figure 6.12: Excitation- and temperature-dependence of TRPL measurements of the samples with different S-contents.

As could be already demonstrated, TRPL-measurements and their interpretation are not always straightforward. Firstly, TRPL-measurements on bare absorbers which are expected to give real minority carrier lifetimes are very sensitive to the measurement environment due to the fast CIGS surface degradation. [146, 147, 148] Secondly, if the measurements are conducted on CdS-covered films, they are complicated by the presence of the carrier separating junction at the absorber/buffer interface. Thirdly, the lifetimes of minority charge carriers extracted from these measurements very often give values of different order of magnitude (from a few *ns* up to hundreds *ns*). [142, 146, 149] Fourthly, there is no accepted standard procedure how to fit correctly measured PL-decays. Therefore, in order to verify experimental results and to ease their interpretation, a theoretical background is needed. A method proposed in this work

Table 6.3: Measured  $V_{oc}$  at room temperature and  $\tau_n$  with extracted  $E_g$  from  $V_{oc}(T)$ -measurements for varied S-contents and deposition temperatures.

Sulfur/ Temperature	$V_{oc}(RT)$ , [V]	$V_{oc}(0K)$ , [V]	$\tau_{n,TRPL}$ [ns]
no / low	0.525	1.0	5
low / low	0.567	1.03	38
high / low	0.583	1.06	45
no / high	0.549	1.01	51
low / high	0.577	1.05	50
high / high	0.595	1.09	68
med / med	0.585	1.07	60

can help to estimate theoretical minority carrier lifetimes by analysing  $V_{oc}(T)$ -characteristics of corresponding devices.

This method is based on the assumption that lifetimes of minority charge carriers in the bulk of the absorber material determine  $V_{oc}$  of a solar cell, and the interface recombination can be neglected. Then, the correlation between  $V_{oc}$  and  $\tau_n$  can be extracted from the expression of the forward current density  $J$  in a pn-junction as described in [53]:

$$J = q \cdot \sqrt{\frac{D_n}{\tau_n}} \cdot \frac{n_i^2}{N_a} \cdot \exp\left(\frac{qV}{kT}\right) + \sqrt{\frac{\pi}{2}} \cdot \frac{kTn_i}{\tau_n E_0} \cdot \exp\left(\frac{qV}{2kT}\right), \quad (6.2)$$

where  $E_0$  is electric field at the location of maximum recombination,  $V$  is applied bias voltage. The electric field at the location of maximum recombination is given by [34]:

$$E_0 = \sqrt{\frac{qN_a \cdot (2\phi_B - V_{oc})}{\epsilon\epsilon_0}}, \quad (6.3)$$

where  $\phi_B$  is the built-in potential of the pn-junction.

Equ. 6.2 combines both recombination in the quasi-neutral region and SRH recombination in the depletion region. Given  $J$  is equal to the photogenerated current density  $J_{ph}$ , the applied bias  $V$  becomes  $V_{oc}$ . Thereby, by solving this equation the minority carrier lifetime  $\tau_n$  can be estimated. This approach to calculate  $\tau_n$  is straightforward, but the temperature dependence of the material parameters has to be taken into account (see footnote 1, Page 71), otherwise the extracted minority carrier lifetimes will be falsely low.

The required experimental input parameters for Equ. 6.2 are  $V_{oc}$ ,  $J_{ph}$ ,  $E_g$  (corrected for  $3 \cdot kT$ ), and  $N_a$ . The other parameters are baseline values recommended for simulations, as, for example, in [34, 81]. A strong shortcoming of the presented method is its sensitivity to  $N_a$ .



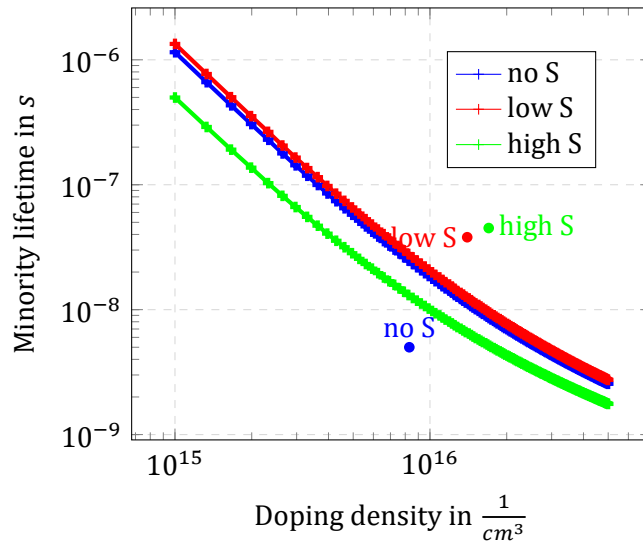


Figure 6.13: Calculated minority carrier lifetimes from the experimental data for the discussed samples with different sulfur contents for low deposition temperatures.

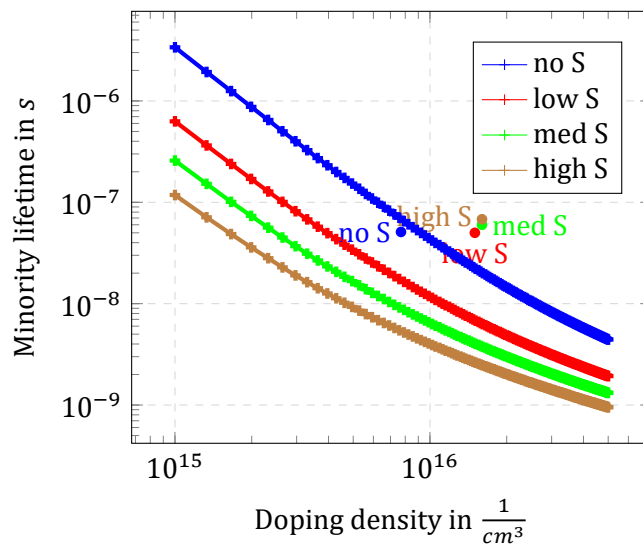


Figure 6.14: Calculated minority carrier lifetimes from the experimental data for the discussed samples with different sulfur contents for medium and high deposition temperatures (for the diffusion coefficient for electrons  $D_n = 2.56 \frac{cm^2}{s}$ ).

The exact estimation of  $N_a$  from CV-measurements is complicated as has been reported, for example, in [85]. Thus, using Equ. 6.2 the correlation between  $N_a$  and expected  $\tau_n$  is shown for the low temperature samples in Figure 6.13 and for the medium and high temperatures ones

in Figure 6.14. Such a representation allows to see in which doping range relevant  $\tau_n$  can be expected. In order to compare calculated values with the experiment the points with the coordinates of measured  $N_a$  and  $\tau_n$  are inserted whose colours correspond to the colours of the calculated curves. The measured  $N_a$  values are taken from Table 6.2 and  $\tau_n$  from Table 6.3. The first observation from the comparison of the experimental and theoretical data is the following. The measured  $N_a$  values are higher than the calculated ones. Higher doping densities could be explained in terms of an increased device capacitance  $C$  due to additional charges introduced by S-induced trapping states. A metastability-induced increase in the  $N_a$  density is not considered as the CV-measurements were performed on the relaxed devices in the dark. From this follows that extracted from CV-measurements doping density values may be misleading to be used for the minority carrier lifetime extraction. The S-free sample from the high temperature process demonstrates very good correlation to the calculated  $N_a$  and  $\tau_n$  values that also confirms the impact of S on the device capacitance. However, the S-free sample from the low temperature process shows rather unexpected behaviour what could be explained by the ambiguous effect of S at low growth temperatures.

#### 6.3.4 Impact on admittance measurements (in terms of non-ohmic contacts)

According to the GDOES data shown in Figure 3.5, a S-incorporation into the absorber surface can also impact the back contact properties as some S is also detected close to the CIGS/Mo interface. The investigation of the impact of the S-incorporation on the back contact properties will be conducted by discussing the Cf(T)-measurements in comparison to the JV(T)-measurements.

Figure 6.15 and 6.16 reproduce temperature-dependent JV-characteristics of the discussed samples. The common feature observed from the curves irrespective of the S-content and the process temperature is the complete blocking of the forward current at low temperatures. Such a behavior has been attributed to a Ga-gradient at the back contact which introduces a potential barrier to the injection current. A voltage-dependence of the photocurrent at low temperatures, especially pronounced for the S-free sample from the low temperature process and the sample with the high S and high T can be seen. A S-rich surface can introduce a potential barrier at the absorber/buffer interface to the photogenerated charge carriers as at  $S/(S+Se)$  ratios higher than 0.5 S impacts both VB and CB presumably leading to a significant CB hump especially pronounced at low temperatures and under high forward bias. A reason for the behaviour of the S-free sample is not clear. The flattening of the JV-curves occurs at higher temperatures for the high temperature process devices. This tendency could be attributed to higher back contact barriers compared to the low temperature devices. [64]

The blocking of the forward current and saturation of  $V_{oc}$  at low temperatures are typical signatures of a back contact barrier as has been discussed in Chapter 5. Therefore, the evaluation of Cf(T)-characteristics in this section will be also based on the model of a non-linear

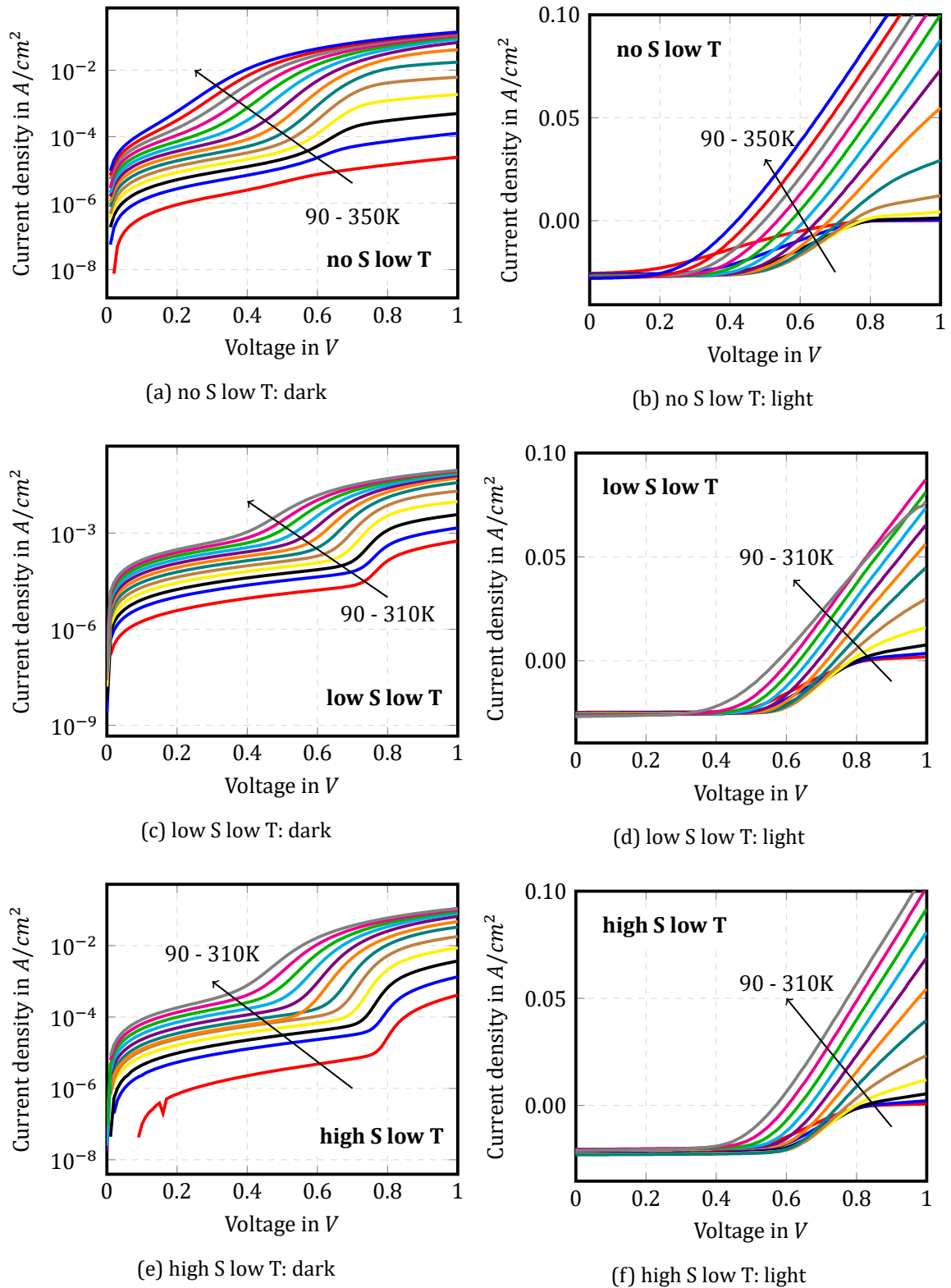


Figure 6.15: Comparison of temperature-dependent JV-measurements of the samples with a varied S-content and chalcogenised at low temperature.

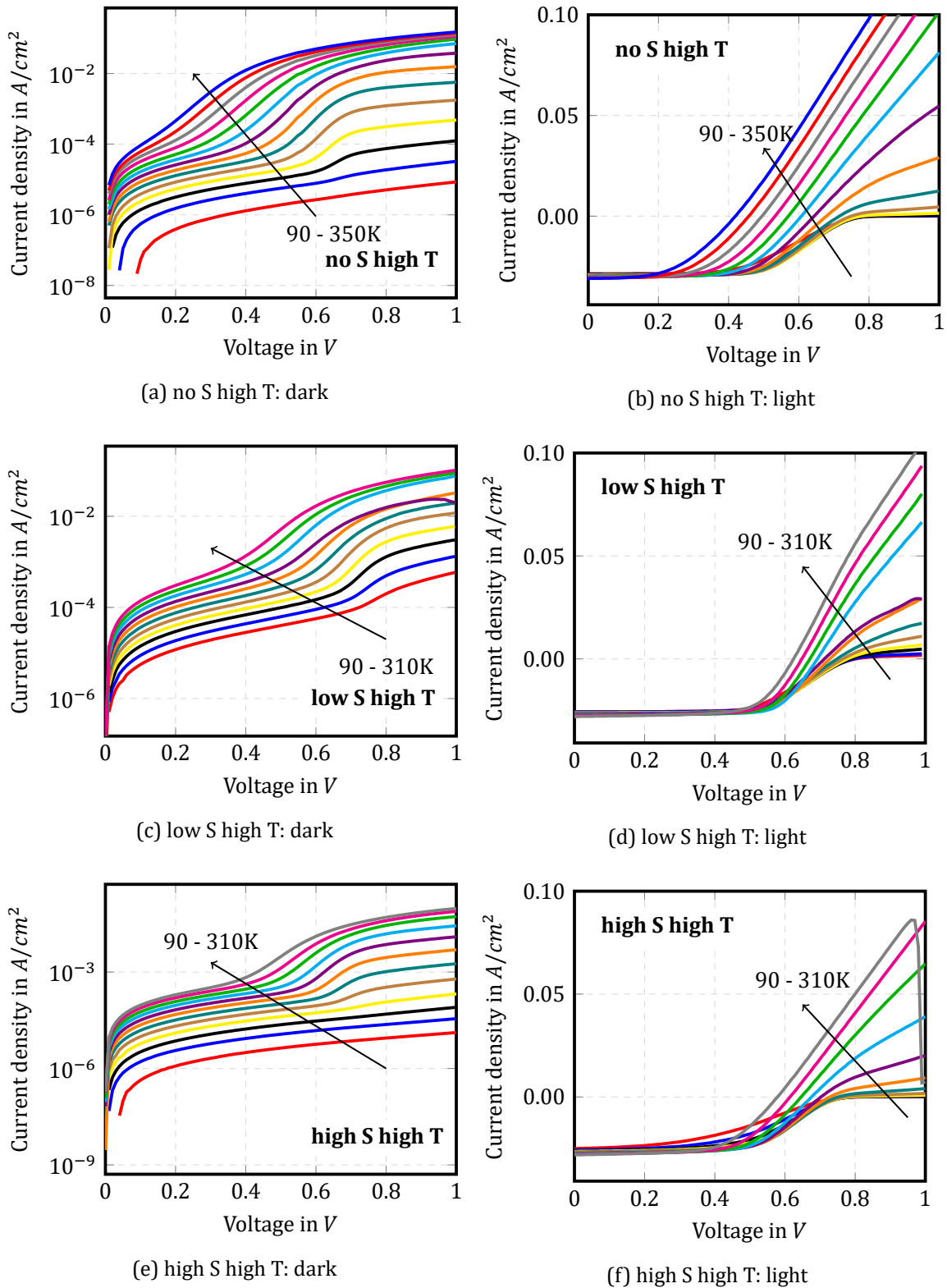


Figure 6.16: Comparison of temperature-dependent JV-measurements of the samples with a varied S-content and chalcogenised at high temperature.

Table 6.4: Comparison of activation energies extracted from JV(T)- and Cf(T)-measurements.

Sulfur content	Temperature	$E_a(\text{JV(T)}),$ [meV]	$E_a(\text{Cf(T)}),$ [meV]
no	low	180	151
low	low	200	154
high	low	180	108
med	med	220	127
no	high	180	159
low	high	180	129
high	high	240	210

resistance introduced to the equivalent circuit by the non-Ohmic back contact. The frequency-dependent admittance measurements for different temperatures are reproduced in Figure 6.17 for the samples grown at low temperatures and in Figure 6.18 for those grown at high temperatures. Irrespective of the deposition conditions the capacitance step can be detected already at temperatures below 200 K. A slightly different behaviour can be observed for the *'high S high T'* sample which demonstrates the capacitance drop at temperatures close to room temperature.

The evaluation of the admittance data has been carried out in accordance with [77]. The proposed method allows to extract the activation energies of the thermally-activated processes responsible for the steps observed in Cf(T)-measurements. The characteristic frequencies  $\omega_0$  deduced from the derivatives of C over frequency range for different temperatures are plotted versus the inverse of the corresponding temperatures in the Arrhenius plots in Figure 6.19a and 6.19b for the low and high temperatures, respectively. The extracted potential barriers at the back contact are summarised in Table 6.4. The values for the back contact barrier deduced from the Cf(T)-measurements are compared then to the back barrier heights extracted from the JV(T)-measurements which are also given in Table 6.4. The results obtained from these two methods demonstrate some deviations. It has to be mentioned that a correlation between the barrier heights extracted from the  $V_{oc}(T)$ - and Cf(T)-measurements for the S-incorporated sample set is significantly better than for the Ga-sample set. However, the reason for that is unclear.

A pronounced increase in a C level among the samples with respect to an increasing S-content as can be seen from the  $\Delta C$  range or the C span on the y-axis (shown by a green vertical line in Figure 6.17, not including the C step values at low temperatures) is another characteristic feature of the studied devices. It has to be noted that the process temperature does not influence the C span as compared to the S-content. A difference in the capacitance level can be caused by varied doping densities as well as a varied junction surface. The latter is anticipated to be a result of different grain sizes grown with a different S-supply. However, the SEM images reproduced in Chapter 3 (see Figure 3.2) do not reveal a significant difference in the grain size

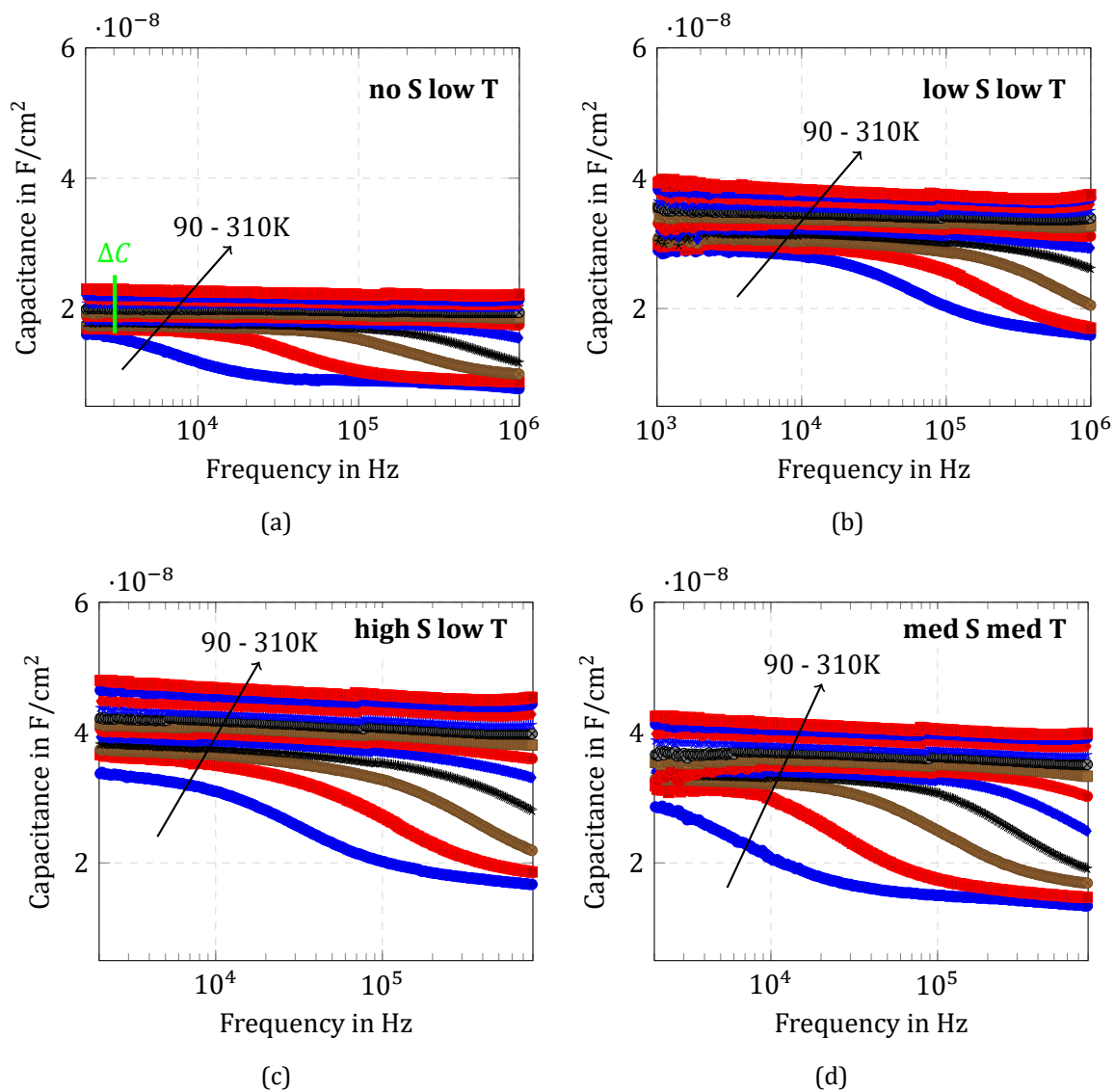


Figure 6.17: Frequency-dependent admittance measurements of the low temperature process samples for different S-contents.

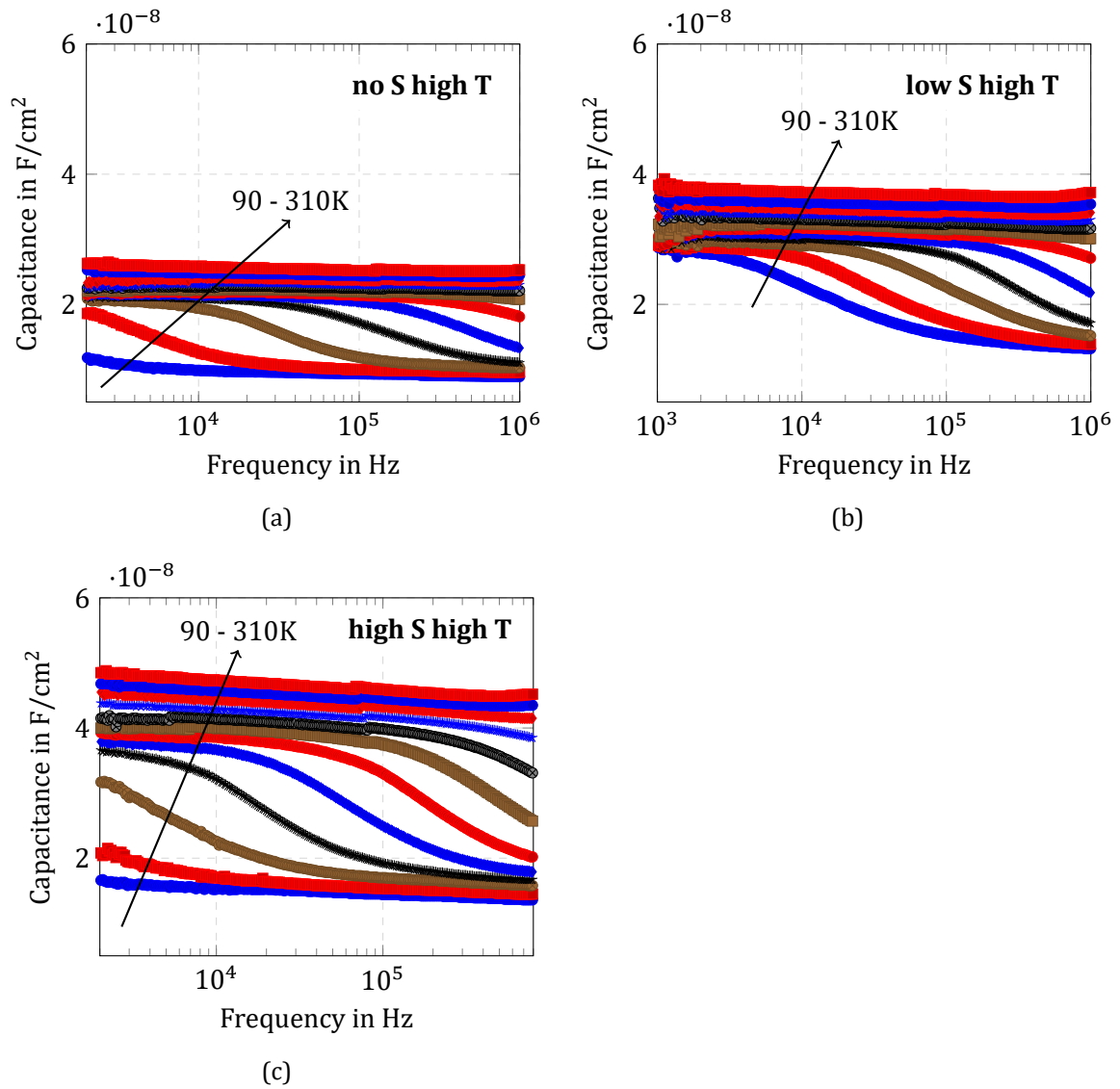


Figure 6.18: Frequency-dependent admittance measurements of the high temperature process samples for different S-contents.

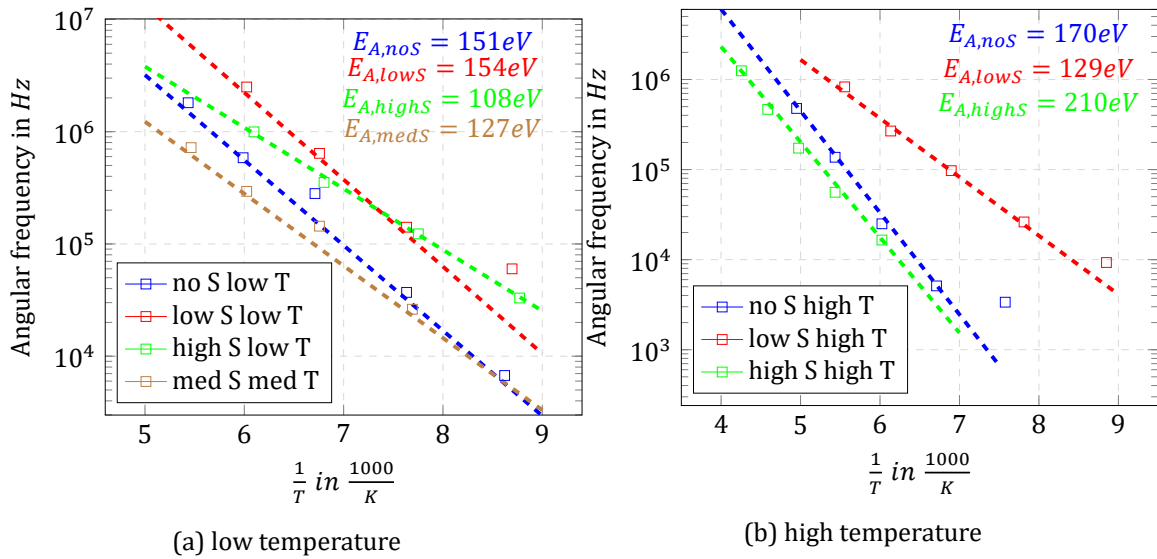


Figure 6.19: Arrhenius plots of the devices with varied S-content with extracted activation energies  $E_a$  which color corresponds to the color of the corresponding curve.

close to the absorber/buffer interface. Therefore, combining the results of the TRPL-decays and CV-measurements one can conclude that the S-addition introduces shallow defect states which additionally contribute to the device capacitance (compare  $N_a$  in Table 6.2) at higher temperatures.

The presence of S-induced trapping states can be also deduced from a C-gradient with respect to a frequency increase (a change in C values measured at low and high frequency limits for different temperatures, a high temperature effect). A S-gradient is less pronounced for the S-free devices what agrees with the temperature-dependence of the TRPL-decays.

## Resume

*The effect of S on admittance measurements has a dual nature. In agreement with TRPL-measurements, a S-incorporation induces localised trapping states which also add to the device capacitance as has been deduced from the admittance measurements. Most interesting is that the device capacitance does not vary a lot among the S-containing devices grown both at low and high temperatures, whereas a pronounced difference is observed with respect to the S-free samples. On the other hand, a capacitance step usually observed at low temperatures and assigned to the presence of a back contact barrier is somewhat enhanced compared to the reference and Ga-samples. A possible impact of the S-incorporation on the back contact properties is supported by the GDOES-measurements which revealed some S-accumulation close to the back contact.*



## 6.4 Conclusion

The first and most important conclusion on the impact of a S-incorporation into the absorber surface from this study (see Figure 6.8) is the possibility to separate the recombination and absorption processes by introducing a S-gradient into the absorber surface region. Such a gradient provides a desired  $V_{oc} - J_{sc}$ - tradeoff as a requisite of an efficient bandgap grading.

Additionally, a S-incorporation has the following effects:

- widening of the  $E_g$  in the SCR due to the replacement of Se-atoms. A bandgap increase will lead to the enhancement of the effective bandgap for recombination which in turn is responsible for the device  $V_{oc}$  enhancement. A decrease in the ideality factors  $A$  with an increasing S-content indicates that nonradiative SRH recombination processes are shifted away from the SCR towards the absorber QNR. This phenomenon can be interpreted as an interface passivation action of S.
- passivation of crystal defects, such as Cu- and Se-vacancies decreases recombination rates in the SCR and in the absorber bulk [138, 140, 134]. This improves the absorber material quality and results in higher minority carrier lifetimes  $\tau_n$  in the absorber bulk. However, the capacitance measurements and PL-transient investigation reveal that S introduces a certain amount of defects which can trap charges and contribute to the device capacitance.
- an accumulation of S at the back contact is expected to modify the back contact properties. The modified back contact leads to the suppressed roll-over effects and phototransistor behaviour at low temperatures, presumably by changing the band alignment at the absorber/back contact interface after a S-incorporation in agreement with [128]. However, it is still not clear whether the back contact improvement is a synergistic effect of the S- and Ga-gradients at the back contact or it is possible to achieve the same effect only with S, modifying the S-incorporation process as has been demonstrated in Figure 5.20.



# Summary

This thesis consists of the experimental results from different measurement techniques. Such a research methodology has been chosen in order to investigate underlying processes in graded gap solar cells from different aspects as sometimes it is difficult to deduce reliable conclusions based on the results of a single measurement technique or due to insufficient statistics. In this chapter, the cumulative knowledge obtained in the course of this work will be summarised in order to correlate the presented measurement results and to determine what are the process aspects which define the performance of the investigated solar cells. The overview of the experimental findings from the thesis is given in Table 6.5. The brackets around values indicate that the measurement data has not been shown in the text. This concerns first of all the sample (a modified S-incorporation process with elemental S) which was introduced in Section 5.2 in the context of the back contact investigation. The table signs must be read in the following way: ✓ means that the mentioned effect is observed; ✓✓ — observed to a great extent; ✗ — not observed; n/a — data not available.

A S-incorporation is an important fabrication step which has a diversified impact on the performance of the investigated solar cells. As has been shown in Section 6.3.1, S-incorporation leads to the enhancement of the effective bandgap for recombination in the SCR improving the device  $V_{oc}$ . A characteristic feature of the sulfurisation step is that S atoms settle mainly at the grain boundaries [140], hence S is mostly detected at the front and rear interfaces (see the GDOES data in Figure 3.6b and 3.5a). Therefore, the bulk of the absorber remains unaffected preserving the benefit of a low bandgap material for absorption and photocurrent collection.

Another contribution of the sulfurisation step is induced trapping states which can be deduced from the TRPL- and CfT-measurement results. The pronounced temperature-dependence of TRPL decays measured on the S-containing absorbers is not detected on the S-free absorbers as has been shown in Section 6.3.3. Moreover, a capacitance gradient with respect to frequency is also more pronounced for the devices with sulfurised absorbers as has been mentioned in Section 6.3.4. Such a gradient as has been mentioned before is an indication of the presence of trapping states.

Another process parameter which plays a decisive role in the device performance is the temperature of the chalcogenisation step (see Table 3.1). A high chalcogenisation temperature and a prolonged annealing time lead to a shift of the effective bandgap for recombination to higher

energies. But, contrary to the S-action, the effective bandgap for absorption and photocurrent collection is also affected as has been presented in Section 5.1.2. The admittance measurements discussed in Section 5.2.4. show that the Ga-sample with a long annealing time has an even stronger C-gradient with respect to a frequency increase if compared to the S-containing devices. It has to be mentioned that a strong temperature-dependence of the TRPL-decays of the Ga-samples has been also observed (not shown here). From the mentioned above, one can conclude that a C-gradient as a likely manifestation of induced trapping states is to a larger extent a consequence of the process temperature, and to a smaller extent - of the S-content.

Furthermore, stronger deviations in the calculated and measured PL emission spectra have been also observed for the high temperature Ga-samples (see Section 4.3) and the sample '*high S high T*'. The discrepancy between the distribution profile of injected electrons and the collection probability of photogenerated electrons indicates that a possible origin of the spectrum deviations can be rooted in the graded region. One possibility why the '*high S high T*' sample behaves differently in comparison to other samples from the S-set is an enhanced content of S at the back contact (see Figure 3.5b). A decisive role of the S-presence at the back contact can be also concluded from the measurements on the introduced sample in Section 5.2.4 which did not exhibit either a cross-over of the JV-characteristics, nor a capacitance step with a modified S-incorporation process. Assuming trapping states induced by S and/or the chalcogenisation process temperature to be located in the graded region close to the back contact, the deviations in the measured and calculated emission spectra could be also explained. If generation of charge carriers in the graded region takes place, their transport will be affected by traps reducing their mobility. A reduced mobility may contribute to enhanced recombination events, and therefore a stronger emission intensity at higher energies can be expected. This is in agreement with the observations in Section 4.3.

Moreover, a mobility barrier in the graded region could also explain anomalously high ideality factors ( $A > 2$  at room temperature) of the Ga-samples shown in Table 5.1. As has been discussed in the SCAPS simulations in Figure 4.23 a reduced carrier mobility in the graded region acts as a non-linear resistance similarly to the Schottky contact what can be clearly seen from the JV-characteristics. Hence, high ideality factors of the Ga-samples extracted from the JV-characteristics should not be interpreted in terms of a stronger impact (larger heights) of the back contact barrier. The barrier heights extracted from the CFT-measurements of the Ga-samples were not higher than those from the S-set samples, nevertheless the S-devices showed the A values lower than 2. Therefore, a low mobility region close to the back contact is rather responsible for the higher ideality factors as well as the deviations in the calculated and measured emission spectra for the Ga-samples.

As far as the back contact is concerned, one can conclude that the S-content, the process temperature or the annealing duration have no pronounced impact on the back contact properties as for all studied devices the blocking of the forward current has been still observed.

However, as one can see from the extracted ideality factors the carrier mobilities in the back contact region can be affected to a certain extent by these parameters.

Table 6.5: Short summary on the investigated solar cells

Sample	Parameters							
	$E_g(\text{abs}),$ $eV$	PL peak, $eV$	$E_g(\text{rec}),$ $eV$	A (dark, RT)	Admittance step	Blocking of current (low T)	Trapping states (CfT)	Trapping states (TRPL(T))
w/o S	$\approx 1.0$	1.0	1.0-1.01	1.65-1.84	✓	✓	✗	✗
w S	$\approx 1.0$	1.0	1.03-1.09	1.52-1.84	✓	✓	✓	✓
high $T_{\text{anneal}}$	1.04 ↑	1.04↑	1.08-1.11	2.52-2.54	✓	✓	✓✓	✓
elem. S	( $\approx 1.0$ )	(1.0)	(1.05)	1.7	✗	✗	✗	n/a
	Bandgap for absorption and recombination			Transport mechanism	Back contact barrier		Trapping states	

# Conclusion

In theory, there is no difference  
between theory and practice.  
But, in practice, there is.

— *Jan L.A. van der Snepscheut*

Nowadays, the fabrication of highly efficient CIGS solar cells, in principle, does not require additional sophisticated technological steps. The recent advances in the demonstrated efficiencies are rather based on the careful optimisation of the well-established production processes which lead to the favorable modifications of the layers properties and layers composition. In this context, the analysis of the major approaches used to enhance the device efficiency is necessary in order to highlight their advantages and identify possible measures for further improvements. Such an identification will enable to re-optimize the process or to suggest an alternative or a novel concept, to reduce an efficiency deficit. In this thesis, the investigation of solar cells based on sequentially grown CIGS absorbers has been performed. The absorbers under investigation have a depth-dependent  $E_g$  with a double grading profile. The gradients in  $E_g$  occur in the  $E_C$  due to the variation in the GGI ratio and in the  $E_V$  due to changes in  $S/(S + Se)$  ratio throughout the absorber film. The optimisation of the aforementioned compositional gradients is one of the main approaches to develop highly efficient CIGS solar cells. Such a double-graded  $E_g$  profile has been expected to increase the conversion efficiency by 0.5%. [150] In combination with the beneficial impact of the optimal incorporation and distribution of the Ga- and S-elements this improvement can be pushed even further.

The evaluation of the industrial process has been based on the assessment of the (beneficial) effects of the bandgap gradients on the overall performance of the completed PV devices. Widely used measurement techniques which describe electrical, optoelectronic and compositional properties of solar cells have been used. The electrical characterisation comprises JV-, CV- as well as admittance-measurements. In order to get information on the thermally-activated processes, the temperature-dependence of the JV- and Cf-characteristics has been analysed. The optoelectronic properties have been evaluated by using EQE and spectral and time-resolved PL-measurements. The experimental results have been correlated with the compositional structure of the absorber layer obtained from GDOES and SEM images. To verify the

deduced conclusions on the effects of the Ga- and S-gradients on the device efficiency SCAPS-1D simulations and analytical modelling have been included.

One of the first-to-think-about and most promising approach to boost the PV device efficiency is to reduce the  $V_{oc}$  deficit. The SQ-limit for CIGS-based solar cells with included optical and non-radiative recombination losses predicts the device  $V_{oc}$  of about 0.8-0.9V [54] with  $\eta \approx 30\%$ . [26] An improved  $V_{oc}$  is directly related to reduced recombination losses. The reduction of recombination events can be enforced by an increased  $E_g$  at the locations with the increased recombination probabilities. This approach has been successfully implemented in the investigated devices. The Ga-accumulation at the back contact as a consequence of the sequential absorber growth first of all influences the back contact properties as has been discussed in Chapter 5. The passivation of the absorber/back contact interface has been confirmed by simulations and theoretical modelling as no reference samples with the uniform Ga-distribution have been available. Under assumption of recombination in the QNR and no recombination in the SCR, the  $V_{oc}$  losses with high  $S_b$  (close to the thermal velocity) may solely account for about 60 mV as estimated for the investigated devices. The beneficial impact of a back grading is present as long as the ratio of the QNR width  $d$  to the minority carrier diffusion length  $L_n$  is less than 2. Otherwise, a back gradient has no impact on the diffusion current, and thereby  $V_{oc}$ . For thin absorbers with  $d/L_n = 0.5$ , the reduction in the diffusion current of about 50% can be achieved according to the calculations in Section 4.2. Furthermore, the photogenerated carrier collection has been predicted to improve as a result of the drift-assisted diffusion length of minority carriers. The collection probability of almost 100% could be ensured throughout the whole absorber with the quasi-electric field strength of  $> 10^4$ V/cm and back surface recombination  $S_b = 10^6$ cm/s. With the same back contact recombination but one order of magnitude lower quasi-electric field strength, the complete loss of photogenerated electrons in the vicinity of the back contact can be expected. This implies that the steepness of a Ga-gradient plays an important role.

Enhanced back contact recombination can be induced by the formation of the Schottky diode at the absorber/back contact interface. The presence of the second diode in the investigated devices can be deduced from the  $JV(T)$ - and  $Cf(T)$ -measurements. The Schottky contact introduces a second junction to the equivalent circuit of a solar cell which has the detrimental impact on both photogenerated electrons and holes. The injection of electrons to the back diode can be prevented by a Ga-gradient as has been discussed above. Moreover, the phototransistor behavior associated with the presence of the Schottky diode in solar cells based on coevaporated absorbers can be also suppressed by the back-grading. However, a problem with the majority carrier transport to the back contact due to the Schottky diode cannot be solved with Ga alone. The incorporation of elemental S into the absorber surface leads to the in-diffusion of S to the back contact and improvement of its metallicity (metallic properties). This results in the formation of the Ohmic-like contact preventing the occurrence of the potential barrier for holes.



In order to ensure a high device  $V_{oc}$  and improved back contact properties, an advanced concept of nano-sized opening contacts can be implemented. This concept has been successfully tested both experimentally and in device simulations by Vermang et al. This concept has been discussed in Chapter 5.3.1. The introduction of the passivation layer will require additional technological steps which inevitably will increase the production costs but at the same time may lead to higher device efficiencies. Therefore, nevertheless a Ga-segregation at the back contact is claimed to be a limiting factor for the device efficiency due to a low  $E_g$  in the SCR, and thus a non-optimal match to the solar spectrum, its positive effect on the stability of the back contact cannot be denied.

In order to ensure a better match to the solar spectrum by increasing the absorber  $E_g$ , the Ga-homogenisation throughout the absorber film has been enforced by prolonged heat treatment. According to simulations in Chapter 5.1, a uniformly increased  $E_g$  leads to an enhanced  $V_{oc}$ . However, the diffusion process has to be limited by an optimal concentration of Ga in the absorber bulk due to the following reasons. A large  $E_g$  absorber material close to the pn-junction may deteriorate the favorable band alignment between the CdS and CIGS layers. A moderate spike-like offset can be changed to a detrimental cliff-like one. The latter induces significant efficiency losses due to increased interface recombination. [62] In order to preserve the benefit of a large bandgap absorber, a different buffer material has to be used or a passivation method to be engineered to tailor the absorber/buffer interface properties. Another issue is an enhanced defect density in the bulk caused by the redundant Ga-concentration. [78] The optimal GGI-ratio has been defined as  $\approx 0.3$ . However, the tolerance of the CIGS material to the Ga-content has been improved with the incorporation of alkali metals [7] or S-atoms [103] and could reach as high as 0.4-0.5. The Ga-in-diffusion towards the front interface suppresses QNR recombination but enhances SRH recombination in the SCR. Moreover, the absorption properties of the absorber layer deteriorates due to the increased absorption bandgap. The ratio of the increased device  $V_{oc}$  ( $\Delta V_{oc}$ ) over the increase in the absorption  $E_g$  with respect to an increasing diffusion time is linear but smaller than unity. This indicates that a prolonged diffusion time in combination with an increased process temperature does not lead to the uniform  $E_g$  throughout the absorber layer. The increase in the optical  $E_g$  is larger than in the device  $V_{oc}$  meaning predominant losses in  $J_{sc}$ . Thus, another approach for the flattening of the Ga-distribution would be preferable. Moreover, the benefit of the increased  $E_g$  as a result of the Ga-enriched absorber has to be evaluated by considering both the increase in  $V_{oc}$  and the loss in  $J_{sc}$  as the enhancement of the absorber  $E_g$  by flattening the Ga-gradient does not allow to separate recombination and absorption processes in the CIGS layer.

An alternative way to mitigate the undesired consequences of the low  $E_g$  in the SCR is the absorber surface sulfurisation. A S-incorporation results in an exponential distribution, with most of S being within first 200-400nm of the absorber film. This implies that most of S-atoms are concentrated in the SCR. The simulations presented in Chapter 6.1 demonstrate that such a distribution profile enhances the device  $V_{oc}$  as a result of the  $E_g$  widening in the SCR with-

out affecting the bulk and deteriorating the absorption properties. This could be seen from the EQE and spectral PL measurements where the absorption cutoffs as well as the emission wavelengths were not affected by the S-presence compared to the S-free devices. The interesting finding from the analytical part of the thesis (see Chapter 4) is that the linear profile of the S-distribution in the SCR would be a most efficient grading profile. In case of a linear front grading,  $\frac{1}{\sqrt{2}}$  of the  $\Delta E_g$  increase between the maximum  $E_g$  at the S-rich side and the bulk  $E_g$  would contribute to increase the effective bandgap for recombination in the SCR. From the practical point of view, oversulfurisation of the absorber surface may have a rather detrimental effect on the overall device performance. An optimal solution then is an exponential distribution of S-atoms, which does not induce resistive losses, and therefore degraded FF associated with a S-excess.

In Chapter 6, the effect of the sulfurisation process temperature and the S-amount during the sulfurisation step have been investigated. It has been found that the temperature and element concentration are important parameters for the final device performance. The higher the process temperature and the higher the S-concentration (in the studied parameter range), the higher the device  $V_{oc}$  with a minimal effect on the absorber bulk and  $J_{sc}$ . A low sulfurisation temperature resulted in the devices with worst  $V_{oc}$  and  $\tau_n$  indicating that the thermal budget of the process was not sufficient.

Furthermore, it can be deduced that a S-incorporation induces trapping states which contribute to the device capacitance as has been discussed in Section 6.3.3 and 6.3.4. Introducing S to the absorber increases the net doping density compared to the S-free devices. The formation of trapping defect states has been also deduced from the TRPL-measurements. This is another beneficial effect of S on the device performance.

Apart from the SCR, some S has been detected at the back contact. The JV(T)- and Cf(T)-measurements indicated the presence of the Schottky contact. The extracted activation energies showed that the barrier height with an increasing S-content is somewhat higher compared to the reference devices and those with the modified Ga-profiles. The presence of the Schottky diode has been reported for different manufacturers implementing the S-incorporation from gaseous atmosphere. However, the problem with the back contact can be solved by using the elemental S-incorporation in the absorber layer. The Ohmic-like contact has been deduced from the mentioned measurements for such devices (this information has been received in a personal conversation with the manufacturer of the investigated devices).

Summarising the findings, the following conclusions can be made. The concept of a double bandgap grading realised by the implementation of the varied Ga- and S-in-depth distributions proved to be an efficient way to improve the device performance. However, analysing the processes of the record holding companies some suggestions regarding the investigated fabrication process can be considered.

Firstly, the absorber growth temperature could be increased. The devices from the studied process suffer from initial shunting which decreases after moderate heat treatment (com-

pare the devices from Chapter 5 to the reference). Therefore, the growth temperature used to enhance the Ga-out-diffusion could be a good starting point. Obviously, an increased process temperature will modify the Ga-distribution profile leading to an increased optical bandgap and reduced  $J_{sc}$ . At this point, a potential device performance has to be evaluated in terms of the improvement of the  $V_{oc} \times J_{sc}$  product rather than single parameters. The improved overall device performance with an increased optical bandgap has been discussed in [6]. However, this step has to be followed by the optimisation of the front gradient to increase further the device  $V_{oc}$ . As the linearisation and enhancement of a S-gradient may lead to the undesired by-effects, the incorporation of alkali metals can be a way out. This technological process can have multiple advantages. The alkali-PDT improves the absorber quality. This improvement reflects in the increase of the net doping density and in the passivation of the grain boundaries making them more electrically benign. The alkali treatment of the absorber surface leads to advantageous surface modifications forming a wide-gap material at the surface. All this can significantly improve the device  $V_{oc}$ . Moreover, the improved morphology of the absorber will allow to grow thinner buffer layers enhancing absorption and the device  $J_{sc}$ .

Secondly, the improvement of the back contact properties has to be considered separately. The measures have to be taken even though no obvious signatures of the Schottky contact can be traced for the studied devices at room temperature,  $V_{oc}$  loss can be still there. To avoid costly and complicated approaches matched up with the Si-technology, a hybrid sulfurisation process could be developed. Similar to the hybrid selenisation process which consists first of the elemental Se-incorporation and then the gaseous treatment in  $H_2Se$  atmosphere, the sulfurisation step could be engineered. The elemental S introduced after the selenisation step would improve the metallicity of the back contact. Afterwards, the inset of  $H_2S$  gas could improve the front grading by forming the S-rich surface. The author has not found the reports on the experimental implementation of the hybrid sulfurisation but thinks this idea could lead to the desired outcome.

Thirdly, the optimisation of the window bi-layer can be also considered for the studied devices. However, this discussion is out of scope of this thesis.

A proposed diagnostic tool which can be easily implemented in a production environment is PL-measurements. These measurements are contactless and could be applied already on the absorber layer. The advantages of this measurement technique is immediately recognisable. The PL intensity directly correlates to the quasi-Fermi level splitting,  $E_{Fn} - E_{Fp}$ . This means that after a proper calibration this parameter can be used to predict the device  $V_{oc}$  already at absorber level. Moreover, spectral PL data in combination with RR can prognose quantum efficiency of the completed devices which allows to determine the  $J_{sc}$  of the finished devices and evaluate the effectiveness of a grading approach. However, the application of RR theorem to graded bandgap absorbers has to be carefully considered as the RR for non-uniform absorbers with induced quasi-electric fields due to compositional gradients can be still approximated but with certain deviations depending on the field strength.



# References

- [1] U. Rau and H.W. Schock. "Electronic properties of Cu(In,Ga)Se<sub>2</sub> heterojunction solar cells-recent achievements, current understanding, and future challenges". In: *Applied Physics A: Materials Science & Processing* 69.2 (Aug. 1999), pp. 131–147. doi: 10.1007/s003390050984.
- [2] Solar Frontier. *Solar Frontier Achieves World Record Thin-Film Solar Cell Efficiency of 23.35%*. Jan. 17, 2019. URL: [http://www.solar-frontier.com/eng/news/2019/0117\\_press.html](http://www.solar-frontier.com/eng/news/2019/0117_press.html).
- [3] Volker Probst, Immo Koetschau, Emmerich Novak, Axel Jasenek, Heinz Eschrich, Frank Hergert, Thomas Hahn, Jochen Feichtinger, Markus Maier, Bernd Walther, and Volker Nadenau. "A New Mass Production Technology for High-Efficiency Thin-Film CIS-Absorber Formation". In: *IEEE Journal of Photovoltaics* 4.2 (Mar. 2014), pp. 687–692. doi: 10.1109/JPHOTOV.2014.2302235.
- [4] Michael Powalla, Stefan Paetel, Dimitrios Hariskos, Roland Wuerz, Friedrich Kessler, Peter Lechner, Wiltraud Wischmann, and Theresa Magorian Friedlmeier. "Advances in Cost-Efficient Thin-Film Photovoltaics Based on Cu(In,Ga)Se<sub>2</sub>". In: *Engineering* 3.4 (Aug. 2017), pp. 445–451. doi: 10.1016/j.eng.2017.04.015.
- [5] Shigeru Niki, Miguel Contreras, Ingrid Repins, Michael Powalla, Katsumi Kushiya, Shogo Ishizuka, and Koji Matsubara. "CIGS absorbers and processes". In: *Progress in Photovoltaics: Research and Applications* 18.6 (2010), pp. 453–466. ISSN: 1099-159X. doi: 10.1002/pip.969. URL: <http://dx.doi.org/10.1002/pip.969>.
- [6] Takuya Kato. "Cu(In,Ga)(Se,S)<sub>2</sub> solar cell research in Solar Frontier: Progress and current status". In: *Japanese Journal of Applied Physics* 56.4S (Feb. 2017), 04CA02. doi: 10.7567/jjap.56.04ca02.
- [7] Theresa Magorian Friedlmeier, Philip Jackson, Andreas Bauer, Dimitrios Hariskos, Oliver Kiowski, Richard Menner, Roland Wuerz, and Michael Powalla. "High-efficiency Cu(In,Ga)Se<sub>2</sub> solar cells". In: *Thin Solid Films* 633 (2017), pp. 13–17. doi: 10.1016/j.tsf.2016.08.021.
- [8] C Frisk, C Platzer-Björkman, J Olsson, P Szaniawski, J T Wätjen, V Fjällström, P Salomé, and M Edoff. "Optimizing Ga-profiles for highly efficient Cu(In, Ga)Se<sub>2</sub> thin film solar cells in simple and complex defect models". In: *Journal of Physics D: Applied Physics* 47.48 (Nov. 2014), p. 485104. doi: 10.1088/0022-3727/47/48/485104.
- [9] Volker Probst, Axel Jasenek, Christian Sandfort, Andreas Letsch, Immo Koetschau, Thomas Hahn, Jochen Feichtinger, and Heinz Eschrich. "Innovative front end processing for next generation CIS module production". In: *Japanese Journal of Applied Physics* 54.8S1 (July 2015), 08KC12. doi: 10.7567/jjap.54.08kc12.

- [10] Martha Ch. Lux-Steiner and Reiner Klenk. "Thin Film Solar Cells: Fabrication, Characterization and Applications". In: ed. by Jef Poortmans and Vladimir Arkhipov. John Wiley & Sons Ltd, 2006. Chap. Chalcopyrite Based Solar Cells, pp. 237–275. ISBN: 978-0-470-09126-5 (H/B).
- [11] Björn Jakob Müller. "Improvement of Cu(In,Ga)(S,Se)<sub>2</sub> thin film solar cells with the help of Gallium and Sulfur gradients". en. PhD thesis. 2017. DOI: 10.18725/oparu-4507.
- [12] Robin Knecht. "Characterization of industrially processed chalcopyrite solar cells with varied absorber composition". PhD thesis. Carl von Ossietzky Universität Oldenburg, 2012. URL: [oops.uni-oldenburg.de/1442/1/knecha12.pdf](https://oops.uni-oldenburg.de/1442/1/knecha12.pdf).
- [13] Daniel Abou-Ras, Sigurd Wagner, Bill J. Stanbery, Hans-Werner Schock, Roland Scheer, Lars Stolt, Susanne Siebentritt, Daniel Lincot, Chris Eberspacher, Katsumi Kushiya, and Ayodhya N. Tiwari. "Innovation highway: Breakthrough milestones and key developments in chalcopyrite photovoltaics from a retrospective viewpoint". In: *Thin Solid Films* 633 (July 2017), pp. 2–12. DOI: 10.1016/j.tsf.2017.01.005.
- [14] Solar Frontier. *Solar Frontier Achieves World Record Thin-Film Solar Cell Efficiency of 22.9%*. Solar Frontier. Dec. 20, 2017. URL: [http://www.solar-frontier.com/eng/news/2017/1220\\_press.html](http://www.solar-frontier.com/eng/news/2017/1220_press.html) (visited on 07/19/2018).
- [15] Thomas Feurer, Patrick Reinhard, Enrico Avancini, Benjamin Bissig, Johannes Löckinger, Peter Fuchs, Romain Carron, Thomas Paul Weiss, Julian Perrenoud, Stephan Stutterheim, Stephan Buecheler, and Ayodhya N. Tiwari. "Progress in thin film CIGS photovoltaics - Research and development, manufacturing, and applications". In: *Progress in Photovoltaics: Research and Applications* 25.7 (Oct. 2016), pp. 645–667. DOI: 10.1002/pip.2811.
- [16] W. S. Chen, J. M. Stewart, B. J. Stanbery, W. E. Devaney, and R. A. Mickelsen. "Development of thin film polycrystalline CuIn<sub>1-x</sub>Ga<sub>x</sub>Se<sub>2</sub> solar cells". In: *19th IEEE Photovoltaic Specialists Conference*. 1987, pp. 1445–1447.
- [17] Daniel Abou-Ras, THomas Kirchartz, and Uwe Rau, eds. *Advanced Characterization Techniques for Thin Film Solar Cells*. Wiley-VCH Verlag GmbH & Co. KGaA, 2011.
- [18] Lars Stolt, Jonas Hedström, John Kessler, Martin Ruckh, Karl-Otto Velthaus, and Hans-Werner Schock. "ZnO/CdS/CuInSe<sub>2</sub> thin-film solar cells with improved performance". In: *Applied Physics Letters* 62.6 (1993), pp. 597–599. DOI: 10.1063/1.108867.
- [19] J. Hedström, H. Ohlsen, M. Bodegård, A. Kylner, L. Stolt, D. Hariskos, M. Ruckh, and H. W. Schock. "ZnO/CdS/Cu(In,Ga)Se<sub>2</sub> thin film solar cells with improved efficiency". In: *Conference Record on the Twenty Third IEEE Photovoltaic Specialists Conference*. 1993, pp. 364–371. DOI: 10.1109/PVSC.1993.347154.
- [20] M. A. Contreras, B. Egaas, P. Dippo, J. Webb, J. Granata, K. Ramanathan, S. Asher, A. Swartzlander, and R. Noufi. "On the Role of Na and Modifications to Cu(In,Ga)Se<sub>2</sub> Absorber Materials Using Thin-MF (M=Na, K, Cs) Precursor Layers". In: *Conference Record of the 26th IEEE Photovoltaic Specialists Conference*. 1997, pp. 359–362. DOI: 10.1109/PVSC.1997.654102.
- [21] D. Rudmann, A. F. da Cunha, M. Kaelin, F. Kurdesau, H. Zogg, and A. N. Tiwari. "Efficiency enhancement of Cu(In,Ga)Se<sub>2</sub> solar cells due to post-deposition Na incorporation". In: *Applied Physics Letters* 84.7 (2004), pp. 1129–1131. DOI: 10.1063/1.1646758.

- [22] Adrian Chirilă, Patrick Reinhard, Fabian Pianezzi, Patrick Bloesch, Alexander R. Uhl, Carolin Fella, Lukas Kranz, Debora Keller, Christina Gretener, Harald Hagendorfer, Dominik Jaeger, Rolf Erni, Shiro Nishiwaki, Stephan Buecheler, and Ayodhya N. Tiwari. "Potassium-induced surface modification of Cu(In,Ga)Se<sub>2</sub> thin films for high-efficiency solar cells". In: *Nature Materials* 12.12 (Nov. 2013), pp. 1107–1111. doi: 10.1038/nmat3789.
- [23] Philip Jackson, Dimitrios Hariskos, Roland Wuerz, Wiltraud Wischmann, and Michael Powalla. "Compositional investigation of potassium doped Cu(In,Ga)Se<sub>2</sub> solar cells with efficiencies up to 20.8%". In: *physica status solidi (RRL) - Rapid Research Letters* 8.3 (Feb. 2014), pp. 219–222. doi: 10.1002/pssr.201409040.
- [24] Philip Jackson, Dimitrios Hariskos, Roland Wuerz, Oliver Kiowski, Andreas Bauer, Theresa Magorian Friedlmeier, and Michael Powalla. "Properties of Cu(In,Ga)Se<sub>2</sub> solar cells with new record efficiencies up to 21.7%". In: *physica status solidi (RRL) - Rapid Research Letters* 9.1 (Dec. 2014), pp. 28–31. doi: 10.1002/pssr.201409520.
- [25] Philip Jackson, Roland Wuerz, Dimitrios Hariskos, Erwin Lotter, Wolfram Witte, and Michael Powalla. "Effects of heavy alkali elements in Cu(In,Ga)Se<sub>2</sub> solar cells with efficiencies up to 22.6%". In: *physica status solidi (RRL) - Rapid Research Letters* 10.8 (July 2016), pp. 583–586. doi: 10.1002/pssr.201600199.
- [26] Susanne Siebentritt. "What limits the efficiency of chalcopyrite solar cells?" In: *Solar Energy Materials and Solar Cells* 95.6 (June 2011), pp. 1471–1476. doi: 10.1016/j.solmat.2010.12.014.
- [27] *Super high efficiency Cu(In, Ga)Se<sub>2</sub> thin-film solar cells approaching 25%*. URL: <http://sharc25.eu> (visited on 07/19/2018).
- [28] M. Malitckaya, H.-P. Komsa, V. Havu, and M. J. Puska. "Effect of Alkali Metal Atom Doping on the CuInSe<sub>2</sub>-Based Solar Cell Absorber". In: *The Journal of Physical Chemistry C* 121.29 (July 2017), pp. 15516–15528. doi: 10.1021/acs.jpcc.7b03083.
- [29] Yanpeng Fu. "Spray-ILGAR® deposition of controllable ZnS nanodots and application as passivation/point contact at the In<sub>2</sub>S<sub>3</sub>/Cu(In,Ga)(S,Se)<sub>2</sub> junction in thin film solar cells". eng. PhD thesis. 2012. doi: 10.5442/d0025.
- [30] Patrick Reinhard, Benjamin Bissig, Fabian Pianezzi, Harald Hagendorfer, Giovanna Sozzi, Roberto Menozzi, Christina Gretener, Shiro Nishiwaki, Stephan Buecheler, and Ayodhya N. Tiwari. "Alkali-Templated Surface Nanopatterning of Chalcogenide Thin Films: A Novel Approach Toward Solar Cells with Enhanced Efficiency". In: *Nano Letters* 15.5 (Apr. 2015), pp. 3334–3340. doi: 10.1021/acs.nanolett.5b00584.
- [31] M Schmid. "Review on light management by nanostructures in chalcopyrite solar cells". In: *Semiconductor Science and Technology* 32.4 (Mar. 2017), p. 043003. doi: 10.1088/1361-6641/aa59ee.
- [32] Nasim Rezaei, Olindo Isabella, Zeger Vroon, and Miro Zeman. "Quenching Mo optical losses in CIGS solar cells by a point contacted dual-layer dielectric spacer: a 3-D optical study". In: *Optics Express* 26.2 (Dec. 2017), A39. doi: 10.1364/oe.26.000a39.
- [33] Uwe Rau and Hans-Werner Schock. "Clean Electricity from Photovoltaics. Series on Photoconversion of Solar Energy". In: ed. by Mary D. Archer and Martin A. Green. 2nd ed. Vol. 4. Imperial College Press, 2015. Chap. Cu(In,Ga)Se<sub>2</sub> and related solar cells, pp. 245–305. ISBN: 978-1-84816-767-4.
- [34] Roland Scheer and Hans Werner-Schock. *Chalcogenide Photovoltaics. Physics, Technologies, and Thin Film Devices*. Wiley-VCH Verlag GmbH & Co. KGaA, 2011.

- [35] Julia Riediger. "Impact of Gallium on the Defect Landscape of Sulfur-Based Chalcopyrite Solar Cells". PhD. University Oldenburg, 2013. URL: <http://oops.uni-oldenburg.de/1632/>.
- [36] Karl W. Böer. *Handbook of the Physics of Thin-Film Solar Cells*. Springer-Verlag Berlin Heidelberg, 2013.
- [37] Angus A. Rockett. "Current status and opportunities in chalcopyrite solar cells". In: *Current Opinion in Solid State and Materials Science* 14 (2010), pp. 143–148. doi: 10.1016/j.cossms.2010.08.001.
- [38] Manz. *16 PERCENT: MANZ ACHIEVES NEW WORLD RECORD FOR EFFICIENCY OF CIGS THIN-FILM SOLAR MODULES*. Sept. 19, 2018. URL: <https://www.manz.com/media/news/16-prozent-manz-erzielt-neuen-weltrekord-bei-wirkungsgrad-von-cigs-duennschicht-solarmodulen-615/>.
- [39] Solibro. *17.52 % EFFICIENCY – NEW WORLD RECORD FOR SOLIBRO'S CIGS THIN-FILM PANELS*. Sept. 19, 2018. URL: <http://solibro-solar.com/en/news-downloads/news/>.
- [40] Hsiu-Po Kuo, Hung-An Tsai, An-Ni Huang, and Wen-Chueh Pan. "CIGS absorber preparation by non-vacuum particle-based screen printing and RTA densification". In: *Applied Energy* 164 (2016), pp. 1003–1011. doi: 10.1016/j.apenergy.2015.04.002.
- [41] C. Broussillou, C. Viscogliosi, A. Rogee, S. Angle, P. P. Grand, S. Bodnar, C. Debauche, J. L. Allary, B. Bertrand, C. Guillou, L. Parissi, and S. Coletti. "Statistical Process Control for Cu(In,Ga)(S,Se)<sub>2</sub> electrodeposition-based manufacturing process of 60x120 cm<sup>2</sup> modules up to 14.0 % efficiency". In: *IEEE 42nd Photovoltaic Specialist Conference (PVSC)*. 2015, pp. 1–5. doi: 10.1109/PVSC.2015.7356224.
- [42] C. Rincón and R. Márquez. "Defect physics of the CuInSe<sub>2</sub> chalcopyrite semiconductor". In: *Journal of Physics and Chemistry of Solids* 60 (1999), pp. 1865–1873.
- [43] Stephan Lany and Alex Zunger. "Light- and bias-induced metastabilities in Cu(In,Ga)Se<sub>2</sub> based solar cells caused by the (VSe-VCu) vacancy complex". In: *Journal of Applied Physics* 100.11 (2006), p. 113725. doi: 10.1063/1.2388256.
- [44] M. Igalson, M. Cwil, and M. Edoff. "Metastabilities in the electrical characteristics of CIGS devices: Experimental results vs theoretical predictions". In: *Thin Solid Films* 515.15 (May 2007), pp. 6142–6146. doi: 10.1016/j.tsf.2006.12.038.
- [45] H. Ruckh, D. Schmid, M. Kaiser, R. Schaffler, T. Walter, and H.W. Schock. "Influence of substrates on the electrical properties of Cu(In,Ga)Se<sub>2</sub>/sub 2/ thin films". In: *Proceedings of 1994 IEEE 1st World Conference on Photovoltaic Energy Conversion - WCPEC (A Joint Conference of PVSC, PVSEC and PSEC)*. IEEE. doi: 10.1109/wcpec.1994.519831.
- [46] Leeor Kronik, David Cahen, and Hans-Werner Schock. "Effects of sodium on polycrystalline Cu(In,Ga)Se<sub>2</sub> and its solar cell performance". In: *Advanced Materials* 10 (1998), pp. 31–36. ISSN: 1521-4095. doi: 10.1002/(SICI)1521-4095(199801)10:1<31::AID-ADMA31>3.0.CO;2-3.
- [47] David W. Niles, Kannan Ramanathan, Falah Hasoon, Rommel Noufi, Brian J. Tielsch, and Julia E. Fulghum. "Na impurity chemistry in photovoltaic CIGS thin films: Investigation with x-ray photoelectron spectroscopy". In: *Journal of Vacuum Science & Technology, A: Vacuum, Surfaces, and Films* 15.6 (1997), pp. 3044–3049. doi: 10.1116/1.580902.
- [48] D. Güttler, A. Chirilla, S. Seyrling, P. Blösch, S. Bücheler, X. Fontané, V. Izquierdo-Roca, L. Calvo-Barrio, A. Pérez-Rodríguez, J. R. Morante, A. Eicke, and A. N. Tiwari. "Influence of NaF incorporation during Cu(In,Ga)Se<sub>2</sub> growth on microstructure and photovoltaic performance". In: *35th IEEE Photovoltaic Specialist Conference*. 2010, pp. 003420–003424. ISBN: 0160-8371. doi: 10.1109/PVSC.2010.5614564.



- [49] P. M. P. Salomé, H. Rodriguez-Alvarez, and S. Sadewasser. "Incorporation of alkali metals in chalcogenide solar cells". In: *Solar Energy Materials & Solar Cells* 143 (2015), pp. 9–20. doi: 10.1016/j.solmat.2015.06.011.
- [50] P. Pistor, D. Greiner, C. A. Kaufmann, S. Brunken, M. Gorgoi, A. Steigert, W. Calvet, I. Lauermann, R. Klenk, T. Unold, and M.-C. Lux-Steiner. "Experimental indication for band gap widening of chalcopyrite solar cell absorbers after potassium fluoride treatment". In: *Applied Physics Letters* 105.6 (Aug. 2014), p. 063901. doi: 10.1063/1.4892882.
- [51] Clas Persson and Alex Zunger. "Anomalous Grain Boundary Physics in PolycrystallineCuInSe<sub>2</sub>: The Existence of a Hole Barrier". In: *Physical Review Letters* 91.26 (Dec. 2003). doi: 10.1103/physrevlett.91.266401.
- [52] Chung-Hao Cai, Rong-Zhi Chen, Ting-Shan Chan, Ying-Rui Lu, Wei-Chih Huang, Chao-Chun Yen, Kejie Zhao, Yu-Chieh Lo, and Chih-Huang Lai. "Interplay between potassium doping and bandgap profiling in selenized Cu(In,Ga)Se<sub>2</sub> solar cells: A functional CuGa:KF surface precursor layer". In: *Nano Energy* 47 (May 2018), pp. 393–400. doi: 10.1016/j.nanoen.2018.03.024.
- [53] S.M. Sze and Kwok K. Ng. *Physics of Semiconductor Devices*. John Wiley & Sons, Inc., Apr. 2006. doi: 10.1002/0470068329.
- [54] Jürgen H. Werner, Julian Mattheis, and Uwe Rau. "Efficiency limitations of polycrystalline thin film solar cells: case of Cu(In,Ga)Se<sub>2</sub>". In: *Thin Solid Films* 480-481 (2005), pp. 399–409. doi: 10.1016/j.tsf.2004.11.052.
- [55] D. Schmid, M. Ruckh, F. Grunwald, and H. W. Schock. "Chalcopyrite/defect chalcopyrite heterojunctions on the basis of CuInSe<sub>2</sub>". In: *Journal of Applied Physics* 73.6 (Mar. 1993), pp. 2902–2909. doi: 10.1063/1.353020.
- [56] Tobias Eisenbarth, Thomas Unold, Raquel Caballero, Christian A. Kaufmann, and Hans-Werner Schock. "Interpretation of admittance, capacitance-voltage, and current-voltage signatures in Cu(In,Ga)Se<sub>2</sub> thin film solar cells". In: *Journal of Applied Physics* 107 (2010), p. 034509. doi: 10.1063/1.3277043.
- [57] Thomas Ott, Francillina Schönberger, Thomas Walter, Dimitrios Hariskos, Oliver Kiowski, and Raymund Schäffler. "Long term endurance test and contact degradation of CIGS solar cells". In: *Proceedings of SPIE*. Vol. 8825. 2013, 88250J. doi: 10.1117/12.2024132.
- [58] Thomas Ott, Thomas Walter, and Thomas Unold. "Phototransistor effects in Cu(In,Ga)Se<sub>2</sub> solar cells". In: *Thin Solid Films* 535 (2013), pp. 275–278. doi: 10.1016/j.tsf.2012.11.084.
- [59] William Shockley and Hans J. Queisser. "Detailed Balance Limit of Efficiency of p-n Junction Solar Cells". In: *Journal of Applied Physics* (1961).
- [60] Thomas Kirchartz. "Generalized detailed balance theory of solar cells". PhD thesis. RWTH Aachen University, 2009.
- [61] Martin A. Green. *Silicon solar cells. Advanced principles and practice*. Centre for Photovoltaic Devices and Systems University of New South Wales, 1995.
- [62] R. Scheer. "Activation energy of heterojunction diode currents in the limit of interface recombination". In: *Journal of Applied Physics* 105.10 (May 2009), p. 104505. doi: 10.1063/1.3126523.
- [63] V. Nadenau, U. Rau, A. Jasenek, and H. W. Schock. "Electronic properties of CuGaSe<sub>2</sub>-based heterojunction solar cells. Part I. Transport analysis". In: *Journal of Applied Physics* 87.1 (Jan. 2000), pp. 584–593. doi: 10.1063/1.371903.

- [64] Thomas Ott, Francillina Schönberger, Thomas Walter, Dimitrios Hariskos, Oliver Kiowski, Oliver Salomon, and Raymund Schäffler. "Verification of phototransistor model for Cu(In,Ga)Se<sub>2</sub> solar cells". In: *Thin Solid Films* 582 (2015), pp. 392–396. DOI: [dx.doi.org/10.1016/j.tsf.2014.09.025](https://doi.org/10.1016/j.tsf.2014.09.025).
- [65] T. Kato, K. Kitani, K.F. Tai, R. Kamada, H. Hiroi, and H. Sugimoto. "Characterization of the Back Contact of CIGS Solar Cell as the Origin of "Rollover" Effect". eng. In: *32nd European Photovoltaic Solar Energy Conference and Exhibition; 1085-1088* (2016). DOI: 10.4229/eupvsec20162016-3ao.5.3.
- [66] Tetiana Lavrenko, Thomas Ott, and Thomas Walter. "Impact of sulfur and gallium gradients on the performance of thin film Cu(In,Ga)(Se,S)<sub>2</sub> solar cells". In: *Thin Solid Films* 582 (2015), pp. 51–55. DOI: 10.1016/j.tsf.2014.11.024.
- [67] B. J. Mueller, C. Zimmermann, V. Haug, F. Hergert, T. Koehler, S. Zweigart, and U. Herr. "Influence of different sulfur to selenium ratios on the structural and electronic properties of Cu(In,Ga)(Se,S)<sub>2</sub> thin film and solar cells formed by the stacked elemental layer process". In: *Journal of Applied Physics* 116 (2014), p. 174503. DOI: 10.1063/1.4900991.
- [68] Tomas Drobiazg, Ludovic Arzel, Adem Dönmez, Pawel Zabierowski, and Nicolas Barreau. "Influence of the indium/gallium gradients on the Cu(In,Ga)Se<sub>2</sub> devices deposited by the co-evaporation with recrystallization". In: *Thin Solid Films* 582 (2015), pp. 47–50. DOI: <https://doi.org/10.1016/j.tsf.2014.09.069>.
- [69] Adrian Chirila, Stephan Buecheler, Fabian Pianezzi, Patrick Bloesch, Christina Gretener, Alexander R. Uhl, Carolin Fella, Lukas Kranz, Julian Perrenoud, Sieghard Seyrling, Rajneesh Verma, Shiro Nishiwaki, Yaroslav E. Romanyuk, Gerhard Bilger, and Ayodhya N. Tiwari. "High efficient Cu(In,Ga)Se<sub>2</sub> solar cells grown on flexible polymer films". In: *Nature Materials* 10 (2011), pp. 857–861. DOI: 10.1038/NMAT3122.
- [70] V. Probst, F. Hergert, B. Walther, R. Thyen, G. Batereau-Neumann, A. Windeck, T. Letzig, and A. Gerlach. "High Performance CIS Solar Modules: Status of Production and Development at Johanna Solar Technology". In: *24th European Solar Energy Conference*. 2009, pp. 2455–2459. DOI: 10.4229/24thEUPVSEC2009-3DO.6.2.
- [71] V. Alberts. "Band gap optimization in Cu (In 1- x Ga x)(Se 1- y S y) <sub>2</sub> by controlled Ga and S incorporation during reaction of Cu-(In, Ga) intermetallics in H<sub>2</sub> Se and H<sub>2</sub> S". In: *Thin solid films* 517.7 (2009), pp. 2115–2120.
- [72] Sunghun Jung, Sejin Ahn, Jae Ho Yun, Jihye Gwak, Donghwan Kim, and Kyunghoon Yoon. "Effects of Ga contents on properties of CIGS thin films and solar cells fabricated by co-evaporation technique". In: *Current Applied Physics* 10.4 (July 2010), pp. 990–996. DOI: 10.1016/j.cap.2009.11.082.
- [73] M. Bär, W. Bohne, J. Röhrich, E. Strub, S. Lindner, M. C. Lux-Steiner, Ch.-H. Fischer, T. P. Niesen, and F. Karg. "Determination of the band gap depth profile of the pentenary Cu(In(1-x)Ga<sub>x</sub>(S<sub>y</sub>Se(1-y)))<sub>2</sub> chalcopyrite from its composition gradient". In: *Journal of Applied Physics* 96 (2004), p. 3857. DOI: <https://doi.org/10.1063/1.1786340>.
- [74] Steven S. Hegedus and William N. Shafarman. "Thin-Film Solar Cells: Device Measurements and Analysis". In: *Progress in Photovoltaics: research and applications* 12 (2004), pp. 155–176. DOI: 10.1002/pip.518.
- [75] John M. Raguse, Christopher P. Muzzillo, James R. Sites, and Lorelle Mansfield. "Effects of Sodium and Potassium on the Photovoltaic Performance of CIGS Solar Cells". In: *IEEE Journal of Photovoltaics* 7.1 (Jan. 2017), pp. 303–306. DOI: 10.1109/jphotov.2016.2621343.

- [76] R. Wuerz, A. Eicke, F. Kessler, S. Paetel, S. Efimenko, and C. Schlegel. "CIGS thin-film solar cells and modules on enamelled steel substrates". In: *Solar Energy Materials & Solar Cells* 100 (2012), pp. 132–137. DOI: 10.1016/j.solmat.2012.01.004.
- [77] T. Walter, R. Herberholz, C. Müller, and H. W. Schock. "Determination of defect distributions from admittance measurements and application to Cu(In,Ga)Se<sub>2</sub> based heterojunctions". In: *Journal of Applied Physics* (1996).
- [78] G. Hanna, A. Jasenek, U. Rau, and H. W. Schock. "Influence of the Ga-content on the bulk defect densities of Cu(In,Ga)Se<sub>2</sub>". In: *Thin Solid Films* 387.1-2 (2001), pp. 71–73.
- [79] R. Herberholz, M. Igalson, and H. W. Schock. "Distinction between bulk and interface states in CuInSe<sub>2</sub>/CdS/ZnO by space charge spectroscopy". In: *Journal of Applied Physics* 83.1 (1998).
- [80] Thomas Walter. "Capacitance Spectroscopy of Semiconductors". In: ed. by Jian V. Li and Giorgio Ferrari. Pan Stanford Publishing Pte. Ltd., 2018. Chap. Admittance Spectroscopy.
- [81] Markus Gloeckler. "Device physics of Cu(In,Ga)Se<sub>2</sub> thin-film solar cells". PhD thesis. Colorado State University, 2005.
- [82] Uwe Rau. "Reciprocity relation between photovoltaic quantum efficiency and electroluminescent emission of solar cells". In: *Physical Review B* 76 (2007), p. 085303. DOI: 10.1103/PhysRevB.76.085303.
- [83] Uwe Rau. "Superposition and Reciprocity in the Electroluminescence and Photoluminescence of Solar Cells". In: *IEEE Journal of Photovoltaics* 2.2 (Apr. 2012), pp. 169–172. DOI: 10.1109/JPHOTOV.2011.2179018.
- [84] Jennifer T. Heath, J. David Cohen, and William N. Shafarman. "Bulk and metastable defects in CuIn<sub>1-x</sub>Ga<sub>x</sub>Se<sub>2</sub> thin films using drive-level capacitance profiling". In: *Journal of Applied Physics* 95.3 (2004), pp. 1000–1010. DOI: 10.1063/1.1633982.
- [85] G. Sozzi, M. Lazzarini, R. Menozzi, R. Carron, E. Avancini, B. Bissig, S. Buecheler, and A. N. Tiwari. "A numerical study of the use of C-V characteristics to extract the doping density of CIGS absorbers". In: *2016 IEEE 43rd Photovoltaic Specialists Conference (PVSC)*. 2016, pp. 2283–2288. DOI: 10.1109/PVSC.2016.7750043.
- [86] Bart Vermang, Viktor Fjällström, Jonas Pettersson, Pedro Salome, and Marika Edoff. "Development of rear surface passivated Cu(In,Ga)Se<sub>2</sub> thin film solar cells with nano-sized local rear point contacts". In: *Solar Energy Materials & Solar Cells* 117 (2013), pp. 505–511. DOI: 10.1016/j.solmat.2013.07.025.
- [87] Bart Vermang, Jörn Timo Wätjen, Viktor Fjällström, Fredrik Rostvall, Marika Edoff, Ratan Kotipalli, Frederic Henry, and Denis Flandre. "Employing Si solar cell technology to increase efficiency of ultra-thin Cu(In,Ga)Se<sub>2</sub> solar cells". In: *Progress in Photovoltaics: research and applications* 22 (2014), pp. 1023–1029. DOI: 10.1002/pip.2527.
- [88] C. Donolato. "An alternative proof of the generalized reciprocity theorem for charge collection". In: *Journal of Applied Physics* 66.1 (1989), pp. 4524–4525. DOI: 10.1063/1.343932.
- [89] O. Lundberg, M. Edoff, and L. Stolt. "The effect of Ga-grading in CIGS thin film solar cells". In: *Thin Solid Films* 480-481 (2004), pp. 520–525. DOI: 10.1016/j.tsf.2004.11.080.
- [90] Arturo Morales-Acevedo. "V<sub>process</sub> band-gap semiconductors as the basis of new solar cells". In: *Solar Energy* 83 (2009), pp. 1466–1471. DOI: 10.1016/j.solener.2009.04.004.
- [91] Alex Niemegeers, Marc Burgelman, Koen Decock, Johan Verschraegen, and Stefaan Degraeve. *SCAPS manual*. Universiteit Gent. 2015.

- [92] Marc Burgelman and Jonas Marlein. "Analysis of graded band gap solar cells with SCAPS". In: *23rd European Photovoltaic Solar Energy Conference*. 2008.
- [93] Michal Cwil, Malgorzata Igalson, Pawel Zabierowski, and Susanne Siebentritt. "Charge and doping distributions by capacitance profiling in Cu(In,Ga)Se<sub>2</sub> solar cells". In: *Journal of Applied Physics* 103 (2008), p. 063701. DOI: 10.1063/1.2884708.
- [94] A. Niemegeers, M. Burgelman, R. Herberholz, U. Rau, D. Hariskos, and H.-W. Schock. "Model for electronic transport in Cu(In,Ga)Se<sub>2</sub> solar cells". In: *Progress in Photovoltaics: Research and Applications* 6.6 (Nov. 1998), pp. 407–421. DOI: 10.1002/(sici)1099-159x(199811/12)6:6<407::aid-pip230>3.0.co;2-u.
- [95] Tetiana Lavrenko, Francillina Robert Runai, Yue Wang, Marcel Teukam, Thomas Walter, Thomas Hahn, and Paul Pistor. "Advanced luminescence imaging of CIGS solar cells". In: *27th European Photovoltaic Solar Energy Conference and Exhibition*. 2012, pp. 2174–2178. ISBN: 3-936338-28-0. DOI: 10.4229/27thEUPVSEC2012-3B0.4.3.
- [96] Rou Hua Chua, Xianglin Li, Thomas Walter, Lay Kuan Teh, Thomas Hahn, Frank Hergert, Subodh Mhaisalkar, and Lydia Helena Wong. "An experimentally supported model for the origin of charge transport barrier in Zn(O,S)/CIGS<sub>2</sub> solar cells". In: *Applied Physics Letters* 108.4 (Jan. 2016), p. 043505. DOI: 10.1063/1.4940913.
- [97] Uli Würfel, Dieter Neher, Annika Spies, and Steve Albrecht. "Impact of charge transport on current–voltage characteristics and power-conversion efficiency of organic solar cells". In: *Nature Communications* 6.1 (Apr. 2015). DOI: 10.1038/ncomms7951.
- [98] A. O. Pudov, A. Kanevce, H. A. Al-Thani, J. R. Sites, and F. S. Hasoon. "Secondary barrier in CdS-CuIn<sub>1-x</sub>Ga<sub>x</sub>Se<sub>2</sub> solar cells". In: *Journal of Applied Physics* 97 (2005), p. 064901. DOI: 10.1063/1.1850604.
- [99] Chien-Yao Huang, Wen-Chin Lee, and Albert Lin. "A flatter gallium profile for high-efficiency Cu(In,Ga)(Se,S)<sub>2</sub> solar cell and improved robustness against sulfur-gradient variation". In: *Journal of Applied Physics* 120 (2016), p. 094502. DOI: <http://dx.doi.org/10.1063/1.4961605>.
- [100] R. Klenk, R. H. Mauch, R. Menner, and H. W. Schock. "Wide bandgap Cu(In,Ga)Se<sub>2</sub>/(Zn,Cd)S heterojunctions". In: *20th IEEE PVSC*. 1988, pp. 1443–1447.
- [101] T. Dullweber, O. Lundberg, J. Malmström, M. Bodegard, L. Stolt, U. Rau, H. W. Schock, and J. H. Werner. "Back surface band gap gradings in Cu(In,Ga)Se<sub>2</sub> solar cells". In: *Thin Solid Films* 387 (2001), pp. 11–13.
- [102] V. Nadenau, U. Rau, A. Jasenek, and H. W. Schock. "Electronic properties of CuGaSe<sub>2</sub>-based heterojunction solar cells. Part I. Transport analysis". In: *Journal of Applied Physics* 87.1 (2000), p. 584.
- [103] Chien-Yao Huang, Wen-Chin Lee, and Albert Lin. "A flatter gallium profile for high-efficiency Cu(In,Ga)(Se,S)<sub>2</sub> solar cell and improved robustness against sulfur-gradient variation". In: *Journal of Applied Physics* 120.9 (Sept. 2016), p. 094502. DOI: 10.1063/1.4961605.
- [104] Thomas Walter and Hans-Werner Schock. "Crystal growth and diffusion in Cu(In,Ga)Se<sub>2</sub> chalcopyrite thin films". In: *Thin Solid Films* 224 (1993), pp. 74–81.
- [105] Wolfram Witte, Daniel Abou-Ras, Karsten Albe, Gottfried H. Bauer, Frank Bertram, Christian Boit, Rudolph Brüggemann, Jürgen Chisten, Jens Dietrich, Axel Eicke, Dimitrios Hariskos, Matthias Maiberg, Roland Mainz, Max Meessen, Matthias Müller, Oliver Neumann, Thomas Orgis, Stefan Paetel, Johan Pohl, Humberto Rodriguez-Alvarez, Roland Scheer, Hans-Werner Schock, Thomas Unold, Alfons Weber, and Michael Powalla. "Gallium gradients in Cu(In,Ga)Se<sub>2</sub> thin-film solar cells". In: *Progress in Photovoltaics: research and applications* 23 (2015), pp. 717–733. DOI: 10.1002/pip.2485.

- [106] Jürgen H. Werner. "Schottky Barrier and pn-Junction I/V Plots - Small Signal Evaluation". In: *Applied Physics A: Solids and Surfaces* (1988).
- [107] Thomas Orgis, Matthias Maiberg, and Roland Scheer. "Influence of band gradients on Cu(In,Ga)Se<sub>2</sub> solar cell diode factors". In: *Journal of applied physics* 114 (2013), p. 214506. doi: 10.1063/1.4840995.
- [108] Michael Richter, M. S. Hammer, T. Sonnet, and J. Parisi. "Bandgap extraction from quantum efficiency spectra of Cu(In,Ga)Se<sub>2</sub> solar cells with varied grading profile and diffusion length". In: *Thin Solid Films* 633 (2016), pp. 213–217. doi: 10.1016/j.tsf.2016.08.022.
- [109] M. Troviano and K. Taretto. "Analysis of internal quantum efficiency in double-graded Bbandg solar cells including sub-bandgap absorption". In: *Solar Energy Materials & Solar Cells* 95 (2011), pp. 821–828. doi: 10.1016/j.solmat.2010.10.028.
- [110] Su-Huai Wei and Alex Zunger. "Band offsets and optical bowings of chalcopyrites and Zn-based II-VI alloys". In: *Journal of Applied Physics* 78.6 (1995), p. 3846.
- [111] Mirjam Theelen and Felix Daume. "Stability of Cu(In,Ga)Se<sub>2</sub> solar cells: A literature review". In: *Solar Energy* 133 (2016), pp. 586–627. doi: 10.1016/j.solener.2016.04.010.
- [112] P. C. Huang, C. C. Sung, J. H. Chen, C. H. Huang, and C. Y. Hsu. "The optimization of a Mo bilayer and its application in Cu(In,Ga)Se<sub>2</sub> solar cells". In: *Applied Surface Science* 425 (2017), pp. 24–31. doi: 10.1016/j.apsusc.2017.06.247.
- [113] Kay Orgassa. "Coherent optical analysis of the ZnO/CdS/Cu(In,Ga)Se<sub>2</sub> thin film solar cell". PhD thesis. University of Stuttgart, 2004.
- [114] Xiaolong Zhu, Zhen Zhou, Yaoming Wang, Lei Zhang, Aimin Li, and Fuqiang Huang. "Determining factor of MoSe<sub>2</sub> formation in Cu(In,Ga)Se<sub>2</sub> solar cells". In: *Solar Energy Materials & Solar Cells* 101 (2012), pp. 57–61. doi: 10.1016/j.solmat.2012.02.015.
- [115] A. Duchatelet, G. Savidand, R. N. Vannier, and D. Lincot. "Optimization of MoSe<sub>2</sub> formation for Cu(In,Ga)Se<sub>2</sub>-based solar cells by using thin superficila molybdenum oxide barrier layers". In: *Thin Solid Films* 545 (2013), pp. 94–99. doi: 10.1016/j.tsf.2013.07.038.
- [116] Xiaofeng Ma, Dingquan Liu, Lihong Yang, Shaohua Zuo, and Ming Zhou. "Molybdenum (Mo) back contacts for CIGS solar cells". In: *Proceedings of 8th International Conference on Thin Film Physics and Applications*. Vol. 9068. 2013, p. 906814. doi: 10.1117/12.2053498.
- [117] W. Jägermann, T. Löher, and C. Pettenkofer. "Surface properties of chalcopyrite semiconductors". In: *Crystal Research and Technology* 31 (1996), p. 273.
- [118] Thomas Ott, Thomas Walter, Dimitrios Hariskos, Oliver Kiowski, and Raymund Schärer. "Accelerated ageing and contact degradation of CIGS solar cells". In: *IEEE Journal of Photovoltaics* 3.1 (2013), pp. 514–519. doi: 10.1109/JPHOTOV.2012.2226141.
- [119] Dennis Muecke, Tetiana Lavrenko, Ricardo Vidal Lorbada, and Thomas Walter. "On the Determination of the Back Contact Barrier Height of Cu(In,Ga)(S,Se)<inf>2</inf> Thin Film Solar Cells". In: *2018 IEEE 7th World Conference on Photovoltaic Energy Conversion (WCPEC) (A Joint Conference of 45th IEEE PVSC, 28th PVSEC & 34th EU PVSEC)*. IEEE, June 2018. doi: 10.1109/pvsc.2018.8547841.
- [120] A. Rockett, J. K. J. van Duren, A. Pudov, and W. N. Shafarman. "First quadrant phototransistor behavior in CuInSe<sub>2</sub> photovoltaics". In: *Solar Energy Materials & Solar Cells* 118 (2013), pp. 141–148. doi: http://dx.doi.org/10.1016/j.solmat.2013.07.032.
- [121] Y. Roussillon, V. G. Karpov, Diana Shvydka, J. Drayton, and A. D. Compaan. "Back contact and reach-through diode effects in thin-film photovoltaics". In: *Journal of Applied Physics* 96.12 (Dec. 2004), pp. 7283–7288. doi: 10.1063/1.1808902.

- [122] Y. Roussillon, D. M. Giolando, V. G. Karpov, Diana Shvydka, and A. D. Compaan. "Reach-through band bending in semiconductor thin films". In: *Applied Physics Letters* 85.16 (Oct. 2004), pp. 3617–3619. doi: 10.1063/1.1803950.
- [123] T. Ott, T. Walter, and R. Schäffler. "On the Interpretation of Admittance and IV(T) Measurements of CIGS Thin Film Solar Cells". In: *31st European Photovoltaic Solar Energy Conference and Exhibition*. 2015, pp. 1014–1018. doi: 10.4229/EUPVSEC20152015-3AO.5.2.
- [124] W.-W. Hsu, J. Y. Chen, T.-H. Cheng, S. C. Lu, W.-S. Ho, Y.-Y. Chen, Y.-J. Chien, and C. W. Liu. "Surface passivation of Cu(In,Ga)Se<sub>2</sub> using atomic layer deposited Al<sub>2</sub>O<sub>3</sub>". In: *Applied Physics Letters* 100 (2012), p. 023508. doi: 10.1063/1.3675849.
- [125] R. Caballero, M. Nichterwitz, A. Steigert, A. Eicke, I. Lauermann, H.W. Schock, and C.A. Kaufmann. "Impact of Na on MoSe<sub>2</sub> formation at the CIGSe/Mo interface in thin-film solar cells on polyimide foil at low process temperatures". In: *Acta Materialia* 63 (Jan. 2014), pp. 54–62. doi: 10.1016/j.actamat.2013.09.051.
- [126] Michael Richter, Christian Schubert, Patrick Eraerds, Jürgen Parisi, Ingo Riedel, Thomas Dalibor, and Jörg Palm. "Comprehensive simulation model for Cu(In,Ga)(Se,S)<sub>2</sub> solar cells". In: *Solar Energy Materials and Solar Cells* 132 (Jan. 2015), pp. 162–171. doi: 10.1016/j.solmat.2014.08.047.
- [127] Dorothea Ledinek, Olivier Donzel-Gargand, Markus Sköld, Jan Keller, and Marika Edoff. "Effect of different Na supply methods on thin Cu(In,Ga)Se<sub>2</sub> solar cells with Al<sub>2</sub>O<sub>3</sub> rear passivation layers". In: *Solar Energy Materials and Solar Cells* 187 (Dec. 2018), pp. 160–169. doi: 10.1016/j.solmat.2018.07.017.
- [128] M. Bär, S. Nishiwaki, L. Weinhardt, S. Pookpanratana, W. N. Shafarman, and C. Heske. "Electronic level alignment at the deep buried absorber /Mo interface in chalcopyrite-based thin film solar cells". In: *Applied Physics Letters* 93 (2008), p. 042110. doi: 10.1063/1.2955532.
- [129] Uwe Rau. "Tunneling-enhanced recombination in Cu(In,Ga)Se<sub>2</sub> heterojunction solar cells". In: *Applied Physics Letters* 74.1 (1999), pp. 111–113.
- [130] Andreas Schenk and Ulrich Krumbein. "Coupled defect-level recombination: Theory and application to anomalous diode characteristics". In: *Journal of Applied Physics* 78.5 (Sept. 1995), pp. 3185–3192.
- [131] Jay M. Shah, Y.-L. Li, Th. Gessmann, and E. F. Schubert. "Experimental analysis and theoretical model for anomalously high ideality factors ( $n \gg 2.0$ ) in AlGaIn/GaNp-n junction diodes". In: *Journal of Applied Physics* 94.4 (Aug. 2003), pp. 2627–2630. doi: 10.1063/1.1593218.
- [132] Haeri Kim, Se Jin Park, Byungwoo Kim, Yun Jeong Hwang, and Byoung Koun Min. "Investigation of Surface Sulfurization in CuIn<sub>1-x</sub>Ga<sub>x</sub>S<sub>2-y</sub>Se<sub>y</sub> Thin Films by Using Kelvin Probe Force Microscopy". In: *ChemPhysChem* 19.3 (Jan. 2018), pp. 261–265. doi: 10.1002/cphc.201701019.
- [133] Marcus Baer, L. Weinhardt, C. Heske, S. Nishiwaki, and William Shafarman. "Chemical structures of the Cu(In,Ga)Se<sub>2</sub>/Mo and Cu(In,Ga)(S,Se)<sub>2</sub>/Mo interfaces". In: *Physical Review B* 78.7 (2008), p. 075404. doi: 10.1103/PhysRevB.78.075404.
- [134] Zacharie Jehl Li Kao, Taizo Kobayashi, and Tokio Nakada. "Modeling of the surface sulfurization of CIGSe-based solar cells". In: *Solar Energy* 110 (Dec. 2014), pp. 50–55. doi: 10.1016/j.solener.2014.08.004.
- [135] M. Turcu, I. M. Kötschau, and U. Rau. "Composition dependence of defect energies and band alignments in the Cu(In<sub>1-x</sub>Ga<sub>x</sub>)(Se<sub>1-y</sub>S<sub>y</sub>)<sub>2</sub> alloy system". In: *Journal of Applied Physics* 91.3 (Feb. 2002), pp. 1391–1399. doi: 10.1063/1.1432126.

- [136] Tokio Nakada, Hiroki Ohbo, Takayuki Watanabe, Hidenobu Nakazawa, Masahiro Matsui, and Akio Kunioka. "Improved Cu(In,Ga)(S,Se)<sub>2</sub> thin film solar cells by surface sulfurization". In: *Solar Energy Materials & Solar Cells* 49 (1997), pp. 285–290.
- [137] Sheng-Hui Chen, Wei-Ting Lin, Shih-Hao Chan, Shao-Ze Tseng, Chien-Cheng Kuo, Sung-Cheng Hu, Wan-Hsuan Peng, and Yung-Tien Lu. "Photoluminescence Analysis of CdS/CIGS Interfaces in CIGS Solar Cells". In: *ECS Journal of Solid State Science and Technology* 4.9 (2015), P347–P350. doi: 10.1149/2.0041509jss.
- [138] D. Ohashi, T. Nakada, and A. Kunioka. "Improved CIGS thin-film solar cells by surface sulfurization using In<sub>2</sub>S<sub>3</sub> and sulfur vapor". In: *Solar Energy Materials & Solar Cells* 67 (2001), pp. 261–265.
- [139] B. D. Ajalkar, S. H. Burungale, D. S. Bhangе, and P. N. Bhosale. "Chemical synthesis and compositional analysis of mixed [Mo(S<sub>1-x</sub>Se<sub>x</sub>)<sub>2</sub>] semiconductor thin films". In: *Journal of Materials Science* 39 (2004), pp. 1659–1664.
- [140] Shin-Hom Lin, Jen-Cheng Sung, and Chung-Hsin Lu. "Effects of the surface sulfurization reactions on the structural and photovoltaic properties of Cu(In,Ga)(Se,S) <sub>2</sub> solar cells". In: *Thin Solid Films* 616 (Oct. 2016), pp. 746–753. doi: 10.1016/j.tsf.2016.08.004.
- [141] U. Rau, M. Schmitt, F. Engelhardt, O. Seifert, J. Parisi, W. Riedl, J. Rimmasch, and F. Karg. "Impact of Na and S incorporation on the electronic transport mechanisms of Cu(In, Ga)Se<sub>2</sub> solar cells". In: *Solid State Communications* 107.2 (May 1998), pp. 59–63. doi: 10.1016/s0038-1098(98)00154-9.
- [142] Matthias Maiberg, Torsten Hölscher, Enrico Jarzembowski, Stefan Hartnauer, Setareh Zahedi-Azad, Wolfgang Fränzel, and Roland Scheer. "Verification of minority carrier traps in Cu(In,Ga)Se <sub>2</sub> and Cu <sub>2</sub> ZnSnSe <sub>4</sub> by means of time-resolved photoluminescence". In: *Thin Solid Films* 633 (July 2017), pp. 208–212. doi: 10.1016/j.tsf.2017.02.002.
- [143] Matthias Maiberg, Torsten Hölscher, Setareh Zahedi-Azad, and Roland Scheer. "Theoretical study of time-resolved luminescence in semiconductors. III. Trap states in the band gap". In: *Journal of Applied Physics* 118.10 (Sept. 2015), p. 105701. doi: 10.1063/1.4929877.
- [144] Th. Glatzel, S. Sadewasser, R. Shikler, Y. Rosenwaks, and M.Ch. Lux-Steiner. "Kelvin probe force microscopy on III–V semiconductors: the effect of surface defects on the local work function". In: *Materials Science and Engineering: B* 102.1-3 (Sept. 2003), pp. 138–142. doi: 10.1016/s0921-5107(03)00020-5.
- [145] T. Lavrenko, T. Walter, and B. Plesz. "On the Interpretation of Photoluminescence and Vibrating Kelvin Probe Method for Quality Control of Cu(in,Ga)(Se,S)<sub>2</sub> Thin Films". eng. In: (2016). doi: 10.4229/eupvsec20162016-3cv.4.4.
- [146] Alex Redinger, Sergiu Levcenko, Charles J. Hages, Dieter Greiner, Christian A. Kaufmann, and Thomas Unold. "Time resolved photoluminescence on Cu(In, Ga)Se<sub>2</sub> absorbers: Distinguishing degradation and trap states". In: *Applied Physics Letters* 110.12 (Mar. 2017), p. 122104. doi: 10.1063/1.4977707.
- [147] W.K. Metzger, I.L. Repins, M. Romero, P. Dippo, M. Contreras, R. Noufi, and D. Levi. "Recombination kinetics and stability in polycrystalline Cu(In,Ga)Se<sub>2</sub> solar cells". In: *Thin Solid Films* 517.7 (Feb. 2009), pp. 2360–2364. doi: 10.1016/j.tsf.2008.11.050.
- [148] Sho Shirakata and Tokio Nakada. "Time-resolved photoluminescence in Cu(In,Ga)Se<sub>2</sub> thin films and solar cells". In: *Thin Solid Films* 515.15 (May 2007), pp. 6151–6154. doi: 10.1016/j.tsf.2006.12.040.

- 
- [149] Wyatt K. Metzger, Ingrid L. Repins, and Miguel A. Contreras. "Long lifetimes in high-efficiency Cu(In,Ga)Se<sub>2</sub> solar cells". In: *Applied Physics Letters* 93.2 (July 2008), p. 022110. DOI: 10.1063/1.2957983.
- [150] M. Gloeckler and J.R. Sites. "Band-gap grading in Cu(In,Ga)Se<sub>2</sub> solar cells". In: *Journal of Physics and Chemistry of Solids* 66.11 (Nov. 2005), pp. 1891–1894. DOI: 10.1016/j.jpcs.2005.09.087.



# Tetiana Lavrenko

## Curriculum vitae

Johann-Stockar-Weg 25  
D-89075, Ulm, Germany  
✉ tetiana.lavrenko@thu.de



---

### Personal data

First name Tetiana  
Family name Lavrenko  
Date of birth 9<sup>th</sup> of October, 1986  
Place of birth Ukraine  
Nationality Ukrainian  
Place of residence Johann-Stockar-Weg 25, 89075 Ulm, Germany  
E-mail tetiana.lavrenko@thu.de

---

### Educational background

since 2011 **Technische Hochschule Ulm**, *Research Assistant*,  
with the prospect of obtaining PhD.  
2010 – 2011 **M.Sc.**, *Master Degree in Solar Energy Engineering*,  
Dalarna University,  
Borlaenge, Sweden.  
2008 – 2010 **Specialist**, *Specialist Degree in Electronic Banking Systems and Protection of  
Information*,  
National Technical University of Ukraine,  
Kiev Polytechnic Institute.  
2004 – 2008 **B.Sc.**, *Bachelor Degree in Electronic Devices*,  
National Technical University of Ukraine,  
Kiev Polytechnic Institute.

---

### Criminal record

There are no criminal records, nor a preliminary investigation has been initiated.